Mathematical Models of Wound Healing

Jonathan Adam Sherratt

Lincoln College
Oxford

A thesis submitted in partial fulfilment of the requirements for the degree of Doctor of Philosophy at the University of Oxford

Trinity Term 1991

Abstract

Jonathan Adam Sherratt

Lincoln College, Oxford

Thesis submitted for
the degree of D.Phil.

Trinity term 1991

Mathematical Models of Wound Healing

The complex mechanisms responsible for mammalian wound healing raise many biological questions that are amenable to theoretical investigation. In the first part of this thesis, we consider the role of mitotic auto-regulation in adult epidermal wound healing. We develop a reaction-diffusion model for the healing process, with parameter values based on biological data. The model solutions compare well with experimental results on the normal healing of circular wounds, and we analyse the solutions in one spatial dimension as travelling waves. We then use the model to perform 'mathematical experiments' on the effects of adding mitosis-regulating chemicals and of varying the initial wound shape.

Recent experiments suggest that in embryos, epidermal wound healing occurs not by lamellipodial crawling as in adults, but rather by contraction of a cable of filamentous actin at the wound edge. We focus on the formation of this cable as a response to wounding, and develop and analyse a mechanical model for the post-wounding equilibrium in the microfilament network. Our model reflects the well-documented phenomenon of stress-induced alignment of actin filaments, which has been neglected in previous mechanochemical models of tissue deformation. The model solutions reflect the key aspects of the experimentally observed response to wounding.

In the final part of the thesis, we consider chemokinetic and chemotactic control of cell movement, which play an important role in many aspects of wound healing. We propose a new model which reflects the underlying receptor-based mechanisms, and apply it to endothelial cell movement in the Boyden chamber assay. We compare our model with a simpler scheme in which cells respond directly to gradients in extracellular chemical concentration, and for both models we use experimental data to make quantitative predictions on the values of the transport coefficients.

Acknowledgements

I would like to express my deep gratitude to Prof. J. D. Murray, who supervised the first part of my doctoral research, and without whose guidance and inspiration this thesis would not have been possible, and to Dr. P. K. Maini, whose help and support during his supervision of the last part of the work has been invaluable. I have been very fortunate to have the opportunity of working directly with experimental biologists in the course of my research, and I am very grateful to Dr. Julian Lewis (ICRF, Oxford), Dr. Paul Martin (Dept. of Human Anatomy, University of Oxford) and Dr. Helene Sage (Dept. of Biological Structure, University of Washington) for our numerous discussions. I am also grateful to my fellow graduate students, who have made the Centre for Mathematical Biology such an enjoyable and productive place to work: Debbie Benson, Daniel Bentil, Meghan Burke, David Crawford, Gerhard Cruywagen, Mick Jenkins, Mark Lewis, Gideon Ngwa, Robert Payne, Faustino Sanchez-Garduno and Louisa Shaw. I have learned a great deal from talking to our many visitors, and I would particularly like to thank Dr. Wendy Brandts (Dept. of Physics, University of Toronto), Dr. Peter Monk (Dept. of Mathematical Sciences, University of Delaware) and Dr. James Sneyd (Dept. of Biomathematics, UCLA).

At a more specific level, I am indebted to Jeremy Martin (OUCS) for help with the Simpleplot package, Malcolm Austin (OUCS) for help with Figure 4.14, Tom Milac (Dept. of Applied Mathematics, University of Washington) for initial help with computing, Dr. Katherine Sprugel (Zymogenetics, Seattle) for introducing me to the Boyden Chamber assay, Dr. Paul Martin for providing the photographs in Figures 3.1 and 3.2, and Prof. J. Kevorkian (Dept. of Applied Mathematics, University of Washington) for excellent instruction in singular perturbation theory. My doctoral research was funded by a graduate studentship from the Science and Engineering Research Council of Great Britain. Finally, sincere thanks to my family and Seana for all their support and encouragement, which has at times made all the difference.

Contents

Introduction: the Biology of Wound Healing

Adult mammalian skin is composed of two parts, as illustrated in Figure 0.1. The outer part is called the epidermis, and consists of several layers of cells. The columnar basal cells undergo frequent mitosis to renew the layers above, and as layers are displaced upwards by these new generations of cells, the tough, fibrous protein keratin accumulates in their interior. The keratin gradually replaces cytoplasm until the cells die, when they are said to be 'keratinized' or 'cornified'. Such cells constitute the external layer of the epidermis, and are gradually sloughed.

Beneath the epidermis is the dermis. They are separated by a basal lamina, and the junction is not flat, but rather has projections of epidermis down into the dermis, known as 'rete ridges', which help to anchor the epidermis (Peacock, 1984). The dermis contains blood vessels, which are not present in the epidermis, nerves, collagen fibres, elastin fibres, pigment cells, fat cells, and fibroblasts. These are embedded in 'ground substance', an amorphous mixture of water, electrolytes, glycoproteins and proteoglycans (Irvin, 1984). In humans, the thickness of the dermis varies from about 1mm on the scalp to about 4mm on the back; the epidermis is about 0.1mm thick (Odland, 1983). Beneath the dermis, but not sharply delimited from it, is a 'subcutaneous layer'. This consists predominantly of fat cells, with blood vessels and nerves also present. It is not considered to be part of the skin.

Mammalian skin contains many hairs. These grow by rapid proliferation of cells in the hair follicle, which, although an epidermal structure, is sunk into the dermis (Figure 0.1); the hair shaft consists of keratinized cells. There are also a wide variety of glands in mammalian skin. In particular, sweat and sebaceous glands can act as sources of epidermal cells after wounding (see page 7).

The overall features of the healing of a full depth wound in mammalian skin are represented in Figure 0.2. The immediate response to injury is vascular. Blood ves-

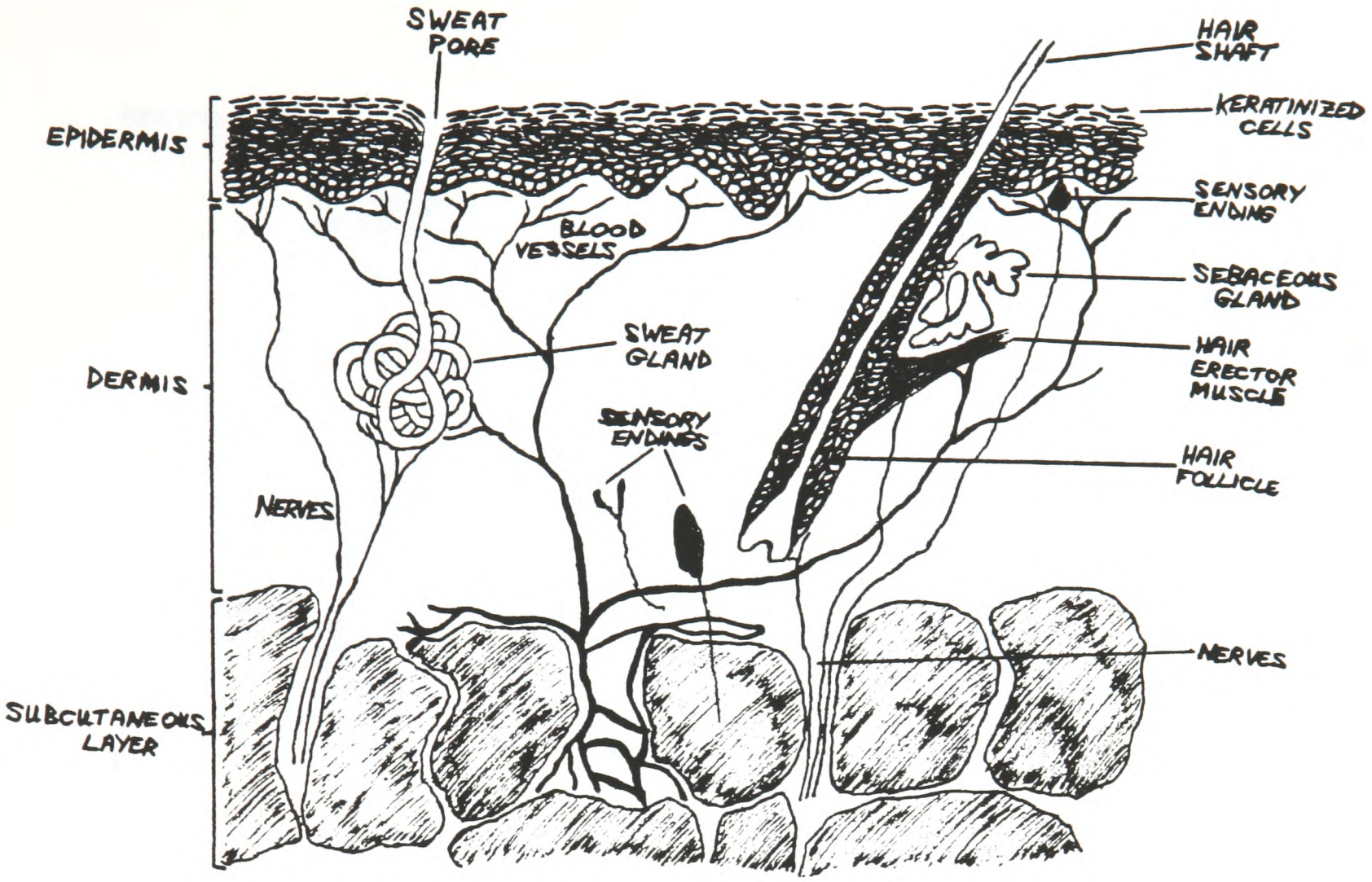

Figure 0.1: A diagrammatic representation of a section through adult mammalian skin.

sel disruption leads to extravasation of blood and blood coagulation, as reviewed by Dvorak *et al.* (1988) and Furie and Furie (1988). This results in the formation of a blood clot (Figure 0.2b) composed of cross-linked fibrin, fibronectin and platelets, that together entrap plasma water, plasma proteins and blood cells, principally erythrocytes. Thus the blood clot is an insoluble water-binding gel (Dvorak *et al.*, 1988).

As the blood clot forms, several types of leukocytes (white blood cells) migrate into the wound, in response to a variety of chemotactic factors (Leibovich and Wiseman, 1988). Neutrophils arrive first, and their primary function is the removal of contaminating bacteria, by phagocytosis and intracellular killing (Clark, 1989). Shortly afterwards, monocytes appear. Upon leaving the blood and entering tissue, these cells differentiate into active phagocytes called macrophages (Gordon, 1986). Macrophages play a much more important role in wound healing than neutrophils: in addition to phagocytosis, they are an important source of regulatory biochemicals (Grotendorst

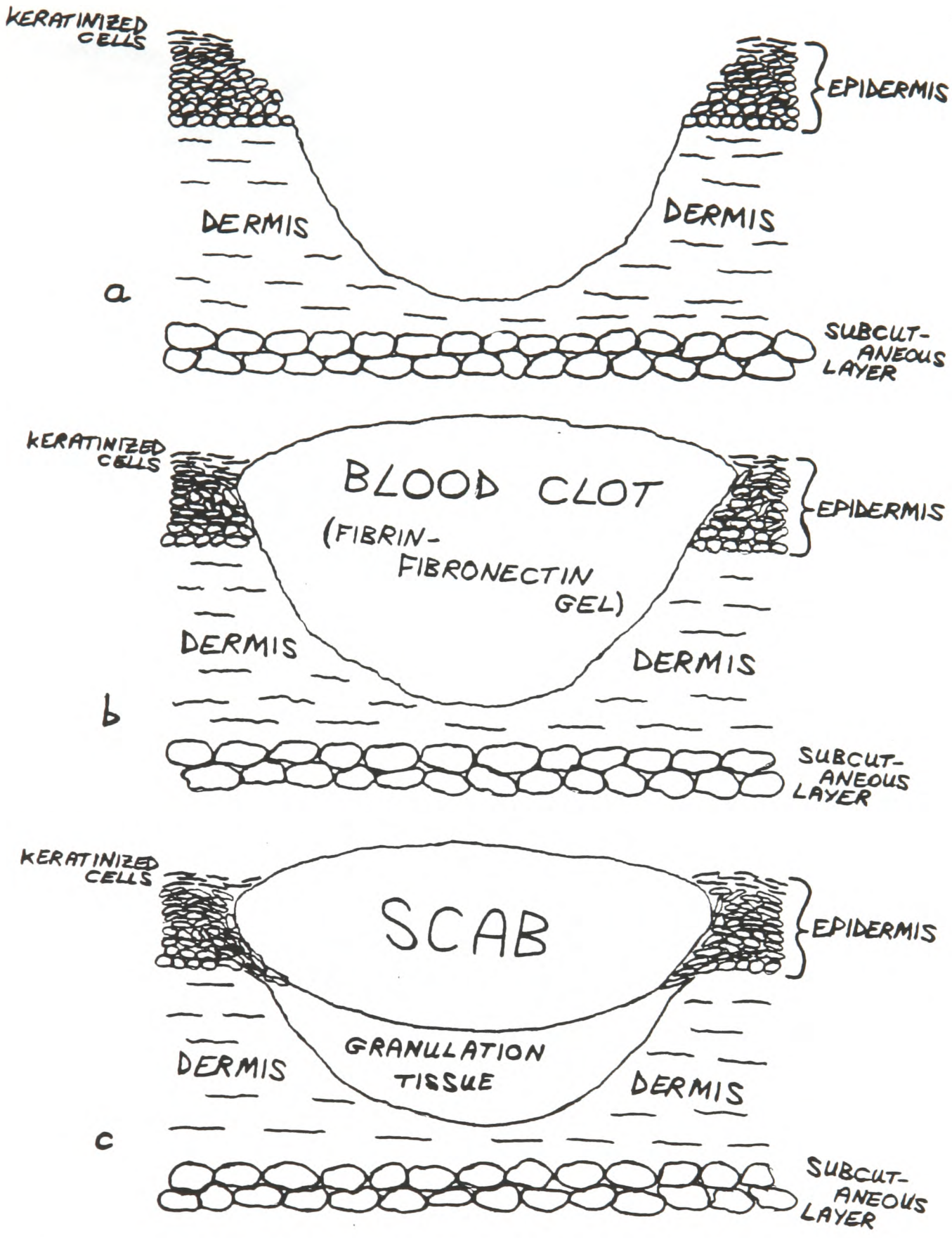

Figure 0.2: A diagrammatic representation of the healing of mammalian skin wounds. (a) Immediately after injury. (b) The blood clot has formed. (c) The upper portion of the blood clot has dessicated, giving a scab; neovasculature has formed by angiogenesis, and fibroblasts have invaded the lower portion, forming granulation tissue. (Continued overleaf).

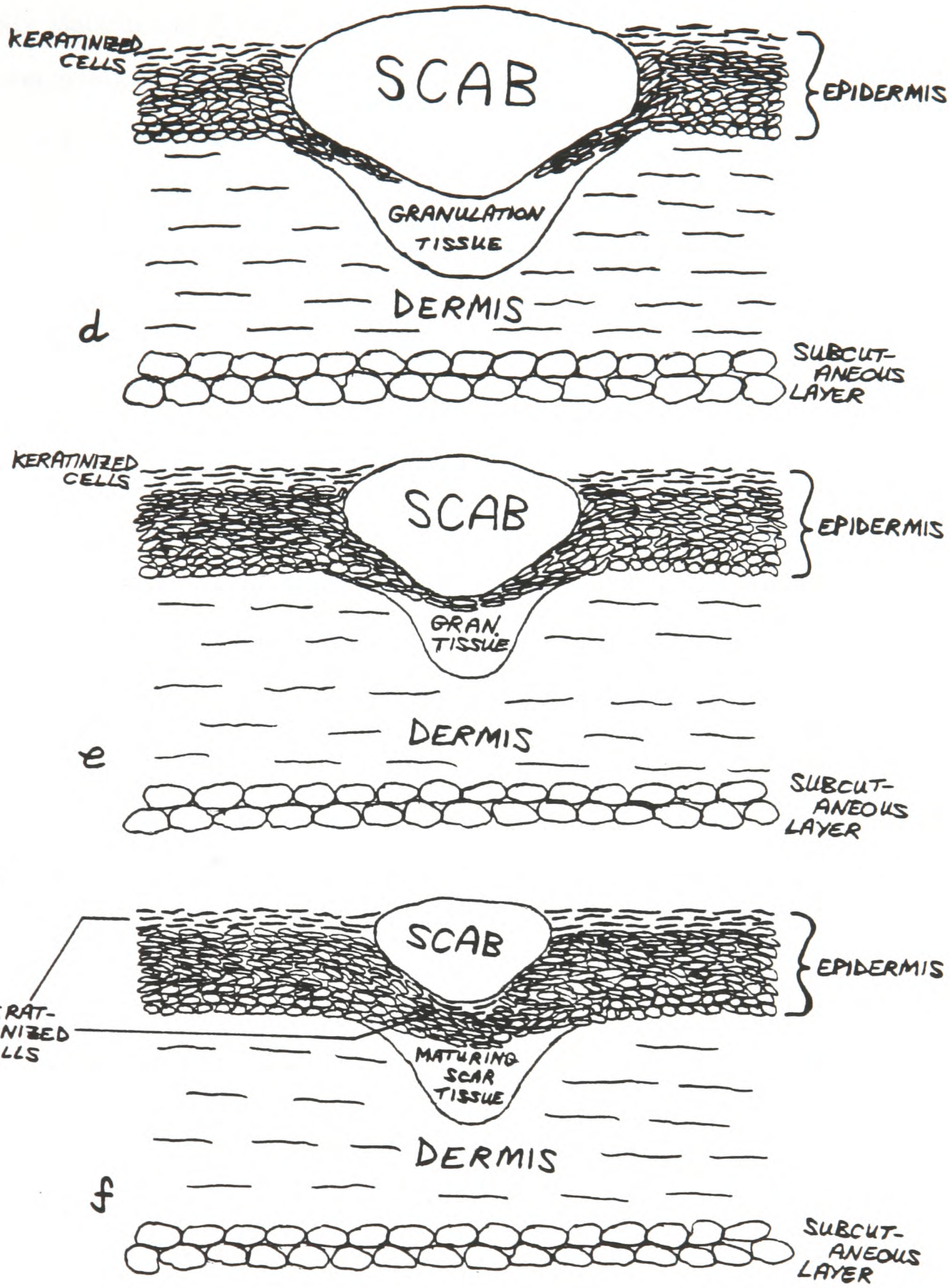

Figure 0.2: A diagrammatic representation of the healing of mammalian skin wounds (continued). (d) Epidermal migration and wound contraction in progress. (e) Epidermal migration and wound contraction complete. (f) Scar tissue has formed and most of the scab has been sloughed.

et al., 1988; Sprugel *et al.*, 1987).

With time, the upper portion of the blood clot dessicates to form the scab, which gradually sloughs during the remainder of the healing process (Dvorak *et al.*, 1988). The lower portion of the clot becomes 'granulation tissue' (Figure 0.2c). This is the fundamental constituent of the healing wound, and consists of a dense population of macrophages, fibroblasts and neovasculature embedded in a loose matrix of collagen, fibronectin and hyaluronic acid (McDonald, 1988). Fibroblasts migrate into the wound space in response to a number of growth and chemotactic factors released by the platelets and macrophages present in the blood clot (Barnes, 1988; Wahl and Allen, 1988). Much of the extracellular matrix of granulation tissue is secreted by fibroblasts (Nusgens *et al.*, 1984), and they also play a major role in matrix organization, via traction morphogenesis (Harris *et al.*, 1981). Simultaneously to this fibroblast influx, neovasculature forms by angiogenesis, that is, capillary buds sprout from blood vessels adjacent to the wound. This process depends on phenotype alteration, migration and proliferation of endothelial cells, and results in a rich vascular supply in granulation tissue (Madri and Pratt, 1988).

As granulation tissue forms, the two processes of wound closure begin (Figure 0.2d). These are epidermal migration, in which epidermal cells spread across the wound between the scab and the granulation tissue, and wound contraction, in which the granulation tissue contracts, causing the wound edges to move inwards. Their relative contributions to closure depend on a variety of factors, such as species, size and site of wound (Peacock, 1984; Snowden *et al.*, 1984). Wound contraction is caused by fibroblasts, which undergo a phenotype change as they migrate into the wound space, forming contractile 'myofibroblasts'. The synchronized contraction of these myofibroblasts, which resemble smooth muscle cells, causes the granulation tissue to contract (Bereiter-Hahn, 1986; Skalli and Gabbianni, 1988). Once the wound has closed, granulation tissue becomes known as scar tissue (Figure 0.2f). From the time of deposition, the extracellular matrix of granulation tissue changes continuously, and this process continues in scar tissue for many months (Clark, 1988; Compton *et al.*, 1989; Forrest, 1983).

In Chapters 1 and 2 of this thesis, we develop a reaction-diffusion model for the healing of epidermal wounds in adult mammalian skin, which has direct application to the process of epidermal migration. Recent experiments in Oxford (Martin and Lewis, 1991a,b) suggest that in embryonic epidermal wounds, the healing mechanism is quite different from that in adults. In Chapters 3 and 4 we use a mechanical model to investigate one aspect of the 'purse string' mechanism proposed by Martin and Lewis (1991a,b). Finally, in Chapter 5 we propose a new model for chemically modulated cell movement. The processes of chemotaxis and chemokinesis are crucial to many aspects of wound healing, in particular the influx of neutrophils and monocytes during the initial 'inflammation' phase of healing, and the movement of fibroblasts and endothelial cells into the wound space during granulation tissue formation. In Chapter 5 we focus on endothelial cells, but a detailed model of chemically controlled cell movement is an important first step in a theoretical understanding of many aspects of the wound healing process.

Chapter 1

Models of Adult Epidermal Wound Healing

1.1 Biological Background

We have described in the Introduction the role of epidermal migration in the healing of full depth wounds in adult mammalian skin. When only the epidermis is injured, epidermal cells again spread across the wound, but without the much more complicated processes of dermal wound healing. Thus epidermal wounds provide a relatively simple context in which to study epidermal migration, a process that is only partially understood. Normal epidermal cells are non-motile, but in the neighbourhood of the wound they undergo marked phenotype alteration ('mobilization') that gives them the ability to move via lamellipodia (Clark, 1989). The main factor controlling cell movement seems to be contact inhibition (Irvin, 1984; Bereiter-Hahn, 1986), although chemotaxis and contact guidance may also be involved (Clark, 1988). Remnants of glands and hair follicles can act as sources of migrating cells, in addition to the wound edges (Winter, 1972; Rudolph, 1980).

Two mechanisms have been proposed for the movement of the cell sheet. In the 'rolling mechanism', the leading cells are successively implanted as new basal cells, and other cells roll over these (Krawczyk, 1971; Winstanley, 1975; Ortonne *et al.*, 1981). In the 'sliding mechanism', on the other hand, the cells in the interior of the sheet respond passively to the pull of the marginal cells, although all of the migrating cells do have the potential to be motile, since if a gap opens up in the migrating sheet, cells at the boundary of the gap develop lamellipodia and move inwards to close it (Trinkaus, 1984). Though the morphological data of mammalian epidermal wound healing are convincingly explained by the rolling mechanism (Stenn and DePalma, 1988), unequivocal evidence is lacking, whereas the sliding mechanism

is well documented in simpler systems such as amphibian epidermal wound closure (Radice, 1980).

Soon after the onset of epidermal migration, mitotic activity increases in a band of epidermis near the wound edge, about 1mm wide, providing an additional population of cells (Bereiter-Hahn, 1986; Jensen and Bolund, 1988; el-Ghorab *et al.*, 1988). The greatest mitotic activity is actually at the wound edge, where it can be as much as 15 times the rate in normal epidermis (Winter, 1972; Danjo *et al.*, 1987); activity decreases rapidly across the band, going away from the wound. The stimulus for this increase in mitotic activity is uncertain. Two factors that are certainly involved are the absence of contact inhibition, which applies to mitosis as well as to cell motion (Clark, 1988), and change in cell shape: as the cells spread out they become flatter, which tends to increase their rate of division (Folkman, 1978; Watt, 1988). There is experimental evidence for the production by epidermal cells of chemicals that regulate mitosis, but we postpone discussion of this to Section 1.3.

1.2 A Basic Model

As a first step in the modelling process, we develop in this section a model for epidermal wound healing under the assumption that all biochemical effects are constant. The governing equation we use is therefore a single conservation equation for cell density $n(\underline{r}, t)$ at position $\underline{r}$ and time t, with the general form

$$\begin{array}{ccccc} \text{Rate of increase} & = & \text{Cell} & + & \text{Mitotic} \\ \text{of cell density} & & \text{migration} & & \text{generation.} \end{array}$$

Following previous deterministic models of epithelial morphogenesis, which are reviewed in detail by Murray (1989), we represent cell migration as a linear diffusive flux, and we take cell proliferation to be reasonably described by a logistic form, $\nu n(1-n/n_0)$, where ν is the linear growth rate and n_0 is the unwounded cell density. This is a commonly used metaphor for simple growth in population biology models.

Thus our model is

$$\frac{\partial n}{\partial t} = D\nabla^2 n + \nu n\left(1 - \frac{n}{n_0}\right),$$

where D is the cellular diffusion coefficient, which we assume to be a (positive) constant. The appropriate initial condition is $n = 0$ inside the wound, with boundary condition $n = n_0$ for all t on the wound boundary. We treat the epidermis as two-dimensional since its thickness is about 10^{-2}cm (Odland, 1983), while the wounds we consider have linear dimensions of about 1cm.

To clarify the roles of the parameters, we nondimensionalize the model using a time scale $1/\nu$, which is of the order of magnitude of the cell cycle time, and a length scale L, a characteristic linear dimension of the wound. For the circular wounds considered below, we take L to be the wound radius. We define the following dimensionless quantities, denoted by *:

$$n^* = n/n_0 \qquad \underline{r}^* = \underline{r}/L \qquad t^* = \nu t \qquad D^* = D/(\nu L^2) \; .$$

With these definitions, the dimensionless equation is, dropping the asterisks for notational simplicity,

$$\frac{\partial n}{\partial t} = D\nabla^2 n + n(1-n) \tag{1.1}$$

with initial condition $n = 0$ inside the wound and boundary condition $n = 1$ for all t on the wound boundary. For circular wounds, the wound boundary is simply $|\underline{r}| = 1$.

Equation (1.1) is the Fisher equation. We expect the solution to have the form of a wave of cells moving across, and eventually closing, the wound. Travelling wave solutions of the Fisher equation in an infinite one-dimensional spatial domain have been studied extensively, and this work is summarized by Murray (1989). In particular, when $\partial n(x,0)/\partial x = 0$ except on a finite region, the dimensionless wave speed is $2\sqrt{D}$ (Kolmogoroff *et al.*, 1937) and the wave form is stable to small finite domain perturbations (Canosa, 1973).

We solved equation (1.1) numerically in a radially symmetric cylindrical geometry for a range of values of D, using the method of lines on a uniform space mesh, and solving the resulting system of ordinary differential equations using Gear's method, which is a numerical scheme based on the Adams-Bashforth-Moulton method (Lambert, 1973). A typical solution is illustrated in Figure 1.1. As expected intuitively, the solution has the form of a wave of cells moving across the wound. As suggested

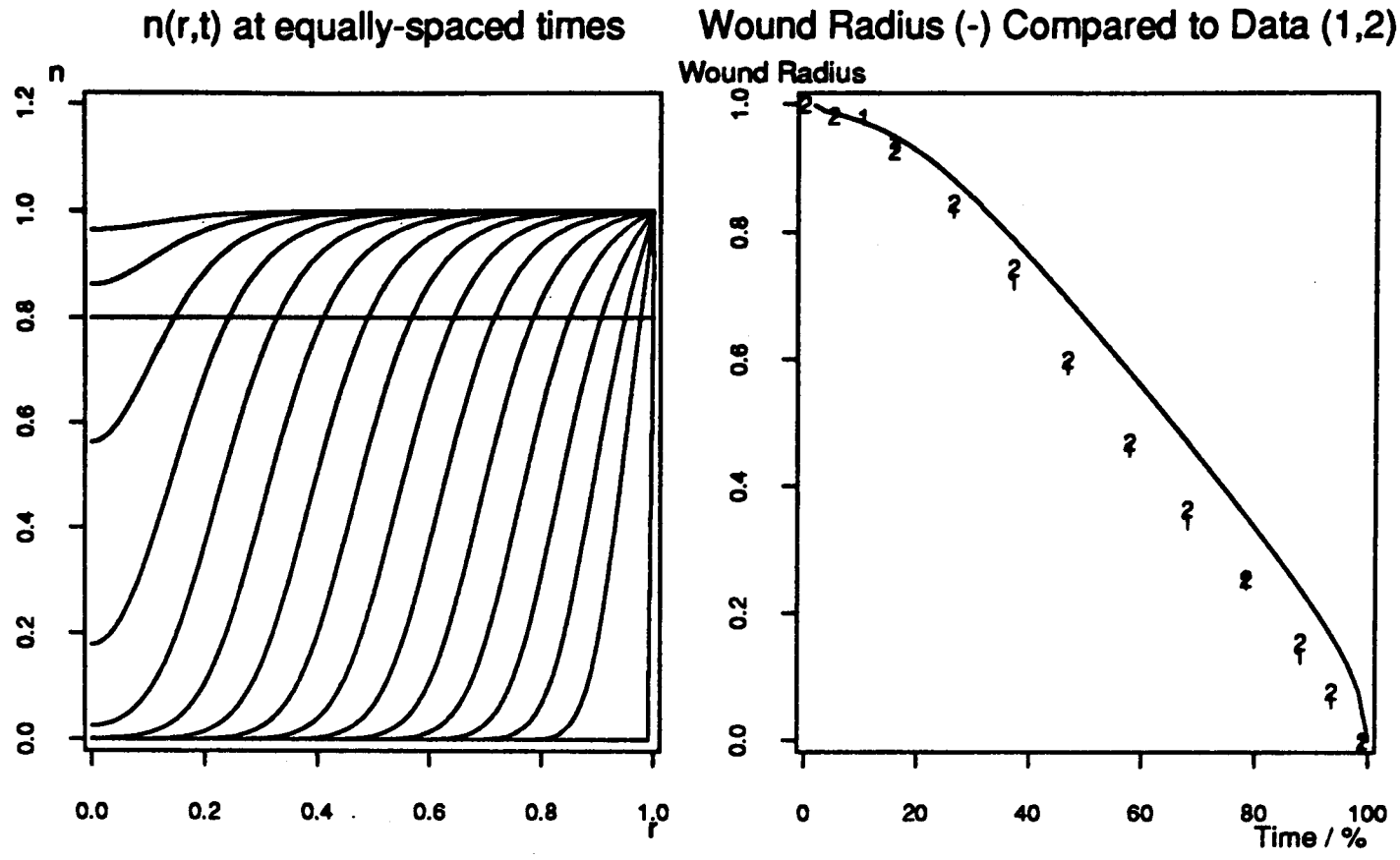

Figure 1.1: Numerical solution of equation (1.1) with $D = 10^{-3}$, which is a biologically reasonable dimensionless value (see Section 1.5). We also plot the corresponding decrease in wound radius with time, expressed as a percentage of total healing time, and compare this to data from Van den Brenk (1956). The agreement between the model solutions and experimental data is poor.

by the analysis of one-dimensional travelling wave solutions of the Fisher equation discussed above, the dimensionless wave speed of about 0.056 in the middle part of healing is of the same order of magnitude as $2\sqrt{D} \approx 0.063$.

Experimental studies of the healing of circular epidermal wounds, which are discussed more fully in Section 1.5, reveal that the process is biphasic. There is an initial 'lag phase', after which the wound radius decreases linearly with time. To capture the concept of 'wound radius' from our model, we take the wound as 'healed' when the cell density reaches 80% of its unwounded level, that is, when $n = 0.8$ for the dimensionless equations. The model prediction of the decrease in wound radius with time is illustrated in Figure 1.1, and is compared to the experimental data of Van den Brenk (1956), one of the more careful quantitative studies of epidermal wounds. The agreement between the model solutions and this data is poor; in particular, the model fails to capture the biphasic nature of the healing process.

1.2.1 Nonlinear cellular diffusion

Given the poor comparison between the numerical solutions of (1.1) and experimental data, we now consider representing cell migration as a nonlinear diffusive process. Biologically, the main factor controlling cell migration seems to be contact inhibition (Irvin, 1984; Bereiter-Hahn, 1986), which could give rise to nonlinearities. Specifically, we take the diffusion coefficient as proportional to $(n/n_0)^p$ with $p > 0$, which is a form often used in models of insect dispersal (Okubo, 1980; Murray, 1989). Using the nondimensionalization discussed above, the dimensionless model is thus

$$\frac{\partial n}{\partial t} = D\,\nabla \cdot [n^p \nabla n] + n(1-n)\,. \tag{1.2}$$

The initial and boundary conditions remain $n = 0$ inside the wound at $t = 0$, and $n = 1$ on the wound boundary for all t.

We solved this new equation numerically in radially symmetric plane polar coordinates, again using the method of lines and Gear's method. For a wide range of values of p and D, the form of the solution was of a front of cells moving into the wound (Figure 1.2). Again we compared the model solutions to data from Van den Brenk (1956). The fit with the data improved somewhat as p increased; however, as in the case of linear cell diffusion, the solutions lack the characteristic 'lag phase followed by linear phase' behaviour.

A phenomenon characteristic of nonlinear diffusion is the existence of waiting time fronts, that is, solutions in which a front that is present in the initial condition moves only after a finite waiting time (Lacey *et al.*, 1982; Kath, 1984). Since our numerical solutions have the form of moving fronts, we consider the relevance of waiting time behaviour to the solutions of (1.2).

Extending the work of Knerr (1977), Aronson *et al.* (1983) showed that when the equation

$$\frac{\partial u}{\partial t} = \frac{\partial}{\partial x}\left(u^p \frac{\partial u}{\partial x}\right) \tag{1.3}$$

is subject to an initial condition of the form

$$u(x,0) = \begin{cases} u_i(x), & x > x_0 \\ 0, & x < x_0 \end{cases} \tag{1.4}$$

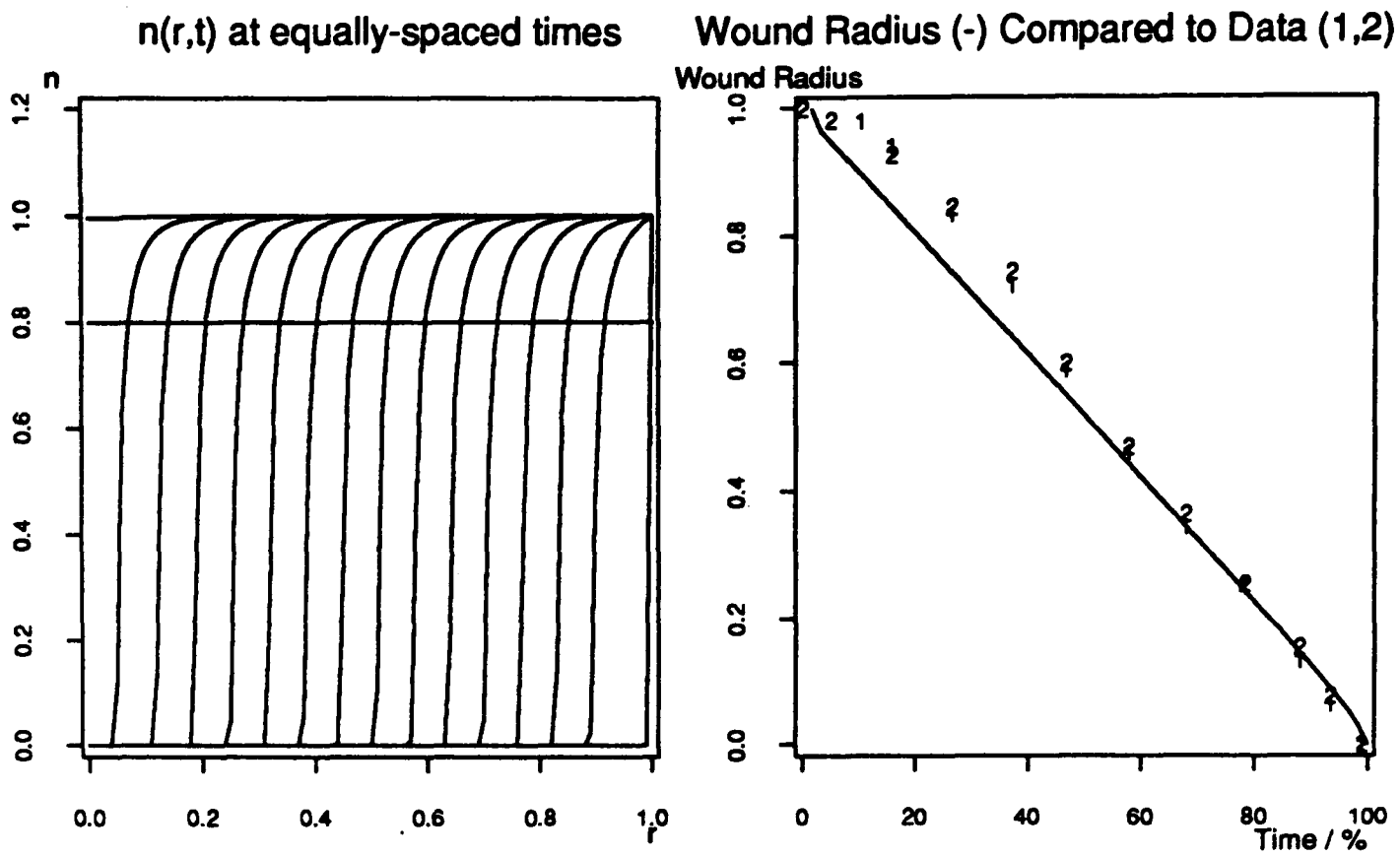

Figure 1.2: Numerical solution of equation (1.2) with $p = 4$ and $D = 10^{-3}$, which is a biologically reasonable dimensionless value (see Section 1.5). We also plot the corresponding decrease in wound radius with time, expressed as a percentage of total healing time, and compare this to data from Van den Brenk (1956). The agreement between the model solutions and experimental data remains poor, despite the introduction of nonlinear diffusion.

for some x_0, the solution has a non-zero finite waiting time if $u_i \sim (x - x_0)^{2/p}$ as $x \to x_0^+$. If $u_i \sim (x - x_0)^\alpha$ with $\alpha < 2/p$, there is no waiting time, while if $\alpha > 2/p$ there is a long waiting time, although in their investigation of a family of similarity solutions, Lacey *et al.* (1982) found that in this last case all solutions appeared to blow up with time.

Returning to the reaction-diffusion equation (1.2), the initial condition is of the form (1.4). Further, near the edge of the front, n is small while its derivatives are large. Thus we expect intuitively that the waiting time properties of the solution will be approximately the same as for equation (1.3). Of course, (1.2) is in a radially symmetric cylindrical geometry while (1.3) is in a one-dimensional geometry; the numerical simulations below suggest that this does not affect the waiting time behaviour, as expected from simple geometrical considerations.

Now in the numerical simulations we treat $n(r, 0)$ as composed of line segments. Thus in the notation of Aronson *et al.* (1983) described above, $\alpha = 1$, so that the

case in which we expect a waiting time is $p \geq 2$. This is confirmed by numerical solutions, obtained as above except that we took $n(r,0)$ as increasing linearly from 0 to 1 on $0.95 < r < 1.0$, rather than between the penultimate mesh point and $r = 1$. Figure 1.3 shows the details of the initial movement of the front when $p = 1, 2, 3$ with $D = 10^{-3}$ in each case. There is a waiting time for $p = 2, 3$ but not for $p = 1$.

We also investigated the effect that varying the form of the initial conditions has on the waiting time behaviour. Specifically, we used

$$n(r,0) = \begin{cases} 0, & 0 < r < 0.95 \\ [(r - 0.95)/0.05]^{\alpha}, & 0.95 < r < 1\,. \end{cases}$$

In this notation, the previous simulations have $\alpha = 1$. Figure 1.4 shows the numerical solutions with $p = 2$ and $\alpha = 0.5, 1, 2$. As expected from the results of Aronson *et al.* (1983), there is a waiting time only for $\alpha = 1, 2$.

The dependence of the movement of the front on the exact form of the initial condition, which is not dictated biologically, is a further shortcoming of the model.

1.3 Biochemical Regulation of Mitosis: an Improved Model

The models presented in the previous section are inadequate for describing epidermal wound healing. The model solutions lack the characteristic 'lag phase followed by linear phase' form, and in the case of nonlinear diffusion, the waiting time behaviour depends on the precise form of the initial conditions. Biologically, this suggests that biochemical mediators are fundamental to the process of epidermal wound healing. In the remainder of this chapter and Chapter 2, we focus on the role of chemical auto-regulation of mitosis in the healing process. There is experimental evidence, which we now briefly review, for the production by epidermal cells of both chemicals that inhibit mitosis and chemicals that stimulate it.

The former are 'chalones', a generic term for inhibitors of cell proliferation that are produced by the cell types on which they act. Although the term itself is somewhat out of vogue (Iversen, 1985), the evidence for such inhibitory growth regulators is

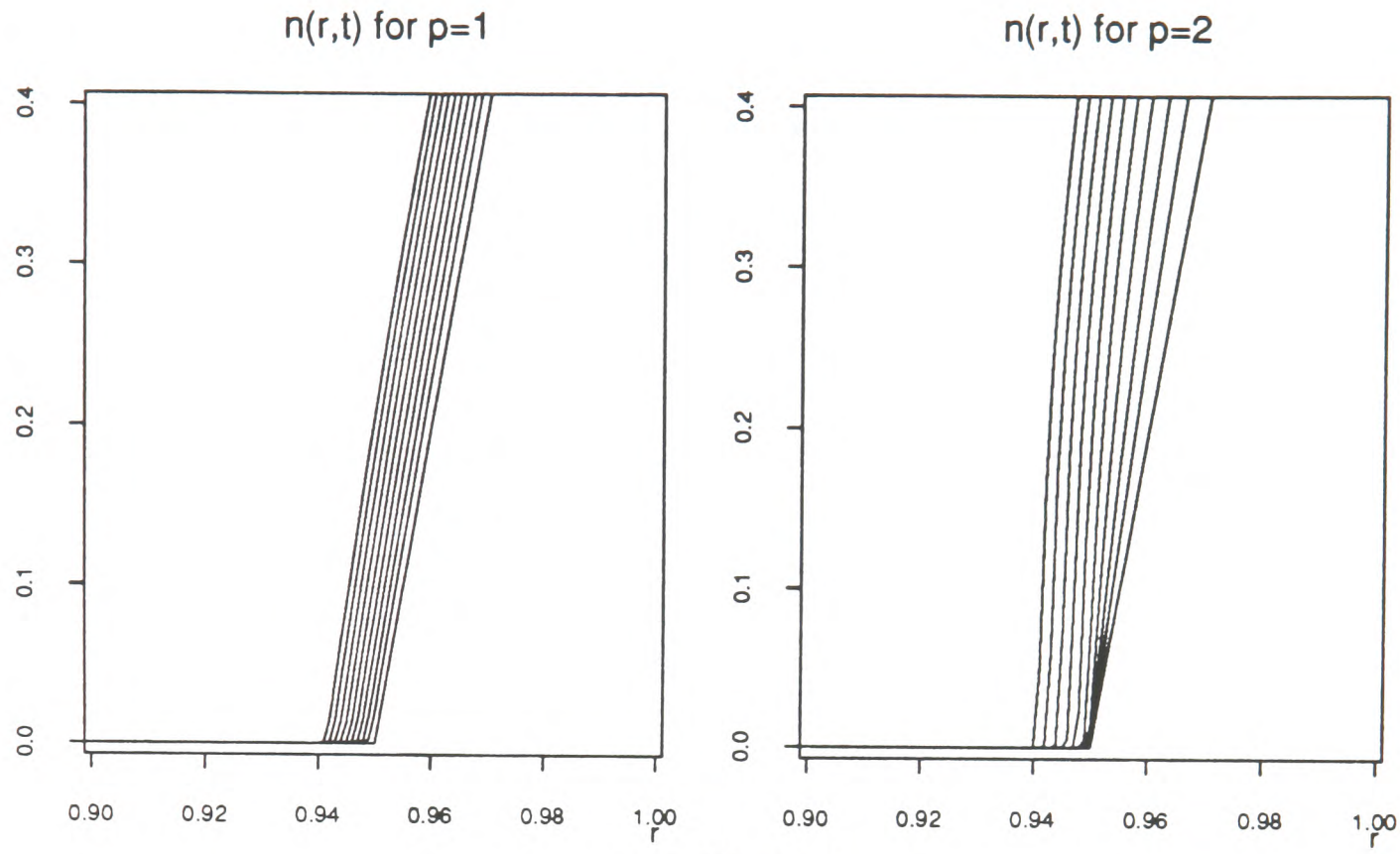

Figure 1.3: Numerical simulations of the initial movement of the wave front for equation (1.2). We plot cell density n against radius r at equally spaced times for $p = 1, 2, 3$, with $D = 10^{-3}$ in each case. There is a waiting time for $p = 2, 3$ but not for $p = 1$.

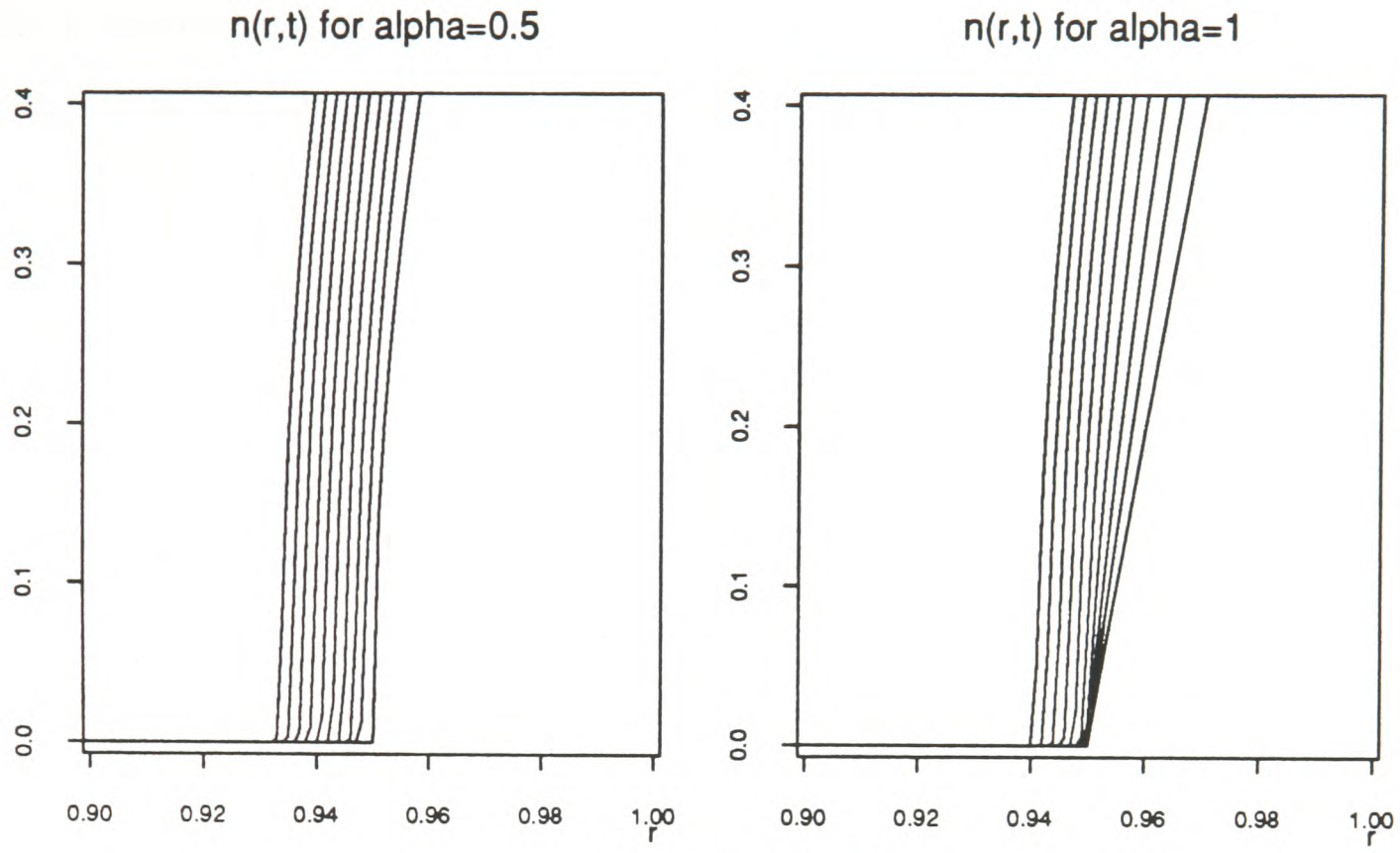

Figure 1.4: Numerical simulations of the initial movement of the wave front for equation (1.2). We plot cell density n against radius r at equally spaced times for $\alpha = 0.5, 1, 2$, with $D = 10^{-3}$ in each case. There is a waiting time for $\alpha = 1, 2$ but not for $\alpha = 0.5$.

now considerable in a wide range of cell types (Iversen, 1981, 1985). In particular, epidermal chalones are well documented in a number of mammalian species (Marks, 1973; Fremuth, 1984; Elgjo *et al.*, 1986a,b; Richter *et al.*, 1990). There are few direct experimental studies on the role of chalones in wound healing, although Yamaguchi *et al.* (1974) used epidermal wounds to investigate chalone inhibition of mitosis in mice.

Evidence for auto-activation of epidermal mitosis comes from two types of experiment. Firstly, epidermal cell extracts and exudates have been found to increase proliferation and healing rates in epidermal wounds, without identification of a particular active ingredient (Eisinger *et al.*, 1988a,b; Madden *et al.*, 1989). Also, specific reagents which are known to be produced by epidermal cells have been found to increase the mitotic rate of these cells, including type alpha transforming growth factor (Coffey *et al.*, 1987) and fibroblast growth factor (O'Keefe *et al.*, 1988; Halaban *et al.*, 1988).

Given the considerable biological evidence for biochemical auto-regulation of epidermal mitosis, we develop a model in which a single chemical, produced by epidermal cells, regulates the proliferation of these cells. The general form of the governing equations we use is

Rate of increase of cell density	=	Cell migration	+	Mitotic generation	−	Natural loss
Rate of increase of chemical concentration	=	Diffusion	+	Production by cells	−	Decay of active chemical.

As in the previous section, we treat the epidermis as two-dimensional. We consider two cases, one in which the chemical activates mitosis, and the other in which it inhibits it. We use linear Fickian diffusion to represent both cell migration and chemical diffusion; the good agreement with experimental data, described in Section 1.5, suggests that any nonlinearities in the diffusive spread of epidermal cells are not fundamental to the healing process. For the four reaction terms, we consider the mathematical representation of each term separately.

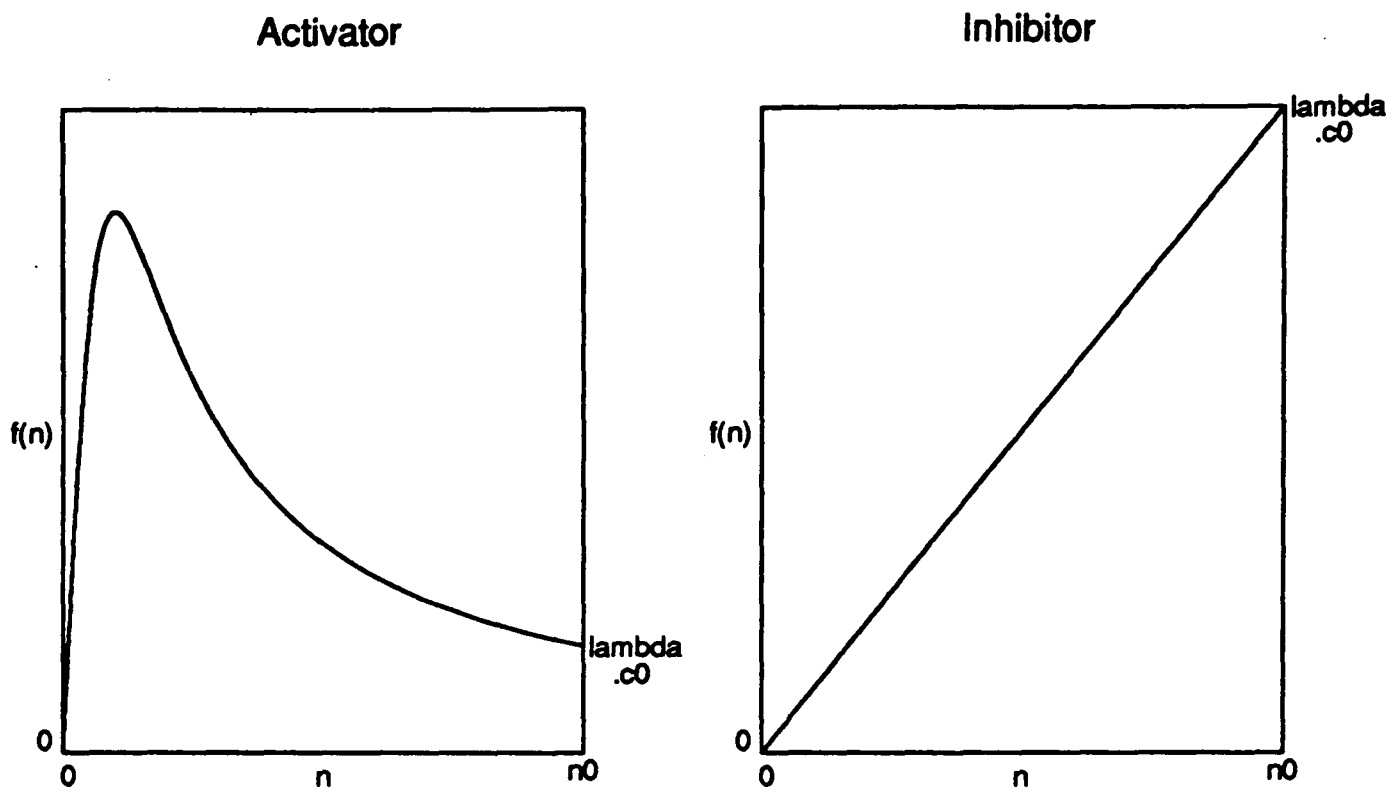

Figure 1.5: The qualitative form of the function $f(n)$, which reflects the rate of chemical production by epidermal cells. (a) Biochemical activation of mitosis; (b) biochemical inhibition of mitosis. The constants n_0 and c_0 represent the unwounded cell density and chemical concentration, respectively; λ is the positive rate constant for the decay of active chemical.

Time decay of active chemical. Such decay is typically governed by first order kinetics, so we model this term by $-\lambda c$, where λ is a positive rate constant, and c is the chemical concentration. In the absence of other terms on the right-hand side of the equation this gives an exponential decay with time.

Production of chemical by the cells. This is a function of n, which must equal zero when $n = 0$ (when there are no cells, nothing can be produced by them) and λc_0 when $n = n_0$, so that the unwounded state is a steady state. Here n_0 and c_0 are the unwounded cell density and chemical concentration respectively: we assume a non-zero concentration of chemical in the unwounded state. Further, the chemical production function, $f(n)$ say, must reflect an appropriate cellular response to injury depending on whether the chemical activates or inhibits mitosis. The qualitative form required for $f(n)$ in the two cases is shown in Figure 1.5. We take simple functional

forms that satisfy these requirements, namely

$$f(n) = \lambda c_0 \cdot \frac{n}{n_0} \cdot \left(\frac{n_0^2 + \alpha^2}{n^2 + \alpha^2} \right) \quad \text{for the activator}$$

$$\text{and} \quad f(n) = \frac{\lambda c_0}{n_0} \cdot n \quad \text{for the inhibitor,}$$

where α is a positive constant which relates to the maximum rate of chemical production.

Rate of natural cell loss. This is due to the sloughing of the outermost layer of epidermal cells, and we take it as proportional to n, say kn, where k is a positive constant.

Chemically controlled cell division. We choose this term so that when $c = c_0$, the unwounded chemical concentration, the net reaction term in the cell conservation equation is of logistic growth form, $kn(1 - n/n_0)$; here k is the linear mitotic rate. Thus we take the rate of cell division as $s(c) \cdot n \cdot (2 - n/n_0)$, where $s(c)$ reflects the chemical control of mitosis, and $s(c_0) = k$. The qualitative form required for $s(c)$ is shown in Figure 1.6. In the case of a chemical activator, a decrease of $s(c)$ to $s(0)$ for large c is included because it is found experimentally *in vitro* (Eisinger *et al.*, 1988a); however, one prediction of the model is that this phenomenon has little effect *in vivo*. For both types of regulation we require $0 < s(\infty) < s_{max} = hk$, say, where h is a positive constant, and we take $s(\infty) = k/2$; the model solutions are not sensitive to variations in $s(\infty)$. Again we take simple functional forms satisfying these criteria, namely

$$s(c) = k \cdot \frac{(h-1)c + hc_0}{2(h-1)c + c_0}$$

for the inhibitor, and

$$s(c) = k \cdot \left\{ \frac{2c_m(h - \beta)c}{c_m^2 + c^2} + \beta \right\} \quad \text{where} \quad \beta = \frac{c_m^2 - 2hc_0c_m + c_0^2}{(c_m - c_0)^2}$$

for the activator. Here c_m $(> c_0)$ is the value of c giving the maximum level of chemical activation of mitosis.

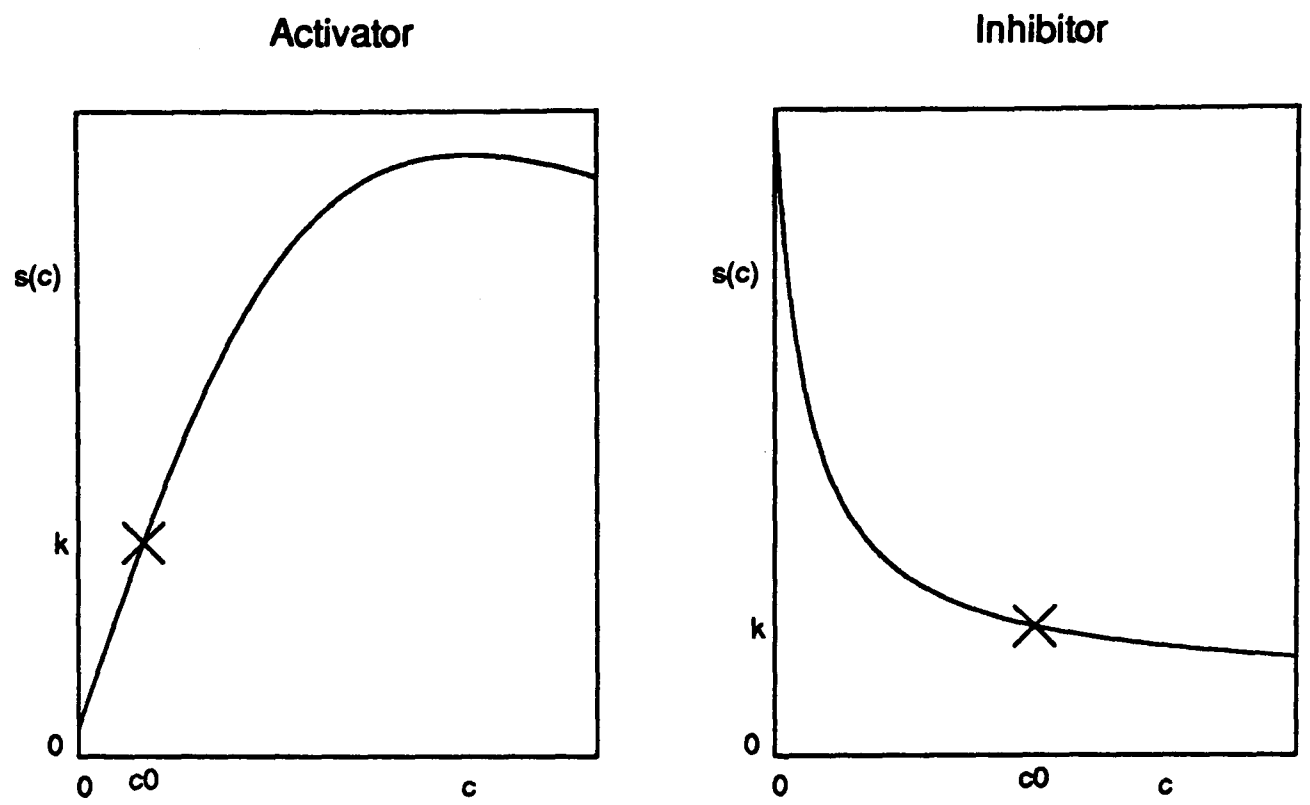

Figure 1.6: The qualitative form of the function $s(c)$, which reflects the chemical control of mitosis. (a) Biochemical activation of mitosis; (b) biochemical inhibition of mitosis. The constant c_0 represents the chemical concentration in the unwounded steady state, and the parameter k is equal to the reciprocal of the cell cycle time.

Thus the model system is

$$\frac{\partial n}{\partial t} = D\,\nabla^2 n + s(c)\cdot n\cdot\left(2-\frac{n}{n_0}\right) - kn \tag{1.5a}$$

$$\frac{\partial c}{\partial t} = D_c\nabla^2 c + f(n) - \lambda c \tag{1.5b}$$

with initial conditions $n = c = 0$ inside the wound domain and boundary conditions $n = n_0$ and $c = c_0$ on the wound boundary, at all times t. To clarify the roles of the various parameters, we nondimensionalize the model using a length scale L (a typical linear dimension of the wound) and time scale $1/k$ (the cell cycle time seems the most relevant time scale). We define the following dimensionless quantities, denoted by *:

$$n^* = n/n_0 \qquad c^* = c/c_0 \qquad \underline{r}^* = \underline{r}/L \qquad t^* = kt$$

$$f^*(n^*) = f(n_0\cdot n^*)/(\lambda c_0) \qquad s^*(c^*) = s(c_0\cdot c^*)/k \qquad D^* = D/(kL^2)$$

$$D_c^* = D_c/(kL^2) \qquad \lambda^* = \lambda/k \qquad c_m^* = c_m/c_0 \qquad \alpha^* = \alpha/n_0\,.$$

For the circular wounds considered below, we take L to be the initial wound radius. In the remainder of this chapter and Chapter 2, we drop the asterisks for notational

simplicity, and use the superscript $^{\text{dim}}$ to denote the dimensional value corresponding to a dimensionless parameter. With these rescalings, the dimensionless model equations are

$$\frac{\partial n}{\partial t} = D\,\nabla^2 n + s(c)\cdot n\cdot(2-n) - n \tag{1.6a}$$

$$\frac{\partial c}{\partial t} = D_c\nabla^2 c + \lambda\, f(n) - \lambda c \tag{1.6b}$$

with initial conditions $n = c = 0$ inside the wound domain and boundary conditions $n = c = 1$ on the wound boundary, at all times t. Here, for the activator kinetics

$$f(n) = \frac{n(1+\alpha^2)}{n^2+\alpha^2}\,, \quad s(c) = \frac{2\,c_m(h-\beta)c}{c_m^2+c^2} + \beta \quad \text{where} \quad \beta = \frac{c_m^2 - 2hc_m + 1}{(c_m-1)^2}$$

and for the inhibitor kinetics

$$f(n) = n, \quad s(c) = \frac{(h-1)c+h}{2(h-1)c+1}\,,$$

where we assume $h > 1$ and $c_m > 1$.

1.4 Linear Analysis and Parameter Values

A biological requirement of the model (1.6) is that the unwounded state is stable to small perturbations in cell density and chemical concentration, while the wounded state is unstable. This imposes various conditions on the model parameters, which we now derive by linearizing about these steady states. Consider first the unwounded state, $n = c = 1$, which is a steady state since $s(1) = f(1) = 1$. Linearizing about this gives

$$\frac{\partial n_1}{\partial t} = D\nabla^2 n_1 + s'(1)\,c_1 - n_1 \tag{1.7a}$$

$$\frac{\partial c_1}{\partial t} = D_c\nabla^2 c_1 + \lambda f'(1)\,n_1 - \lambda c_1 \tag{1.7b}$$

where $n_1 = n-1$ and $c_1 = c-1$, with $|n_1|, |c_1| \ll 1$. We look for plane wave solutions, $n_1 = \hat{n}_1 e^{i(\underline{K}\cdot\underline{r}-\omega t)}$, $c_1 = \hat{c}_1 e^{i(\underline{K}\cdot\underline{r}-\omega t)}$, where $\underline{K}$ is the wave vector and $\hat{n}_1$, $\hat{c}_1$ and ω are constants. Since the equations (1.7) are linear, any solution can be written as a sum

of such plane wave solutions. Substituting these forms into (1.7) gives

$$\begin{aligned}(1 + DK^2 - i\omega)\hat{n}_1 &= s'(1)\hat{c}_1 \\ (\lambda + D_c K^2 - i\omega)\hat{c}_1 &= \lambda f'(1)\hat{n}_1 \,,\end{aligned}$$

where $K = |\underline{K}|$. Thus for non-trivial solutions we require

$$(1 + DK^2 - i\omega)(\lambda + D_c K^2 - i\omega) = \lambda\, f'(1)\, s'(1)\,,$$

a quadratic dispersion relation for $\omega(K)$. For stability to small perturbations it is necessary and sufficient that $\mathrm{Im}(\omega) < 0$ for all K. By solving the quadratic, this occurs if and only if for all $K > 0$,

$$\begin{aligned}1 + \lambda + (D + D_c)K^2 &> 0 \\ \text{and} \quad (1 + DK^2)(\lambda + D_c K^2) &> \lambda\, f'(1)\, s'(1)\,.\end{aligned}$$

The first of these inequalities holds since λ, D and D_c are positive, and the second is satisfied since in both the activator and inhibitor cases, $f'(1)$ and $s'(1)$ have opposite signs. Thus the stability requirement for the unwounded state imposes no constraints on the parameter values.

Linearizing about the wounded steady state $n = c = 0$ and looking for plane wave solutions in the same way gives the dispersion relation

$$(DK^2 - i\omega - 2s(0) + 1)(D_c K^2 - i\omega + \lambda) = 0.$$

We assume that any perturbation involves all wave numbers K. This is a standard assumption in biological contexts (see, for example, Murray, 1989), and is justified because of a degree of stochasticity in all biological systems. For instability, one of the two roots for ω must therefore have a positive imaginary part for some K. But D_c and λ are positive so we require that, for some K, $DK^2 - 2s(0) + 1 < 0$, that is $s(0) > 1/2$. For the activator kinetics, this condition is $c_m > (2h - 1) + \sqrt{(2h-1)^2 - 1}$, and for the inhibitor kinetics, it is simply $h > 1/2$.

It is possible to estimate the parameters λ, h and k from experimental data. We estimate λ in the case of a chemical inhibitor using data on chalones. Brugal

and Pelmont (1975) found a decrease in the proliferation rate in intestinal epithelium during the 12 hours after injection with epithelial extract. Also Hennings *et al.* (1969) were able to maintain suppression of epidermal DNA synthesis by repeated injection of epidermal extract at 12 hour intervals. Based on these studies, we take the half-life of chemical decay as 12 hours. If we consider only the decay term in equation (1.5b), this gives exponential decay with a dimensional half-life of $(\log 2)/\lambda^{\mathrm{dim}}$. We therefore take $\lambda^{\mathrm{dim}} = 0.05\ (\approx \frac{1}{12}\log 2)\,\mathrm{h}^{-1}$.

In the case of a chemical activator, there is little quantitative experimental data. However, comparison of the work of Eisinger *et al.* (1988a,b) on the role of chemical activators in wound healing with the clinical studies of chalone effects by Rytömaa and Kiviniemi (1969, 1970) suggests a longer time scale for the chalone activity, by a factor of about 6, so we take $\lambda^{\mathrm{dim}} = 0.3\,\mathrm{h}^{-1}$ for the activator.

The parameter k is simply the reciprocal of the epidermal cell cycle time. This varies from species to species, but is typically about 100 hours (Wright, 1983), so we take $k = 0.01\,\mathrm{h}^{-1}$. The value of h is the maximum factor by which the mitotic rate can increase as a result of chemical regulation. We take $h = 10$, since this factor is suggested both by a study of epidermal wound healing in pigs (Winter, 1972) and by experiments on corneal wound healing in rabbits (Danjo *et al.*, 1987). The values of the diffusion coefficients D and D_c were estimated by comparing the model solutions with experimental data on wound healing, as discussed below, since there is at present no direct experimental data from which they can be determined.

In the activator case, the parameters α and c_m have to be chosen so that the functions $f(n)$ and $s(c)$ have appropriate qualitative forms. The linear analysis imposes the constraint $c_m > 37.97$ when $h = 10$, and we take $c_m = 40$ and $\alpha = 0.1$.

1.5 Numerical Solution of the Improved Model

We solved the system of reaction-diffusion equations (1.6) numerically in a radially symmetric cylindrical geometry, using the method of lines on a uniform space mesh, and solving the resulting system of ordinary differential equations using Gear's

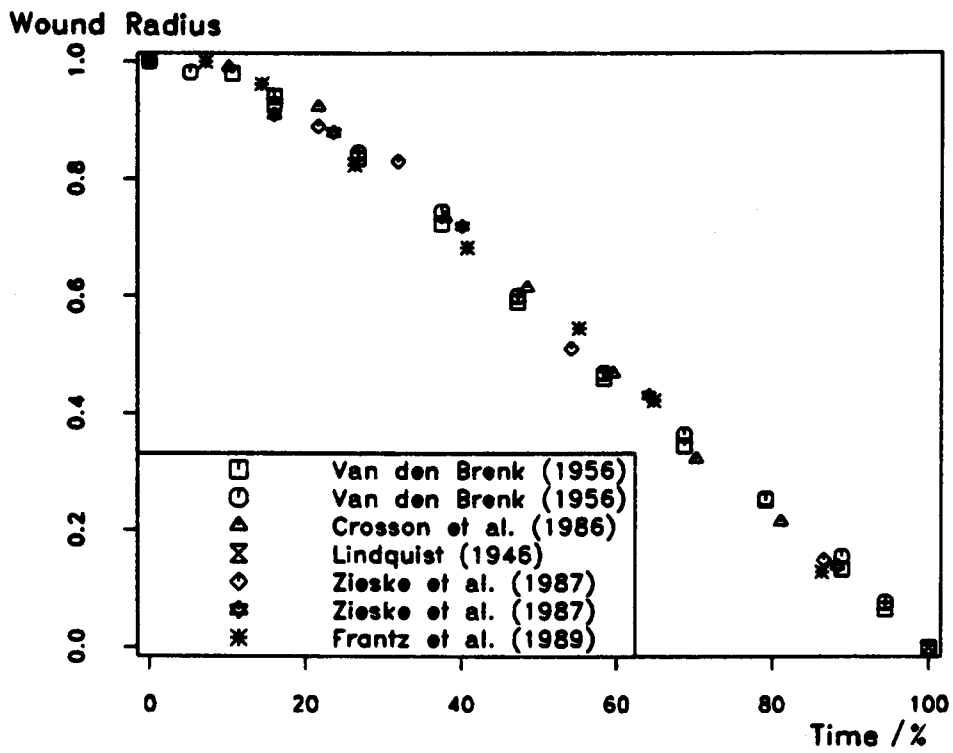

Figure 1.7: Comparison of data from a number of quantitative studies on the healing of circular epidermal wounds. The sources of the data are as indicated in the key. In Lindquist's (1946) experiments there is some dermal contraction, and we have extrapolated to the case of no contraction. These studies involve a range of species and wounding locations, and the speed of healing varies by almost an order of magnitude. However, when time is expressed as a percentage of total healing time, as here, the agreement between the different data sets is remarkable.

method, as in Section 1.2.

As explained above, determination of the diffusion coefficients D and D_c requires comparison of the model solutions with data from quantitative studies of epidermal wound healing. There are a number of such studies, and almost all involve circular wounds. The speed of healing differs widely between species and wounding location, almost by an order of magnitude. However, when time is expressed as a fraction of total healing time, the agreement between different sets of data is remarkable (Figure 1.7). As discussed in Section 1.2, the key aspect of this data is the biphasic nature of the healing process: a lag phase followed by a linear phase. Given that we are basing the values of parameters in the reaction terms on experiments spanning a range of species and cell locations, we felt it inappropriate to select one set of data and to then choose the diffusion coefficients D and D_c by fitting the model solution to both the form and precise time course of this data. Rather, we fit the model solution to the data as illustrated in Figure 1.7, with time expressed as a fraction

of total healing time. Of course we look for the model to predict wound speeds of the observed order of magnitude, but more exact quantitative prediction of both the form and speed of healing will require data from the particular species and wound location, from which the parameters in the reaction terms can be estimated.

The results of this approach are illustrated in Figure 1.8, which shows the numerically calculated decrease in wound radius with time for the two sets of kinetics. As in Section 1.2, we capture the concept of 'wound radius' from our model by taking the wound as 'healed' when the cell density reaches 80% of its unwounded level, that is when $n = 0.8$ for the dimensionless equations. The choice of this critical level as 80% is somewhat arbitrary, but does not significantly affect the results since the solutions for n and c are of travelling wave form, as discussed below. For clarity, in Figure 1.8 we have compared this predicted variation in wound radius to the data of only one of the authors discussed above. The dimensional diffusion coefficients giving this healing profile are $D = 4 \times 10^{-10}\text{cm}^2\text{s}^{-1}$, $D_c = 3 \times 10^{-7}\text{cm}^2\text{s}^{-1}$ for the activator kinetics, and $D = 7 \times 10^{-11}\text{cm}^2\text{s}^{-1}$, $D_c = 6 \times 10^{-6}\text{cm}^2\text{s}^{-1}$ for the inhibitor kinetics. These are biologically reasonable for cells and biochemicals of moderate molecular weight, respectively. In Figure 1.8 we also plot the cell density n and chemical concentration c as a function of the radius r at a selection of equally spaced times. As expected intuitively, the form of the solutions is of a front of epidermal cells moving into the wound, with an associated wave of chemical. For a wound of radius 0.5cm, the speed of these fronts in the 'linear phase' of healing corresponds to dimensional wave speeds of $2.6\mu\text{m hr}^{-1}$ for the activator and $1.2\mu\text{m hr}^{-1}$ for the inhibitor, which are of the experimentally observed order of magnitude.

Since the exact form of the initial conditions is somewhat arbitrary, we investigated the stability of the linear phase solution forms to perturbations in the initial conditions. The initial values at $r = 1$ were maintained at $n = c = 1$, and a variety of initial values for n and c were assigned to the adjacent space nodes. For both types of chemical, the solution form was found to be stable to these perturbations: the wave form quickly settled down to that shown in Figure 1.8.

We should stress that the agreement between data sets illustrated in Figure 1.7

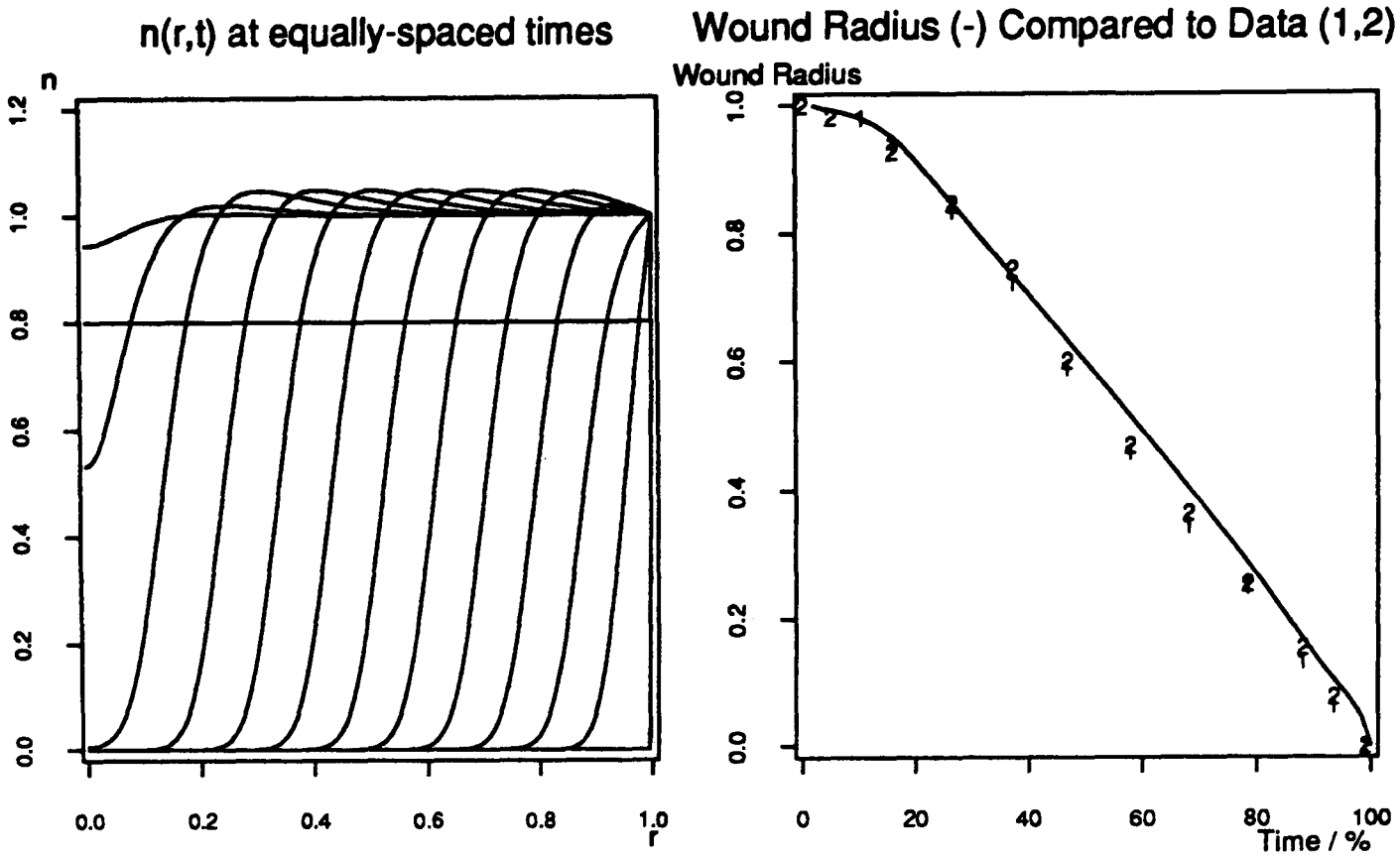

Figure 1.8: (a) Numerical solutions of equation (1.6) in a radially symmetric geometry for the activator kinetics. Cell density n and chemical concentration c are plotted against radius r at a selection of equally spaced times. We also show the corresponding decrease in wound radius with time, expressed as a percentage of total healing time, and compare this to experimental data from Van den Brenk (1956). The dimensionless parameter values are as indicated.

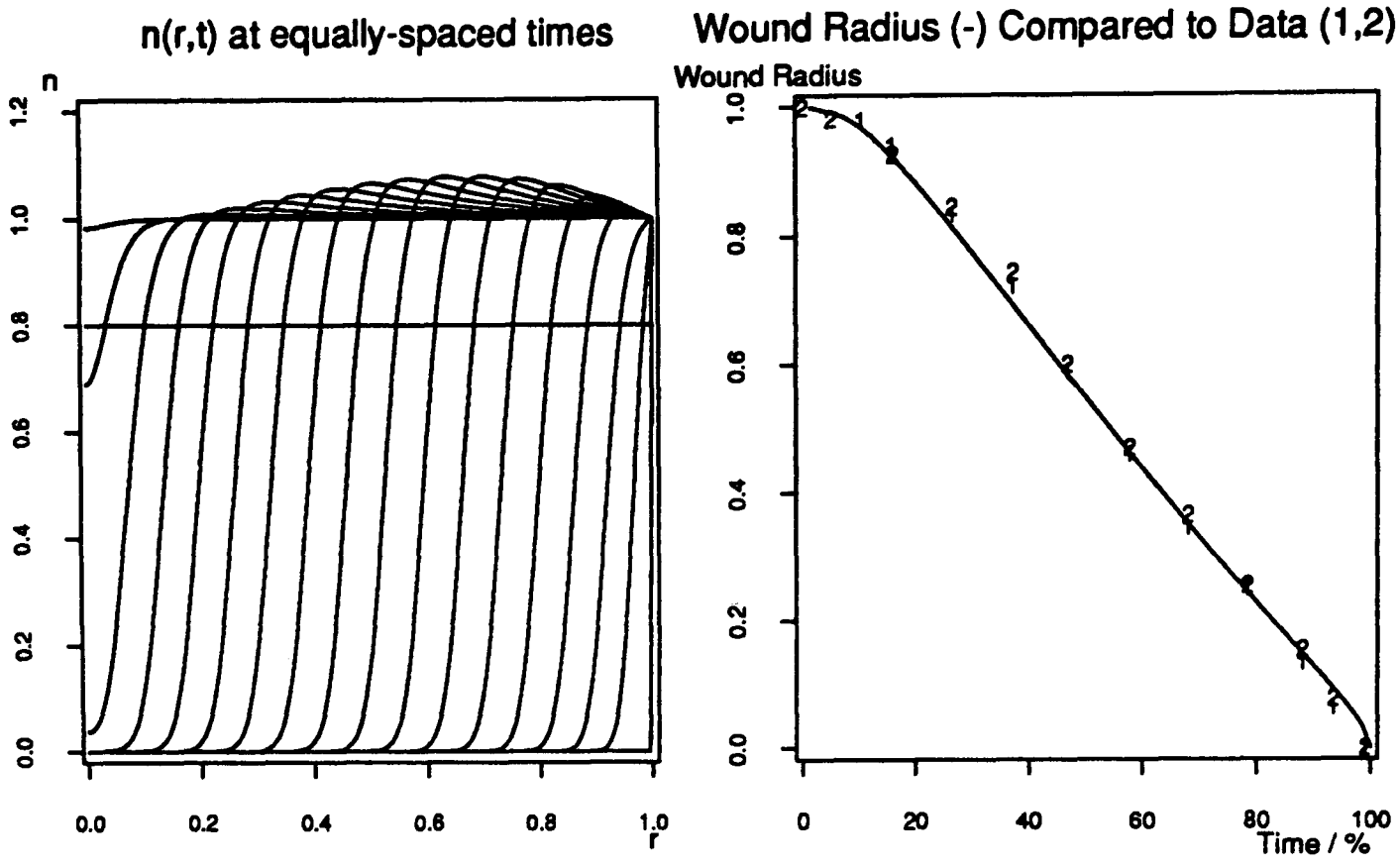

Figure 1.8: (b) Numerical solutions of equation (1.6) in a radially symmetric geometry for the inhibitor kinetics. Cell density n and chemical concentration c are plotted against radius r at a selection of equally spaced times. We also show the corresponding decrease in wound radius with time, expressed as a percentage of total healing time, and compare this to experimental data from Van den Brenk (1956). The dimensionless parameter values are as indicated.

does depend crucially on all the wounds having roughly the same initial size. It is clear intuitively that for a large wound, the lag phase will represent a smaller fraction of the total healing time, and vice versa. This phenomenon is reflected in the model solutions, since as the wound radius R increases, the dimensionless diffusion coefficients decrease in proportion to $1/R^2$.

1.6 Travelling Wave Solutions

For both types of chemical, the qualitative form of the solution in the 'linear phase' of healing is of waves of cells and chemical moving into the wound with constant shape and constant speed. Such a solution is amenable to analysis if we consider a one-dimensional geometry, rather than the two-dimensional radially symmetric geometry of Section 1.5. This is biologically relevant for large wounds of any shape, since to a good approximation these are one-dimensional during much of the healing process. Numerical solutions of the model equations for this new geometry are shown in Figure 1.9; there are no significant differences between these solutions and those of the two-dimensional system illustrated in Figure 1.8. The dimensionless wave speeds in this case are about 0.05 for the activator and 0.03 for the inhibitor.

Mathematically, solutions of constant shape and speed are travelling waves, that is, solutions of the form $n(x,t) = N(z)$, $c(x,t) = C(z)$, $z = x + at$, where x is the spatial coordinate and a is the wave speed, positive since we consider waves that are moving to the left. Substituting these solution forms into the reaction-diffusion system (1.6) gives the ordinary differential equations

$$aN' = DN'' + s(C) \cdot N \cdot (2 - N) - N \tag{1.8a}$$

$$aC' = D_c C'' + \lambda f(N) - \lambda C\,, \tag{1.8b}$$

where prime denotes d/dz. Equation (1.6) holds on a finite space domain and a semi-infinite time domain, which does not correspond to a well-defined z domain. However, during the majority of the 'linear phase' of healing, numerical solutions of (1.6) have $n, c \approx 0$ near the centre of the wound and $n, c \approx 1$ near the wound edge,

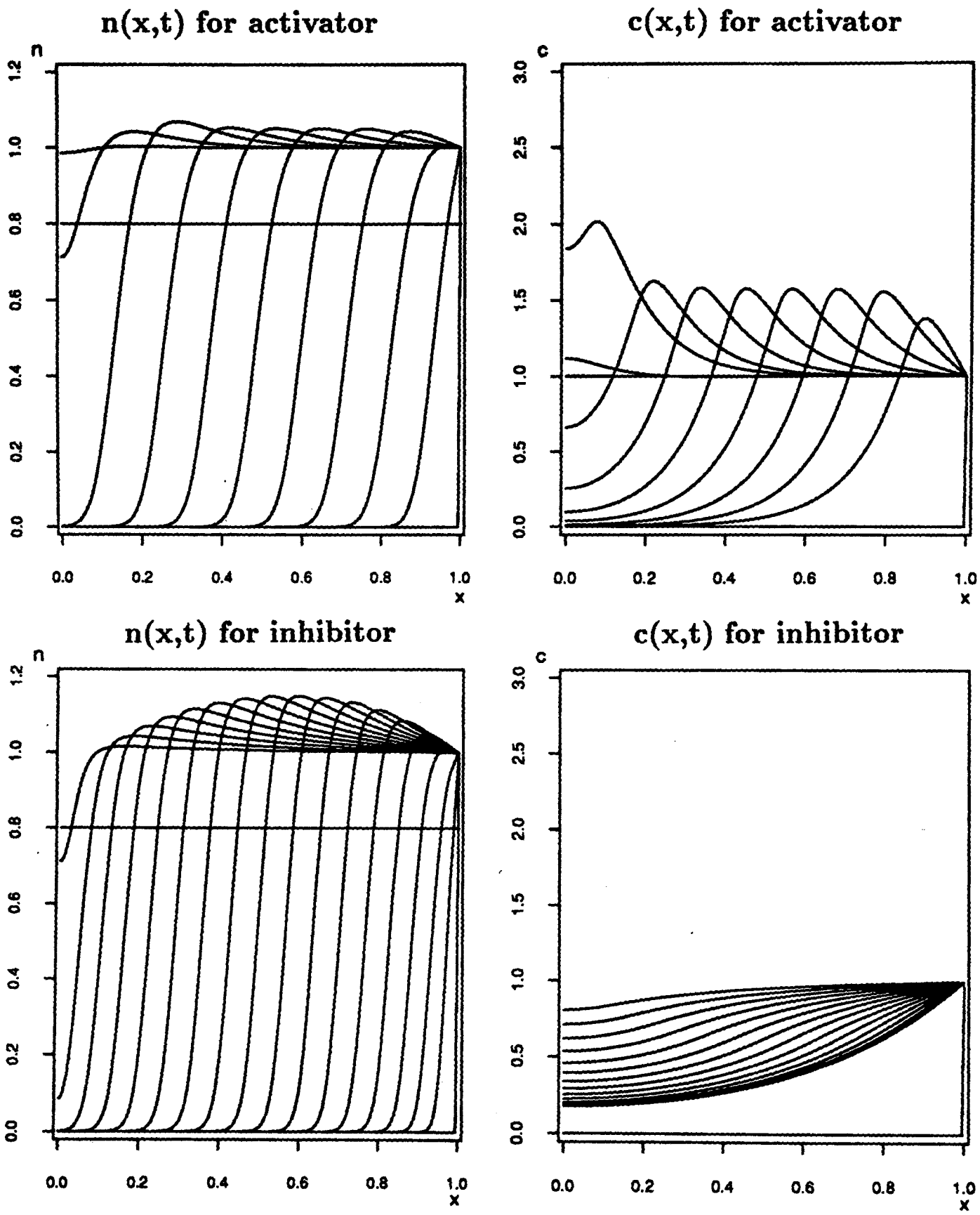

Figure 1.9: Numerical solutions of equation (1.6) in a one-dimensional geometry, for both chemical activation and chemical inhibition of mitosis. Cell density n and chemical concentration c are plotted as a function of the spatial coordinate x at a selection of equally spaced times. The dimensionless wound domain is $-1 < x < 1$. The parameter values are as in Figure 1.8.

and differ from these steady state values only in a localized region. The wave form can therefore be reasonably represented by solving (1.8) on $-\infty < z < \infty$, with boundary conditions $N(-\infty) = C(-\infty) = 0$ and $N(+\infty) = C(+\infty) = 1$.

In the remainder of this chapter, we investigate these travelling wave forms. In particular, since the system of ordinary differential equations is fourth order and thus difficult to analyse globally, we consider two approximations which reduce the order of the system: firstly treating λ as infinite and secondly treating D as zero. Biologically, the first approximation corresponds to active chemical decaying as it is produced, and the second corresponds to an absence of cellular diffusion, so that changes in cell density are due only to mitosis.

In the case of the activator kinetics, recall that

$$s(c) = \frac{2c_m(h-\beta)c}{c_m^2 + c^2} + \beta \quad \text{where} \quad \beta = \frac{c_m^2 - 2hc_m + 1}{(c_m - 1)^2}.$$

But $c \ll c_m$ for all x and t (Figure 1.9), and thus it is a good approximation to take $s(c)$ as simply a linear function. Specifically, we approximate $c_m^2 + c^2 \approx c_m^2$ and $\beta \approx (c_m - 2h)/(c_m - 2)$, which give $s(c) \approx \gamma c + 1 - \gamma$ where $\gamma = 2(h-1)/(c_m - 2)$. Numerical solutions of the model equations (1.6) using this form differ negligibly from those with the original $s(c)$ in both the one-dimensional and radially symmetric two-dimensional geometries. We use this linear approximation in the subsequent analysis, since it makes this analysis much easier algebraically. The approximation is valid provided $c_m \gg 1$.

1.6.1 Solutions with $\lambda = \infty$

In the first approximation we consider the derivative terms in the second equation to be negligible compared to the reaction terms. Intuitively this seems a reasonable approximation in the case of the inhibitor mechanism ($\lambda = 5$), and a good approximation for the activator kinetics ($\lambda = 30$). The fourth order system (1.8) then reduces to a second order ordinary differential equation for N, which can be analysed relatively

easily. Specifically, we have

$$N'' = \frac{a}{D}N' - \frac{1}{D}\psi(N) \tag{1.9}$$

where $\psi(N) = s[f(N)]\cdot(2N - N^2) - N$. We look for a solution subject to $N(+\infty) = 1$ and $N(-\infty) = 0$, with $N \geq 0$ for all z. Straightforward algebra gives the functional form of $\psi(N)$ as

$$\begin{aligned}\psi(N) &= \frac{N}{(c_m - 2)(N^2 + \alpha^2)} \cdot \Big\{[2h - c_m]N^3 + [2\alpha^2(1-h) - 6h + c_m + 4]N^2 \\ &\quad + [4(h-1) + \alpha^2(6h - c_m - 4)]N + \alpha^2(2 - 4h + c_m)\Big\} \end{aligned} \tag{1.10a}$$

for the activator, and

$$\psi(N) = \frac{N(1-N)[(h-1)(N+2)+1]}{2(h-1)N + 1} \tag{1.10b}$$

for the inhibitor. These are shown graphically in Figure 1.10 for the parameter values used in Figure 1.8. Crucially, on the interval $[0, 1]$ both functions have an essentially parabolic shape. Thus we expect much of the standard analysis for travelling wave solutions of the Fisher equation $u_t = u_{xx} + u(1-u)$ to be applicable here, albeit with more complicated algebra. This standard analysis is described in detail by Murray (1989).

The system (1.9) has singular points $N = N' = 0$ and $N = 1$, $N' = 0$. At (0,0) the eigenvalues are $\left[a \pm \{a^2 + 4D - 8Ds(0)\}^{1/2}\right]/2D$. Now the linear analysis presented in Section 1.4 implies that $s(0) > 1/2$. Thus (0,0) is an unstable node or unstable focus according to the sign of $[a^2 + 4D - 8Ds(0)]$. Since we require N non-negative, we have a condition on the wave speed for a solution of the required form to exist, namely $a \geq a_{min} = 2\{D(2s(0) - 1)\}^{1/2}$.

For (1,0) the eigenvalues are $\left[a \pm \{a^2 + 4D - 4Ds'(1)f'(1)\}^{1/2}\right]/2D$. In both the activator and inhibitor cases $s'(1)$ and $f'(1)$ have opposite signs, so that this equilibrium is a saddle point.

For both fixed points, the eigenvector corresponding to an eigenvalue μ is $(1, \mu)$. Therefore, provided $a \geq a_{min}$, the phase portrait has the form shown in Figure 1.11. Thus there is a unique solution of the required form for each $a \geq a_{min}$, corresponding

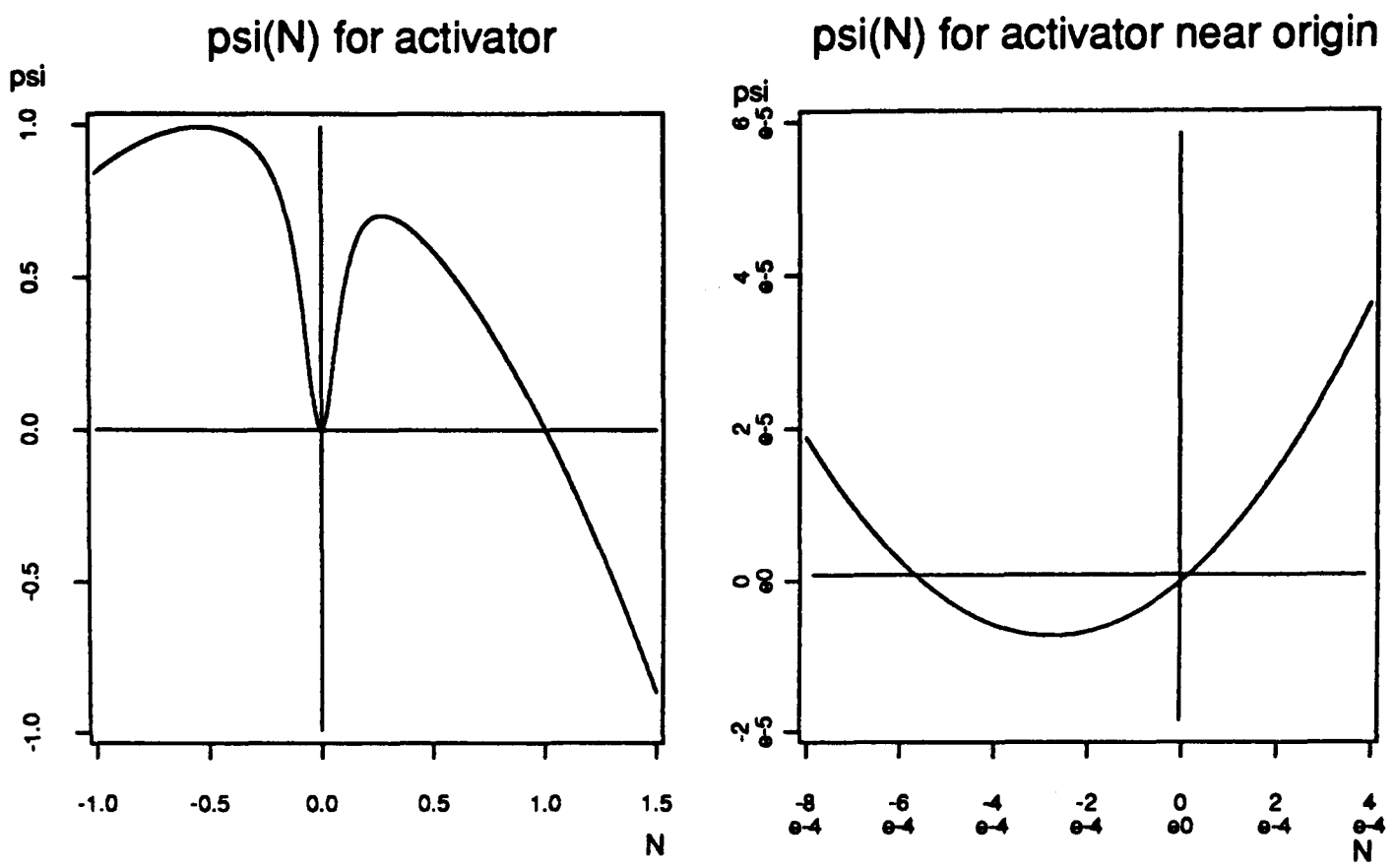

Figure 1.10: The function $\psi(N)$, defined in (1.10), for the activator and inhibitor kinetics. A more detailed plot near the origin is shown in the activator case. The parameter values are as in Figure 1.8.

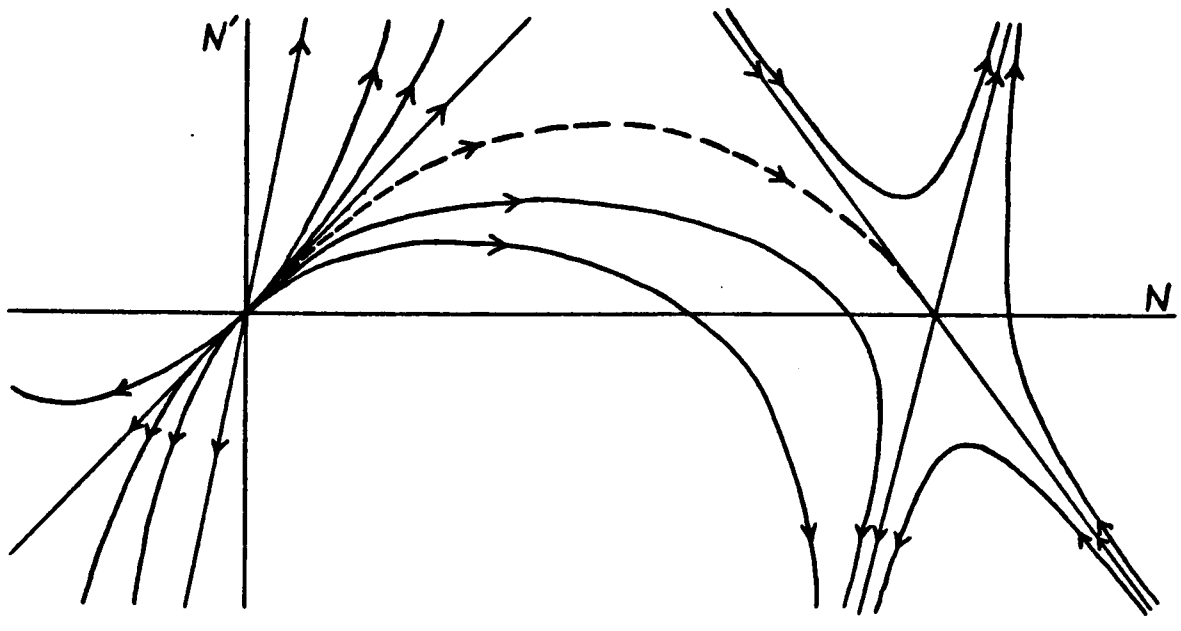

Figure 1.11: The qualitative form of the phase portrait for (1.9) with $a \geq a_{min}$. The dashed trajectory corresponds to the unique solution satisfying $N(+\infty) = 1$, $N(-\infty) = 0$ and $N \geq 0$.

to the dashed trajectory in Figure 1.11. However, Kolmogoroff *et al.* (1937) showed that for a class of one-dimensional reaction-diffusion equations that includes (1.6) when $\lambda = \infty$, as t increases the solution approaches the travelling wave form with $a = a_{min}$ when the initial conditions have compact support, that is $n = 1$ for sufficiently large positive x, and $n = 0$ for sufficiently large negative x. (A simplified translation of the paper of Kolmogoroff *et al.* (1937) is given in Oliveira-Pinto and Conolly, 1982, Chapter 7). For the parameter values we are using, a_{min} is about is 0.01 for the activator and 0.09 for the inhibitor. These values compare to the wave speeds 0.05 and 0.03 respectively found in the one-dimensional numerical solutions of the partial differential equation system (1.6). The discrepancy indicates inadequacies in the approximation of chemical decaying as it is formed; intuitively, we expect this approximation to give a lower wave speed for the activator kinetics and a higher wave speed for the inhibitor kinetics.

Rescaling the independent variable in the Fisher equation ($z_{new} = z_{old}/a$) gives $\epsilon\, u'' - u' + u(1-u) = 0$, where $\epsilon = a^{-2}$. This enables the equations to be solved analytically as a regular perturbation problem in the small parameter ϵ (see, for example, Murray, 1989). A corresponding rescaling for (1.9) gives

$$\epsilon N'' - N' + \psi(N) = 0 \tag{1.11}$$

where $\epsilon = D/a^2$ and prime denotes $d/d\zeta$, $\zeta = z/a$. Therefore a solution can be

obtained in the same way for the inhibitor kinetics ($D/a_{min}^2 \approx 0.01$), but not for the activator kinetics ($D/a_{min}^2 \approx 5$). We look for a solution of the form

$$N(\zeta;\epsilon) = N_0(\zeta) + \epsilon N_1(\zeta) + \epsilon^2 N_2(\zeta) + \ldots .$$

Substituting this into (1.11) and equating coefficients of powers of ϵ gives

$$N_0' = \psi(N_0) \tag{1.12a}$$

$$N_1' = N_1 \cdot \frac{d\psi(N_0)}{dN_0} + N_0'' \tag{1.12b}$$

$$\vdots \qquad \vdots \qquad \vdots ,$$

subject to $N_0(-\infty) = 0$, $N_0(0) = 1/2$, $N_0(+\infty) = 1$, and $N_i(-\infty) = N_i(0) = N_i(+\infty) = 0$ for $i \geq 1$. The value of $N(0)$ is arbitrary; it must be specified to give a unique solution. Since we choose $N(0) = 1/2$,

$$\begin{aligned} \zeta &= \int_{\frac{1}{2}}^{N_0} \frac{d\xi}{\psi(\xi)} \\ &= \left(\frac{1}{2h-1}\right) \ln[2N_0] - \left(\frac{2h-1}{3h-2}\right) \ln[2(1-N_0)] + \\ &\qquad \frac{(4h-3)(h-1)}{(2h-1)(3h-2)} \ln\left[\frac{2(h-1)N_0 + 2(2h-1)}{5h-3}\right] \end{aligned} \tag{1.13}$$

for the inhibitor kinetics, using (1.10b). This cannot be inverted explicitly. However, observing that ζ is a monotonically increasing function of N_0 when $h > 1$, we take N_0, rather than ζ, as the independent variable. Dividing (1.12b) by $dN_0/d\zeta$ gives

$$\begin{aligned} \frac{dN_1}{dN_0} &= \frac{N_1}{dN_0/d\zeta} \cdot \frac{d\psi(N_0)}{dN_0} + \frac{d}{dN_0}\left(\frac{dN_0}{d\zeta}\right) \\ &= \frac{N_1}{\psi(N_0)} \frac{d\psi(N_0)}{dN_0} + \frac{d\psi(N_0)}{dN_0} , \end{aligned}$$

using (1.12a). Dividing through by $\psi(N_0)$ gives

$$\frac{d}{dN_0}\left[\frac{N_1}{\psi(N_0)} - \ln[\psi(N_0)]\right] = 0.$$

Thus, since $N_1 = 0$ when $N_0 = 1/2$ (at $\zeta = 0$),

$$N_1 = \psi(N_0) \ln\left[\frac{\psi(N_0)}{\psi(1/2)}\right] . \tag{1.14}$$

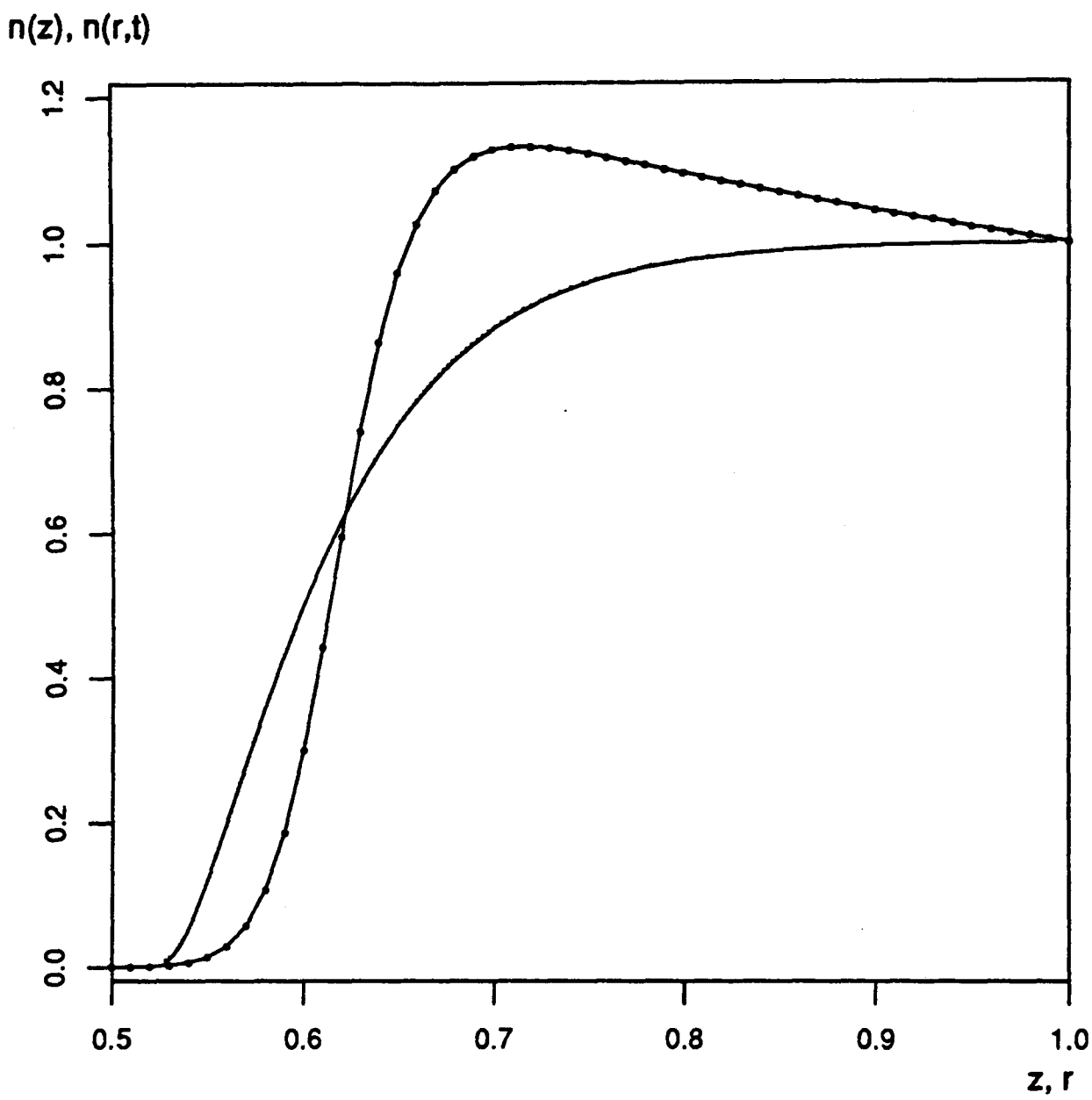

Figure 1.12: Comparison of N_0 (full curve), $N_0 + \epsilon N_1$ (small dots) and the numerical solution of the partial differential equations (1.6) at a time in the middle of the 'linear phase' of healing (curve and large dots) for the inhibitor kinetics. Here N_0 and N_1 are the first two terms in the asymptotic expansion of $N(z)$, given in (1.13) and (1.14) respectively. The parameter values are as in Figure 1.8, with $a = a_{min} \approx 0.09$. The $O(\epsilon)$ correction to N_0 is barely visible.

Plots of N_0 and $N_0 + \epsilon N_1$ against z are shown in Figure 1.12 and compared to the numerical solution of the partial differential equations (1.6) at a time in the middle of the 'linear phase' of healing. These show that the first order correction ϵN_1 is already very small. The agreement between the partial differential equation solution and the travelling wave form is poor. In particular, the travelling wave solution fails to capture the important feature that $n > 1$ in part of the wave front. This is an inadequacy in the approximation $\lambda = \infty$.

Numerical solutions of (1.9) for the activator kinetics with $a = a_{min}$ show a similar poor agreement with the partial differential equation wave form. As explained on page 33, the perturbation theory method of solution that we have used is invalid in this case since $D/a_{min}^2 \approx 5$. However, the method can be used for both types of kinetics if we take a as the wave speed observed in the numerical solution of the partial differential equations. This gives $D/a^2 \approx 0.2$ for the activator kinetics and $D/a^2 \approx 0.1$ for the inhibitor kinetics. For the activator, analytic evaluation of the integral for $z(N_0)$ is algebraically infeasible, and we evaluated it numerically using Gauss-Legendre quadrature. For the inhibitor mechanism, the analytic solution above is still valid for this new wave speed. Again, the solutions thus obtained do not compare well with the partial differential equation wave forms, and again this is an inadequacy in the approximation $\lambda = \infty$ rather than in the truncation of the asymptotic expansion.

1.6.2 Solutions with $D = 0$

Given the shortcomings of the approximation investigated in the previous section, we now consider the approximation $D = 0$. Recall that in Section 1.5 we determined the values $D = 5 \times 10^{-4}$ for the activator kinetics and $D = 10^{-4}$ for the inhibitor kinetics, by fitting to experimental data. Putting $D = 0$, the fourth order system (1.8) reduces to a third order system

$$N' = -\frac{N}{a} + \frac{1}{a} s(C)(2N - N^2) \tag{1.15a}$$

$$C'' = \frac{a}{D_c} C' + \frac{\lambda}{D_c} C - \frac{\lambda}{D_c} f(N). \tag{1.15b}$$

We look for a solution subject to boundary conditions $N(-\infty) = C(-\infty) = 0$, $N(+\infty) = C(+\infty) = 1$, with $N, C \geq 0$ for all z.

We solved this system numerically using a shooting method. We integrated the equations on a finite interval $[z_l, z_r]$, treating $N(z_l)+C(z_l) = 0$ and $N(z_r)+C(z_r) = 2$ as nonlinear algebraic equations for the unknowns $C(z_m)$ and $C'(z_m)$, where z_m is some intermediate point; the value of $N(z_m)$ is arbitrary since the travelling wave form is only determined up to a translation in z. Initially we took $z_l = 0$, $z_r = 1$, with initial estimates for $C(z_m)$ and $C'(z_m)$ taken from the numerical solutions of the partial differential equations. The ordinary differential equations were integrated both forwards and backwards from z_m using a Runge-Kutta-Merson method. With the solutions thus obtained for $C(z_m)$ and $C'(z_m)$ as initial estimates, we repeated the simulation with $z_l = -0.5$, $z_r = 1.5$. We continued this process of expanding the interval until the effect on the solution within [0,1] was negligible.

The solutions thus obtained are compared with the numerical solutions of the partial differential equations (1.6) in Figure 1.13 for both the activator and inhibitor kinetics; in both cases the agreement is good.

Phase space considerations

For steady states of (1.15), $C' = 0$, $C = f(N)$ and $N = s(C)N(2 - N)$, that is $C' = 0$, $C = f(N)$ and $\psi(N) = 0$, where the function $\psi(N)$ is defined in (1.10) and illustrated in Figure 1.10. The only non-negative roots of $\psi(N) = 0$ are at $N = 0, 1$. Thus we have two steady states: $N = 0$, $C = 0$, $C' = 0$ and $N = 1$, $C = 1$, $C' = 0$.

Linearizing about (0,0,0) gives eigenvalues

$$\mu_1 = \frac{2s(0) - 1}{a} \qquad \text{and} \qquad \mu_2,\, \mu_3 = \frac{a \pm \sqrt{a^2 + 4\lambda D_c}}{2D_c}\,.$$

Thus in both the activator and inhibitor cases there are three real eigenvalues, two positive and one negative, since the linear analysis in Section 1.4 implies that $s(0) > 1/2$. The corresponding eigenvectors are

$$\left[\frac{\lambda + a\mu_1 - D_c\mu_1^2}{\lambda f'(0)}\,, 1, \mu_1\right], \qquad [0, 1, \mu_2]\,, \qquad [0, 1, \mu_3]\,.$$

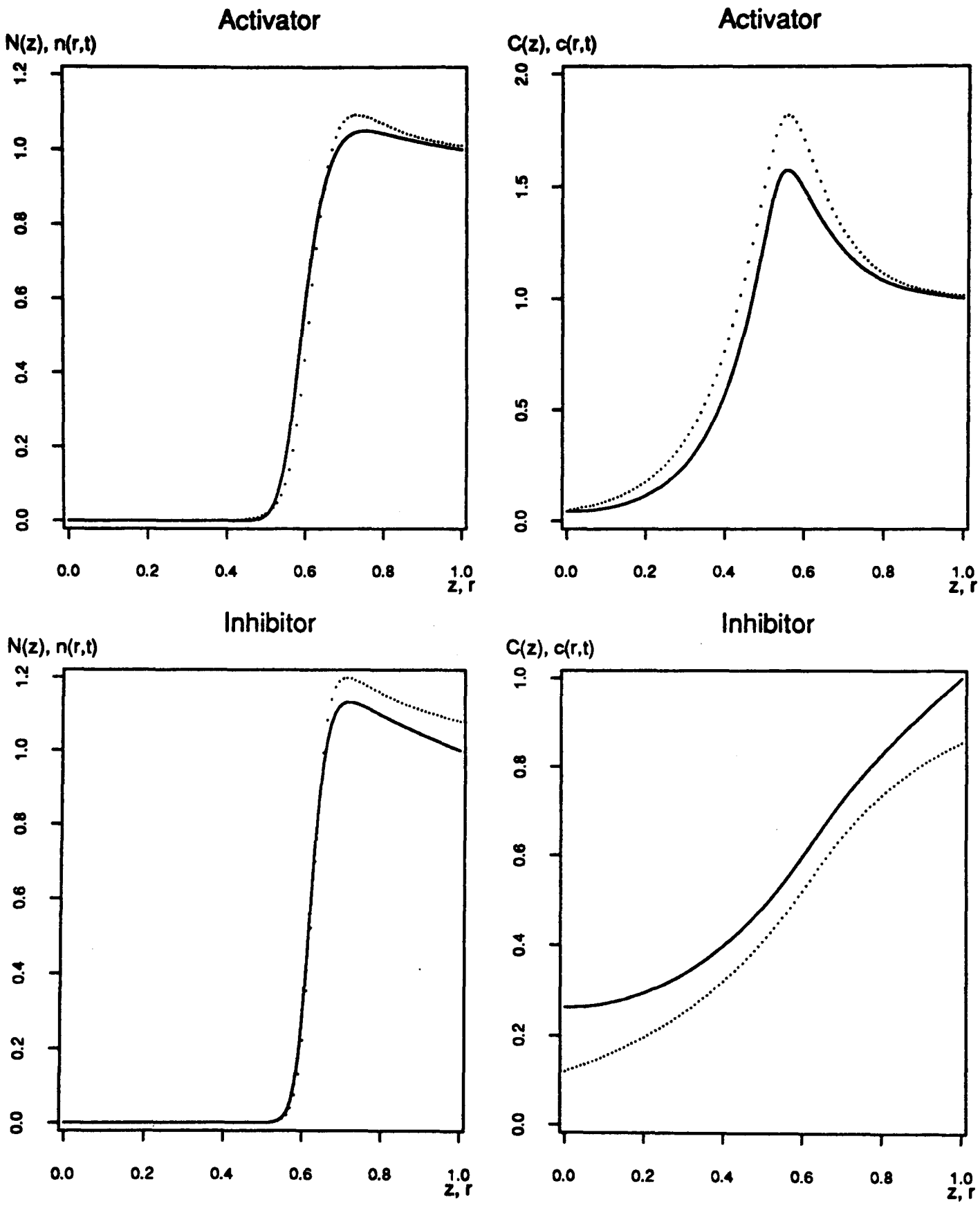

Figure 1.13: Comparison of numerical solutions of the full model equations (1.6) in one space dimension (full curves) and the travelling wave equations under the approximation $D = 0$, given in (1.15) (dotted curves). The parameter values are as in Figure 1.8, with $a = 0.05$ for the activator and $a = 0.03$ for the inhibitor. These are the dimensionless wave speeds observed in the one-dimensional solutions of (1.6).

For (1,1,0) the eigenvalues are the roots of

$$\mu^3 + \left(\frac{1}{a} - \frac{a}{D_c}\right)\mu^2 - \left(\frac{1+\lambda}{D_c}\right)\mu + \frac{\lambda}{aD_c}[s'(1)f'(1) - 1] = 0\,, \qquad (1.16)$$

which is plotted in Figure 1.14 for both the activator and inhibitor kinetics, for a range of wave speeds around that observed in the numerical solution of the one-dimensional partial differential equations. In the inhibitor case there are three real eigenvalues, two negative and one positive; in the activator case either this is also the case or there is one real positive and two complex eigenvalues, depending upon the wave speed.

For this steady state, analytic determination of the eigenvalues and eigenvectors is algebraically unfeasible, so we determined them numerically. The results are shown in Tables 4.1 and 4.2, again for both types of chemical and for a range of wave speeds around those found in the numerical solutions of the one-dimensional partial differential equations.

For the activator kinetics, these considerations imply an upper bound on the wave speed a. This is because we look for a solution with a monotonic rather than oscillatory approach to the unwounded steady state (1,1,0). Thus our upper bound is the value of a at which (1.16) has two equal negative roots. We write this cubic as $p(x) \equiv x^3 + \alpha x^2 - \beta x - \gamma$, where α and γ depend on a. If $p(x) = p'(x) = 0$ for some x, then

$$x\{9\gamma - \alpha\beta\}\{(3x+\alpha)p'(x) - 9p(x)\} = \{2\alpha^2 + 6\beta\}\{(\beta x + 3\gamma)p'(x) - 3\beta p(x)\}.$$

If $x \neq 0$, this simplifies to

$$\alpha^2\beta^2 + 4\beta^3 + 18\alpha\beta\gamma - 27\gamma^2 + 4\alpha^3\gamma = 0\,. \qquad (1.17)$$

Now

$$\alpha = \frac{1}{a}\left(1 - \frac{a^2}{D_c}\right)\,, \quad \beta = \frac{1+\lambda}{D_c}\,, \quad \gamma = \frac{\lambda}{aD_c}[1 - s'(1)f'(1)]\,;$$

substituting these into (1.17) and multiplying through by a^4 gives a cubic in a^2,

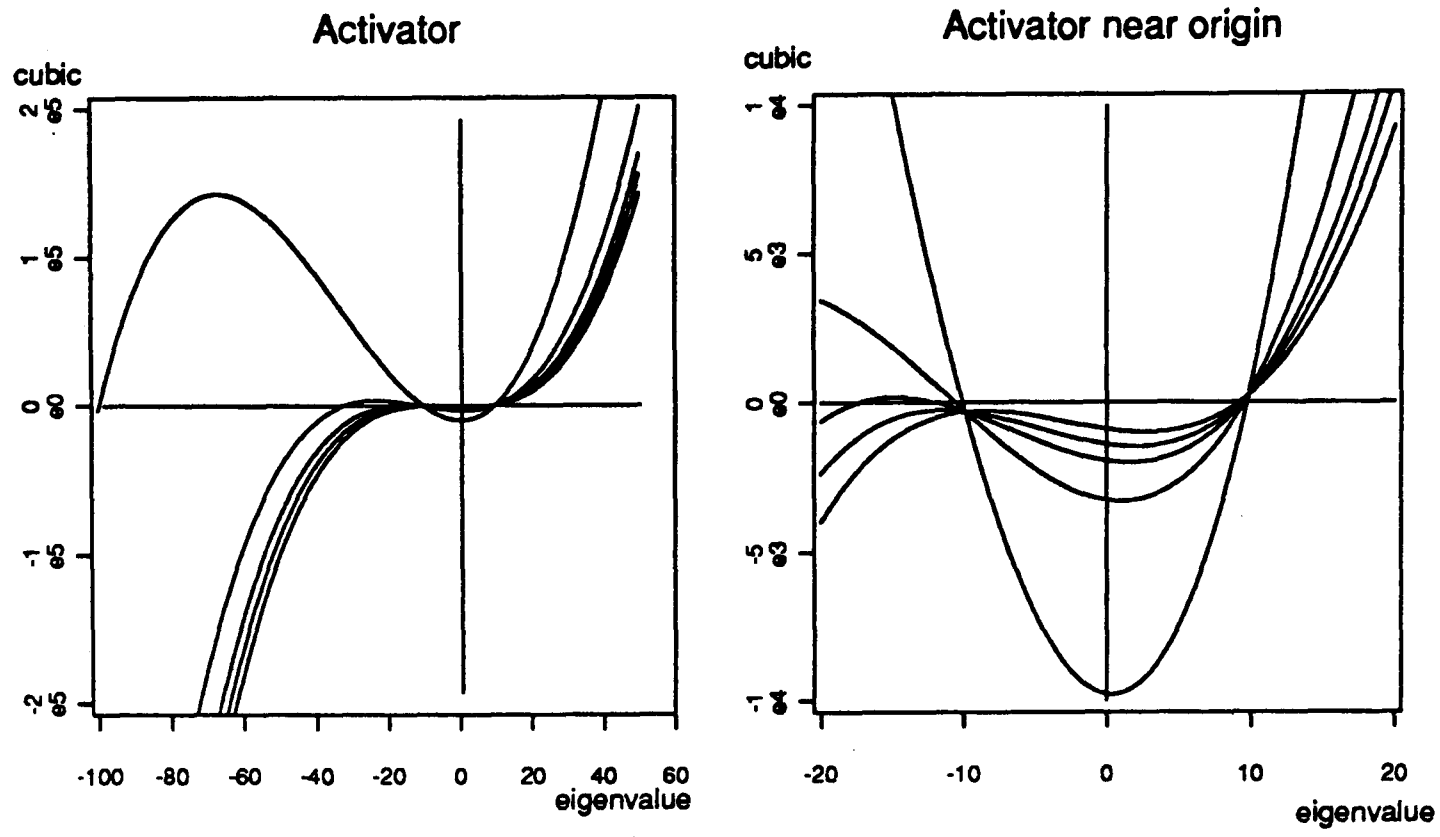

Figure 1.14: The left-hand side of the cubic eigenvalue equation (1.16), plotted against λ, in the activator and inhibitor cases, for 5 values of the wave speed a, which are 0.01, 0.03, 0.05, 0.07, 0.11 for the activator, and 0.01, 0.025, 0.035, 0.05, 0.1 for the inhibitor. The wave speeds observed in the numerical solution of the one-dimensional partial differential equations are about 0.05 for the activator and 0.03 for the inhibitor. The intercept on the vertical axis becomes less negative as the wave speed increases.

Speed, a	*Eigenvalues*	*Corresponding eigenvectors*
0.038	-24.84	(0.322,0.038,-0.946)
	9.50	(0.036,0.105, 0.994)
	-10.89	(0.074,0.091,-0.993)
0.048	-11.65	(0.092,0.085,-0.992)
	9.43	(0.034,0.105, 0.994)
	-18.51	(0.224,0.053,-0.973)
0.058	9.38	(0.033,0.106,0.994)
	$-13.24 \pm$	$(-0.128 \pm 0.042i,$
	$2.02i$	$-0.073 \mp 0.011i, 0.988)$

Table 1.1: Eigenvalues and eigenvectors of equations (1.15) at the steady state (1,1,0), for the activator kinetics, for three values of the wave speed a. The other parameter values are as in Figure 1.8.

Speed, a	*Eigenvalues*	*Corresponding eigenvectors*
0.0204	-48.96	(0.993,-0.002, 0.120)
	-2.96	(0.159,-0.316, 0.935)
	2.93	(0.143,-0.320,-0.937)
0.0304	-32.81	(0.984,-0.005,0.177)
	-2.97	(0.164,-0.314, 0.935)
	2.92	(0.139,-0.321,-0.937)
0.0404	-24.64	(0.972,-0.009, 0.234)
	-2.98	(0.169,-0.313, 0.935)
	2.92	(0.136,-0.321, 0.937)

Table 1.2: Eigenvalues and eigenvectors of equations (1.15) at the steady state (1,1,0), for the activator kinetics, for three values of the wave speed a. The other parameter values are as in Figure 1.8.

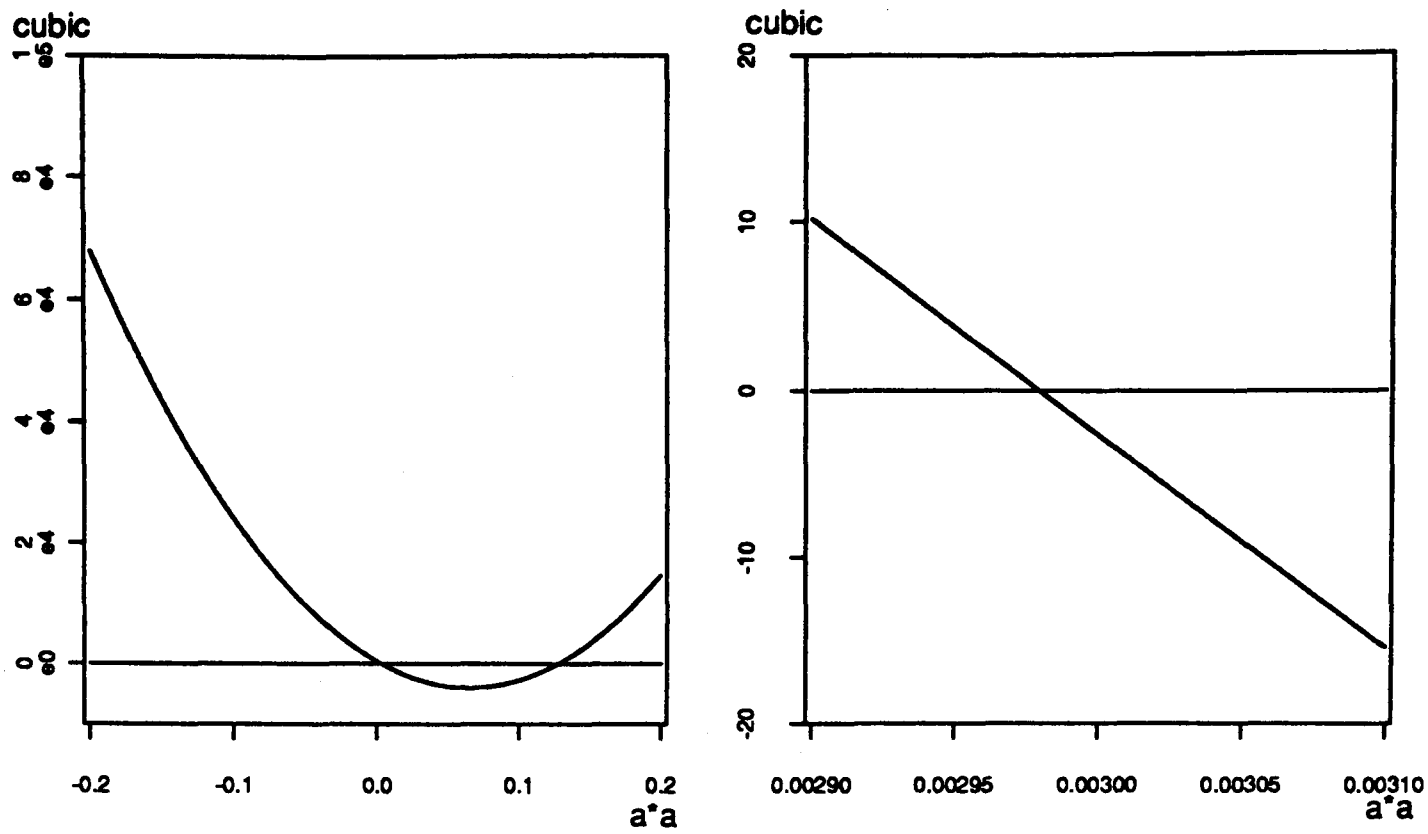

Figure 1.15: The cubic equation (1.18) for a^2_{max}, with a more detailed plot near the biologically relevant root.

$$\{[(1+\lambda)^2 - 4\Gamma]/4D_c\}a^6 + \{4\Gamma(3+D_c^2) - 18(1+\lambda)\Gamma + 2(1+\lambda)^2(1+2\lambda)\}a^4$$

$$+ D_c\{(1+\lambda)^2 + 3\Gamma(6\lambda + 2 - 9\Gamma)\}a^2 + 4D_c^2\Gamma = 0\,. \qquad (1.18)$$

This is plotted in Figure 1.15 for the parameter values we are using. There is a unique solution in (0.0,0.1), which must therefore be a^2_{max}, where a_{max} is the upper bound. Solving the cubic numerically gives $a_{max} \approx 0.0546$, which is close to the wave speed of about 0.05 observed for the activator mechanism in the numerical solutions of the partial differential equations (1.6) in one space dimension.

Perturbation analysis for the activator mechanism

For the activator kinetics, we can obtain an analytic approximation to the travelling wave form with $D = 0$ using regular perturbation theory. We rewrite (1.15) as

$$aN' = \epsilon(C-1)(2N-N^2) + (N-N^2) \qquad (1.19a)$$

$$D_cC'' - aC' - \lambda C = -\lambda \cdot \frac{(1+\alpha^2)N}{N^2+\alpha^2}\,, \qquad (1.19b)$$

and treat $\epsilon = 2(h-1)/(c_m - 2) \approx 0.47$ as a small parameter. With this value for ϵ, we will require the $O(\epsilon)$ correction to the $O(1)$ solution. The boundary conditions remain $N(-\infty) = C(-\infty) = 0$ and $N(+\infty) = C(+\infty) = 1$, with $N(0) = 1/2$ for uniqueness. We look for a solution of the form

$$N(z;\epsilon) = N_0(z) + \epsilon N_1(z) + \epsilon^2 N_2(z) + \cdots \tag{1.20a}$$

$$C(z;\epsilon) = C_0(z) + \epsilon C_1(z) + \epsilon^2 C_2(z) + \cdots . \tag{1.20b}$$

Substituting this into (1.19) and equating coefficients of ϵ^0 gives

$$\begin{aligned} aN_0' &= N_0 - N_0^2 \\ D_c C_0'' - aC_0' - \lambda C_0 &= -\lambda \cdot \frac{(1+\alpha^2)N_0}{N_0^2 + \alpha^2} . \end{aligned}$$

Changing the independent variable to $\xi = e^{z/a}$, these become

$$\begin{aligned} \xi N_0' &= N_0 - N_0^2 \\ \kappa\xi(\xi C_0')' - \xi C_0' - \lambda C_0 &= -\lambda \cdot \frac{(1+\alpha^2)N_0}{N_0^2 + \alpha^2} \end{aligned} \tag{1.21}$$

where $\kappa = a^{-2}D_c$ and prime denotes $d/d\xi$. The relevant boundary conditions are $N_0(+\infty) = C_0(+\infty) = 1$, $N_0(0) = C_0(0) = 0$ and $N_0(1) = 1/2$. Straightforward separation of variables gives $N_0 = \xi/(1+\xi)$. The equation for C_0 can then be solved using the method of undetermined coefficients. The corresponding homogeneous equation has linearly independent solutions $y \propto \xi^{q^\pm}$, where

$$q^\pm = \frac{1 \pm \sqrt{1 + 4\lambda\kappa}}{2\kappa} . \tag{1.22}$$

Therefore we look for a solution of the form $C_0 = \gamma_+(\xi)\,\xi^{q^+} + \gamma_-(\xi)\,\xi^{q^-}$ subject to the constraint $\gamma_+'\xi^{q^+} + \gamma_-'\xi^{q^-} = 0$. Substituting this into (1.21) gives linear equations for $\gamma_\pm'$, whose solution is

$$\gamma_\pm' = \frac{\mp\xi^{-(q^\pm+1)}}{\sqrt{1+4\lambda\kappa}} \cdot \lambda \cdot \frac{(1+\alpha^2)N_0}{N_0^2 + \alpha^2} .$$

Therefore

$$C_0 = \frac{\lambda(1+\alpha^2)}{\sqrt{1+4\lambda\kappa}}\left[\xi^{q^+}\int_\xi^{+\infty}\frac{1}{u^{(q^+ +1)}}\cdot\frac{N_0(u)}{N_0(u)^2+\alpha^2}\,du\;+\right.$$

$$\left.\xi^{q^-}\int_0^{\xi}\frac{1}{u^{(q^- +1)}}\cdot\frac{N_0(u)}{N_0(u)^2+\alpha^2}\,du\right]. \qquad (1.23)$$

Here the values of the constant limits are necessary (but not sufficient) for convergence at $\xi = 0$ and $+\infty$ respectively.

We consider the boundary conditions, which imply convergence, by investigating the behaviour of each of the two integrals in (1.23) as ξ approaches 0 and $+\infty$. We have

$$\lim_{\xi\to+\infty}\xi^{q^+}\int_\xi^{+\infty}\frac{1}{u^{(q^+ +1)}}\cdot\frac{N_0(u)}{N_0(u)^2+\alpha^2}\,du$$

$$= \lim_{\theta\to 0}\frac{1}{\theta^{q^+}}\int_{1/\theta}^{+\infty}\frac{1}{u^{(q^+ +1)}}\cdot\frac{N_0(u)}{N_0(u)^2+\alpha^2}\,du$$

$$= \lim_{\theta\to 0}\frac{1}{q^+\theta^{(q^+ -1)}}\cdot\frac{-\theta^{q^+}(1+1/\theta)}{\theta^{-2}+\alpha^2(1+1/\theta)^2}\cdot(-\theta^{-2})$$

$$= \frac{1}{q^+(1+\alpha^2)},$$

using L'Hôpital's rule and the expression for N_0. Similarly

$$\lim_{\xi\to+\infty}\xi^{q^-}\int_0^{\xi}\frac{1}{u^{(q^- +1)}}\cdot\frac{N_0(u)}{N_0(u)^2+\alpha^2}\,du = \frac{-1}{q^-(1+\alpha^2)}.$$

Thus

$$C_0(+\infty) = \frac{\lambda(1+\alpha^2)}{\sqrt{1+4\lambda\kappa}}\cdot\frac{1}{1+\alpha^2}\cdot\left(\frac{1}{q^+}-\frac{1}{q^-}\right)$$

$$= 1$$

using (1.22). Similarly the condition at $\xi = 0$ is satisfied.

We now consider the first order perturbations. Equating coefficients of ϵ^1 in the original ordinary differential equations (1.19) gives

$$\xi N_1' = N_1(1-2N_0) + (C_0-1)(2N_0-N_0^2) \qquad (1.24a)$$

$$\kappa\xi(\xi C_1')' - \xi C_1' - \lambda C_1 = -\lambda(1+\alpha^2)\cdot\left[\frac{\alpha^2-N_0^2}{(\alpha^2+N_0^2)^2}\right]\cdot N_1 \qquad (1.24b)$$

subject to $N_1(0) = N_1(+\infty) = C_1(0) = C_1(+\infty) = N_1(1) = 0$. Substituting for N_0 in (1.24a) and multiplying through by the integrating factor $(1 + 1/\xi)^2$ gives

$$\frac{d}{d\xi}\left[\left(\xi + 2 + \frac{1}{\xi}\right) N_1\right] = \left\{(C_0 - 1)\left(1 + \frac{2}{\xi}\right)\right\}$$

where C_0 is given in (1.23). Thus

$$N_1 = \frac{1}{\xi + 2 + 1/\xi} \int_1^{\xi} (C_0(u) - 1)(1 + 2/u)\, du\,.$$

Use of L'Hôpital's rule as above shows that the boundary conditions are satisfied. With this solution for N_1, (1.24b) can be solved using the method of undetermined coefficients, as above, giving

$$\begin{aligned} C_1 &= \frac{\lambda(1+\alpha^2)}{\sqrt{1+4\lambda\kappa}}\left[\xi^{q^+} I_1 + \xi^{q^-} I_2\right] \\ \text{where} \quad I_1 &= \int_{\xi}^{+\infty} \frac{1}{u^{(q^+ + 1)}} \cdot \frac{\alpha^2 - N_0(u)^2}{[\alpha^2 + N_0(u)^2]^2} N_1(u)\, du \\ \text{and} \quad I_2 &= \int_0^{\xi} \frac{1}{u^{(q^- + 1)}} \cdot \frac{\alpha^2 - N_0(u)^2}{[\alpha^2 + N_0(u)^2]^2} N_1(u)\, du\,. \end{aligned}$$

Again, we use l'Hôpital's rule to confirm that the boundary conditions are satisfied.

By repeating this process we can derive all the terms in the asymptotic expansion. The integrals involved, even for C_0, cannot be done analytically. However, it is clear without evaluating the integrals that λ, D_c and a occur in each term of the series (1.20), and thus in the solution as a whole, only in the groupings $q^{\pm}$ and $\lambda/\sqrt{1+4\lambda\kappa}$.

Chapter 2

Mathematical Experiments and Implications for Wound Geometry

2.1 Addition of Chemicals

In Chapter 1 we constructed a mathematical model for epidermal wound healing. The parameter values are based as far as possible on experimental data, and solutions of the model with either chemical activation or inhibition of mitosis compare well with experimental data on the normal healing of circular wounds. In this chapter, we use this model to perform various 'mathematical experiments', which will enable us to make clinically testable predictions.

The model (1.6) is based on chemical auto-regulation of cell division, and we begin by investigating the effect of putting additional quantities of the mitosis-regulating chemical onto the wound surface. Such a procedure is feasible experimentally, since some growth factors are available in isolated forms. Moreover, cell extracts and exudates have also been successfully added to wounds *in vivo* (Yamaguchi *et al.*, 1974; Eisinger *et al.*, 1988a; Madden *et al.*, 1989). To simulate such an addition of chemical, we solved the model equations in a two-dimensional radially symmetric geometry, as in Section 1.5, but when the wound area had decreased to half of its initial value, we increased the dimensionless chemical concentration by c_{add} at all points within the wound area. Here the 'wound area' is defined by the condition $n < 0.8$, as discussed on page 24. The effects of this single addition of mitosis-regulating chemical on the healing profile are illustrated in Figure 2.1, for both types of regulation. In both cases the effects are significant only for extremely large values of c_{add}. Addition of such high concentrations of any chemical is experimentally infeasible, since problems of side-effects and toxicity arise.

We therefore considered a different approach. Rather than a single addition of

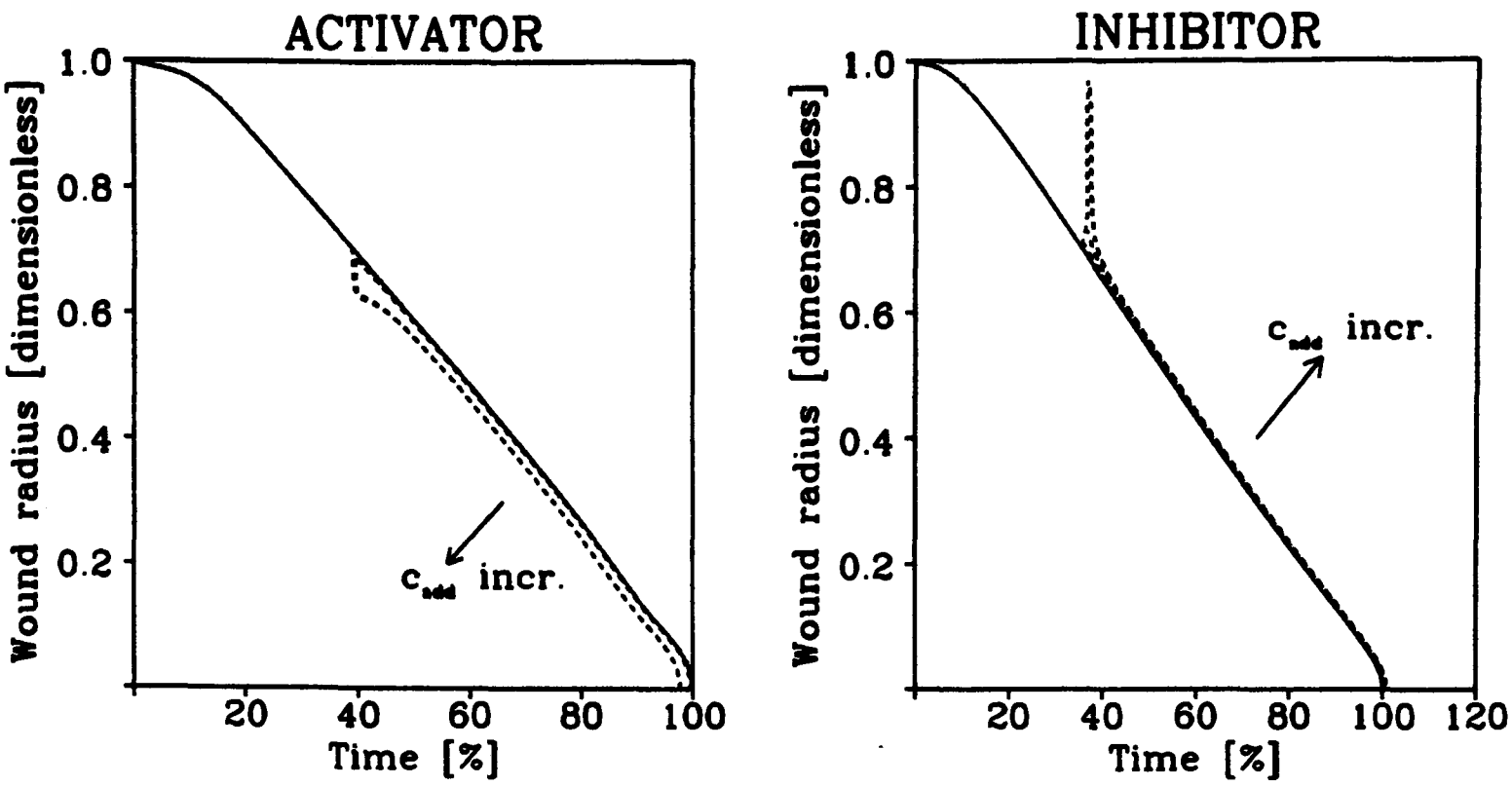

Figure 2.1: A simulation of the effects of a single addition of mitosis-regulating chemical to a healing epidermal wound. We have increased the dimensionless chemical concentration c by c_{add} at all points within the wound area, when this area is equal to half its initial value, for both the activator and inhibitor kinetics. The dimensionless wound radius is plotted against time for $c_{add} = 0$ (full curves) and $c_{add} = 10, 500, 10000$ (dashed curves). The effect on the healing profile is insignificant unless c_{add} is unrealistically large.

chemical, we investigated the effects of adding the regulatory chemical at a constant rate at all points within the wound area, once this area is less than half its initial value. This can be achieved experimentally by using a wound dressing soaked either in a solution of isolated chemical or in an epidermal cell extract or exudate; this is the approach used by Eisinger *et al.* (1988a) and Madden *et al.* (1989) in their experimental investigations into the role of chemical activation of mitosis in wound healing. To simulate the effects of such a dressing in our model, we amend the dimensionless model equations (1.6) in radially symmetric plane polar coordinates as follows

$$\frac{\partial n}{\partial t} = D\,\frac{1}{r}\frac{\partial}{\partial r}\left(r\frac{\partial n}{\partial r}\right) + s(c)\cdot n\cdot(2-n) - n \qquad (2.1a)$$

$$\frac{\partial c}{\partial t} = D_c\frac{1}{r}\frac{\partial}{\partial r}\left(r\frac{\partial c}{\partial r}\right) + \lambda g(n) - \lambda c + c_{dress}.I[n(r) < 0.8].I\left[n\left(\tfrac{1}{\sqrt{2}}\right) > 0.8\right]. \qquad (2.1b)$$

Here c_{dress} is the constant rate of chemical addition resulting from the dressing, and $I[.]$ is an indicator function, that is $I[.\text{TRUE.}] = 1$, $I[.\text{FALSE.}] = 0$. The initial and

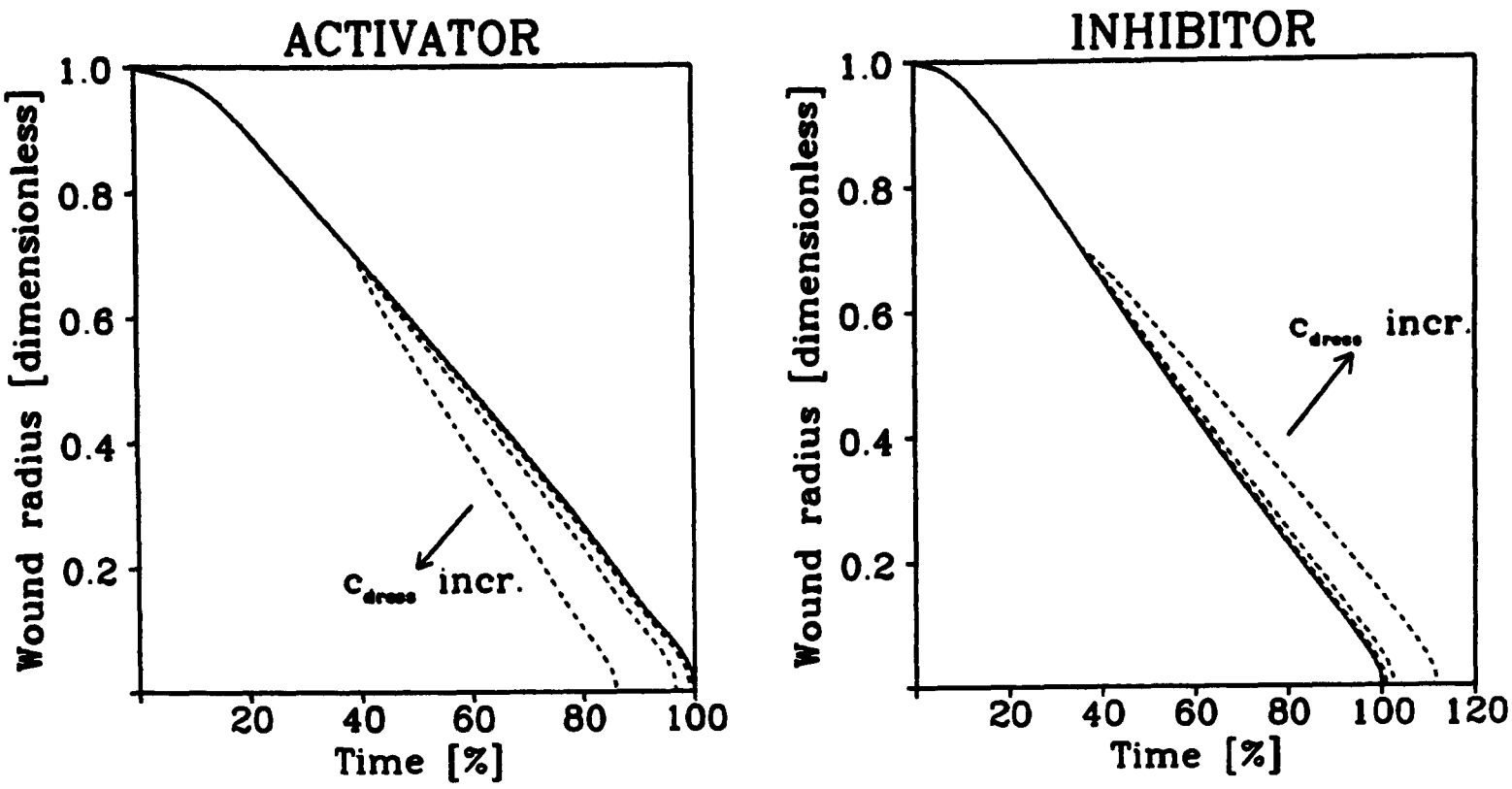

Figure 2.2: A simulation of the effects of applying a dressing soaked in mitosis-regulating chemical to a healing epidermal wound. We have added chemical at a constant dimensionless rate c_{dress} within the wound area, when this area is less than half its initial value, for both the activator and inhibitor mechanisms. The amended model equations are given in (2.1). The dimensionless wound radius is plotted against time for $c_{dress} = 0$ (full curves) and $c_{dress} = 2, 10, 50$ (dashed curves, activator case), $c_{dress} = 0.2, 1, 5$ (dashed curves, inhibitor case). These predicted healing profiles could in principle be tested experimentally.

boundary conditions remain $n = c = 0$ at $t = 0$, $r < 1$ and $n = c = 1$ for all t at $r = 1$.

The effects of this constant addition of chemical on the healing profile are illustrated in Figure 2.2 for a range of values of c_{dress}. In contrast to the case of a single addition of chemical, these effects are significant for experimentally relevant values of c_{dress}. As expected intuitively, a given value of c_{dress} has a greater effect for the inhibitor kinetics than for the activator kinetics, since the rate of chemical decay is significantly higher in the activator case (recall that $\lambda = 30$ for the activator mechanism and $\lambda = 5$ for the inhibitor mechanism). The solutions $n(r, t)$ and $c(r, t)$ corresponding to the amended equations (2.1) are illustrated in Figure 2.3. This shows that the 'dressing' effects not only the speed of healing, but also the travelling wave forms.

The experiments of Eisinger *et al.* (1988a) and Madden *et al.* (1989) are unfortu-

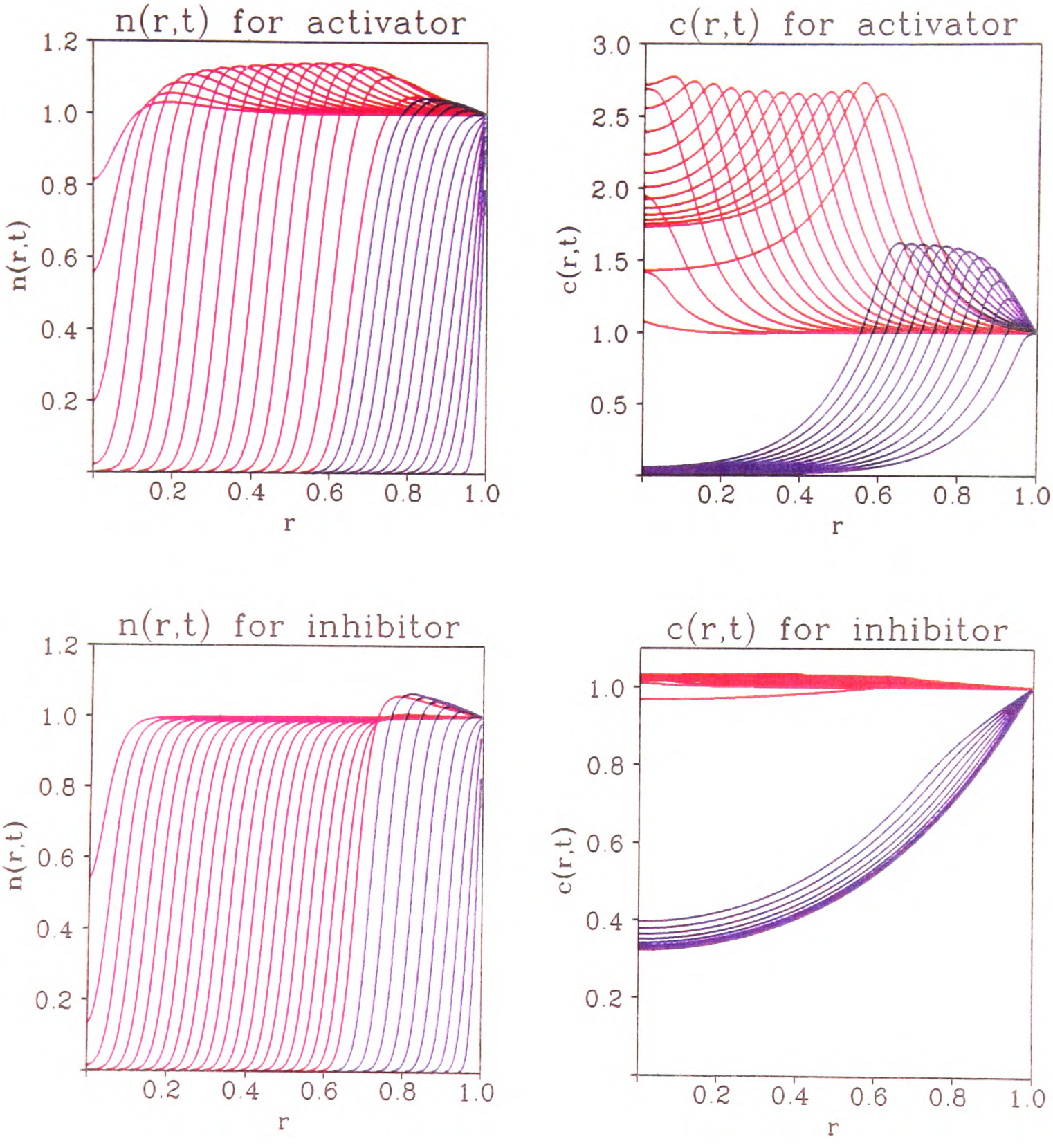

Figure 2.3: The solutions of (2.1) for $c_{dress} = 50$ (activator kinetics) and $c_{dress} = 5$ (inhibitor kinetics); the other parameter values are as in Figure 1.8. Cell density n and chemical concentration c are plotted against radius r at a selection of equally spaced times. These solutions are drawn in blue when the wound area is greater than 1/2, and in red when the wound area is less than 1/2. The latter case corresponds to addition of chemical at rate c_{dress}.

nately only qualitative. However, the mathematical 'wound dressing' experiments we have discussed would correspond to similar quantitative biological experiments. Data from such experiments would not only serve as a further test of the model, but would also enable the model solutions to predict the concentrations of mitosis-regulating chemical that are present in unwounded skin *in vivo*.

2.2 Model Solutions for General Wound Geometries

The solutions of the dimensionless model equations (1.6) presented in Chapter 1 and Section 2.1 have all been for either one-dimensional or radially symmetric two-dimensional geometries. We now consider solutions for more general wound shapes. To investigate this, we solved (1.6) numerically on a uniform two-dimensional space mesh using a fully explicit finite difference method. That is, in the numerical discretization, all the terms on the right-hand side of the equation, including the diffusion terms, were evaluated at the current time point. For a linear diffusion equation, $u_t = D_u(u_{xx} + u_{yy})$, this numerical method is stable provided

$$\rho_{num} = \frac{\delta t}{(\delta x)^2} \leq \frac{1}{4D_u}$$

(see, for example, Hildebrand, 1968). Here δx is the node separation of the uniform space mesh, and δt is the time step. For systems of reaction-diffusion equations, a corresponding convergence condition cannot be derived analytically, but most numerical studies have found that for convergence, the ratio $\rho_{num} \cdot \max\{D_1, D_2, \ldots\}$ must be less than a critical value which depends on the reaction terms, but is usually slightly less than 1/4 (Arcuri, 1984). Here $D_1, D_2, \ldots$ are the diffusion coefficients. For the system (1.6), we found that the convergence condition was indeed of this form: specifically, convergence required $\rho_{num} \cdot D_c \lesssim 0.18$ for the activator kinetics and $\rho_{num} \cdot D_c \lesssim 0.23$ for the inhibitor kinetics.

Most clinically relevant wound shapes have four-fold symmetry, so that it is sufficient to solve the model equations on one quarter of the wounded region. We

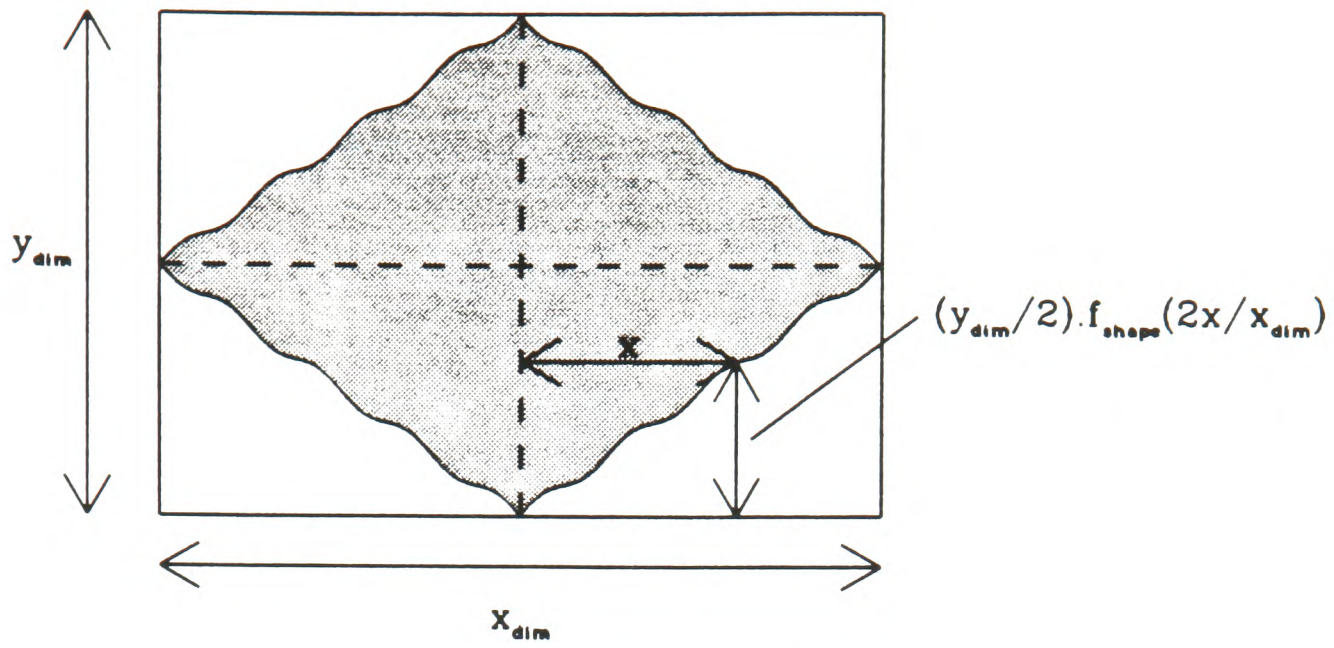

Figure 2.4: An illustration of an initial wound shape, defined by the function f_{shape} in the lower right-hand quadrant, and by four-fold symmetry elsewhere. The initially wounded region is shaded.

define the initial wound shape by the function $f_{shape} : [0,1] \mapsto [0,1]$. The initial wound edge in the lower right-hand quadrant of the wounded region is then $y = \frac{1}{2} y_{dim} \cdot f_{shape}(2x/x_{dim})$, referred to an origin at the lower left-hand corner of this quadrant, where x_{dim} and y_{dim} are the lengths of the initial wound midlines in the x and y directions respectively (Figure 2.4). We consider only wound shapes satisfying $f_{shape}(0) = 0$ and $f_{shape}(1) = 1$, with f_{shape} increasing.

A common wound geometry is an 'eye-shaped' wound, which results from the initial dermal gaping of a linear slash wound. To simulate this, we took $f_{shape} = 1 - \sqrt{1 - \sqrt{x}}$. The solutions of the model (1.6) for this initial wound shape with $x_{dim}/y_{dim} = 4$ are illustrated in Figure 2.5, in which we plot the values of n and c on the two midlines at a selection of equally spaced times. As in the case of a circular wound discussed in Chapter 1, the solutions consist of a wave of cells moving inwards to close the wound, with an associated wave of chemical. These solutions can also be instructively illustrated by plotting the location of the wound edge at equally spaced times, and this is done in Figure 2.6. As discussed on page 24, we take the 'wound edge' as the contour of points at which the cell density is 80% of its unwounded level, that is $n = 0.8$.

Apart from circular wounds, one of the wound shapes that can be most easily made experimentally is a rectangular wound (see, for example, Martin and Lewis,

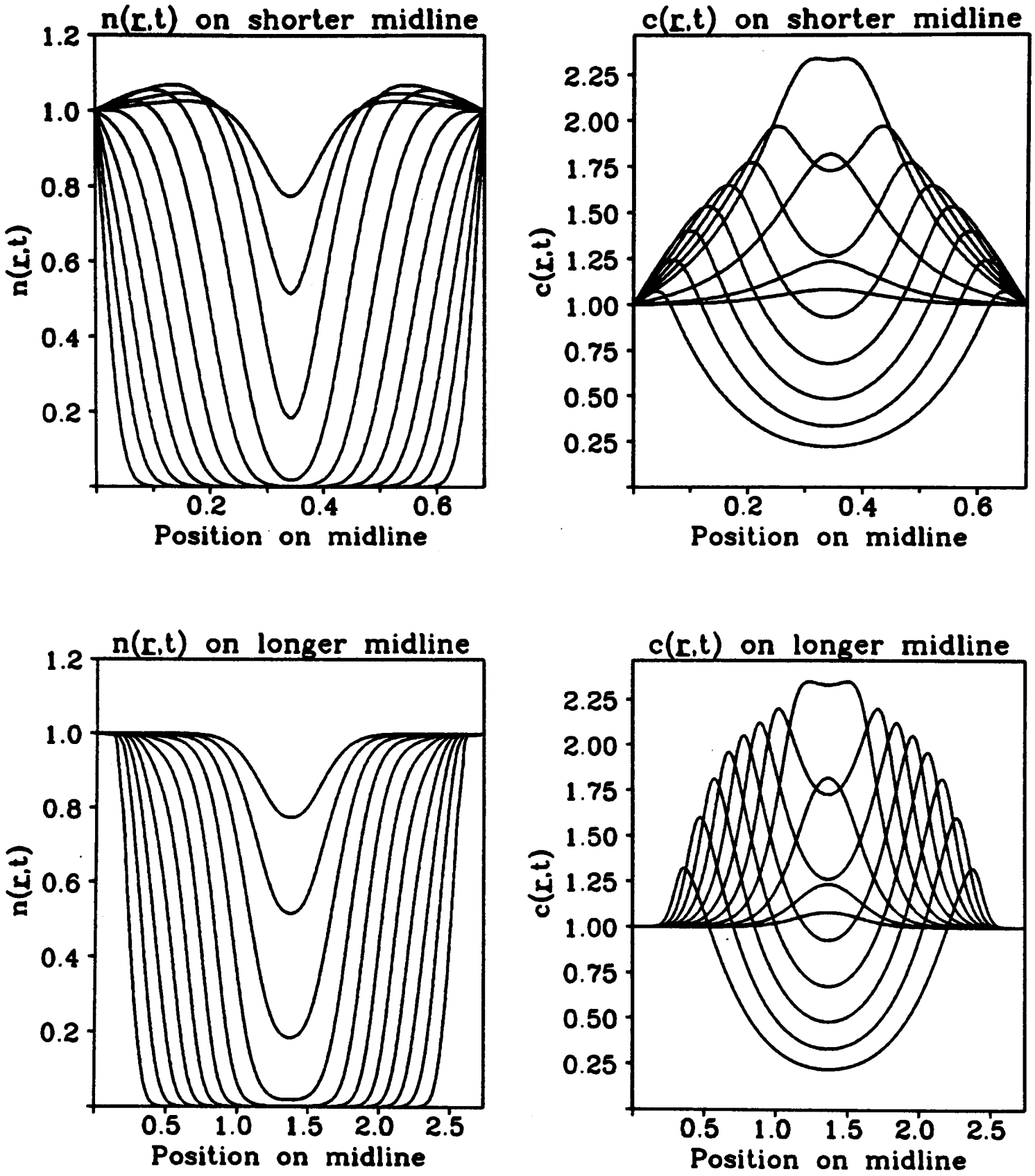

Figure 2.5: (a) The solution of (1.6) for an 'eye-shaped' wound, defined by $f_{shape} = 1 - \sqrt{1 - \sqrt{x}}$, with the activator kinetics. The cell density n and chemical concentration c on the two midlines are plotted at a selection of equally spaced times. The parameter values are as in Figure 1.8, and the initial ratio of midline lengths is $y_{dim}/x_{dim} = 4$. The initial wound area has a dimensionless value of 1.

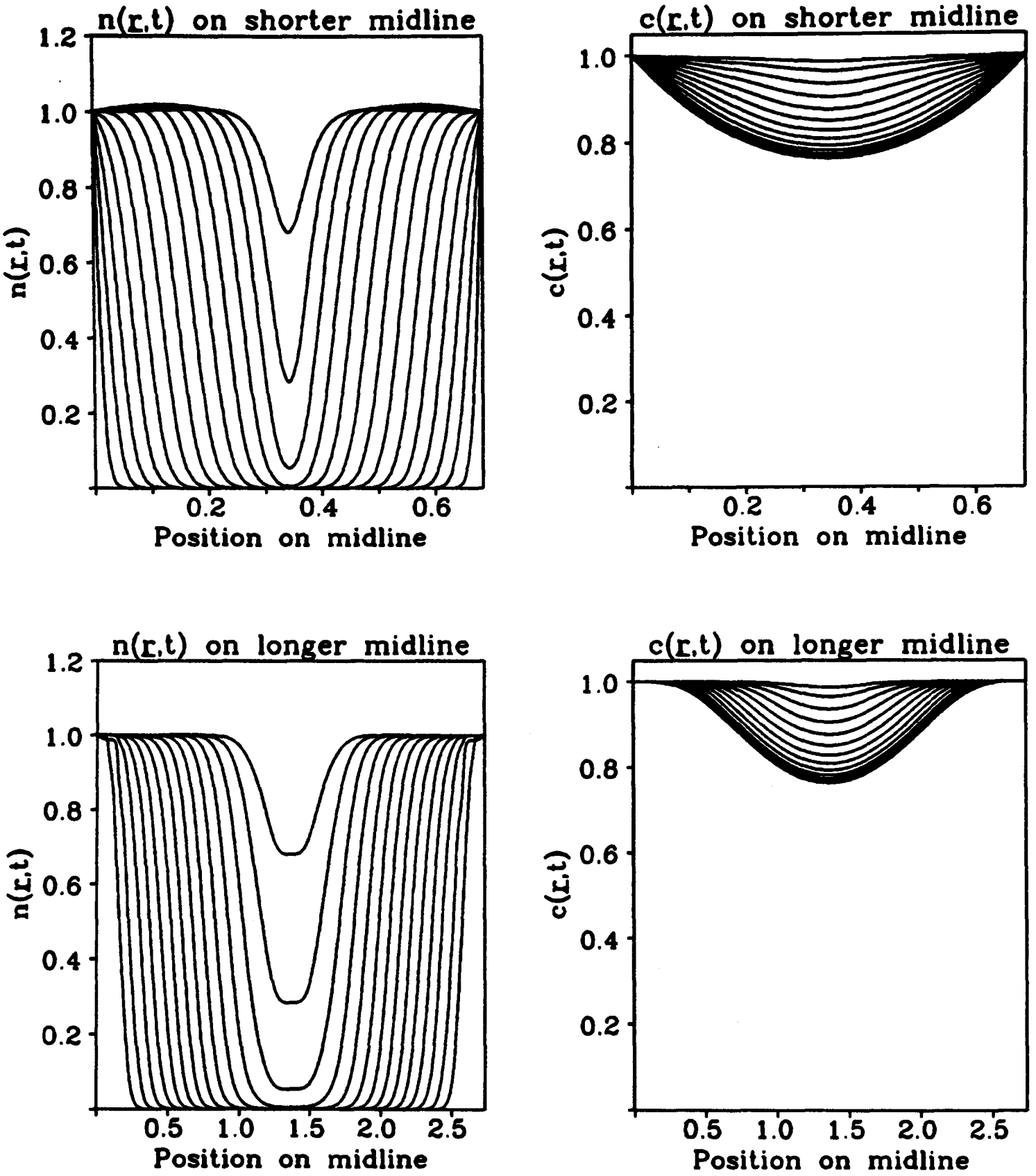

Figure 2.5: (b) The solution of (1.6) for an 'eye-shaped' wound, defined by $f_{shape} = 1 - \sqrt{1 - \sqrt{x}}$, with the inhibitor kinetics. The cell density n and chemical concentration c on the two midlines are plotted at a selection of equally spaced times. The parameter values are as in Figure 1.8, and the initial ratio of midline lengths is $y_{dim}/x_{dim} = 4$. The initial wound area has a dimensionless value of 1.

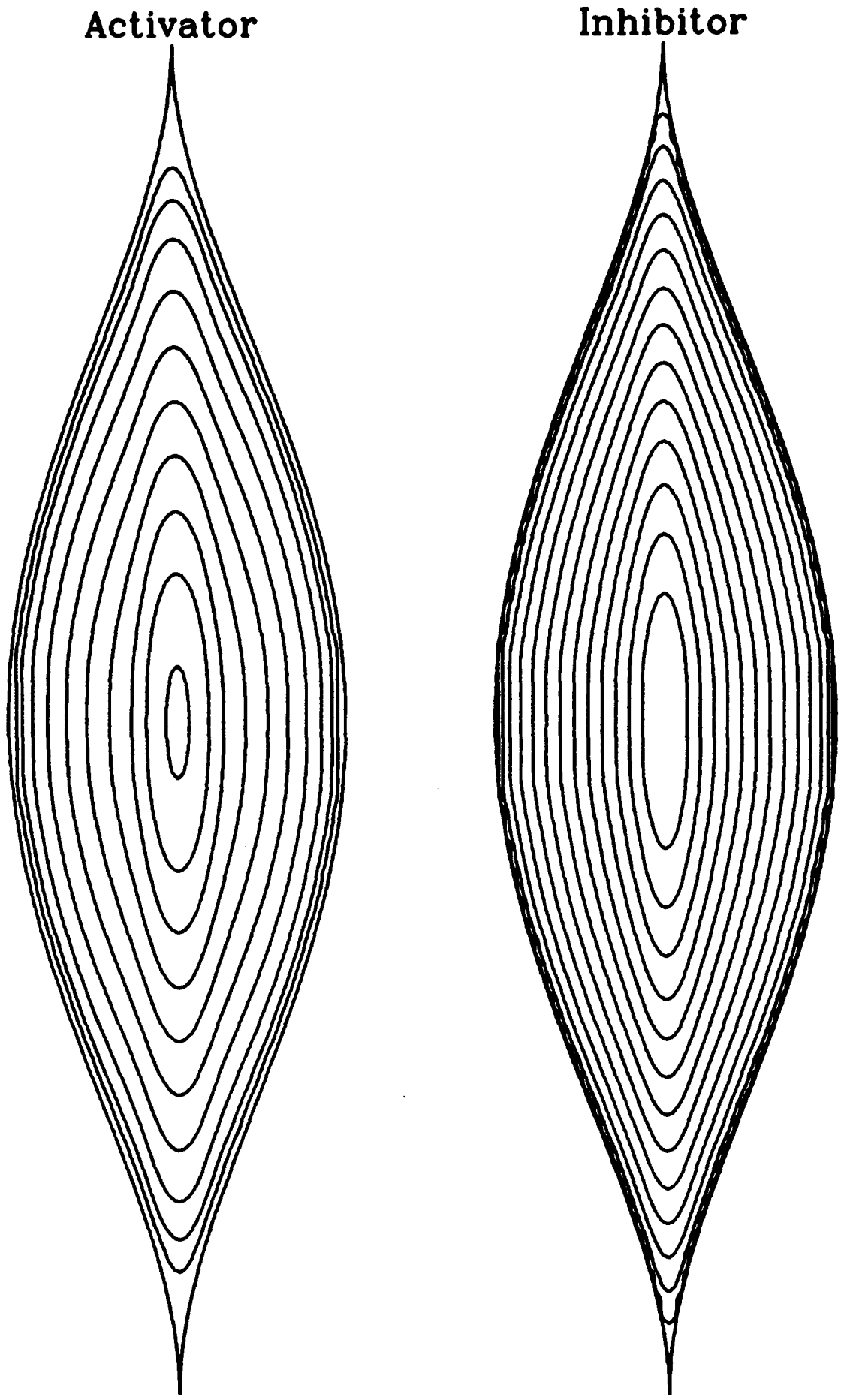

Figure 2.6: The wound edge at a selection of equally spaced times for an initially 'eye-shaped wound', defined by $f_{shape} = 1 - \sqrt{1 - \sqrt{x}}$. The 'wound edge' is defined as the contour $n = 0.8$. The parameter values are as in Figure 1.8, and the initial ratio of midline lengths is $y_{dim}/x_{dim} = 4$. The initial wound area has a dimensionless value of 1.

1991a). Figure 2.7 illustrates the solutions of the model (1.6) for such a wound, with initial side-length ratio 2.5. The corresponding wound edge contours are shown in Figure 2.8. A simple prediction that can be made using the model is on the variation in healing time with the side-length ratio of rectangular wounds of a given initial area. The variation predicted by the model is illustrated in Figure 2.9 for the two regulatory mechanisms. Here the 'healing time' is taken to be the time at which the cell density at the centre of the wound reaches 80% of its unwounded level; the 'wound area', as defined on page 24, is then zero. A decrease in healing time as the side-length ratio increases is expected intuitively, but quantitative data against which the curves in Figure 2.9 could be tested are not currently available. However, these curves are in principle experimentally testable.

2.3 Quantifying Wound Shape

One of our original aims in modelling epidermal wound healing was to investigate the variation in healing time with wound shape. Such a study requires the identification of quantifiable aspects of the initial wound geometry. In the previous section, we chose the initial midline ratio, and considered the variation in healing time with this ratio for rectangular wounds. This variation is illustrated in Figure 2.9, and is very similar for a variety of forms of the wound shape function f_{shape}.

A more interesting trend, however, is to fix the midline ratio and vary the function f_{shape} in a quantifiable way. To this end, we have investigated two single parameter families of wound shapes. The first family is composed of arcs of circles, defined by

$$f_{shape}(\xi;\alpha) = \frac{1}{2}\left(1+\frac{1}{\alpha}\right) - \text{sign}\,(\alpha)\left[\frac{1}{2}\left(1+\frac{1}{\alpha^2}\right) - \left(\xi+\frac{1}{2\alpha}-\frac{1}{2}\right)^2\right]^{1/2}, \qquad (2.2)$$

$-1 < \alpha < 1$. This is the functional form of an arc of a circle with centre $(1/2 - 1/2\alpha, 1/2 + 1/2\alpha)$ and radius $\sqrt{(1+1/\alpha^2)/2}$ (Figure 2.10). Therefore as the parameter α increases from -1, the wound changes from a cusped shape, through a diamond at $\alpha = 0$, to an ovate shape, and finally to an ellipse at $\alpha = +1$ (Figure 2.11). For clarity, all the wound shapes in Figure 2.11 are shown with the same midline lengths,

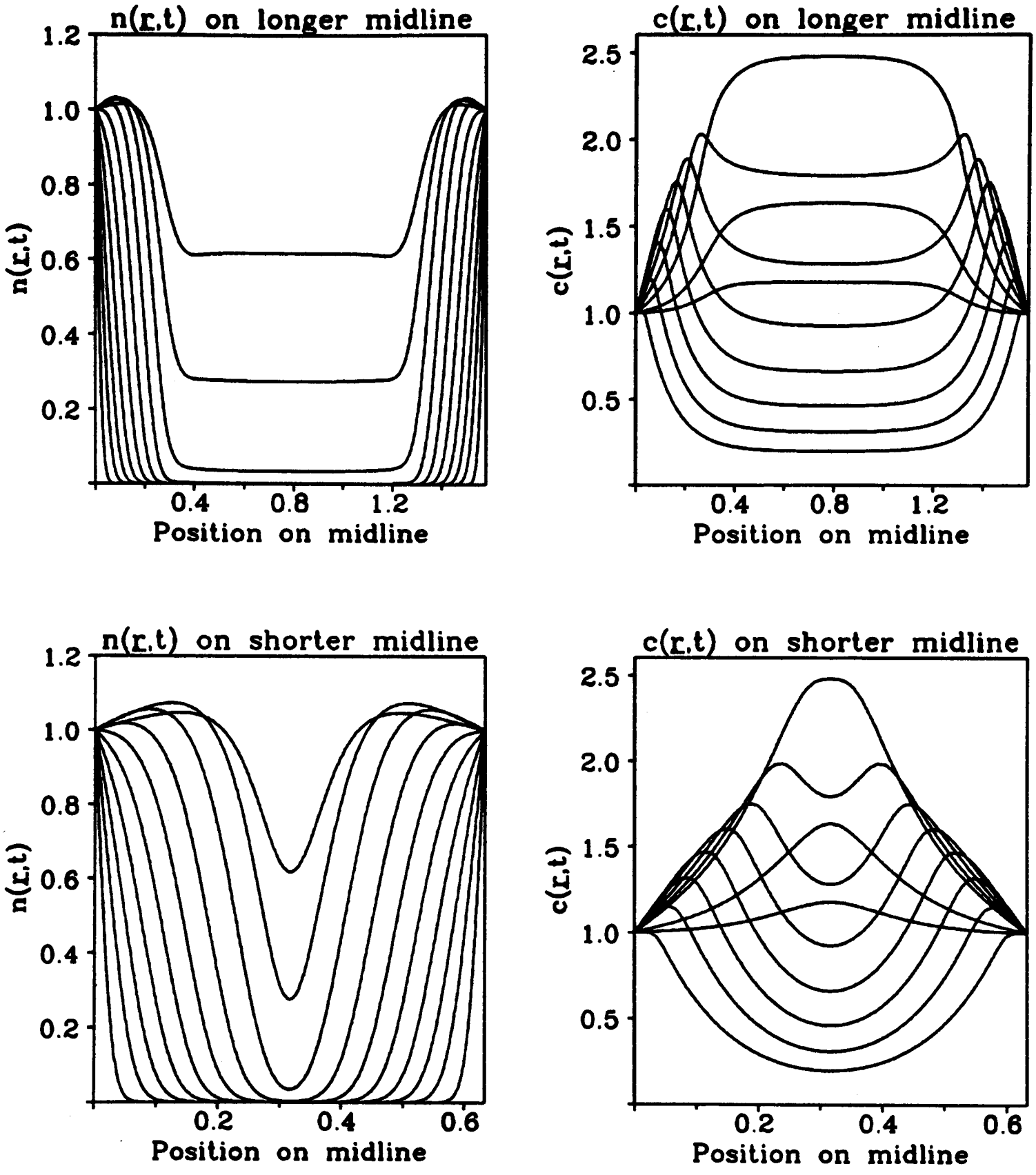

Figure 2.7: (a) The solution of (1.6) for a rectangular wound, with the activator kinetics. The cell density n and chemical concentration c on the two midlines are plotted at a selection of equally spaced times. The parameter values are as in Figure 1.8, and the initial side-length ratio is 2.5. The initial wound area has a dimensionless value of 1.

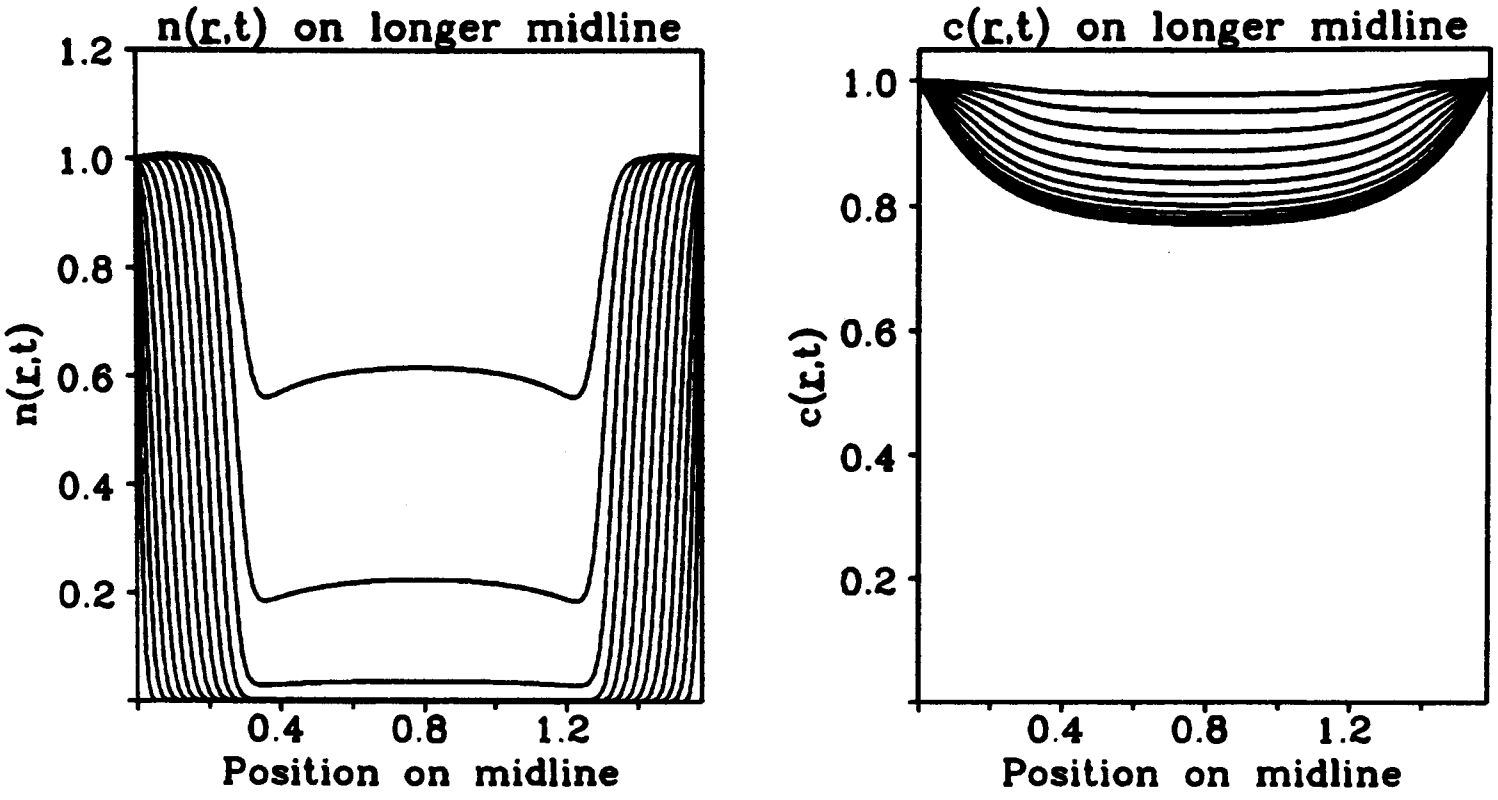

Figure 2.7: (b) The solution of (1.6) for a rectangular wound, with the inhibitor kinetics. The cell density n and chemical concentration c on the two midlines are plotted at a selection of equally spaced times. The parameter values are as in Figure 1.8, and the initial side-length ratio is 2.5. The initial wound area has a dimensionless value of 1.

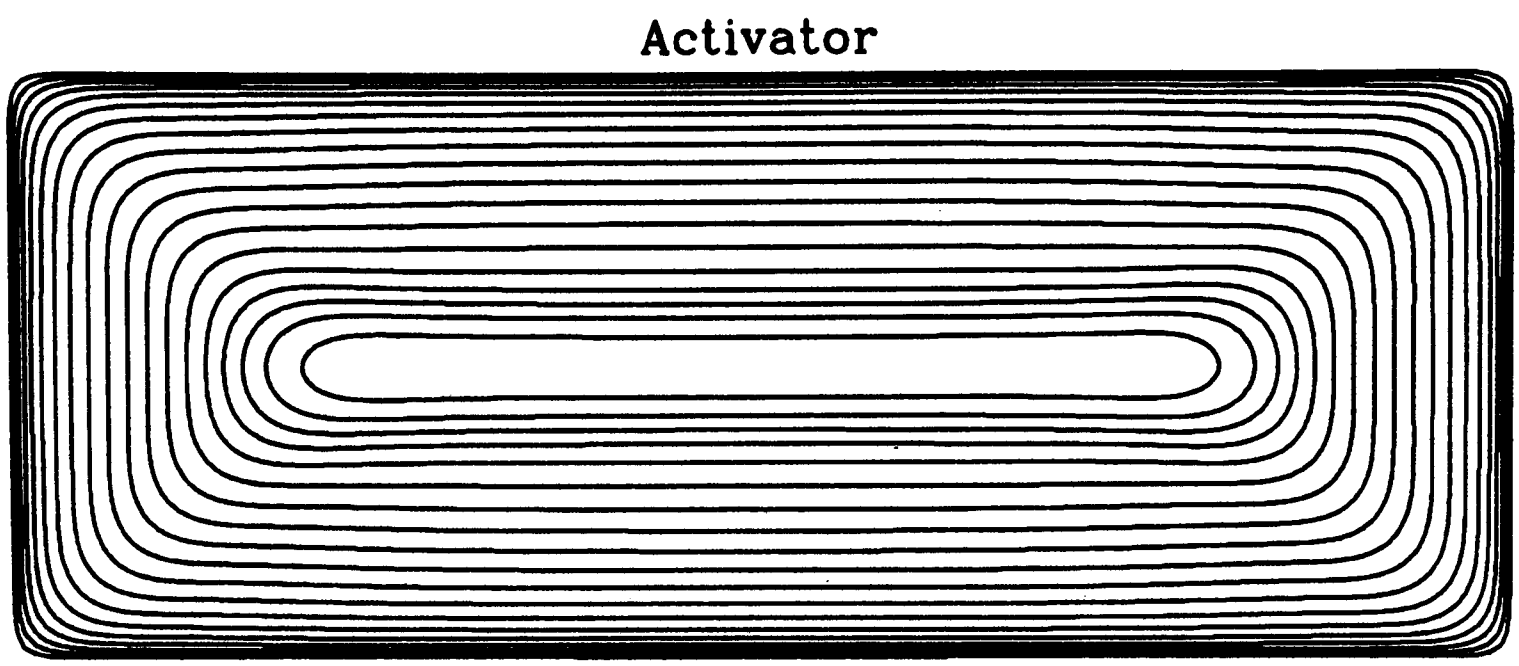

Figure 2.8: The wound edge at a selection of equally spaced times for an initially rectangular wound. The 'wound edge' is defined as the contour $n = 0.8$. The parameter values are as in Figure 1.8, and the initial side-length ratio is 2.5. The initial wound area has a dimensionless value of 1.

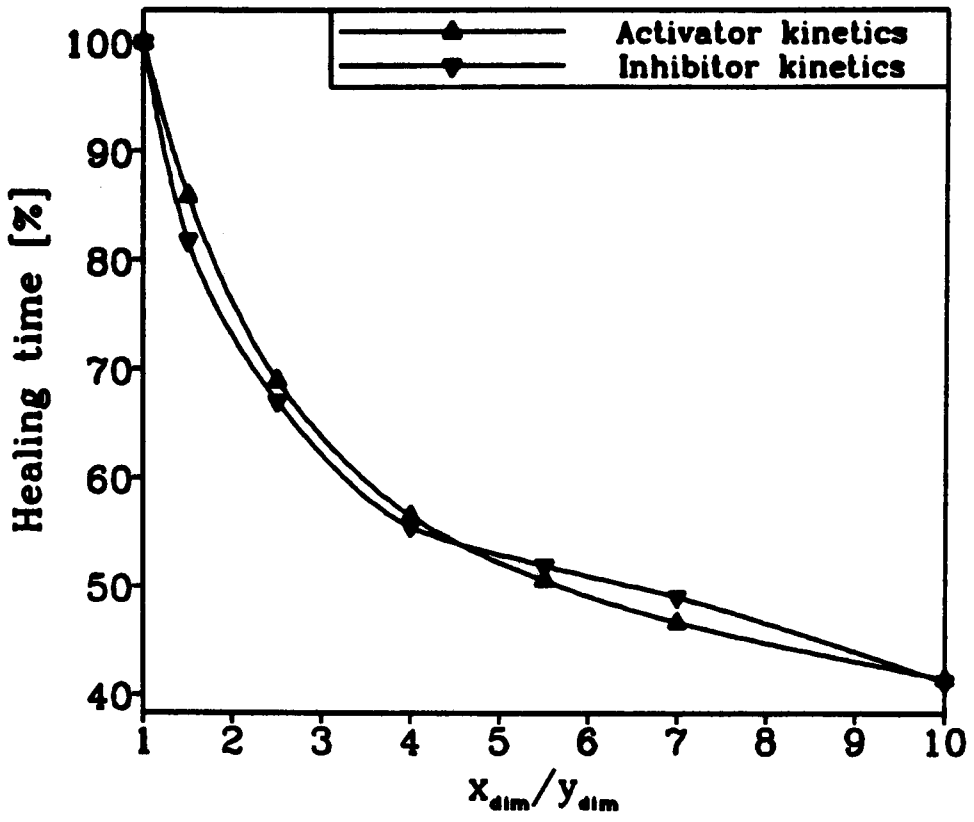

Figure 2.9: The variation in healing time with the side-length ratio x_{dim}/y_{dim} of rectangular wounds, as predicted by the model. For both regulatory mechanisms, the healing time is plotted as a percentage of that for a square wound. All the wounds have an initial dimensionless area of 1, and the parameter values are as in Figure 1.8.

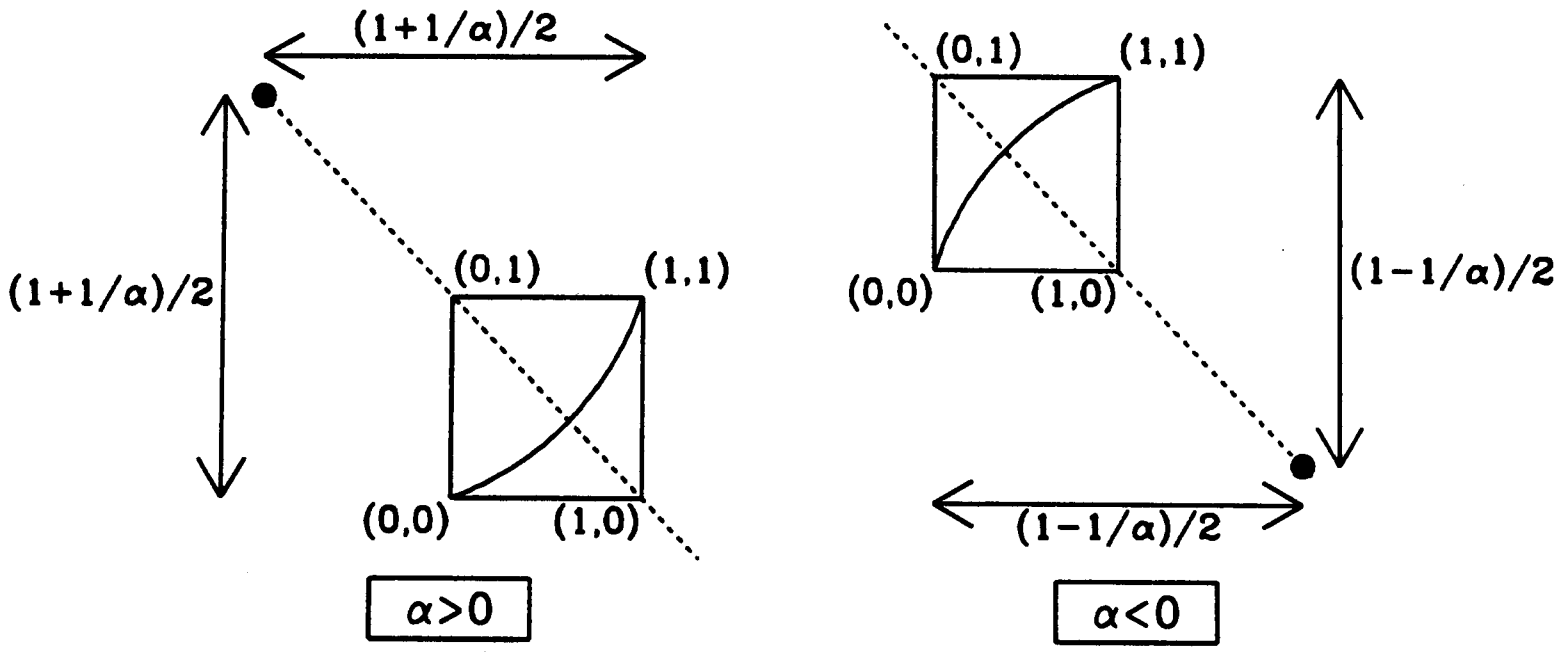

Figure 2.10: An illustration of the form of $f_{shape}(\xi;\alpha)$, defined in (2.2), for both $\alpha > 0$ and $\alpha < 0$.

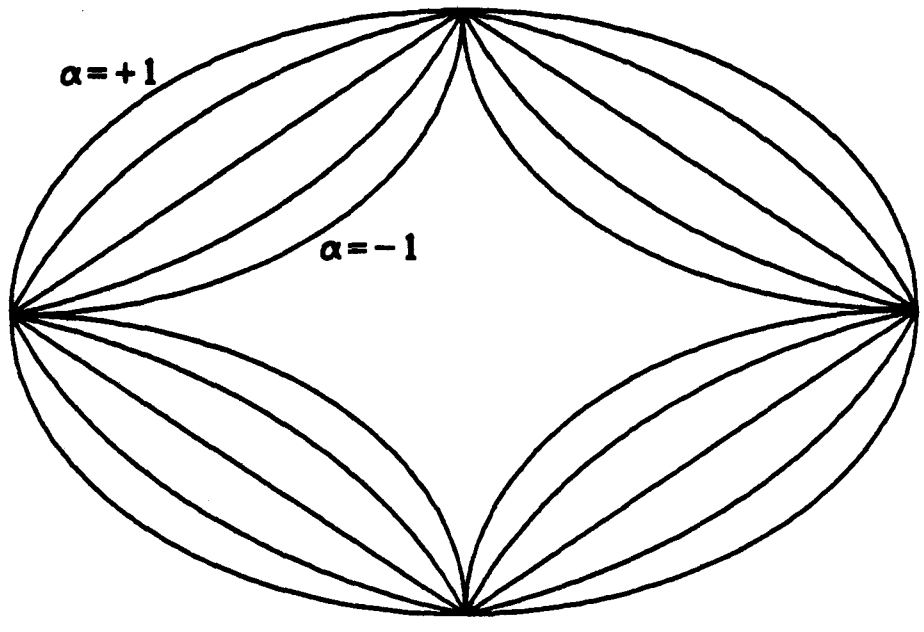

Figure 2.11: The family of wound shapes defined by (2.2), parameterized by α. For clarity, all the shapes are illustrated with the same midline lengths, but in the numerical simulations, the lengths of the midlines are chosen, in a specified ratio, so that in each case the initial wound area has a dimensionless value of 1.

but in the numerical simulations, the lengths of the midlines are chosen, in a specified ratio, so that in each case the initial wound area has a dimensionless value of 1. Figure 2.12 illustrates the solutions of the model (1.6) for $\alpha = -0.8$, with midline lengths x_{dim} and y_{dim} in the ratio 1.5, and the corresponding wound edge contours are shown in Figure 2.13. The solutions and contours for $\alpha = +0.8$ are shown in Figures 2.14 and 2.15, respectively, again with $x_{dim}/y_{dim} = 1.5$.

The variation in healing time with the parameter α, as predicted by the activator and inhibitor mechanisms, is shown in Figure 2.16. It appears that this variation is similar for the two mechanisms when the wound shape is concave when viewed from the centre, but quite different for convex wound shapes. To investigate this further, we considered a second family of wound shapes, given by

$$f_{shape}(\xi; p) = \xi^p, \qquad 0 < p < \infty. \tag{2.3}$$

This family is illustrated in Figure 2.17; as the parameter p increases from zero, the wound changes from a highly cusped shape, through a diamond at $p = 1$, to an ovate shape, and finally to a rectangle as $p \to \infty$. Again, for clarity all the shapes are shown with the same midline lengths, but in the numerical simulations, these lengths are chosen so that the initial wound area has a dimensionless value of 1 in each case. The variation in healing time with the parameter p, as predicted by the two regulatory

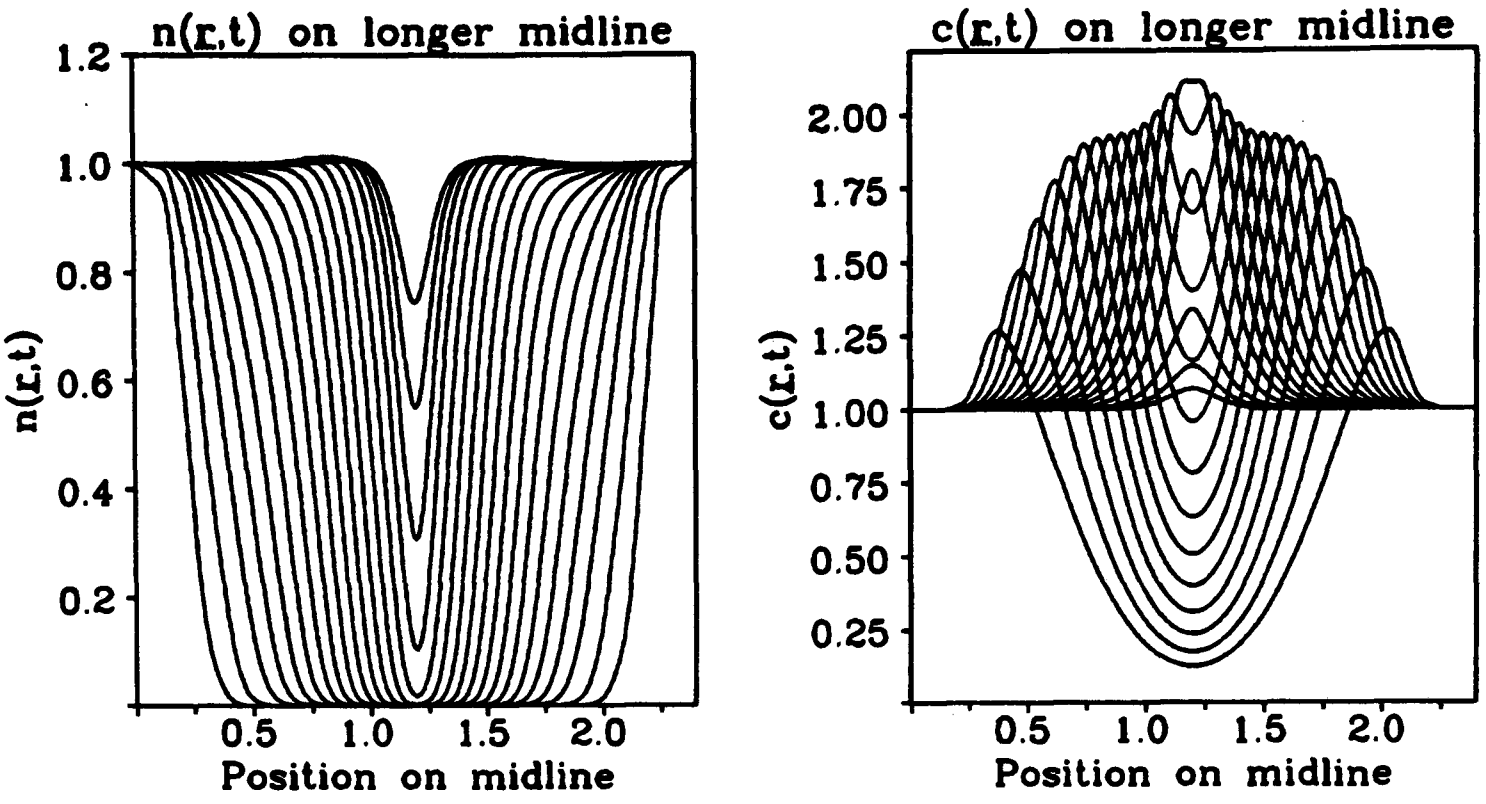

Figure 2.12: (a) The solution of (1.6) with the wound shape function f_{shape} as in (2.2) and $\alpha = -0.8$, with the activator kinetics. The cell density n and chemical concentration c on the two midlines are plotted at a selection of equally spaced times. The parameter values are as in Figure 1.8, and the initial ratio of midline lengths is 1.5. The initial wound area has a dimensionless value of 1.

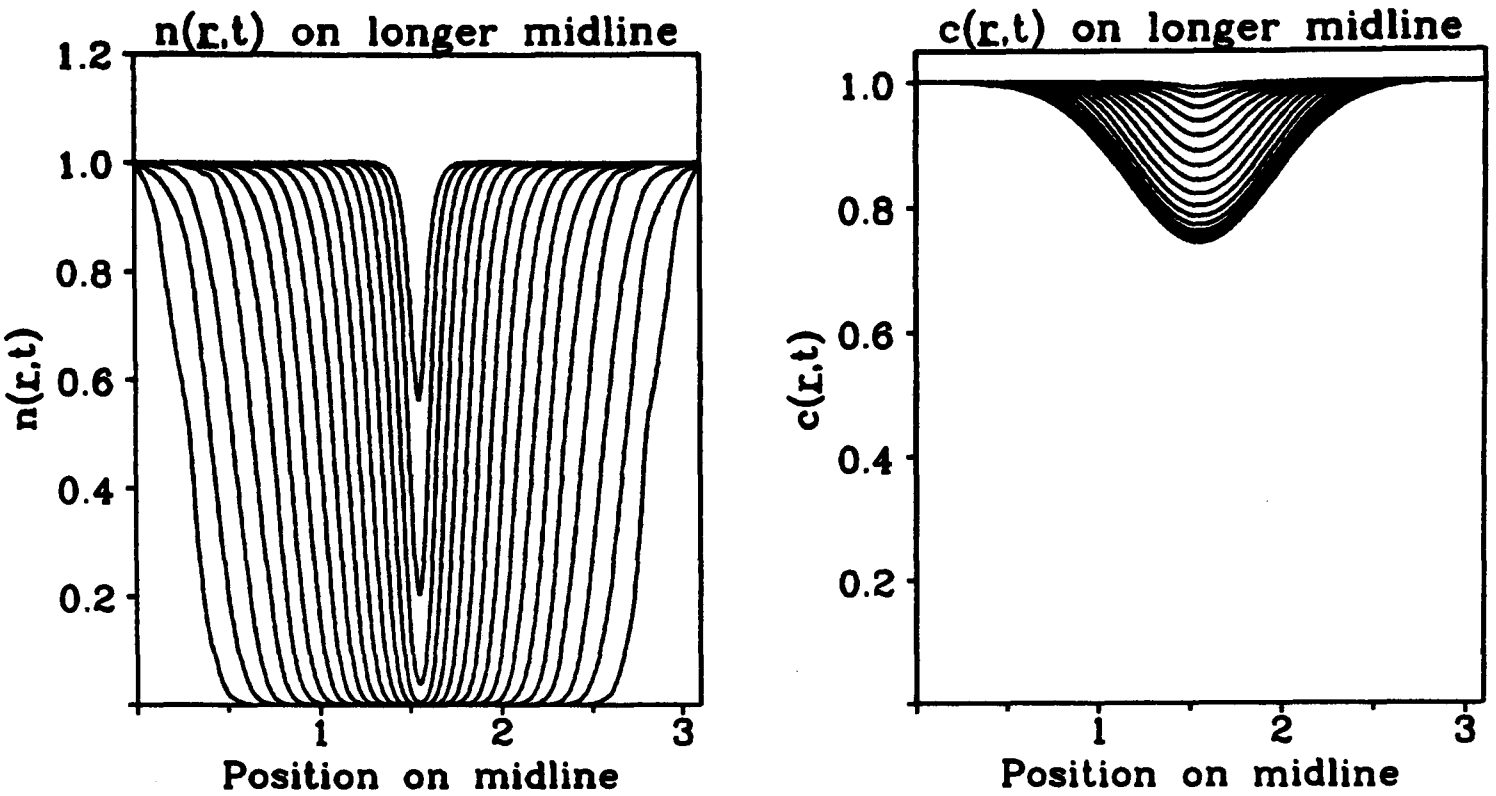

Figure 2.12: (b) The solution of (1.6) with the wound shape function f_{shape} as in (2.2) and $\alpha = -0.8$, with the inhibitor kinetics. The cell density n and chemical concentration c on the two midlines are plotted at a selection of equally spaced times. The parameter values are as in Figure 1.8, and the initial ratio of midline lengths is 1.5. The initial wound area has a dimensionless value of 1.

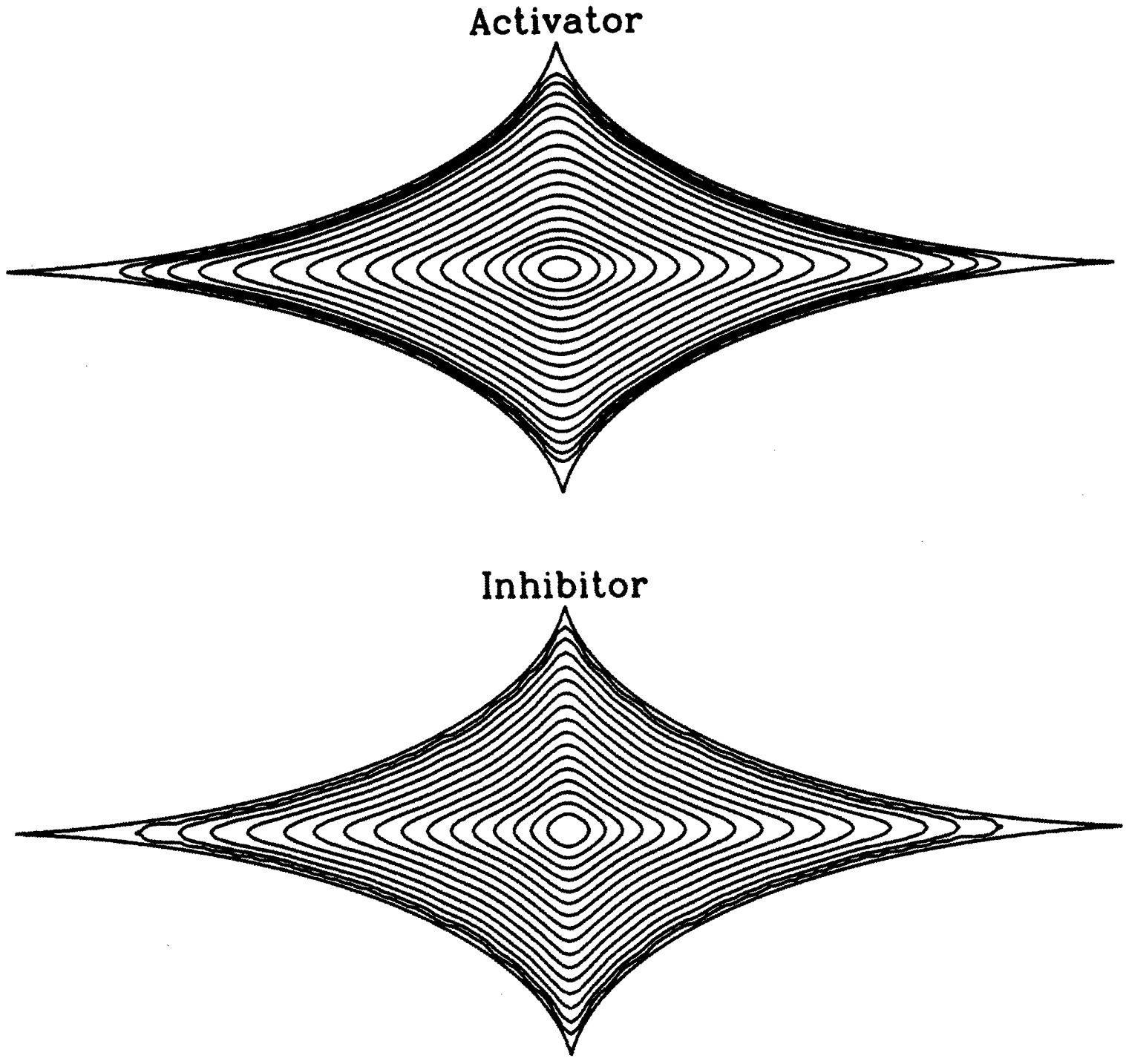

Figure 2.13: The wound edge at a selection of equally spaced times with the wound shape function f_{shape} as in (2.2) and $\alpha = -0.8$. The 'wound edge' is defined as the contour $n = 0.8$. The parameter values are as in Figure 1.8, and the initial ratio of midline lengths is 1.5. The initial wound area has a dimensionless value of 1.

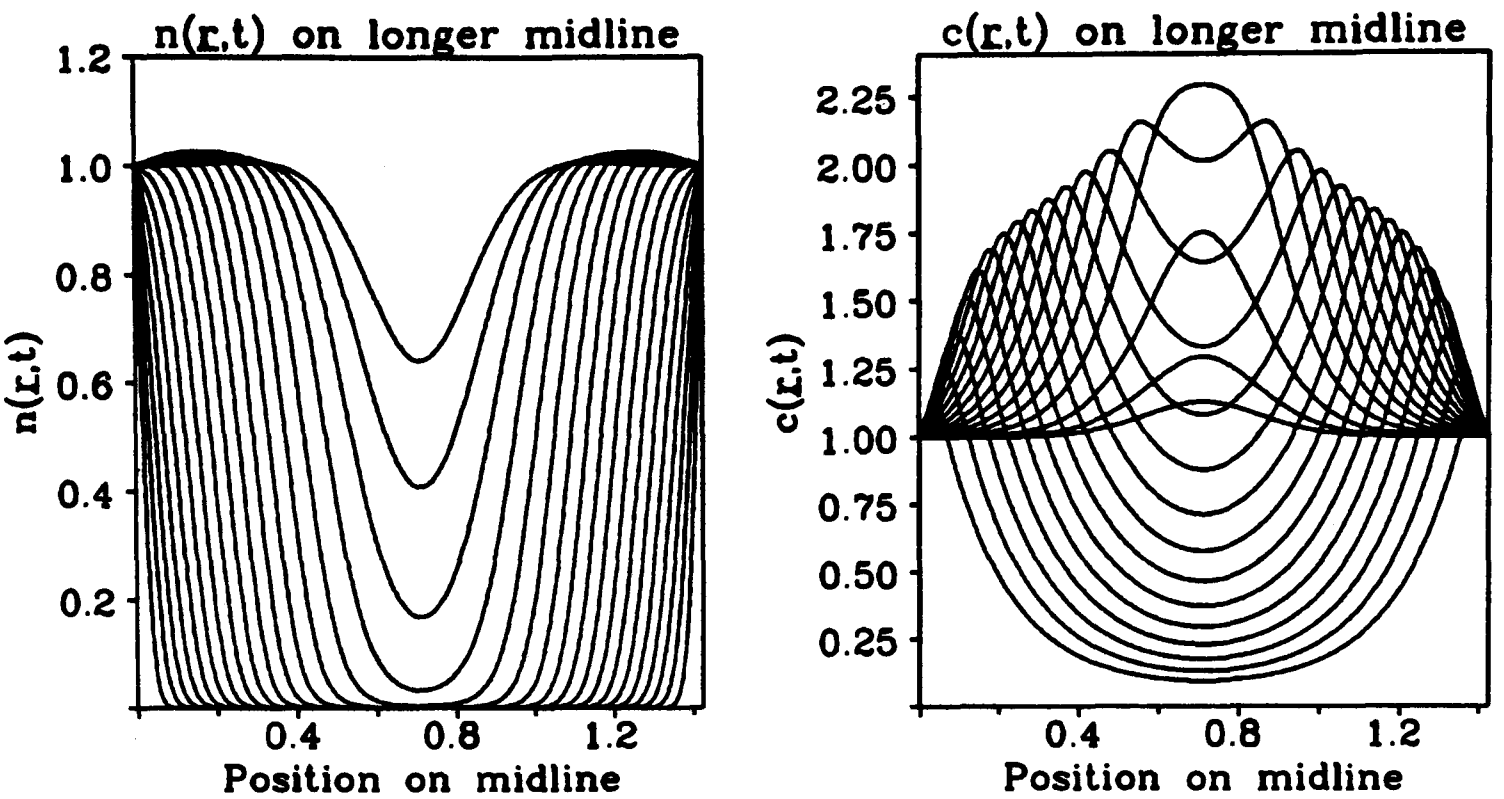

Figure 2.14: (a) The solution of (1.6) with the wound shape function f_{shape} as in (2.2) and $\alpha = 0.8$, with the activator kinetics. The cell density n and chemical concentration c on the two midlines are plotted at a selection of equally spaced times. The parameter values are as in Figure 1.8, and the initial ratio of midline lengths is 1.5. The initial wound area has a dimensionless value of 1.

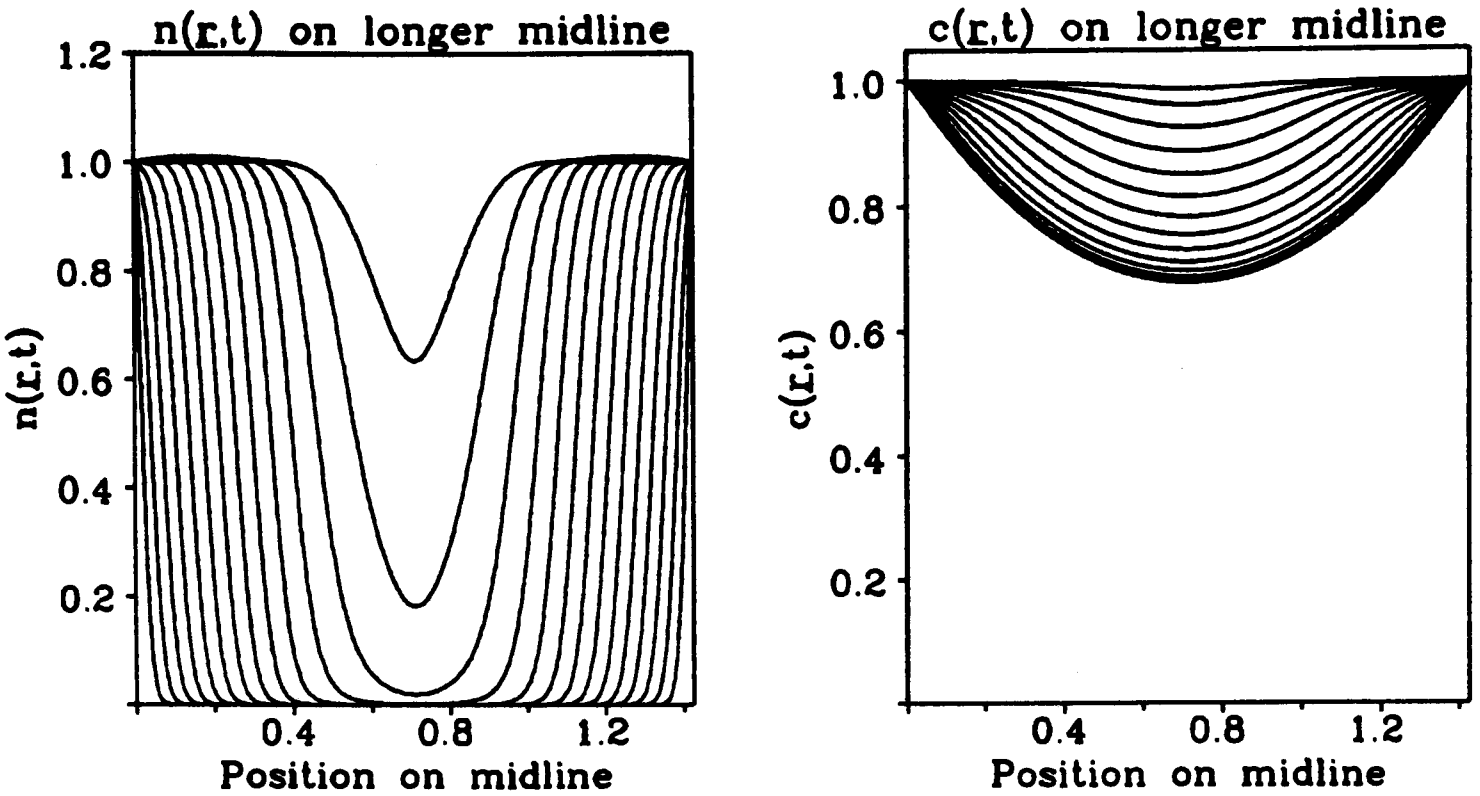

Figure 2.14: (b) The solution of (1.6) with the wound shape function f_{shape} as in (2.2) and $\alpha = 0.8$, with the inhibitor kinetics. The cell density n and chemical concentration c on the two midlines are plotted at a selection of equally spaced times. The parameter values are as in Figure 1.8, and the initial ratio of midline lengths is 1.5. The initial wound area has a dimensionless value of 1.

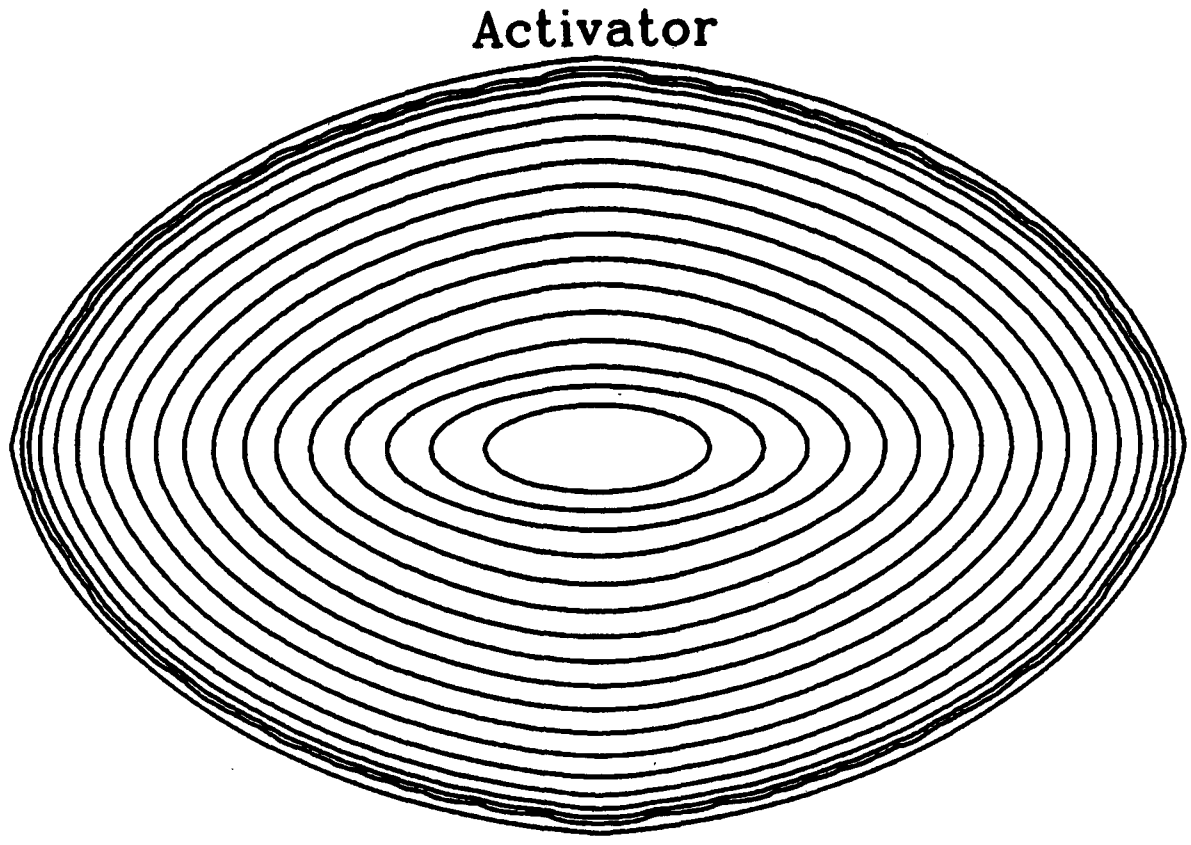

Figure 2.15: The wound edge at a selection of equally spaced times with the wound shape function f_{shape} as in (2.2) and $\alpha = 0.8$. The 'wound edge' is defined as the contour $n = 0.8$. The parameter values are as in Figure 1.8, and the initial ratio of midline lengths is 1.5. The initial wound area has a dimensionless value of 1.

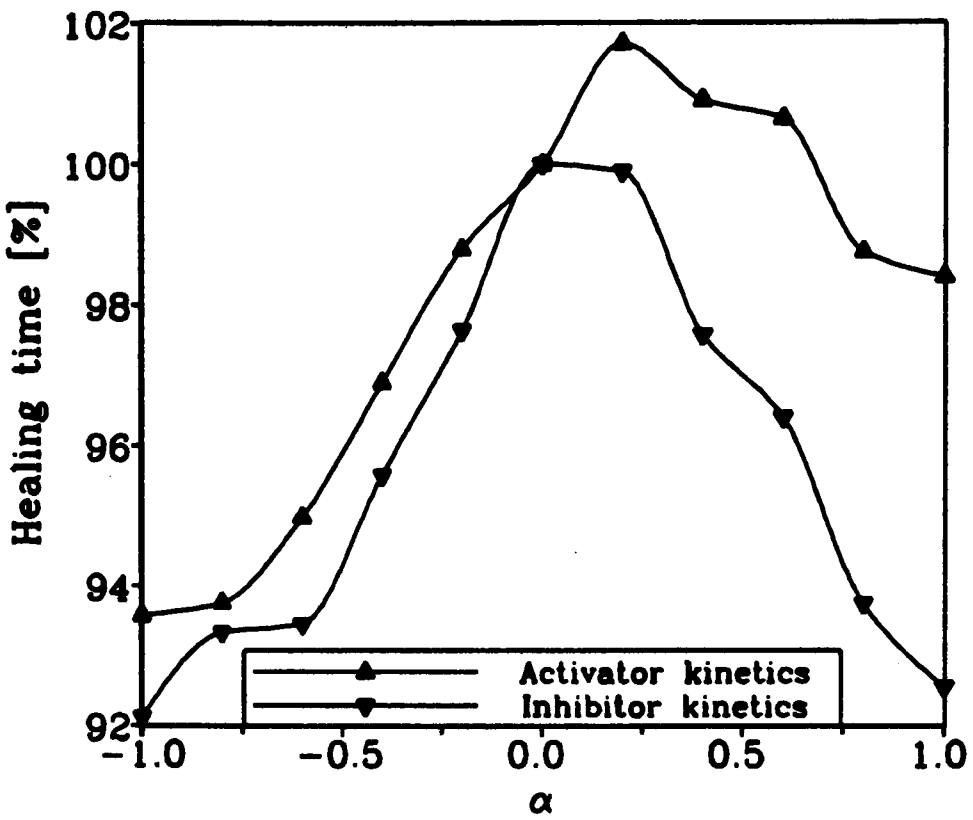

Figure 2.16: The variation in healing time with the parameter α as predicted by the model, with the wound shape function $f_{shape}(\xi;\alpha)$ as defined in (2.2). For both regulatory mechanisms, the healing time is plotted as a percentage of that for a diamond-shaped wound, given by $\alpha = 0$. All the wounds have an initial dimensionless area of 1 and midline length ratio of 1.5, and the parameter values are as in Figure 1.8.

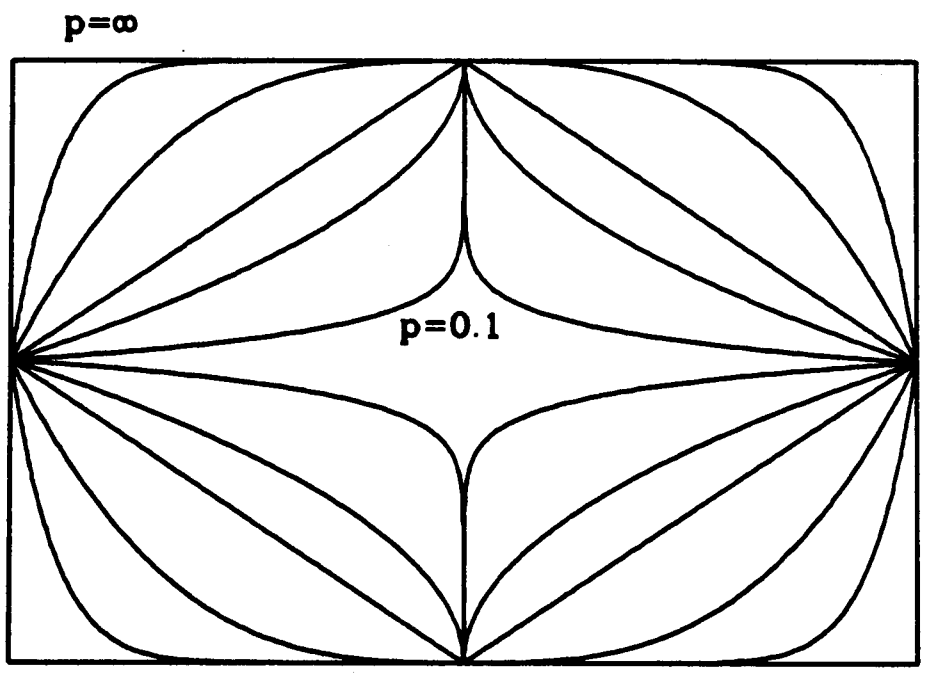

Figure 2.17: The family of wound shapes defined by (2.3), parameterized by p. For clarity, all the shapes are illustrated with the same midline lengths, but in the numerical simulations, the lengths of the midlines are chosen, in a specified ratio, so that in each case the initial wound area has a dimensionless value of 1.

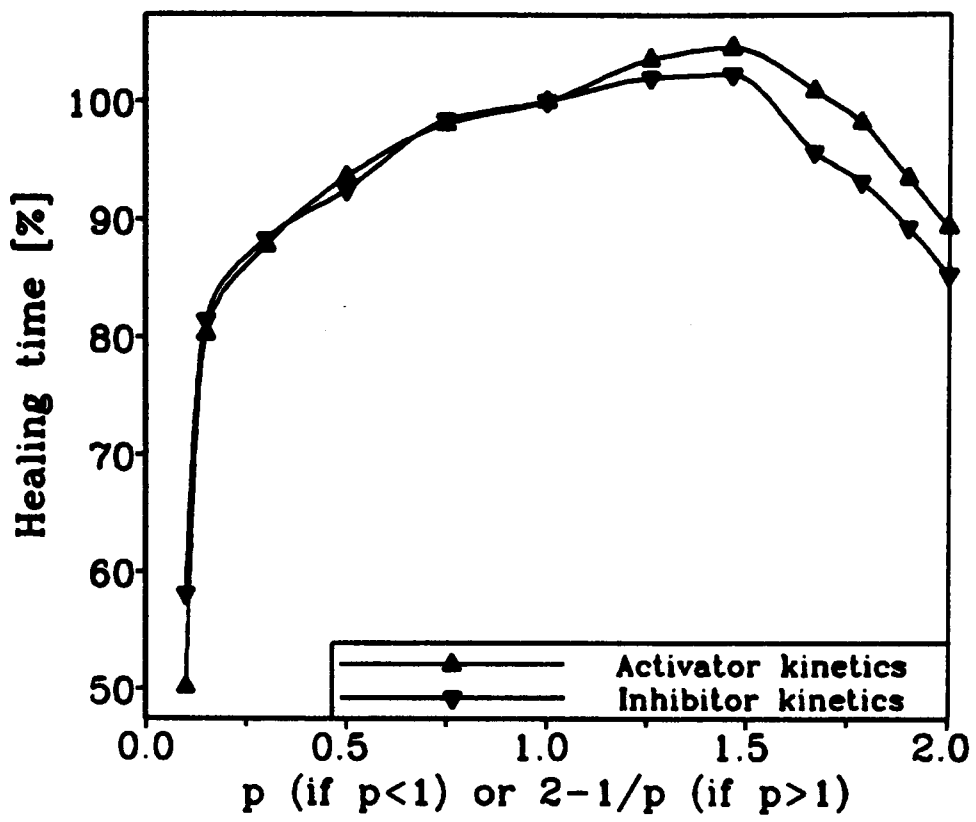

Figure 2.18: The variation in healing time with the parameter p as predicted by the model, with the wound shape function $f_{shape}(\xi; p)$ as defined in (2.3). For both regulatory mechanisms, time is plotted as a percentage of that for a diamond-shaped wound, given by $p = 1$. To give equal emphasis to convex and concave wound shapes, we plot the relative healing time against p when $p < 1$, and against $2 - 1/p$ when $p > 1$. All the wounds have an initial dimensionless area of 1 and midline length ratio $x_{dim}/y_{dim} = 1.5$, and the parameter values are as in Figure 1.8.

mechanisms, is shown in Figure 2.18. These results again suggest that the variation in healing time is similar for the two mechanisms when the wound shape is concave when viewed from the centre, but quite different for convex wound shapes.

An explanation for this trend is suggested by the wound edge contours in Figures 2.13 and 2.15. The first of these figures shows that for a highly cusped (that is, concave when viewed from the centre) wound shape, the wound edge rounds up during healing, for both the activator and inhibitor kinetics, and is almost circular as the wound closes. In contrast, for the convex wound shape illustrated in Figure 2.15, the wound edge tends to flatten out, so that the ratio of midline lengths increases during healing. Moreover, this increase is significantly greater for the inhibitor kinetics than for the activator kinetics. Now for a given initial wound area, the healing time will be shorter if the wound edge tends to flatten out more during healing, since the wound perimeter is then greater; this trend was discussed for rectangular wounds on page 54. Thus the differences between concave and convex wound shapes

in Figures 2.16 and 2.18 can be explained in terms of shape change during healing.

This explanation raises an important question: what are the key factors controlling the extent to which an ovate wound flattens out during healing that is governed by the model equations? We were able to answer this by returning to the basic model (1.1), in which chemical regulation of mitosis is neglected. We rescale the dimensionless time coordinate in (1.1) so that the model equation is

$$\frac{\partial n}{\partial t} = \nabla^2 n + \Gamma n(1-n)\,. \tag{2.4}$$

In this form, the model has a single dimensionless parameter Γ, which reflects the relative contributions of mitosis and diffusion to the healing process. The wound edge contours predicted by this basic model are shown in Figure 2.19 for a range of values of Γ, for a wound that is initially elliptical with midline length ratio 2. The wound edge becomes more flattened during healing as Γ increases, and this is quantified in Figure 2.20, in which we plot against Γ the midline length ratio of the wound when its area has decreased to 10% of its initial value. This figure shows that shape change during the healing of an ovate wound is a competitive process, with diffusion tending to cause rounding up of the wound, while mitosis tends to cause the wound to flatten. In contrast, both diffusion and mitosis tend to cause a concave wound to round up during healing.

Returning to the full model (1.6) with biochemical regulation of mitosis, it is now clear why ovate wounds flatten more during healing with the inhibitor kinetics than with the activator kinetics. The extent to which post-wounding mitosis is stimulated by biochemical effects is approximately the same for the two mechanisms; however, the determination of diffusion coefficients by fitting to experimental data, which we discussed in Section 1.4, gave the cellular diffusion coefficient D to be 5 times larger for the activator kinetics than for the inhibitor kinetics.

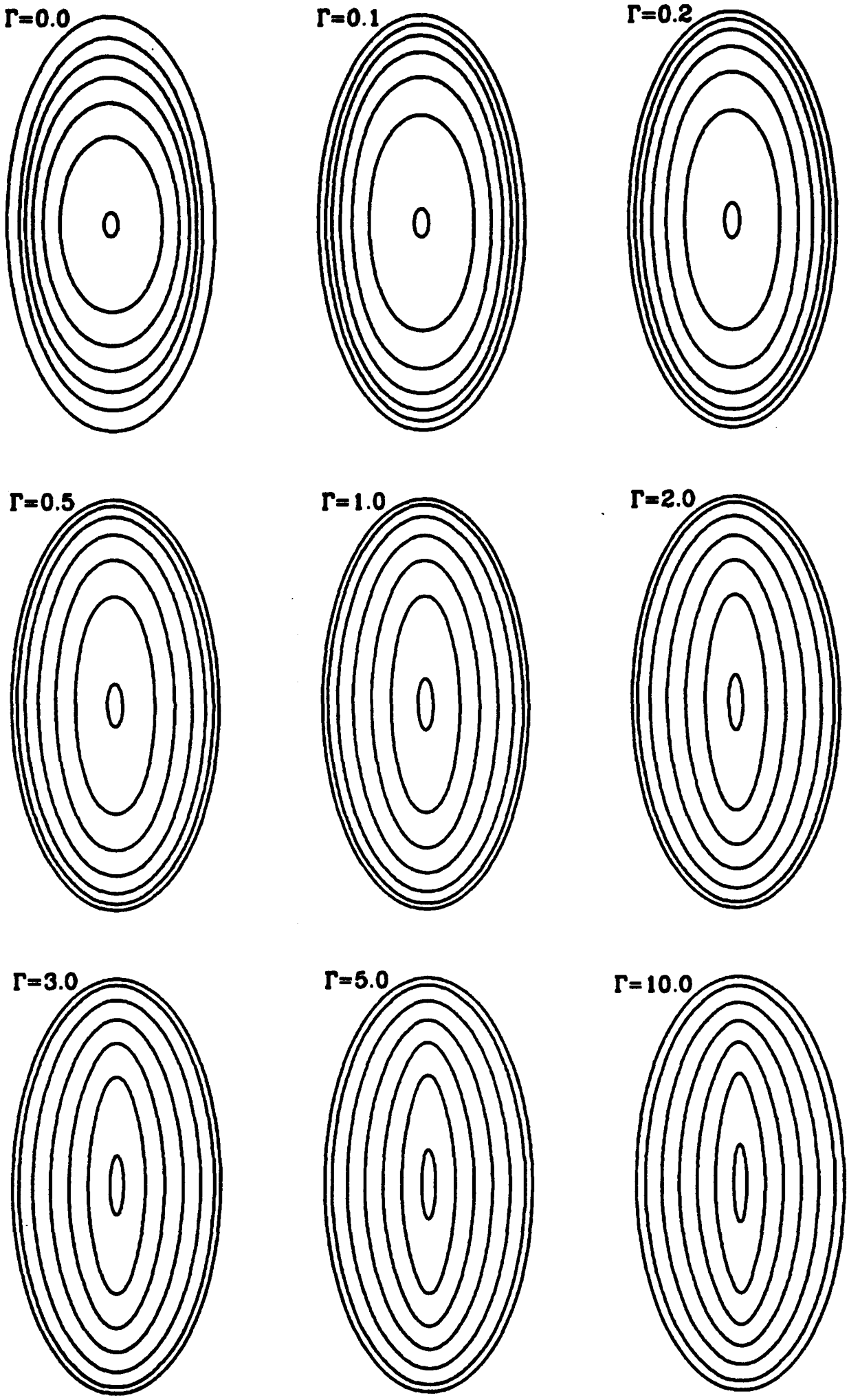

Figure 2.19: The wound edge at a selection of equally spaced times for a wound that is initially elliptical with midline length ratio 2 and dimensionless area 1, as predicted by the basic model (2.4), for a range of values of Γ. The wound becomes more flattened during healing as Γ increases.

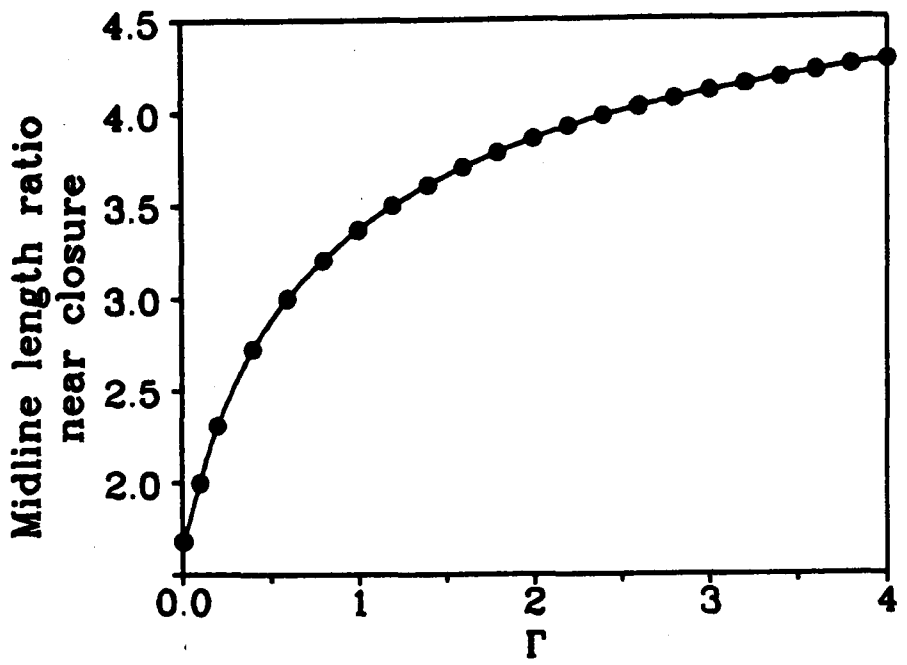

Figure 2.20: The midline length ratio of a wound near to closure, when its area reaches 10% of its initial value, as predicted by the basic model (2.4), plotted against Γ. In each case, the wound is initially elliptical, with midline length ratio 2 and dimensionless area 1.

2.4 Conclusions

In this chapter and Chapter 1, we have developed a reaction-diffusion model for epidermal wound healing in which the parameter values are based as far as possible on experimental results. Numerical solutions of the model with either chemical activation or inhibition of mitosis compare well with experimental data on the normal healing of circular wounds, supporting the view that biochemical regulation of mitosis is fundamental to the process of epidermal migration in wound healing. Analytical investigation of the solutions as travelling waves was possible in one spatial dimension. We studied the travelling wave system of ordinary differential equations under two biologically relevant approximations, which clarified the accuracy of these approximations and the roles of the various model parameters in the wave form and the speed of healing. We went on to perform 'mathematical experiments', from which we made experimentally testable predictions on the effects of adding mitotic regulators to healing wounds, and on the variation of healing time with wound shape. This latter investigation led to an understanding of the competitive processes controlling changes in wound shape during healing. It may be possible to exploit the differences in such shape changes as predicted by the activator and inhibitor kinetics to distinguish experimentally between these two regulatory mechanisms.

Chapter 3

The Response of Embryonic Epidermis to Wounding: a Basic Model

3.1 Biological Background

The process of cells crawling across exposed connective tissue to close adult epidermal wounds has been described in detail in the Introduction and Section 1.1. Although debate continues on many aspects of adult epidermal wound healing, this basic process of lamellipodial migration is well established. In contrast, the mechanisms underlying the healing of embryonic epidermal wounds remain largely unknown. Recently, the process has been studied in detail by Martin and Lewis (1991a,b). Using a tungsten needle, they made lesions on the dorsal surface of four-day chick embryonic wing buds. These wounds were 0.5mm square, with thickness 0.1mm, so that the basal lamina was cut and there was some bleeding. They healed perfectly and rapidly, typically in about 24 hours. Although the epidermis moved actively across the contracting mesenchyme, they found no evidence of lamellipodia at the wound front in either the basal or peridermal layers (Figure 3.1). This absence of lamellipodia was consistent with a second observation: when a small island of embryonic skin was grafted onto a denuded region of the limb bud surface, the grafted epidermis, far from expanding over the adjacent exposed mesenchyme, actually contracted, leaving its own mesenchyme exposed. This phenomenon suggested that the mechanism underlying epidermal movement might be a circumferential tension at the free edge, acting like a purse string. Such a mechanism would cause contraction of both an epidermal island and a hole in the epidermis.

Martin and Lewis (1991a,b) pursued this possibility further by staining spec-

imens with fluorescently tagged phalloidin, which binds selectively to filamentous actin (Faulstich *et al.*, 1983; Wulf *et al.*, 1979), and thus reveals the distribution of filamentous actin in the healing wounds. Actin is the most abundant protein in many eukaryotic cells, often constituting more than 5% of the total cell protein. It exists in two forms, unpolymerized ('globular actin') and polymerized ('filamentous actin'), and typically about half of the actin molecules in a cell are polymerized. Actin filaments, also known as microfilaments, are held in three-dimensional networks by cross-linking proteins; the resulting microfilament network is a fundamental part of the cell cytoskeleton, and is responsible for many aspects of cellular mechanics. Alberts *et al.* (1989, Chapters 11 and 14) present a detailed review of the role of actin in the cytoskeleton. Filamentous actin is therefore an obvious candidate for the protein causing this purse string effect. Staining with phalloidin revealed a thick cable of actin around almost all of the epidermal wound margin (Figure 3.2), localized within the leading layer of basal cells. The cable appeared to be continuous from cell to cell, presumably via adherens junctions, except at a very few points. The thickness of the cable did not change noticeably during healing: it was present certainly within an hour of wounding, and persisted until the wound was closed.

To gauge more accurately the time course of the establishment of the actin cable, Midwinter *et al.* (in preparation) have investigated simple slash wounds running along the proximodistal axis of the limb. This lesion takes only seconds to make, as opposed to the 5–10 minutes required to dissect a square of skin from the limb bud. The slash lesion data indicate that the actin cable begins to form within minutes of wounding. In this chapter and Chapter 4 we investigate, from a theoretical point of view, the formation of the actin cable as a response to wounding. Specifically, we use a mathematical model to address the possibility that the cable forms by compaction and reorientation of the actin filament network, without either depolymerization of actin in one part of the cell and corresponding repolymerization in another part, or *de novo* synthesis of filamentous actin. The results of our modelling enable us to suggest a possible mechanism for the formation of the actin cable.

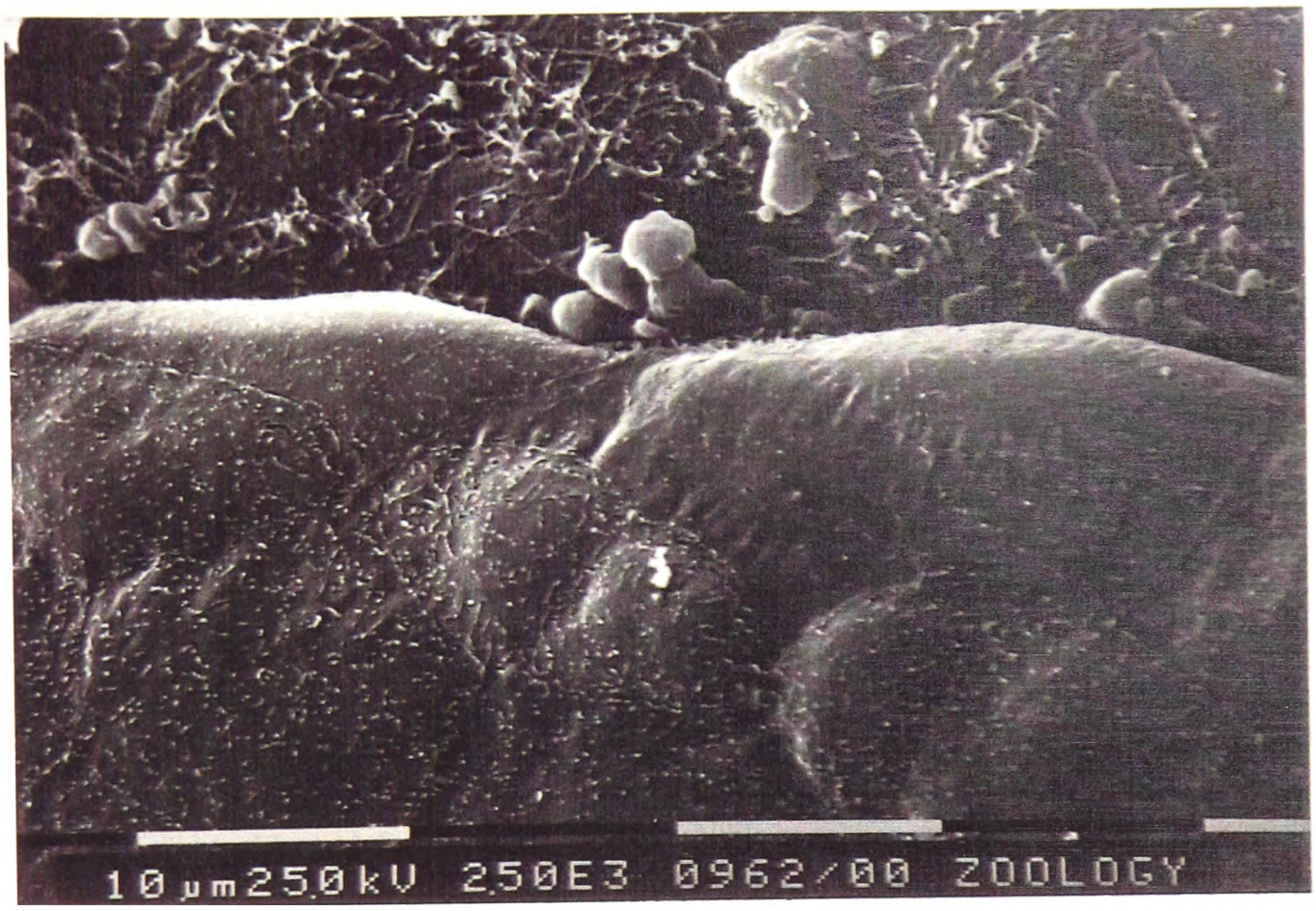

Figure 3.1: Scanning electron micrograph of a wound edge in chick embryonic epidermis, 12 hours after the operation. The wound was made by removing a square patch of embryonic skin from the dorsal surface of the wing bud at 4 days of incubation (stage 22/23). The epidermis overlies the flattened surface of the exposed mesenchyme. Note the smooth edge of the epidermis and the absence of lamellipodia.

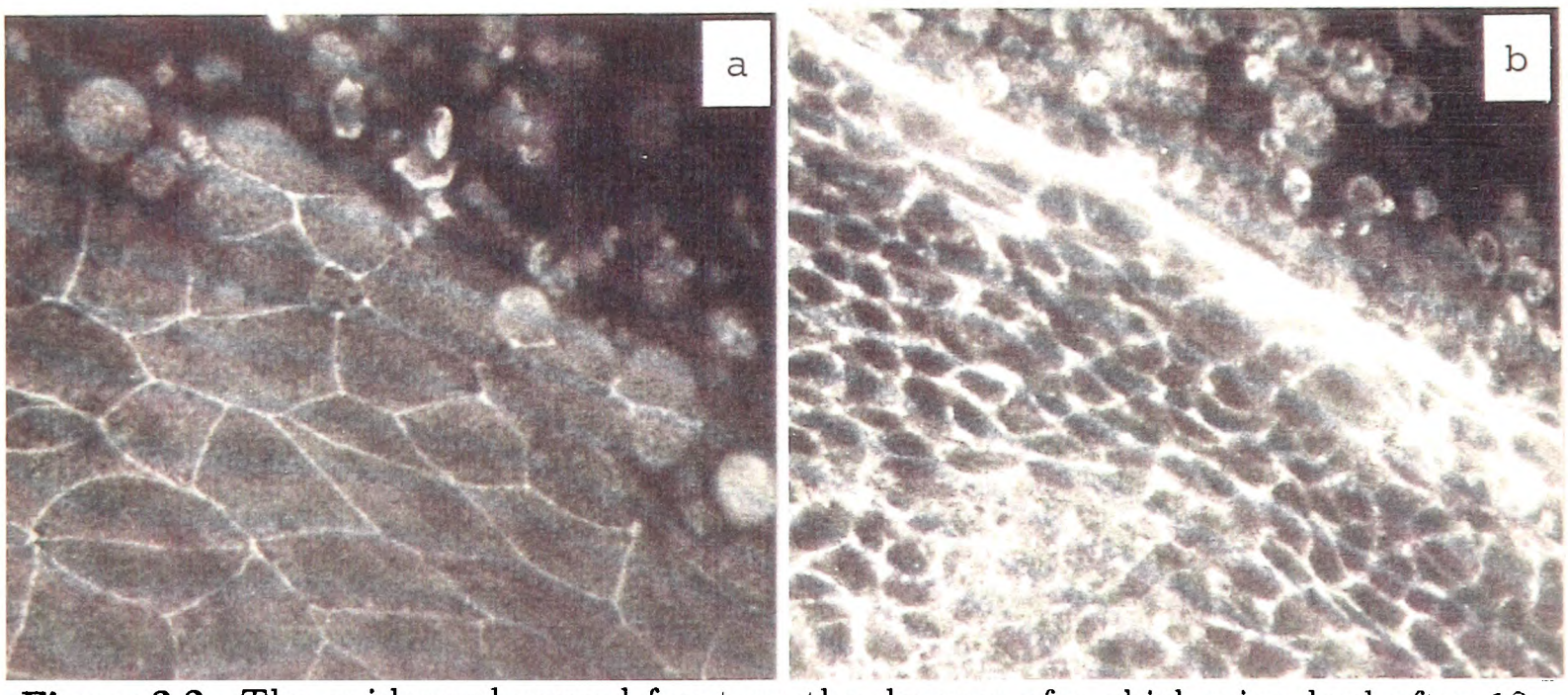

Figure 3.2: The epidermal wound front on the dorsum of a chick wing bud after 12 hours of healing, as seen in optical section by confocal scanning laser microscopy. The tissue has been stained with rhodamine-labelled phalloidin, which binds to filamentous actin, and the sections are parallel to the plane of the epidermis. The epidermis is at the lower left, with the exposed mesenchyme (largely below the plane of section) at the upper right. (a) Superficial section, in the plane of the periderm, whose broad flat cells are outlined by their cortical actin. (b) Section about 4μm deeper, in the plane of the basal epidermal cells, showing the actin cable at the wound front.

3.2 The Mechanical Approach to Modelling

At the developmental stages at which the experiments discussed above (Martin and Lewis, 1991a,b) were performed, the embryonic epidermis is two cell layers thick, consisting of a superficial, pavement-like periderm layer and a cuboidal basal layer. The actin cable develops in the basal layer, and it is to this layer that our modelling considerations apply. The basal cells form a confluent sheet of cells, attached to the underlying basal lamina at focal contacts (see, for example, Alberts *et al.*, 1989, Chapter 11). We model the initial response of this sheet to wounding by modifying the mechanochemical model for the deformation of epithelial sheets proposed by Murray and Oster (1984). This was the first continuum mechanochemical model for epithelial morphogenesis, and was based on the discrete model of Odell *et al.* (1981). Murray (1989) gives an in depth review of mechanical models for morphogenesis.

The model of Murray and Oster (1984) treats the epithelial sheet as a linear, isotropic, viscoelastic continuum, an approach which the authors justify as a reasonable first approximation in the absence of detailed knowledge of the mechanical properties of cytogel, and which is discussed from a rheological viewpoint by Elson (1988). In Murray and Oster's (1984) model and other related models (see Murray, 1989), cellular contraction forces are controlled by the concentration of free calcium. We modify this model to investigate the new equilibrium reached by the basal cell sheet after wounding. Since we are only interested in the equilibrium state, chemical control is equivalent to an imposed spatial variation in parameter values; we neglect such affects, and assume that the mechanical properties of the cell sheet change only in response to the local stress and strain fields. Following wounding, the cytoskeleton undergoes rapid changes, on a time scale of a few minutes (Midwinter *et al.*, in preparation), reaching a new state which is the "quasi-equilibrium" we are considering. Of course, this new state also changes over a time scale of a few hours, as healing proceeds, but we do not consider the processes occurring on this longer time scale.

The mechanical properties of a confluent cell sheet are determined largely by the intracellular actin filaments (Pollard, 1990). In epithelial sheets, cell-cell adherens junctions form a continuous 'adhesion belt' around the cell, just below the tight

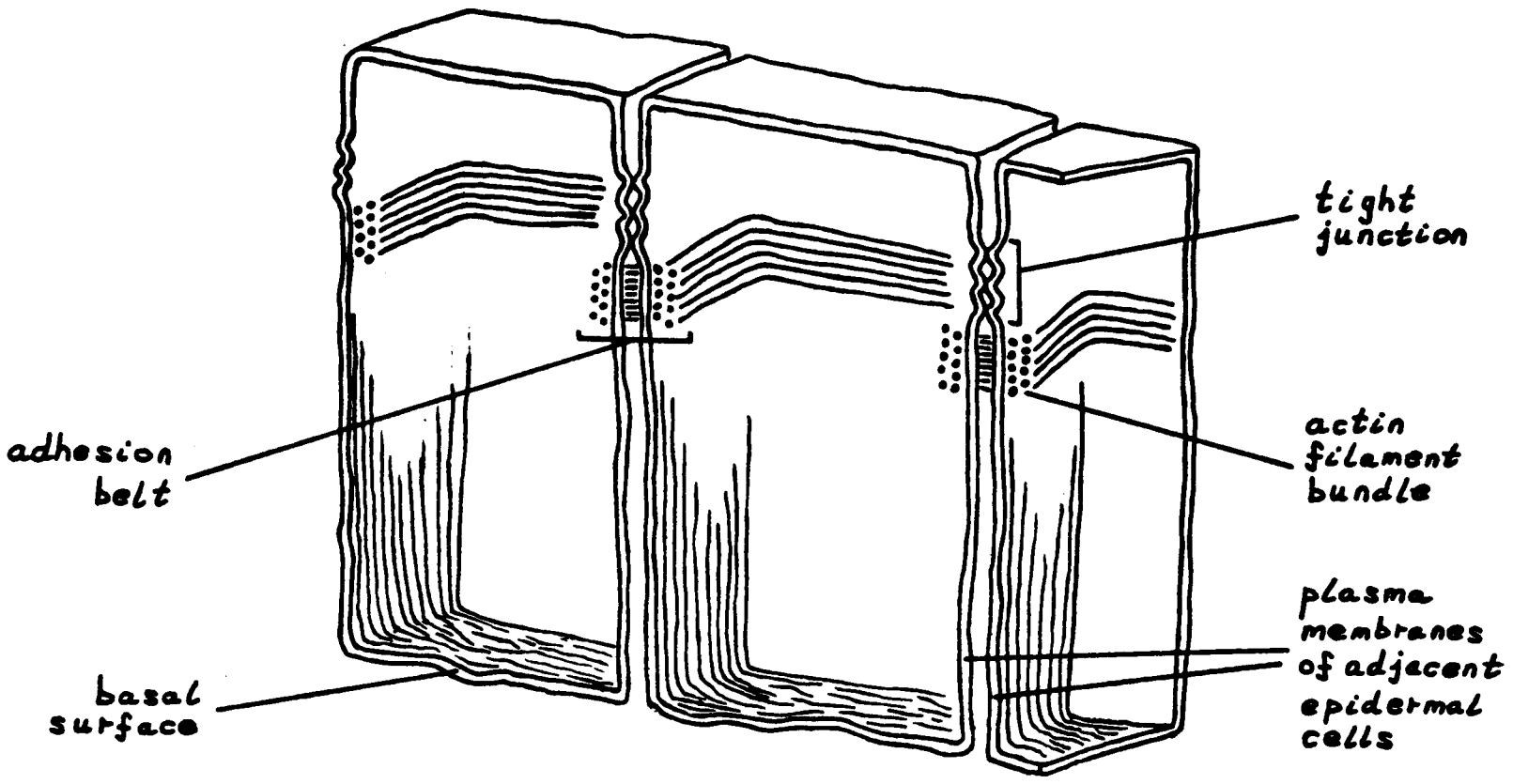

Figure 3.3: Adhesion belts between epidermal cells. This belt-like intercellular junction encircles each of the interacting cells, linking the intracellular actin filaments in a transcellular network.

junctions, as illustrated in Figure 3.3. These adherens junctions are connection sites for actin filaments, and thus the intracellular actin filaments are linked, via transmembrane proteins at the adhesion belt, in a transcellular network. Our model addresses the equilibrium state of this network.

At equilibrium, the stress tensor in the cell sheet is taken to be

$$\underline{\underline{\sigma}} = \underbrace{G\left(E\underline{\underline{\varepsilon}} + \Gamma\nabla\cdot\underline{u}\,\underline{\underline{I}}\right)}_{\substack{\text{elastic}\\ \text{stress}}} + \underbrace{\tau G\underline{\underline{I}}}_{\substack{\text{active}\\ \text{contraction}\\ \text{stress}}} \tag{3.1}$$

where $\underline{u}(\underline{r})$ is the displacement of the material point initially at $\underline{r}$, the strain tensor $\underline{\underline{\varepsilon}} = \frac{1}{2}(\nabla\underline{u} + \nabla\underline{u}^T)$, $G(\underline{r})$ is the density of intracellular actin filaments at the material point initially at $\underline{r}$, E and Γ are positive constants, and $\underline{\underline{I}}$ is the unit tensor. As discussed below, the traction stress per filament, τ, is in general a function of the local compaction. The exertion of traction forces by fibroblasts has been extensively studied (see, for example, Harris, 1982; Stopak and Harris, 1982), and traction forces have been observed in a range of other cell types, including chick embryonic corneal epithelial cells (Mattey and Garrod, 1984). The elasticity of the actin filament net-

work arises from the extensive interpenetration of the long actin filaments, which tends to immobilize them (Janmey *et al.*, 1988). The form (3.1) is used extensively in the literature: see, for example, Oster *et al.* (1983), Murray and Oster (1984), Oster (1984), Oster *et al.* (1985), Murray *et al.* (1988). In contrast to the majority of these models, (3.1) has no viscous contribution because we are considering the equilibrium situation.

At equilibrium, these elastic and traction forces balance the elastic restoring forces that arise from attachment to the substratum. The importance of such attachments is illustrated in recent experiments by Hergott *et al.* (1989) on the response of chick embryonic corneal cells to wounding in an organ culture system. In this study, cells migrate into the wound along the exposed basal lamina. They find that focal contacts form with the basal lamina at the ends of actin filament bundles, and they attribute the considerable tensile forces generated by the migrating cells to the interaction of actin filament bundles with the substratum, via these focal contacts. Following Murray and Oster (1984), we model these restoring forces by $\lambda G\underline{u}$, where the positive constant λ reflects the strength of the attachments. The term is proportional to G since most of the intracellular actin filaments terminate at, or close to, a region of adhesion to the substratum (Alberts *et al.*, 1989, Chapter 11). Hergott *et al.* (1989) also present direct experimental evidence for this proportionality: they find that the density of focal contacts increases in parallel to that of actin filament bundles in the response to wounding. A similar observation was made by Wechezak *et al.* (1989) in experiments on the cytoskeletal response of isolated endothelial cells to shear stress, applied using a flow chamber.

Thus the equation to be solved for the new equilibrium configuration is

$$\nabla \cdot \underline{\underline{\sigma}} - \lambda G\underline{u} = \underline{0} \tag{3.2}$$

with $\underline{\underline{\sigma}}$ as in (3.1). We treat the cell sheet as infinite, which is a valid approximation provided the wound area is small compared to the whole sheet, which certainly holds in the experiments of Martin and Lewis (1991a,b) discussed in the previous section. Thus the boundary conditions are $\underline{u}(\infty) = \underline{0}$, and $\underline{\underline{\sigma}} \cdot \hat{\underline{n}} = \underline{0}$ at the free edge, where

$\hat{\underline{n}}$ is the unit vector normal to this edge. Our approach in deriving (3.1), (3.2) and the boundary conditions assumes that in the pre-wounding state, $\underline{u} = \underline{0}$ everywhere. This is not an entirely trivial assumption in a developing embryo, but observations of the epithelial sheet prior to wounding indicate that, to a good approximation, the cell density is uniform and the substratum attachments are reforming sufficiently fast that the restoring forces exerted by them are negligible (Paul Martin, personal communication, 1990).

A crucial feature of the model (3.2) is the relationship between G and $\underline{u}$. In this chapter we address the question of whether the actin cable observed by Martin and Lewis at the wound edge could be formed simply as a result of compaction- and stress-induced changes in filamentous actin density. Specifically, we make the following key assumption:

> *the response to wounding involves neither depolymerization of actin in one part of the cell and corresponding repolymerization in another part,* nor de novo *synthesis of filamentous actin, nor intracellular movement of intact actin filaments, so that the amount of filamentous actin in a given region of cytogel remains constant as that region is deformed.*

The time scale over which the actin cable forms (a few minutes) is certainly consistent with this assumption, but does not exclude actin polymerization. For instance, on sudden exposure to a chemoattractant peptide, neutrophils form pseudopodia over their entire surface, and the proportion of intracellular actin that is polymerized rises from about 30% to about 60% in 20 seconds (Carson *et al.*, 1986).

There is limited experimental evidence that this is the mechanism of cytoskeletal reorganization in some other systems. In a study on chick heart fibroblasts, Chen (1981) found that following removal from the substratum, the mesh of actin filament bundles in the fibroblast tails rearranged from a nonuniform to a uniform, random arrangement by reorientation, without any disassembly or reassembly of actin filaments. In more recent experiments involving micromanipulation of cellular protrusions in 3T3 cells, Albrecht-Buehler (1987) found that the expression of tension in

the cells was insensitive to the chemical cytochalasin B, which inhibits the polymerization of actin monomers (see page 146). Thus, while Albrecht-Buehler's findings do not preclude microfilament depolymerization, they can be explained more naturally by a simple reorientation of the filaments. Albrecht-Buehler also found that when detached from the substratum, cellular protrusions shortened by 20-50% within a few seconds, with further relaxation to equilibrium over 3-5 minutes. These time scales of cytoskeletal reorganization are consistent with those for the formation of the actin cable found by Midwinter *et al.* (in preparation). Thus, we assume that the amount of filamentous actin in a given region of cytogel remains constant as that region is deformed, so that $G(1-\Delta) = \kappa$, a spatially independent constant. Here Δ is the fraction of its pre-wounding volume by which a small region of cytogel contracts in the response to wounding. Substituting this into (3.2) gives the governing equation as

$$\nabla \cdot \left[\frac{\kappa}{1-\Delta} \left\{ E \underline{\underline{\varepsilon}} + \Gamma \nabla \cdot \underline{u}\, \underline{\underline{I}} + \tau \underline{\underline{I}} \right\} \right] - \frac{\lambda \kappa}{1-\Delta} \underline{u} = \underline{0}. \tag{3.3}$$

In this chapter we approximate Δ as the negative dilation, that is $\Delta \approx -\nabla \cdot \underline{u}$, following classical linear elasticity theory (see, for example, Segel, 1977a). However, this approximation is reconsidered in Section 4.1.

It remains to consider the functional form of τ, the traction stress per filament. When a region of the actin filament network is compressed, the degree of filament overlap increases. Consequently additional myosin cross-bridges form between actin filaments (Oster and Odell, 1984a), with a corresponding increase in the traction stress per filament. (The role of myosin in the contractile forces exerted by actin filaments is discussed in detail in the book by Alberts *et al.*, 1989, Chapter 11; see also page 137). This is effectively a synergy phenomenon: actin filaments together exert a greater traction force than the sum of the traction forces they exert separately. We model this synergy effect by taking τ to be an increasing function of the local compaction Δ, following previous mechanochemical models of epithelium (Oster, 1984; Oster and Odell, 1984a,b; Oster *et al.*, 1985). Specifically, we take $\tau = \tau_0/(1-\beta\Delta)$. With this form for τ, a decrease in dilation at a point causes an increase in the cell traction stress at that point both because of an increase in the actin filament density

at the point and because of an increase in the traction stress per filament. Intuitively, we expect the former effect to be larger than the latter, and we thus require that $\beta < 1$. With this constraint, τ is bounded, since $\Delta < 1$ (a region cannot be compressed to a point). When discussing model solutions, we will consider not only $0 < \beta < 1$, but also the case $\beta = 0$. This corresponds to the traction stress per actin filament being independent of dilation, so that the effects of additional myosin cross-bridging are neglected. This is the form used by Murray and Oster (1984) in the first continuum mechanochemical model for epithelial morphogenesis.

To clarify the roles of the various model parameters, we nondimensionalize (3.3) by defining

$$\underline{r}^* = \underline{r}/L \qquad \underline{u}^* = \underline{u}/L \qquad E^* = E/\tau_0 \qquad \Gamma^* = \Gamma/\tau_0 \qquad \lambda^* = \lambda a^2/\tau_0$$

where * denotes a dimensionless quantity and L is a typical linear dimension of the wound; for circular wounds we take L to be the initial wound radius. Substituting these into (3.3) with $\Delta = -\nabla \cdot \underline{u}$, and dropping the asterisks for notational simplicity, gives

$$\nabla \cdot \left[\frac{1}{1 + \nabla \cdot \underline{u}} \left\{ E \underline{\underline{\epsilon}} + \Gamma \nabla \cdot \underline{u}\, \underline{\underline{I}} + \frac{1}{1 + \beta \nabla \cdot \underline{u}} \underline{\underline{I}} \right\} \right] - \frac{\lambda}{1 + \nabla \cdot \underline{u}} \underline{u} = \underline{0}. \qquad (3.4)$$

As in other applications of mechanochemical models, the experimental data currently available to give estimates for parameter values is very limited, and is in fact insufficient to determine any of the dimensionless parameters in equation (3.4). For completeness, however, we briefly review the few relevant quantitative experiments. There are a number of studies which address the mechanical properties of actin gels from a rheological viewpoint, for instance Jen *et al.* (1982), Sato *et al.* (1985), Sato *et al.* (1987), Zaner and Hartwig (1988), Janmey *et al.* (1988). The rheological terminology they use is explained in the book by Ferry (1980). Typically, these studies consider an actin gel held between two plates, with the lower plate oscillating sinusoidally. The phase difference and amplitude ratio of the displacements of the upper and lower plates are recorded, enabling the storage elastic modulus and loss (viscous) modulus to be calculated as a function of frequency (see Ferry, 1980, for details). The

study by Janmey *et al.* (1988) calculates similar quantities using a torsion pendulum apparatus. Unfortunately, these quantities are not sufficient to calculate any of the parameters in our representation of the viscoelastic continuum, which is a simplification of that used in rheological treatments. There is also a relevant quantitative study by Dennerll *et al.* (1988) on tension and compression in neurites. They record rest tensions and spring constants by applying a force with a calibrated glass needle. These values could be used to calculate $(E + \Gamma)$ and τ_0, but this would not be sufficient to determine any of the parameters in our dimensionless model equation (3.4). Also, these experiments are on a very different cell type, and the results vary over several orders of magnitude.

We treat the basal cell layer as two-dimensional, which is a reasonable assumption since its thickness is about 10μm, compared to the wound dimensions of about 500μm in the experiments of Martin and Lewis (1991a,b). In fact the adhesion belt confers a genuinely two-dimensional structure on the transcellular actin filament network (Figure 3.3). We consider the full radially symmetric two-dimensional problem in Section 3.4. First we investigate the solutions of the dimensionless governing equation (3.4) in one spatial dimension.

3.3 One-Dimensional Solutions

Solutions of the model in one spatial dimension are important for two reasons. Firstly, a study of the one-dimensional equations increases our mathematical understanding of the system, which can then be extended to the more biologically relevant two-dimensional equations. Secondly, the solutions may be applicable to regions of square wounds away from the corners, so that the one-dimensional model solutions can be compared to some aspects of the data from the experiments of Martin and Lewis (1991a,b) discussed in Section 3.1.

In one spatial dimension, the dimensionless governing equation (3.4) is

$$\frac{d}{dx}\left[\frac{1}{1+u_x}\left\{(E+\Gamma)u_x + \frac{1}{1+\beta u_x}\right\}\right] - \frac{\lambda}{1+u_x}u = 0 \qquad (3.5)$$

with boundary conditions

$$(E+\Gamma)u_x + \frac{1}{1+\beta u_x} = 0 \quad \text{at } x = 0 \qquad \text{and} \qquad u = 0 \quad \text{at } x = \infty, \tag{3.6}$$

where u_x denotes du/dx, and we take $x = 0$ to be the wound edge. Integrating this equation and using the boundary condition at $x = \infty$ gives

$$\frac{1}{2}\lambda u^2 = P(u_x) \tag{3.7}$$

where if $\beta \neq 1$

$$P(u_x) = (E+\Gamma)\left[u_x - \log(1+u_x)\right] + \frac{1}{1-\beta}\log(1+u_x) - \frac{2-\beta}{\beta(1-\beta)}\log(1+\beta u_x) - \frac{1}{\beta(1+\beta u_x)} + \frac{1}{\beta}\,, \tag{3.8a}$$

and if $\beta = 1$

$$P(u_x) = (E+\Gamma)u_x - (E+\Gamma+2)\log(1+u_x) - \frac{2}{1+u_x} + 2\,. \tag{3.8b}$$

The case $\beta = 1$ is not relevant biologically, but we will consider it briefly for mathematical completeness. We write the boundary condition at $x = 0$ in (3.6) as

$$Q(u_x) \equiv (E+\Gamma)\beta u_x^2 + (E+\Gamma)u_x + 1 = 0\,. \tag{3.9}$$

3.3.1 Existence and uniqueness of solutions

We now prove that (3.7) subject to (3.9) has a unique monotonically decreasing solution satisfying $u_x > -1$ if and only if

$$\hat{E} > \frac{1}{1-\beta} \quad \text{and} \quad 0 < \beta \leq 1/2$$
$$\text{or} \qquad \hat{E} \geq 4\beta \quad \text{and} \quad \beta > 1/2\,.$$

The condition $u_x > -1$ is a physical constraint: a region cannot be compressed to a point. Here, and throughout the derivation of these conditions, we write $\hat{E} = (E+\Gamma)$ for notational simplicity.

Consider first the case $\beta < 1$. As discussed above, this is the case of interest biologically; we consider $\beta \geq 1$ later for mathematical completeness. The form of

$P(u_x)$ on $-1 < u_x \leq 0$ depends on $\hat{E}$ and β. For $\hat{E} > 1/(1-\beta)$, $P(u_x) \to +\infty$ as $u_x \to -1$, while for $\hat{E} < 1/(1-\beta)$, $P(u_x) \to -\infty$ as $u_x \to -1$. For $\hat{E} = 1/(1-\beta)$,

$$P(-1) = \frac{-2\beta - (2-\beta)\log(1-\beta)}{\beta(1-\beta)} = \frac{2-\beta}{\beta(1-\beta)}\left[\frac{-2\beta}{2-\beta} - \log(1-\beta)\right] .$$

This is strictly positive when $0 < \beta < 1$, since then $[(2-\beta)/(\beta(1-\beta))] > 0$, and also

$$\frac{d}{d\beta}\left[\frac{-2\beta}{2-\beta} - \log(1-\beta)\right] = \frac{\beta^2}{(2-\beta)^2(1-\beta)} > 0$$

$$\begin{aligned} \text{with} \quad & \left[\frac{-2\beta}{2-\beta} - \log(1-\beta)\right] = 0 \quad \text{when } \beta = 0\,, \\ \text{so that} \quad & \left[\frac{-2\beta}{2-\beta} - \log(1-\beta)\right] > 0 \quad \text{when } 0 < \beta < 1\,. \end{aligned}$$

Differentiating (3.8a) with respect to u_x gives

$$P'(u_x) = \frac{\hat{E}u_x}{1+u_x} - \frac{\beta u_x}{(1+\beta u_x)^2} - \frac{u_x}{(1+u_x)(1+\beta u_x)}$$

$$P''(u_x) = \frac{\hat{E}}{(1+u_x)^2} - \frac{1}{1-\beta}\frac{1}{(1+u_x)^2} + \frac{2-\beta}{1-\beta}\frac{\beta}{(1+\beta u_x)^2} - \frac{2\beta}{(1+\beta u_x)^3} .$$

Thus $P'(0) = 0$ and, after simplification, $P''(0) = \hat{E} - (1+\beta)$. Thus for small u_x, $P(u_x)$ has the same sign as $\hat{E} - (1+\beta)$.

Apart from the root at $u_x = 0$,

$$\begin{aligned} P'(u_x) = 0 &\iff \hat{E}(1+\beta u_x)^2 = \beta(1+u_x) + (1+\beta u_x) \\ &\iff \hat{E}\beta^2 u_x^2 + 2\beta(\hat{E}-1)u_x + (\hat{E}-\beta-1) = 0 \\ &\iff u_x = \frac{(1-\hat{E}) \pm \sqrt{\hat{E}\beta - \hat{E} + 1}}{\hat{E}\beta} . \end{aligned}$$

These roots are real if and only if $\hat{E} \leq 1/(1-\beta)$. Then the larger (less negative) root lies in $[-1, 0)$ if $\hat{E} > 1+\beta$, and is positive if $\hat{E} < 1+\beta$; the smaller (more negative) root is less than -1. For

$$\begin{aligned} \frac{(1-\hat{E}) + \sqrt{\hat{E}\beta - \hat{E} + 1}}{\hat{E}\beta} < 0 &\iff \sqrt{\hat{E}\beta - \hat{E} + 1} < \hat{E} - 1 \\ &\iff \hat{E} > 1 \text{ and } \hat{E}\beta - \hat{E} + 1 < (\hat{E}-1)^2 \\ &\iff \hat{E} > 1 + \beta\,; \end{aligned}$$

$$\frac{(1-\hat{E})+\sqrt{\hat{E}\beta-\hat{E}+1}}{\hat{E}\beta} > -1 \iff \sqrt{\hat{E}\beta-\hat{E}+1} > -(\hat{E}\beta-\hat{E}+1)$$

which is trivially satisfied

provided $\hat{E} \neq 1/(1-\beta)$, in which

case the root is equal to -1;

$$\frac{(1-\hat{E})-\sqrt{\hat{E}\beta-\hat{E}+1}}{\hat{E}\beta} < -1 \iff -\sqrt{\hat{E}\beta-\hat{E}+1} < -(\hat{E}\beta-\hat{E}+1)$$

$$\iff \hat{E}\beta-\hat{E}+1 < 1\,,$$

since $\hat{E} \leq 1/(1-\beta)$

$$\iff \beta < 1\,.$$

Taking all these considerations into account, the form of $P(u_x)$ as $\hat{E}$ and β vary is as shown in Figure 3.4.

The roots $q_\pm$ of the boundary condition $Q(u_x) = 0$ are

$$q_\pm = \frac{-\hat{E} \pm \sqrt{\hat{E}^2 - 4\hat{E}\beta}}{2\hat{E}\beta}\,.$$

These are real if and only if $\hat{E} > 4\beta$, in which case they are both negative. Now $Q(0) = 1$ and $Q(-1) = \hat{E}(\beta-1)+1$. Thus if $\hat{E} > 1/(1-\beta)$, exactly one root of the quadratic Q lies in (-1,0), that is

$$q_+ \in (-1,0) \text{ and } q_- < -1 \qquad \text{if} \quad \hat{E} > \frac{1}{1-\beta}\,. \tag{3.10}$$

Conversely, if $4\beta < \hat{E} < 1/(1-\beta)$, both roots of Q lie in $(-1,0)$ if $q_{min} \in (-1,0)$, and both roots are less than -1 if $q_{min} < -1$. Here q_{min} is the value of u_x minimizing Q, and straightforward differentiation gives $q_{min} = -1/2\beta$. Thus when $4\beta < \hat{E} < 1/(1-\beta)$,

$$-1 < q_+, q_- < 0 \qquad \text{if} \quad \beta > 1/2 \tag{3.11a}$$

$$q_+, q_- < -1 \qquad \text{if} \quad \beta < 1/2\,. \tag{3.11b}$$

We are now in a position to prove the conditions for the existence and uniqueness of solutions of (3.7) subject to (3.9) in the case $\beta < 1$. From the forms of $P(u_x)$

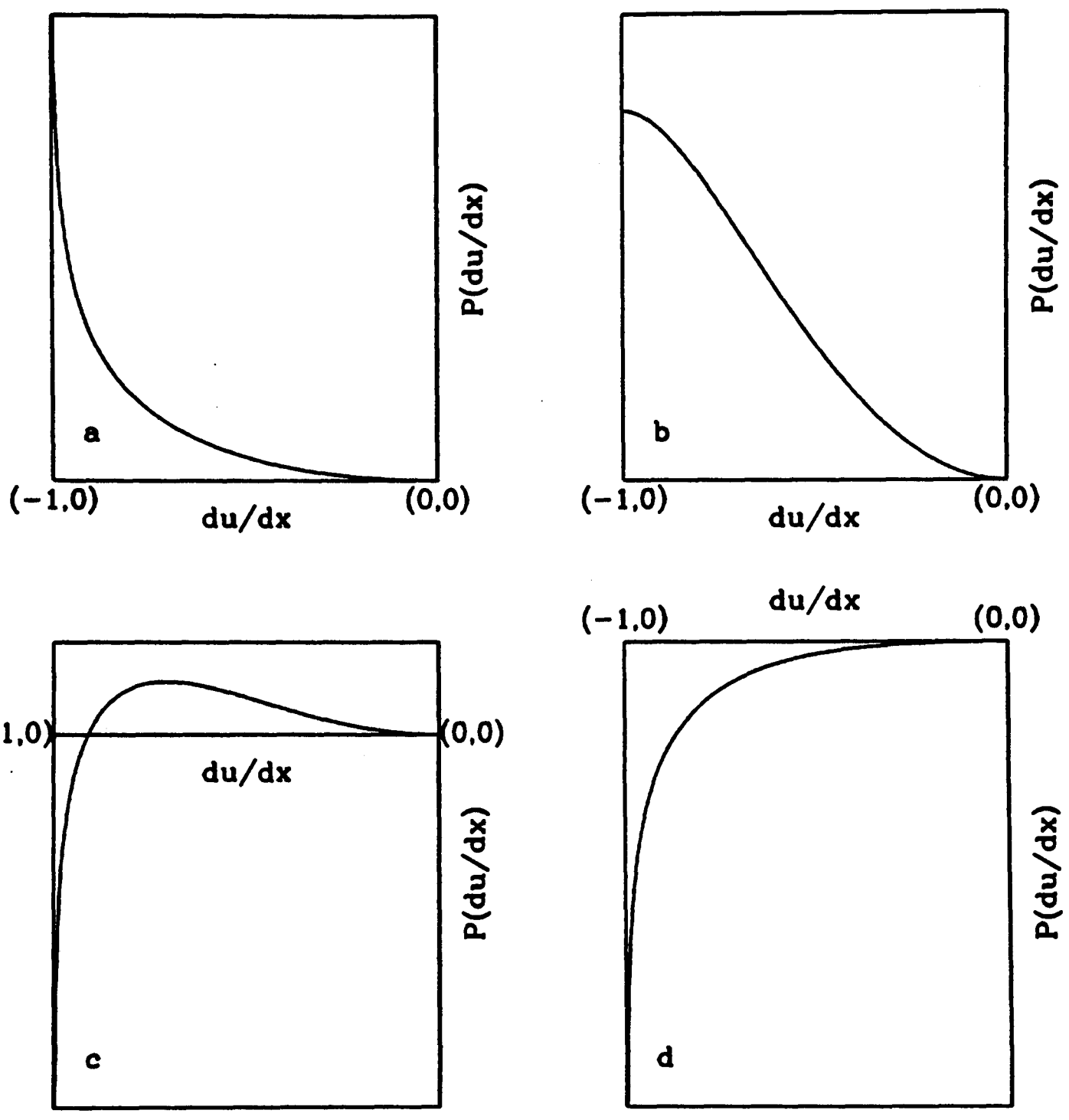

Figure 3.4: The qualitative form of the function $P(u_x)$, given in (3.8), as $\hat{E}$ and β vary with $\beta < 1$. (a) $\hat{E} > 1/(1-\beta)$; (b) $\hat{E} = 1/(1-\beta)$; (c) $(1+\beta) < \hat{E} < 1/(1-\beta)$; (d) $\hat{E} < (1+\beta)$.

in Figure 3.4 and results (3.10) and (3.11), it is clear that if $\hat{E} > 1/(1-\beta)$ there is a unique monotonically decreasing solution of (3.7) subject to (3.9). For then $P(u_x)$ decreases monotonically from $+\infty$ to zero on $(-1,0]$. Thus given any $u \geq 0$, there is exactly one value of $u_x \in (-1,0]$ satisfying the governing equation (3.7), and moreover exactly one of the roots for u_x of the boundary condition (3.9) lies in $(-1,0)$.

In addition, if $1+\beta < \hat{E} < 1/(1-\beta)$, there is a unique monotonically decreasing solution provided $\beta > 1/2$, $\hat{E} > 4\beta$ (so that $q_\pm$ are real) and $q_- < p_{max} < q_+$; we prove below that the first two of these conditions together imply the third. Here p_{max} is the value of u_x at which P attains its maximum on $(-1,0)$, that is

$$p_{max} = \frac{(1-\hat{E}) + \sqrt{\hat{E}\beta - \hat{E} + 1}}{\hat{E}\beta}.$$

For then $P(u_x)$ decreases monotonically to zero on $[p_{max}, 0]$. Thus there is a 1–1 correspondence between $u \in [0, P(p_{max})]$ and $u_x \in [p_{max}, 0]$, given by the governing equation (3.7). Moreover, exactly one of the roots for u_x of the boundary condition (3.9) lies in $(p_{max}, 0)$. Note that $\beta > 1/2$ and $\hat{E} > 4\beta$ together imply that the condition $\hat{E} > 1+\beta$ is satisfied. Moreover, these three conditions are necessary when $1+\beta < \hat{E} < 1/(1-\beta)$ except for the case of $\hat{E} = 4\beta$. But then if $\beta > 1/2$, $p_{max} = q_+ = q_- = -1/2\beta$, and thus there is a unique monotonically decreasing solution, while if $\beta < 1/2$, $q_+ = q_- = -1/2\beta < p_{max}$, and thus there is no solution.

For completeness, we now consider solving (3.7) as an initial value problem in the parameter domain $4\beta < \hat{E} < 1/(1-\beta)$, $\beta > 1/2$, with $u_x(0) = q_-$. Although this does not give a solution of (3.5) subject to (3.6), the boundary condition (3.9) at $x = 0$ is satisfied. The solution follows the curve $P(u_x)$, the form of which is shown in Figure 3.4c, in the direction of decreasing u_x. Thus u decreases monotonically, and $u = 0$ at some finite value of x, with the corresponding slope u_x being the unique root of P on $(-1,0)$. As x continues to increase, u becomes negative so that u^2 increases again, and the solution follows the curve $P(u_x)$ back in the direction of increasing u_x, passing through the point corresponding to the initial condition, but with u now negative. Finally, at some finite value of x, $u_x = p_{max}$ and $u = -2\sqrt{P(u_x)}/\lambda$. At

this point $d(u^2)/dx$ is positive, but the curve $P(u_x)$ has a local maximum, and thus equation (3.7) cannot be integrated further. Intuitively one would expect the solution to break down at this point, since a function does not have a local inverse on any neighbourhood of a local maximum, and thus equation (3.7) cannot be inverted to express u_x as a function of u on any neighbourhood of $u_x = p_{max}$.

We now prove that $q_- < p_{max} < q_+$ when $4\beta < \hat{E} < 1/(1-\beta)$ and $\beta > 1/2$. We have that

$$
\begin{aligned}
q_- < p_{max} &\iff -\sqrt{\hat{E}^2 - 4\hat{E}\beta} < 2 - \hat{E} + 2\sqrt{\hat{E}\beta - \hat{E} + 1} \\
&\iff \hat{E}^2 - 4\hat{E}\beta > \left[2 - \hat{E} + 2\sqrt{\hat{E}\beta - \hat{E} + 1}\right]^2 \\
&\qquad \text{or } 2 - \hat{E} + 2\sqrt{\hat{E}\beta - \hat{E} + 1} > 0 \\
&\iff 2(\hat{E}\beta - \hat{E} + 1) < (\hat{E} - 2)\sqrt{\hat{E}\beta - \hat{E} + 1} \\
&\qquad \text{or} \quad 2\sqrt{\hat{E}\beta - \hat{E} + 1} > (\hat{E} - 2) \\
&\iff 2\sqrt{\hat{E}\beta - \hat{E} + 1} \neq (\hat{E} - 2) \\
&\iff \hat{E} \neq 4\beta \\
\text{and } p_{max} < q_+ &\iff 2 - \hat{E} + 2\sqrt{\hat{E}\beta - \hat{E} + 1} < \sqrt{\hat{E}^2 - 4\hat{E}\beta} \\
&\iff \left[2 - \hat{E} + 2\sqrt{\hat{E}\beta - \hat{E} + 1}\right]^2 < \hat{E}^2 - 4\hat{E}\beta \\
&\qquad \text{or } 2 - \hat{E} + 2\sqrt{\hat{E}\beta - \hat{E} + 1} < 0 \\
&\iff 2(\hat{E}\beta - \hat{E} + 1) < (\hat{E} - 2)\sqrt{\hat{E}\beta - \hat{E} + 1} \\
&\qquad \text{or} \quad 2\sqrt{\hat{E}\beta - \hat{E} + 1} < (\hat{E} - 2) \\
&\iff 2\sqrt{\hat{E}\beta - \hat{E} + 1} < (\hat{E} - 2) \\
&\iff \hat{E} > 4\beta\,.
\end{aligned}
$$

In these inequalities, we use the fact that $\hat{E} > 4\beta$ and $\beta > 1/2$ together imply that $\hat{E} > 2$.

Finally, for $\beta < 1$, consider the outstanding case of $\hat{E} = 1/(1-\beta)$. Then $P(u_x)$ has the form shown in Figure 3.4b: $P(-1)$ is finite and strictly positive, and $P'(-1) = 0$. But when $\hat{E} = 1/(1-\beta)$, the roots of Q are

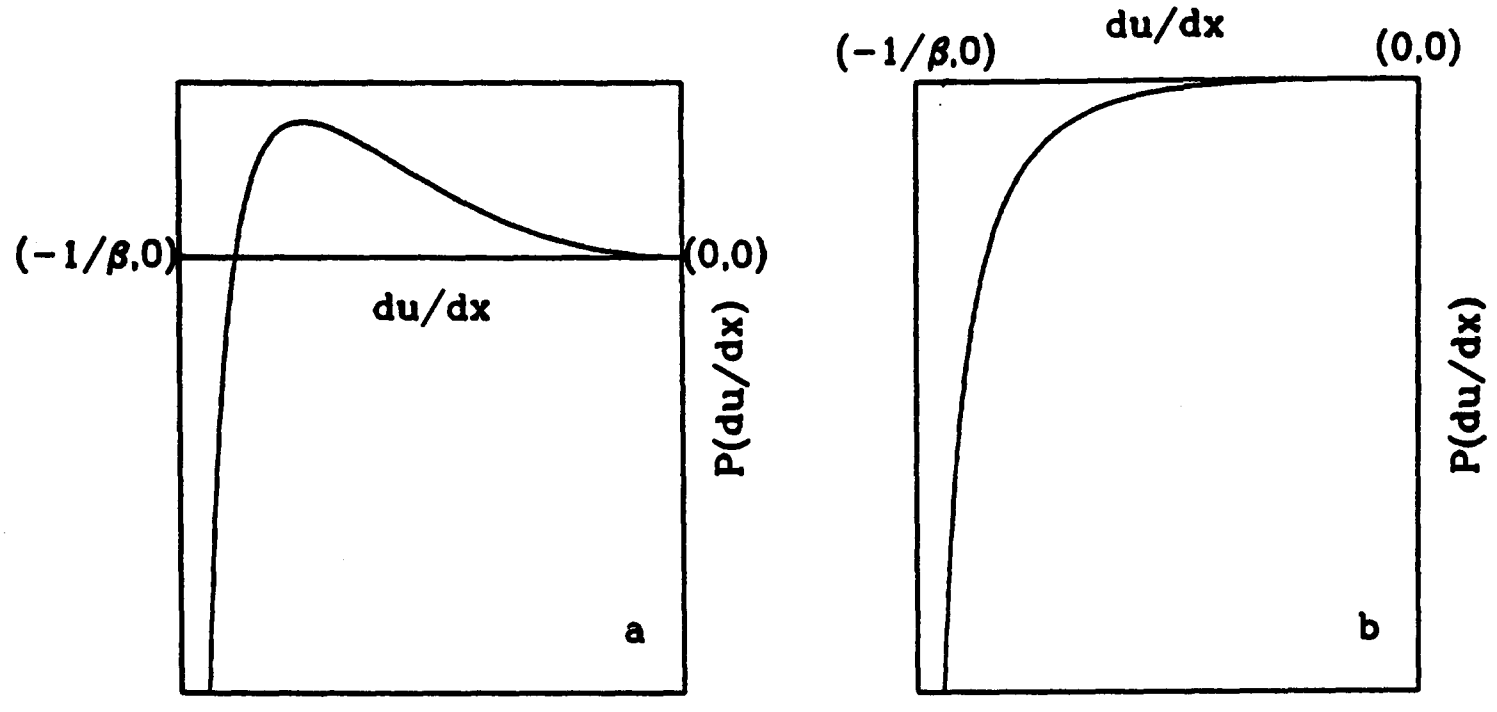

Figure 3.5: The qualitative form of the function $P(u_x)$, given in (3.8a), as $\hat{E}$ and β vary with $\beta > 1$. (a) $\hat{E} > 1 + \beta$; (b) $\hat{E} < 1 + \beta$.

$$q_+ = -1 \quad \text{and} \quad q_- = 1 - \frac{1}{\beta} < -1 \qquad \text{if} \quad \beta < 1/2$$

$$q_- = -1 \quad \text{and} \quad q_+ = 1 - \frac{1}{\beta} \in (-1, 0) \quad \text{if} \quad \beta > 1/2.$$

Thus when $\hat{E} = 1/(1-\beta)$, there is a unique monotonically decreasing solution satisfying $u_x > -1$ if and only if $\beta > 1/2$.

For completeness, we now consider the case of $\beta \geq 1$. If $\beta = 1$, similar calculations to those above show that $P(u_x)$ has the qualitative form shown in Figure 3.4c if $\hat{E} > 2$ and that shown in Figure 3.4d if $\hat{E} < 2$. Also, the roots of Q are real if and only if $\hat{E} > 4$, in which case $-1 < q_{min} < p_{max} < q_{max} < 0$. Thus there is a unique monotonically decreasing solution of (3.7) subject to (3.9) if and only if $\hat{E} > 4$.

If $\beta > 1$, the form of $P(u_x)$ is different. For then $P(u_x) \to -\infty$ as $u_x \to -(1/\beta)^+$. The qualitative form of $P(u_x)$ on $(-1/\beta, 0)$ depends on the sign of $P''(0) = \hat{E} - 1 - \beta$, and the two cases are shown in Figure 3.5. Now $Q(-1/\beta) = 1 = Q(0)$. Thus, provided $\hat{E} > 4\beta$ so that Q has real roots, both the roots, q_+ and q_-, lie in $(-1/\beta, 0)$. Moreover, the inequalities $q_- < p_{max} < q_+$ are still valid when $\hat{E} > 4\beta$. Thus when $\beta > 1$, there is a unique monotonically decreasing solution of (3.7) subject to (3.9) if and only if $\hat{E} \geq 4\beta$. (When $\hat{E} = 4\beta$, $q_- = q_+ = p_{max} = -1/2\beta$, as for $1/2 < \beta < 1$).

3.3.2 Numerical solutions

We solved (3.7) subject to (3.9) numerically as an initial value problem, with $u_x(0) = q_+$, and with u_x determined at each value of u as the unique value satisfying (3.7) on $-1 < u_x < 0$ if $\beta < 1/2$, and on $p_{max} < u_x < 0$ if $\beta > 1/2$. We solved this algebraic equation for u_x as a function of u numerically, and we integrated the initial value problem using a Runge-Kutta-Merson method. In order that the parameter values correspond to those in the two-dimensional solutions discussed in Section 3.4, we take L, the length scale in the nondimensionalization, to be 500μm, which is about 50 cell diameters.

In comparing the one-dimensional model solutions with data from the experiments of Martin and Lewis (1991a,b) involving square wounds on embryonic chick wing buds, we look in particular for the model to capture the intense aggregation of filamentous actin at the wound edge that constitutes the actin cable. However, we also require that the solutions capture the more superficial aspects of the response to wounding, that is the extent to which the various cell layers retract. It is difficult to gauge this accurately in the square lesions, both because of the time taken to make the wound (5-10 minutes) and because it is difficult to distinguish between epidermal and mesenchymal retraction, since the wound edges are so shallow. Neither of these problems arise in the simple slash wounds considered by Midwinter *et al.* (in preparation), and their data indicate an epidermal retraction of about 60μm at the wound edge, with only the leading 4–5 cell layers significantly contracted. We found that the model solutions were able to capture this second important aspect of the data for a wide range of parameter values. We illustrate this in Figures 3.6 and 3.7, which also show the effect of variations in λ, $\hat{E}$ and β on the form of the solution. However, to capture the phenomenon of the actin cable, that is $G(x)$ having a sharp peak at $x = 0$, required both $\beta < 1/2$ and $[\hat{E} - 1/(1-\beta)]$ small and positive; recall that for $\beta < 1/2$, a solution exists if and only if $\hat{E} > 1/(1-\beta)$. There was therefore a range of parameter values in which we were able to capture both aspects of the experimentally observed response of the embryonic epidermis to wounding, as illustrated in Figure 3.8.

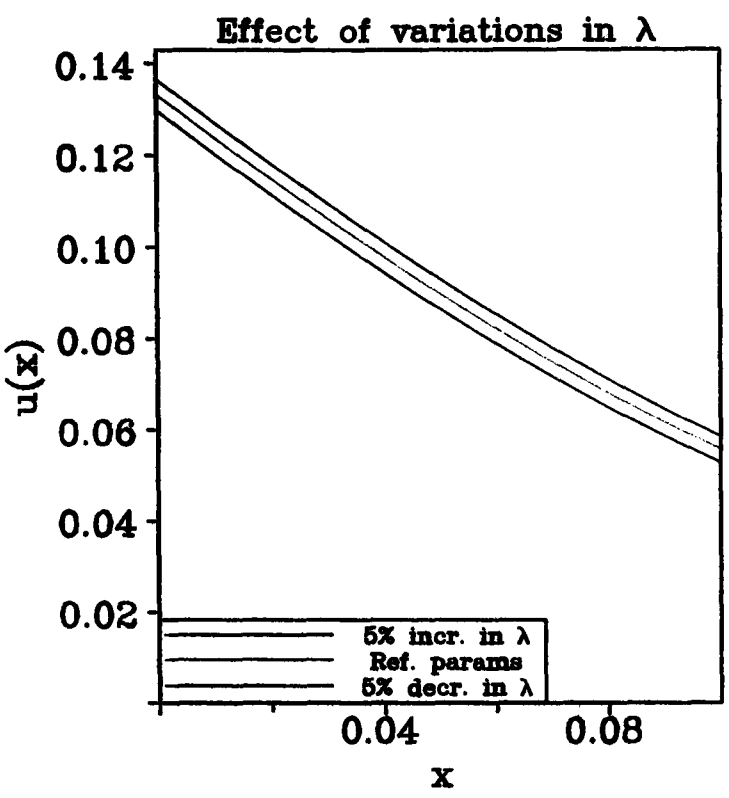

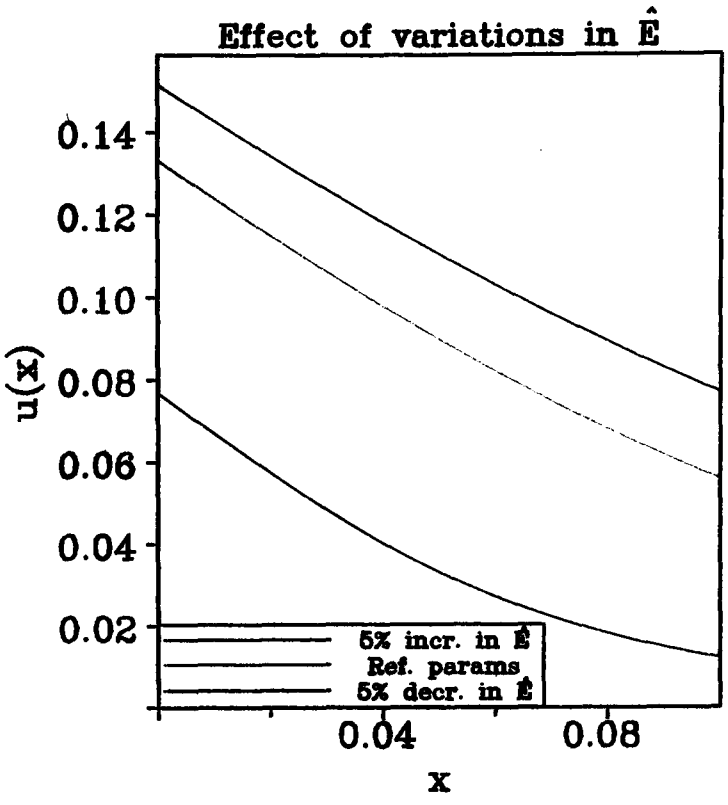

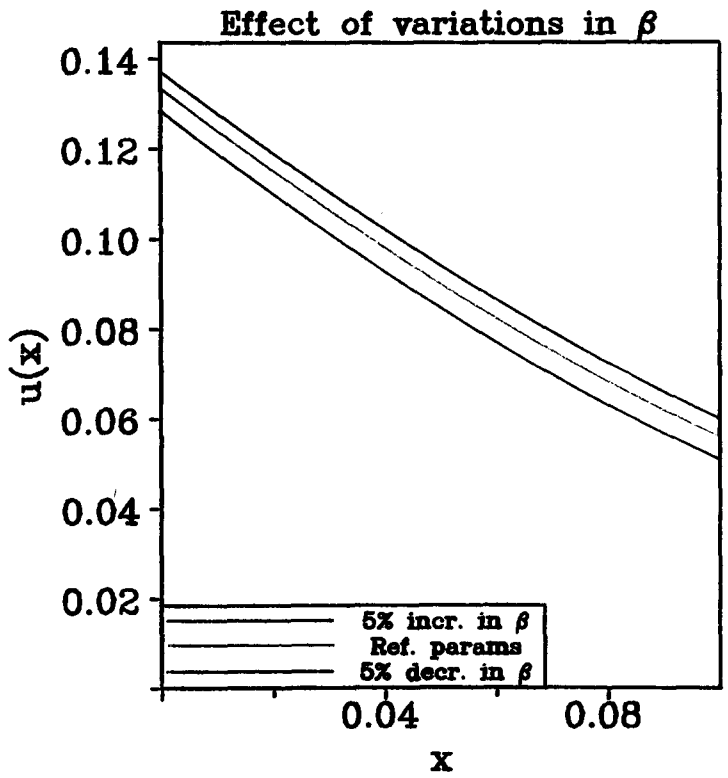

Figure 3.6: The effect of parameter variation on the numerical solution for $u(x)$ of (3.7) subject to (3.9). The solutions in green are for the parameter values $\lambda = 15.0$, $\hat{E} = 1.25$, $\beta = 0.15$. Those in red correspond to a 5% increase in one parameter, and those in blue correspond to a 5% decrease in that parameter. The x–interval shown corresponds to the leading 5 cell layers. The solution is particularly sensitive to the decrease in $\hat{E}$ because the lower limit of $1/(1-\beta)$ is approached.

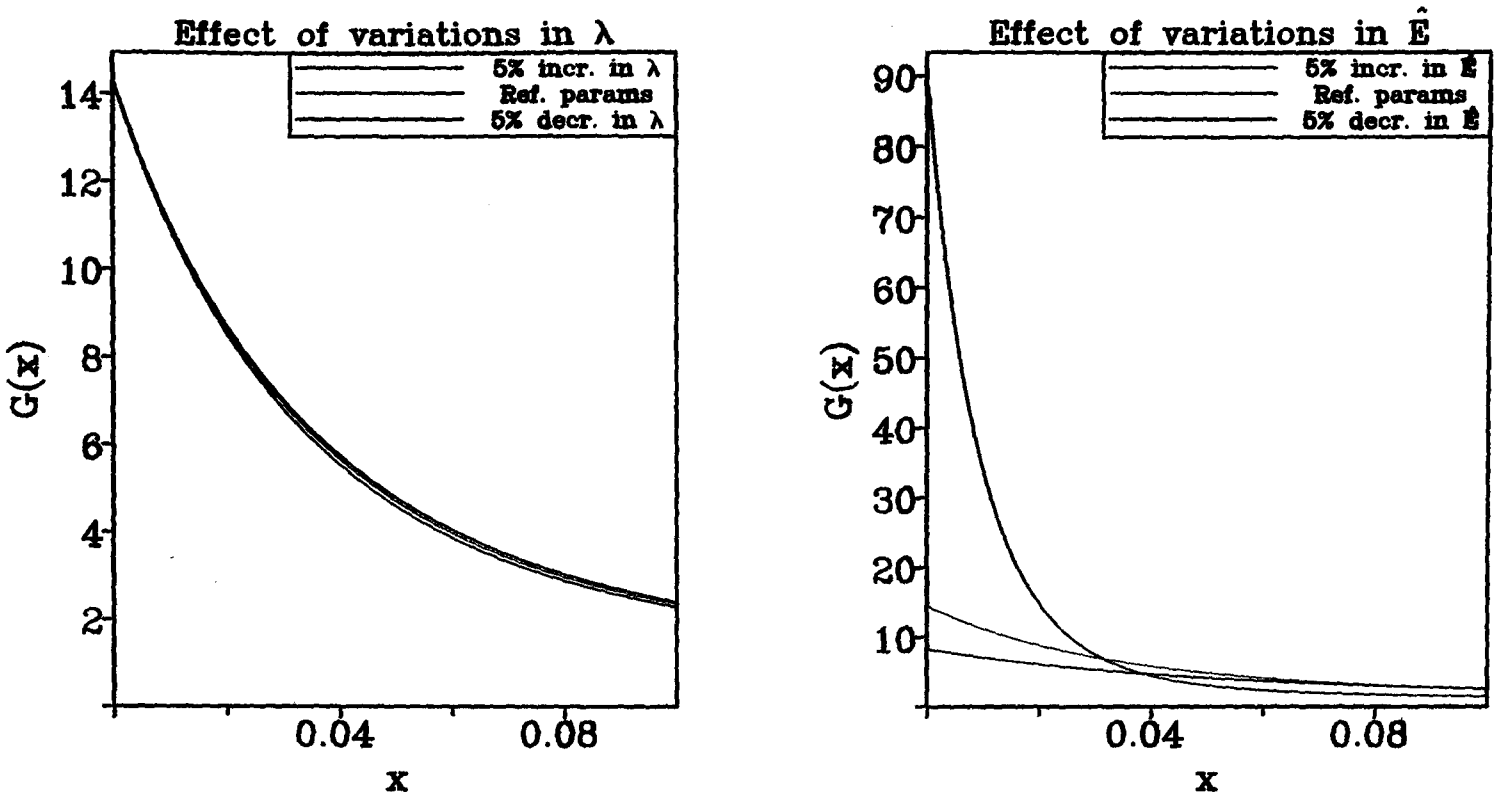

Figure 3.7: The effect of parameter variation on the filamentous actin density $G(x) = 1/(1 + u_x)$, as predicted by the numerical solution of (3.7) subject to (3.9). The solutions in green are for the parameter values $\lambda = 15.0$, $\hat{E} = 1.25$, $\beta = 0.15$. Those in red correspond to a 5% increase in one parameter, and those in blue correspond to a 5% decrease in that parameter. The x–interval shown corresponds to the leading 5 cell layers. The solution is particularly sensitive to the decrease in $\hat{E}$ because the lower limit of $1/(1 - \beta)$ is approached.

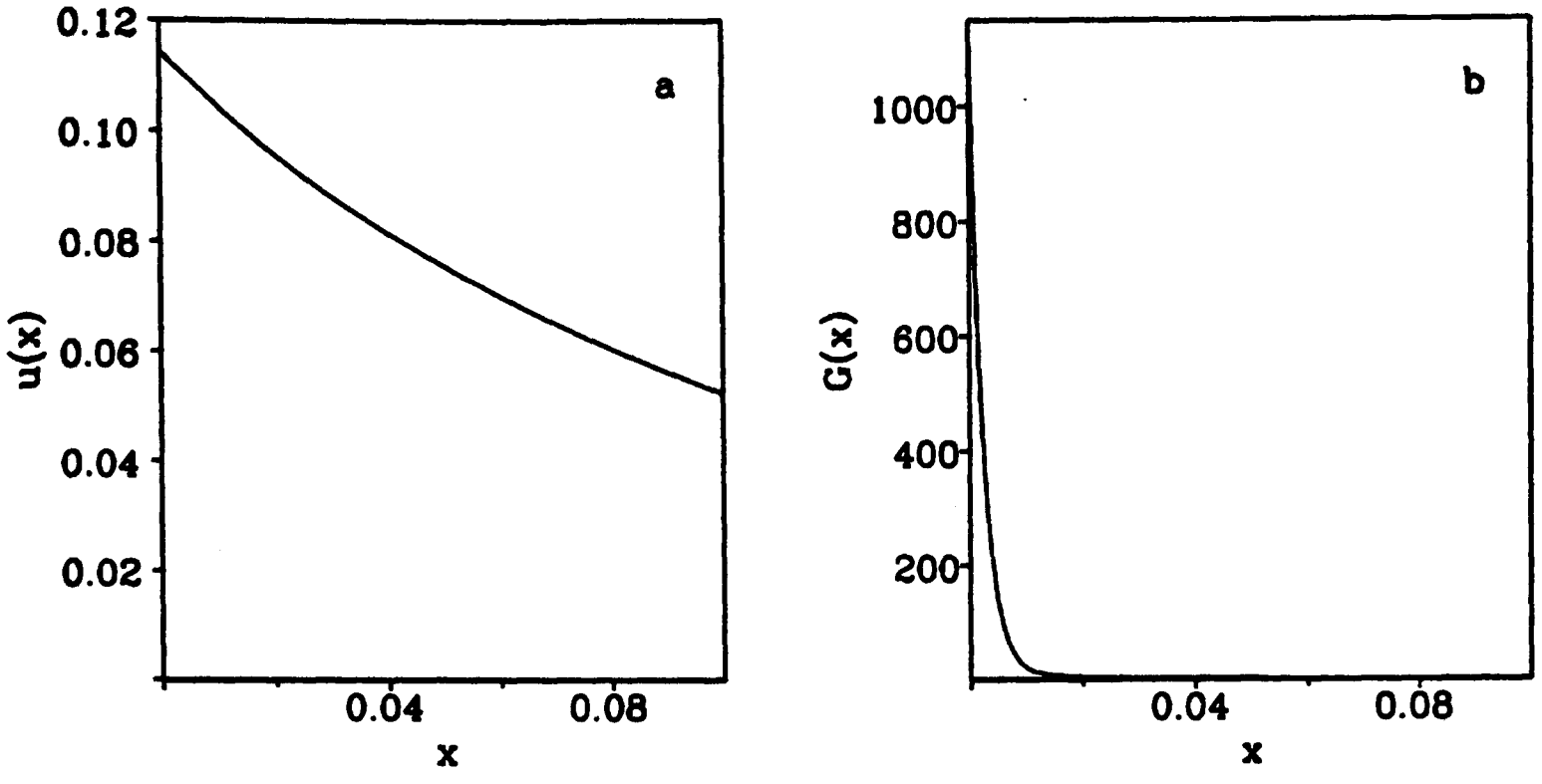

Figure 3.8: (a) The numerical solutions of (3.7) subject to (3.9) for $\lambda = 3.0$, $\hat{E} = 1.3$, $\beta = 0.2303$. (b) The corresponding dimensionless actin filament density $G(x) = 1/(1 + u_x)$. This solution captures the key aspects of the experimental observations of Martin and Lewis (1991a,b) and Midwinter *et al.* (in preparation), including the phenomenon of the actin cable. The wound edge is at $x = 0$.

For $\beta > 1/2$, a parameter search failed to find any sets of parameter values for which there was a significant aggregation of filamentous actin density at the wound edge. Figure 3.9 shows $u(x)$ and $G(x)$ for $\lambda = 5$, $\beta = 0.75$ and $\hat{E} = 3 = 4\beta$. Crucially, as $\hat{E}$ tends to its minimum value of 4β when $\beta > 1/2$, the solution does not approach a singularity, and indeed $\hat{E} = 4\beta$ is a regular point of parameter space. This is in contrast to the case $0 < \beta < 1$, in which case $u_x(0) \to -1$ as $\hat{E}$ decreases towards its minimum value of $1/(1 - \beta)$, which implies that $G(0) \to \infty$.

3.4 Two-Dimensional Radially Symmetric Solutions

In the previous section we investigated solutions of the model equations in one spatial dimension. Building on our understanding of the one-dimensional system, we now investigate the more biologically relevant two-dimensional equations. Specifically, we consider solutions of equation (3.4) in a radially symmetric geometry, corresponding

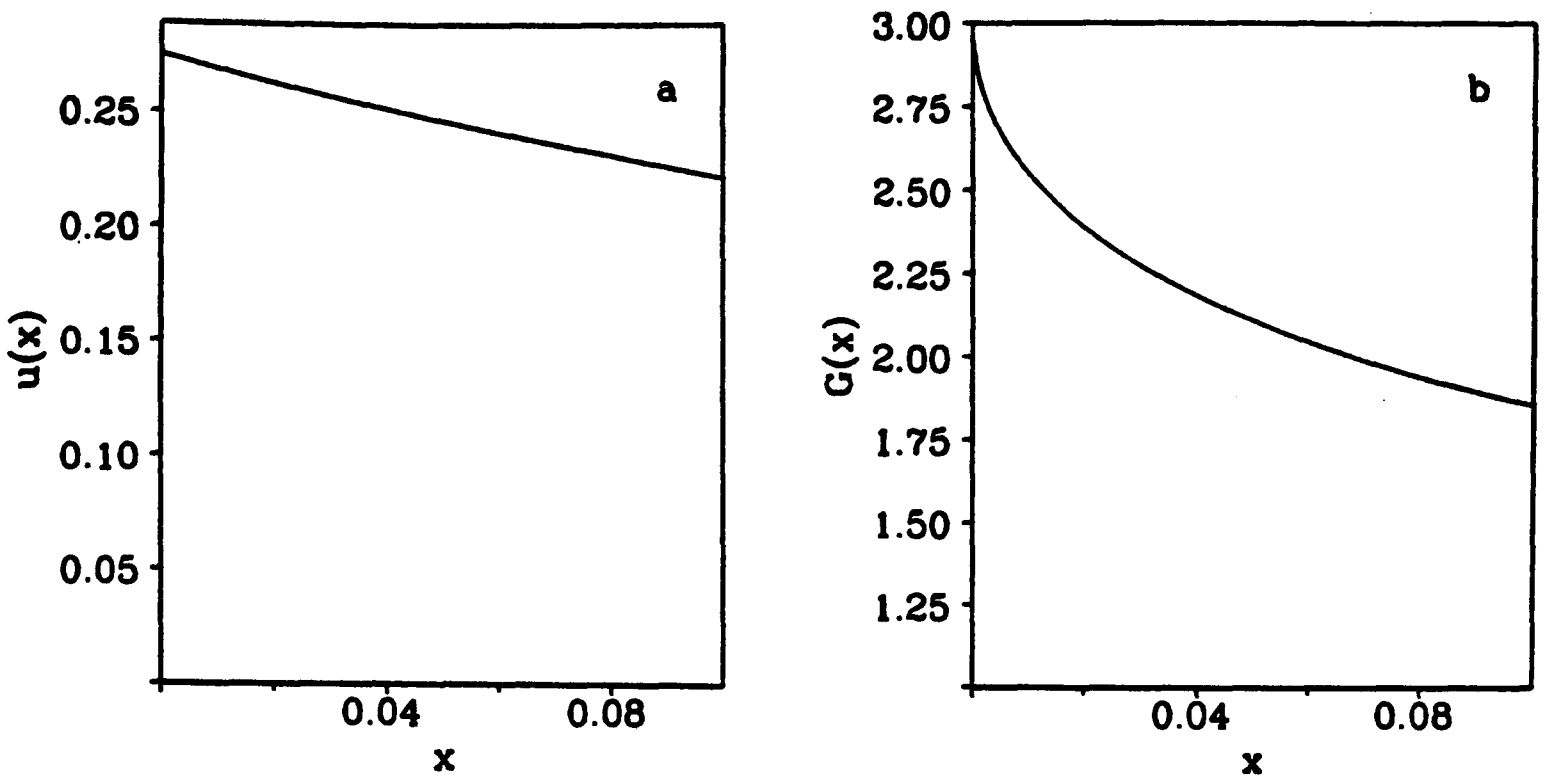

Figure 3.9: (a) The numerical solution of (3.7) subject to (3.9) for $\lambda = 5$, $\beta = 0.75$, $\hat{E} = 3$. (b) The corresponding dimensionless actin filament density $G(x) = 1/(1+u_x)$. The value of $\hat{E}$ is 4β, the minimum value for a solution to exist, but there is no singularity.

to a circular wound. Although the experiments described in Section 3.1 involved square and slash wounds, the use of a circular geometry for the model greatly reduces the computational expense of solution, while retaining the key aspects of the biology. Moreover, similar experiments involving circular wounds in mouse embryos, made by amputating the hindlimb after 11.5 days of gestation, have also revealed a cable of filamentous actin within the leading layer of basal epidermal cells (Martin and Lewis, in preparation).

In plane polar coordinates, the dimensionless stress tensor in (3.1) has the form

$$\underline{\underline{\sigma}} = \begin{bmatrix} p(r) & 0 \\ 0 & q(r) \end{bmatrix}$$

where $p(r)$ and $q(r)$ are the radial and tangential principal values of stress, and are given by

$$p(r) = \frac{Eu' + \Gamma(u' + u/r) + 1/[1 + \beta(u' + u/r)]}{1 + u' + u/r} \tag{3.12a}$$

$$q(r) = \frac{Eu/r + \Gamma(u' + u/r) + 1/[1 + \beta(u' + u/r)]}{1 + u' + u/r}. \tag{3.12b}$$

Here prime denotes d/dr and $\underline{u} = u(r)\hat{\underline{r}}$; we use the fact that $\nabla \cdot \underline{u} = u' + u/r$ in

radially symmetric plane polar coordinates. Thus

$$\begin{aligned}
\nabla \cdot \underline{\underline{\sigma}} &= \left(\hat{\underline{r}}\frac{\partial}{\partial r} + \frac{1}{r}\hat{\underline{\theta}}\frac{\partial}{\partial \theta}\right) \cdot \left(p(r)\hat{\underline{r}}\,\hat{\underline{r}} + q(r)\hat{\underline{\theta}}\,\hat{\underline{\theta}}\right) \\
&= \frac{dp}{dr}\hat{\underline{r}} + \frac{p}{r}\left(\hat{\underline{\theta}} \cdot \frac{\partial \hat{\underline{r}}}{\partial \theta}\right)\hat{\underline{r}} + \frac{q}{r}\left(\hat{\underline{\theta}} \cdot \frac{\partial \hat{\underline{\theta}}}{\partial \theta}\right)\hat{\underline{\theta}} + \frac{q}{r}\frac{\partial \hat{\underline{\theta}}}{\partial \theta} \\
&= \left(p' + \frac{p}{r} - \frac{q}{r}\right)\hat{\underline{r}} \qquad (3.13)
\end{aligned}$$

using the relations

$$\frac{\partial \hat{\underline{r}}}{\partial r} = \underline{0}\,, \qquad \frac{\partial \hat{\underline{\theta}}}{\partial r} = \underline{0}\,, \qquad \frac{\partial \hat{\underline{r}}}{\partial \theta} = \hat{\underline{\theta}}\,, \qquad \frac{\partial \hat{\underline{\theta}}}{\partial \theta} = -\hat{\underline{r}}\,.$$

Substituting the forms for $p(r)$ and $q(r)$ in (3.12) into (3.13) gives

$$\nabla \cdot \underline{\underline{\sigma}} = \frac{d}{dr}\left[\frac{Eu' + \Gamma(u' + u/r) + 1/[1 + \beta(u' + u/r)]}{1 + u' + u/r}\right] + \frac{E}{r}\,\frac{u' - u/r}{1 + u' + u/r}\,.$$

Thus the dimensionless governing equation (3.4) in this geometry is

$$r\frac{d}{dr}\left[\frac{Eu' + \Gamma(u' + u/r) + 1/[1 + \beta(u' + u/r)]}{1 + u' + u/r}\right] + E\frac{u' - u/r}{1 + u' + u/r} = \frac{r\lambda u}{1 + u' + u/r}\,. \qquad (3.14)$$

We take L, the length scale used in the nondimensionalization, to be the wound radius, so that the boundary conditions are

$$Eu' + \Gamma(u' + u/r) + 1/[1 + \beta(u' + u/r)] = 0 \quad \text{at } r = 1 \qquad (3.15a)$$

$$u = 0 \quad \text{at } r = \infty\,. \qquad (3.15b)$$

Throughout the remainder of this chapter and Chapter 4, we consider wounds of radius 500μm; all the wounds in the various experiments described above are of about this length-scale. At the developmental stages we are considering, a typical cell diameter is about 10μm, so that the dimensionless cell length is about 0.02.

3.4.1 Solutions with constant traction

We begin by considering solutions of equation (3.14) subject to (3.15) with constant traction stress per actin filament, so that $\beta = 0$. This is the form taken by Murray

and Oster (1984) in the first continuum model of epithelial morphogenesis. Equation (3.14) is then

$$r\frac{d}{dr}\left[\frac{Eu'+\Gamma(u'+u/r)+1}{1+u'+u/r}\right]+E\frac{u'-u/r}{1+u'+u/r}=\frac{r\lambda u}{1+u'+u/r}\,. \tag{3.16}$$

For algebraic simplicity, we assume that $\Gamma \neq 1$, and write

$$T=\Gamma/(1-\Gamma) \qquad \tilde{E}=E/(1-\Gamma) \qquad \tilde{\lambda}=\lambda/(1-\Gamma)\,. \tag{3.17}$$

It is highly unlikely that a specific value of a parameter such as $\Gamma = 1$ would ever arise in a biological situation, so that the constraint $\Gamma \neq 1$ is biologically acceptable. Moreover, we show below that a solution of the required form does not exist when $\Gamma > 1$. This change of parameters simplifies the equation since the dimensionless parameter T appears only in the boundary condition at $r = 1$. In terms of these new parameters, equation (3.16) is

$$r\frac{d}{dr}\left[\frac{\tilde{E}u'+1}{1+u'+u/r}\right]+\frac{\tilde{E}(u'-u/r)}{1+u'+u/r}=\frac{r\tilde{\lambda}u}{1+u'+u/r}$$

that is
$$r\tilde{E}u''\left(1+u'+\frac{u}{r}\right)-r\left(\tilde{E}u'+1\right)\left(u''+\frac{u'}{r}-\frac{u}{r^2}\right)$$
$$+\tilde{E}\left(u'-\frac{u}{r}\right)\left(1+u'+\frac{u}{r}\right)=r\tilde{\lambda}u\left(1+u'+\frac{u}{r}\right)$$

which reduces to

$$u''+\frac{u'}{r}-\frac{u}{r^2}=\frac{r\tilde{\lambda}u(1+u'+u/r)}{\tilde{E}u+r(\tilde{E}-1)}\,. \tag{3.18}$$

The boundary condition (3.15a) is in this case

$$u'=-\left[\frac{Tu+T+1}{\tilde{E}+T}\right]\,. \tag{3.19}$$

Recall that in one dimension for the case of constant traction, that is $\beta = 0$, a necessary and sufficient condition for a solution of the required form to exist is that $E+\Gamma > 1$. In the case $\Gamma < 1$, we now show that this is also a necessary condition in the radially symmetric geometry. When $\Gamma < 1$, $E + \Gamma > 1$ if and only if $\tilde{E} > 1$. Suppose that on the contrary $\tilde{E} < 1$. Then since $u(\infty) = 0$, and u and $1 - \Delta = (1 + u' + u/r)$ are positive for all r, the right-hand side of equation (3.18) is negative for sufficiently

large r, since all the terms are positive except for $r(\tilde{E}-1)$. The requirement that this right-hand side must always be finite thus implies by continuity that for all $r \geq 1$

$$0 > u'' + \frac{u'}{r} - \frac{u}{r^2} = \frac{d}{dr}(\nabla \cdot u) \ .$$

But as $r \to \infty$, $\nabla \cdot u \to 0$. Thus $\nabla \cdot u > 0$ for all $r \geq 1$. However, we look for a solution in which $\nabla \cdot u < 0$ everywhere. Thus we require $\tilde{E} \geq 1$ for a solution of the required form to exist. But if $\tilde{E} = 1$ equation (3.18) can easily be solved analytically. This is done in Section 3.5, and the solution, given in (3.24), cannot satisfy the condition $u(\infty) = 0$. Thus for $\Gamma < 1$, the strict condition $(E+\Gamma) > 1$ is necessary for a solution of the required form to exist. Numerical solutions suggest that it is also sufficient, and that the solution is unique.

In Section 3.5 we discuss the possibility of finding a uniformly valid asymptotic approximation to the solution of (3.18) subject to (3.19) and (3.15b) using singular perturbation theory. Here we consider numerical solutions and their relationship to the experimental observations described above.

We have successfully used two methods of numerical solution, which we now discuss. The first was a shooting method, in which we treated (3.18) subject to (3.19) as a nonlinear algebraic equation, with $u(1)$ as the unknown and $u(\infty)$ as the function of $u(1)$ that was to be set to zero. We solved for the value of $u(1)$ such that $u(r_\infty) = 0$, starting arbitrarily with $r_\infty = 3$, and gradually increasing r_∞ until the effect of further increase on the solution near the wound edge was negligible; the ordinary differential equation was integrated using a Runge-Kutta-Merson method.

We found this method to be successful provided $(\tilde{E} - 1)$ was not too small. The reason for the numerical difficulties as $\tilde{E}$ decreases to 1 is that the problem is not well posed as an initial value problem. For, if $u(1) = u_0$ is the required initial value such that $u(\infty) = 0$, then a necessary condition for the initial value problem to be well posed is that the solution $u(r)$ is Lipschitz continuous in u_0, that is that for some positive constant k_L and for sufficiently small δ,

$$\left| u(r)\,|_{u(1)=u_0+\delta} - u(r)\,|_{u(1)=u_0} \right| < k_L \delta \quad \text{for all} \quad r > 1 \ .$$

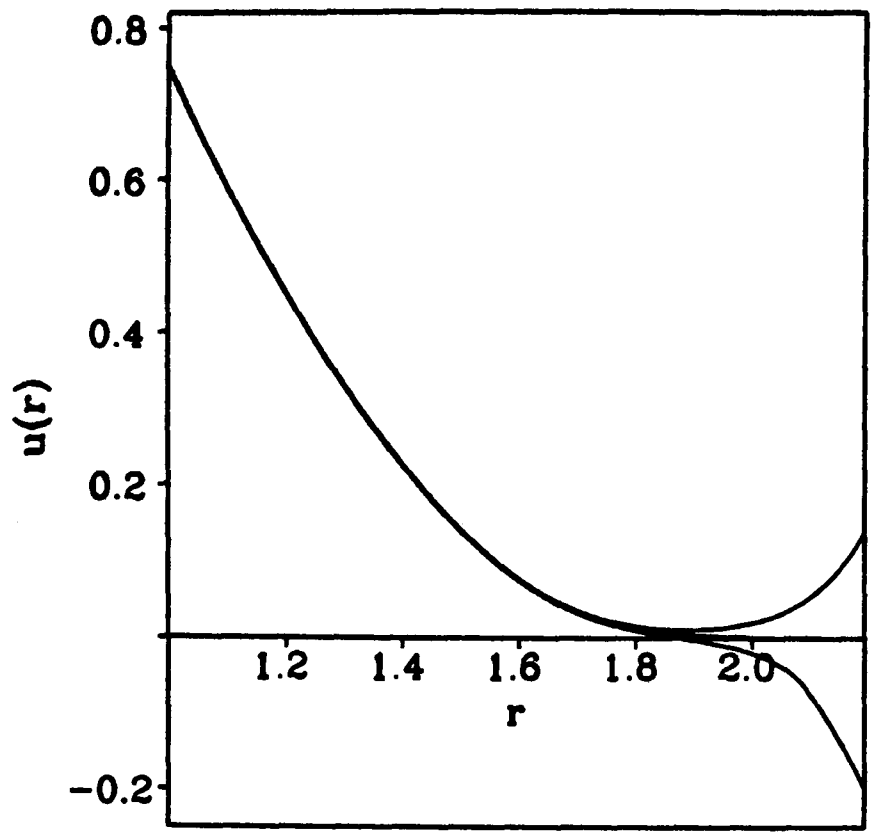

Figure 3.10: Numerical solutions of (3.18) as an initial value problem, with the three initial conditions $u(1) = u_0$, $u_0 \cdot (1 \pm 2.5 \times 10^{-3})$; $u'(1)$ is calculated from (3.19), and the equation is integrated using a Runge-Kutta-Merson method. Here u_0 is the required initial value such that $u(\infty) = 0$; the parameter values are $T = 20$, $\tilde{E} = 1.03$ and $\tilde{\lambda} = 4$. The rapid divergence of the solutions in the region $r > 1.7$ illustrates that equation (3.18) is not well posed as an initial value problem because the solution is not Lipschitz continuous in u_0.

Numerical solutions indicate that this is definitely not satisfied: Figure 3.10 shows the effect of a $\pm 0.25\%$ change in $u(1)$ relative to $u(1) = u_0$, for $\tilde{E} = 1.03$, $T = 20$ and $\tilde{\lambda} = 4$. In this figure, the solutions diverge in the neighbourhood of $r = 1.7$, and this is also the case for perturbations in the solution at $r = 1.2$, 1.4 and 1.6 (numerical solutions not shown). It is unclear from a superficial inspection of equation (3.18) why this region should be problematic, but the singular perturbation analysis in Section 3.5 shows that it is simply the intermediate layer (see page 102).

The second method of numerical solution used deferred correction and Newton iteration. We solved (3.18) as a boundary value problem on $[1, r_\infty]$, subject to (3.19) and $u(r_\infty) = 0$, with r_∞ chosen sufficiently large that increasing its value had a negligible effect on the solution near the wound edge. We found that $r_\infty = 5$ was an appropriate value. We used a nonuniform initial space mesh based on the layered nature of the solution discussed in Section 3.5. Successful implementation of this method required a reasonable initial approximation to the solution, and we found two

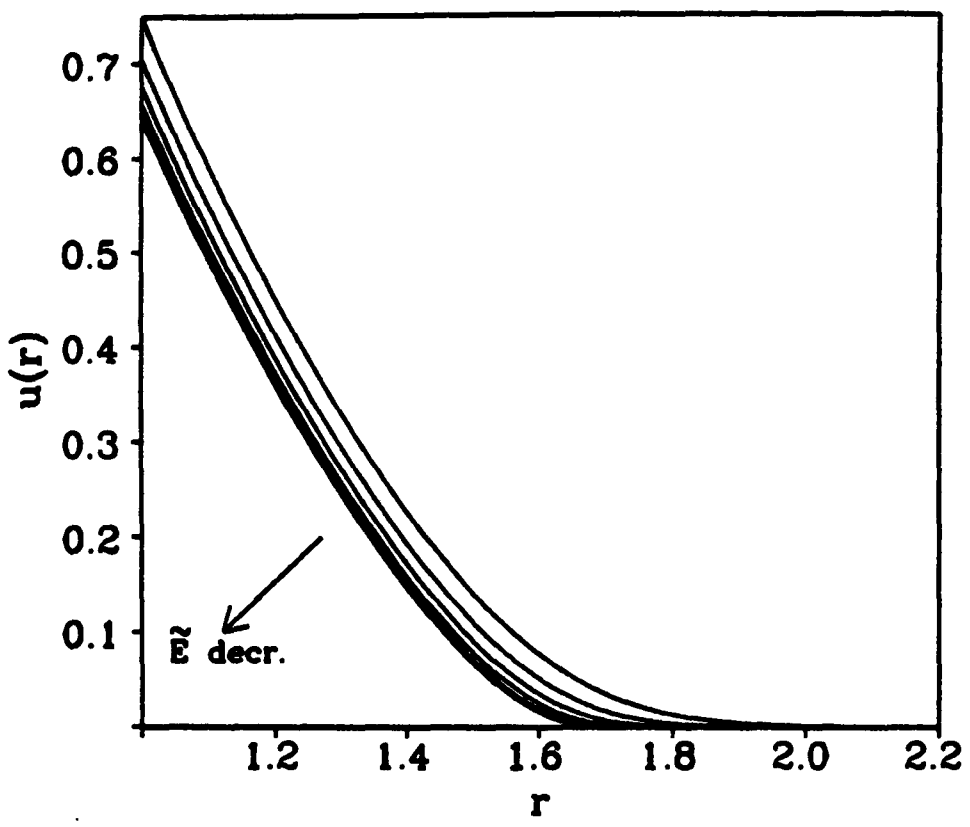

Figure 3.11: Numerical solutions of equation (3.18) subject to 3.19 and (3.15b) for $\tilde{E} = 1 + 0.04 \times 2^{-n}$, $n = 0, 1, \ldots, 6$. The other parameter values are $T = 20$ and $\tilde{\lambda} = 4$. The convergence of these solutions as $(\tilde{E} - 1)$ is successively halved justifies the continuation method used to obtain numerical solutions for values of $\tilde{E}$ close to 1.

ways of obtaining such an approximation. The first was to use the leading order uniformly valid composite expansion obtained using perturbation theory in Section 3.5 and given in equation (3.32). The second, which enabled numerical solutions to be obtained for small values of $(\tilde{E} - 1)$ without appealing to the analysis of Section 3.5, was to obtain the solution for a larger value of $\tilde{E}$ using the shooting method, and to then use continuation in $(\tilde{E} - 1)$ to obtain the solution for the required value of $\tilde{E}$. That is, we successively halved $(\tilde{E}-1)$, and solved (3.18) using the deferred correction technique, with the solution for the previous value of $\tilde{E}$ as the initial approximation. The convergence of the solutions as $(\tilde{E} - 1)$ is successively halved is illustrated in Figure 3.11. We found this deferred correction method to be extremely successful, especially when using (3.32) as the initial approximation.

As in Section 3.3, we look for the model solutions to capture not only the phenomenon of the actin cable at the wound edge, but also the extent to which the various cell layers retract in response to wounding. Although it is difficult to be very precise, in experiments involving circular wounds in mouse embryos made by amputating the

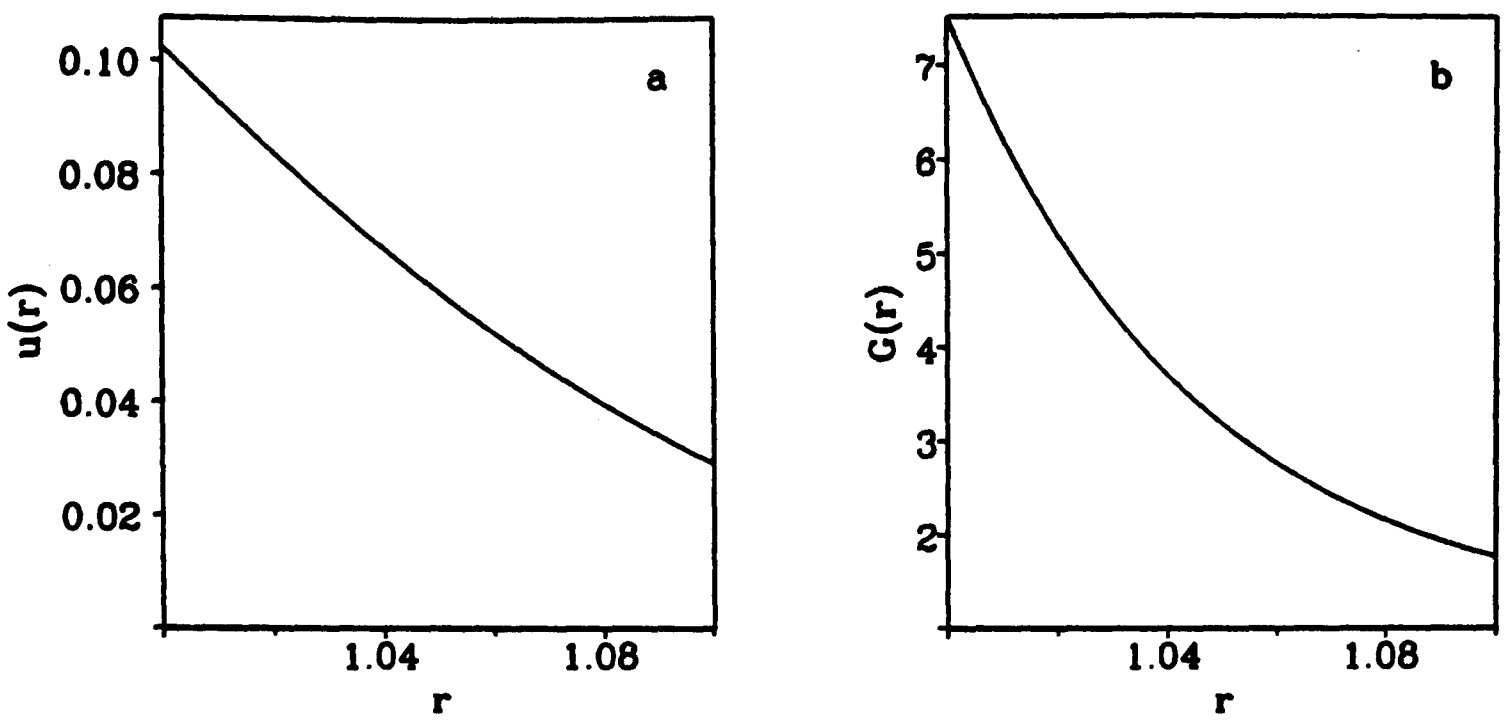

Figure 3.12: (a) The solution of equation (3.18) subject to (3.19) and (3.15b) for $\tilde{\lambda} = 40$, $\tilde{E} = 1.1$ and $T = 0.5$. (b) The corresponding dimensionless actin density $G(r) = 1/(1 + \nabla \cdot \underline{u})$. The solution captures the superficial aspects of the response to wounding observed experimentally, but fails to capture the phenomenon of the actin cable.

hindlimb bud after 11.5 days of gestation (Martin and Lewis, in preparation), a retraction of the wound edges by about 10-15% of the wound radius is observed, with only the leading 4–5 cell layers significantly contracted.

The model solutions were able to capture these more superficial aspects of the response to wounding, as illustrated in Figure 3.12. Crucially, $(\tilde{E} - 1)$ must be small and positive to capture such behaviour. Since there are only three unknown parameter values, an extensive parameter search is possible. However, in the course of such a search we were unable to capture the intense aggregation of actin at the wound edge that constitutes the actin cable. The band of aggregated actin in Figure 3.12 spans several cell lengths. (Recall that the dimensionless cell length is about 0.02).

We conclude our investigation of solutions with $\beta = 0$ by considering the case of $\Gamma > 1$, in which case $\tilde{E}$, T and $\tilde{\lambda}$ are negative. This parameter domain includes the case of a rubber sheet, which is given by putting $\tau_0 = 0$. However, with $\tilde{E}$, T and $\tilde{\lambda}$ negative we were unable to capture even the overall features of the initial response to wounding, that is we were unable to find solutions in which $u(1)$ was between about 0.1 and 0.15, with u decreasing rapidly over a dimensionless length scale of about

0.1. This numerical investigation suggests that $\Gamma < 1$ is a necessary condition for a solution of the required form to exist.

3.4.2 Solutions with variable traction

We now consider the solutions of the model equation in a radially symmetric two-dimensional geometry with $\beta > 0$, so that there is actin filament synergy in cell traction forces. Expanding equation (3.14) then gives

$$r\left[\Gamma - Eu'\right]\left(u'' + \frac{u'}{r} - \frac{u}{r^2}\right) + rEu''\left(1 + u' + \frac{u}{r}\right) + E\left(u' - \frac{u}{r}\right)\left(1 + u' + \frac{u}{r}\right)$$

$$- \frac{r\left(u'' + u'/r - u/r^2\right)}{1 + \beta(u' + u/r)}\left[\frac{\beta(1 + u' + u/r)}{1 + \beta(u' + u/r)} + 1\right] = \lambda ru\left(1 + u' + \frac{u}{r}\right). \quad (3.20)$$

For notational simplicity, we write henceforth

$$\tau_1(r, u, u') = \frac{1}{1 + \beta(u' + u/r)}\left[\frac{\beta(1 + u' + u/r)}{1 + \beta(u' + u/r)} + 1\right] - \Gamma.$$

Equation (3.20) then simplifies to give

$$u'' + \frac{u'}{r} - \frac{u}{r^2} = \frac{\lambda ru(1 + u' + u/r)}{Eu + r(E - \tau_1)}. \quad (3.21)$$

We solved equation (3.21) subject to the boundary conditions (3.15) numerically, using deferred correction and Newton iteration with continuation in β. Methods of numerical solution when $\beta = 0$, the case of constant traction, were discussed above. Using this solution as a starting point, we gradually increased the value of β, using the solution for the previous value as the initial approximation. As expected from the one-dimensional equations investigated in Section 3.3, there appeared to be a critical value of β, dependent on the other three parameters, above which solutions could not be obtained. Throughout the wide range of parameter values we have considered, this critical upper limit was lower in this new geometry than in one space dimension.

In contrast to the case of constant traction considered above, as β approached its critical upper limit, the band of aggregated actin at the wound edge in the model solutions became much sharper, to such an extent that it was localized within the leading cell layer. Such a solution is illustrated in Figure 3.13. However, in this

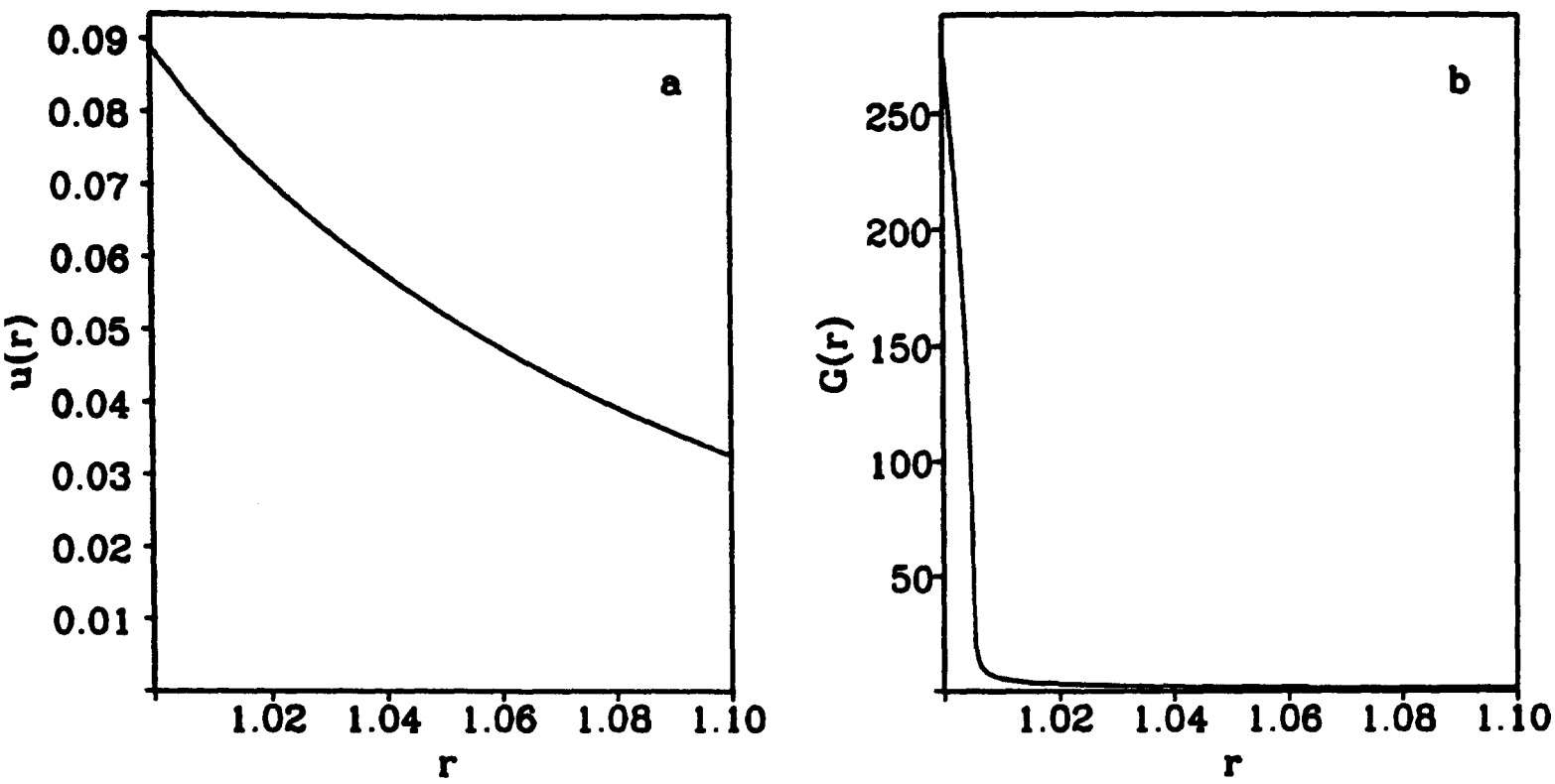

Figure 3.13: (a) The solution of equation (3.21) subject to (3.15) for $\lambda = 3.0$, $E = 0.5$, $\Gamma = 0.8$, and $\beta = 0.255$. (b) The corresponding dimensionless actin filament density $G(r) = 1/(1 + \nabla \cdot \underline{u})$. The band of aggregated actin at the wound edge ($r = 1$) is sharp enough to correspond to the actin cable observed experimentally.

solution, the derivative du/dr is less than -1. Moreover, this was true in all solutions which captured the phenomenon of the actin cable. Note that since the actin density at the wound edge is $G(1) = 1/[1 + u'(1) + u(1)]$ and $u(1) > 0$, large $G(1)$ requires $u'(1) < -1$. In such a solution, the dilation is still greater than -1. However, the biological implication of $u'(1) < -1$ is that cell layers near the wound edge 'change places' after wounding, so that the leading cell layer prior to wounding does not remain the leading cell layer after wounding. Such a phenomenon is certainly not observed experimentally. This inadequacy in the model predictions occurs because the approximation $\Delta = -\nabla \cdot \underline{u}$, which was introduced on page 78, breaks down as du/dr approaches -1. In the next chapter we consider an improved form of the model in which we use a more accurate representation of the local compaction Δ. We conclude this chapter by deriving an approximate solution of equation (3.18) subject to (3.19) and (3.15b) using singular perturbation theory.

3.5 Singular Perturbation Analysis of the Case of Constant Traction

We have shown that for the solution of equation (3.18) subject to the boundary conditions (3.15) to capture the cell retraction aspects of the initial response to wounding, it is necessary that $(\tilde{E}-1)$ is small. In this section we exploit this fact, and look for a uniformly valid asymptotic approximation to this solution using singular perturbation theory. Such methods are clearly surveyed in the book by Kevorkian and Cole (1985). In this section we write $\epsilon = (\tilde{E}-1)$, and for notational simplicity we drop the tilde on the parameter $\tilde{\lambda}$. With this notation, equation (3.18) is

$$u'' + \frac{u'}{r} - \frac{u}{r^2} = \frac{\lambda r u(1+u/r+u')}{(1+\epsilon)u+\epsilon r} \tag{3.22}$$

and the boundary conditions (3.15) have the form

$$u'(1) = -\left[\frac{Tu(1)+T+1}{T+1+\epsilon}\right] \tag{3.23a}$$

$$u(\infty) = 0\,. \tag{3.23b}$$

We begin by attempting to solve equation (3.22) subject to (3.23) when $\epsilon = 0$. This is a linear problem which integrates immediately to give

$$u' - u(\lambda r - 1/r) = \lambda r^2/2 + \text{constant}\,.$$

The integrating factor here is $r\exp(-\lambda r^2/2)$, which gives the general solution of (3.22) when $\epsilon = 0$ as

$$u = \frac{A}{r} - \frac{r}{2} + \frac{B}{r}\exp[\lambda(r^2-1)/2] \tag{3.24}$$

where A and B are constants of integration.

This solution does not satisfy $u(\infty) = 0$ for any values of A and B, so that the problem is singular as $\epsilon \to 0$. Imposing the condition (3.23a) gives a solution $\tilde{u}_0$ of the form

$$\tilde{u}_0 = \frac{1}{2}\left(\frac{1}{r} - r\right) + \frac{B}{r}\left\{\lambda(T+1) - 1 + \exp[\lambda(r^2-1)/2]\right\}. \tag{3.25}$$

This solution is plotted in Figure 3.14 for a range of values of B. We use parameter values $\lambda = 4$ and $T = 20$ in this figure, rather than the values $\lambda = 40$, $T = 0.5$ used in

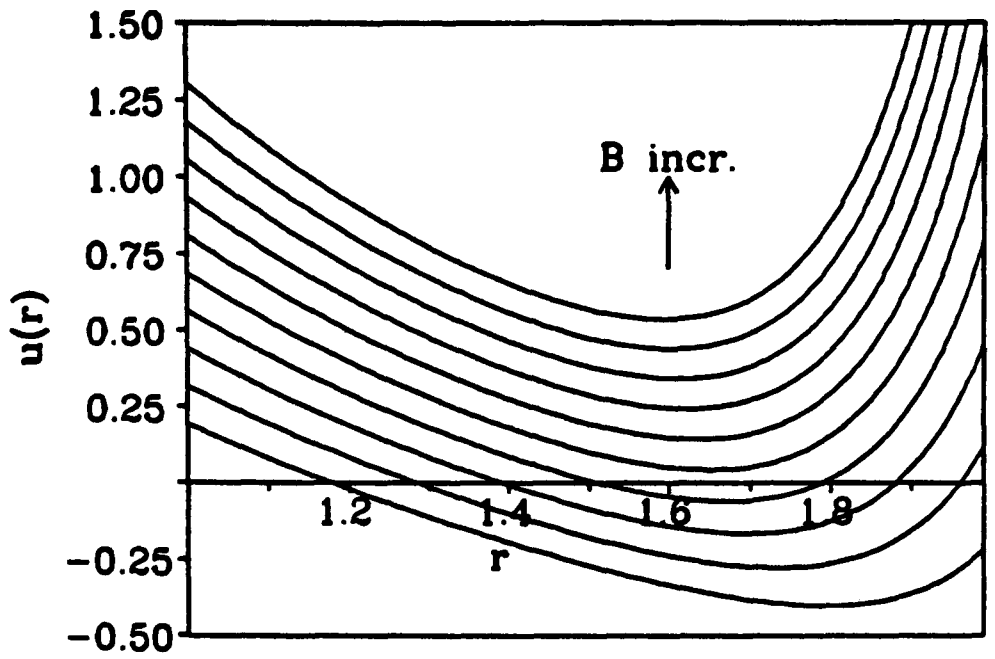

Figure 3.14: The solution (3.25) of equation (3.18), for ten evenly spaced values of the constant of integration B, between 0.0023 and 0.0155. The parameter values are $\lambda = 4$ and $T = 20$.

the solutions in Figure 3.12 which capture the overall features of the initial response to wounding. This is also done in the other figures in this section, and is for reasons of clarity, as explained below.

3.5.1 Possible rescalings

We look for a rescaling that will capture the behaviour of the solution of (3.22) subject to (3.23) for large r. Such a rescaling has the general form $\hat{r} = \hat{\mu}(\epsilon)r$, $\hat{u} = u/\hat{\nu}(\epsilon)$, with $\hat{\mu}(\epsilon) = O(1)$, $\hat{\nu}(\epsilon) = O(1)$ and $\hat{\mu} \cdot \hat{\nu} = o(1)$ as $\epsilon \to 0$. Here, as usual, the notation $f(\epsilon) = O(1)$ includes the case $f(\epsilon) = o(1)$; the condition $\hat{\mu} \cdot \hat{\nu} = o(1)$ ensures that we do have a genuine rescaling. This gives

$$\hat{\mu}^2 \left[\frac{d^2\hat{u}}{d\hat{r}^2} + \frac{1}{\hat{r}} \frac{d\hat{u}}{d\hat{r}} - \frac{\hat{u}}{\hat{r}^2} \right] \cdot [\hat{\mu}\hat{\nu}(1+\epsilon)\hat{u} + \epsilon\hat{r}] = \lambda \hat{r}\hat{u} \left\{ 1 + \hat{\mu}\hat{\nu} \left(\frac{\hat{u}}{\hat{r}} + \frac{d\hat{u}}{d\hat{r}} \right) \right\}.$$

All the terms in this equation are $o(1)$ except $\lambda\hat{r}\hat{u}$. Thus $\hat{u}|_{\epsilon=0} = 0$, and similarly all terms in any asymptotic expansion for $\hat{u}$ are zero.

Therefore we have to introduce a layer rescaling to give a solution intermediate between this zero solution at large r and the regular solution (3.25) near $r = 1$. The general form of the variables in such a layer is $r^* = (r - R)/\mu(\epsilon)$, $u^* = u/\nu(\epsilon)$, where $\mu(\epsilon) = o(1)$ and $\nu(\epsilon) = O(1)$ as $\epsilon \to 0$. Here $r = R$ is the centre of the layer.

Substituting into (3.22) gives

$$\frac{\nu}{\mu^2}\frac{d^2u^*}{dr^{*2}} + \frac{\nu}{R+\mu r^*}\left(\frac{1}{\mu}\frac{du^*}{dr^*} - \frac{u^*}{R+\mu r^*}\right) = \frac{\lambda\nu u^*(R+\mu r^*)\left(1+\frac{\nu u^*}{R+\mu r^*}+\frac{\nu}{\mu}\frac{du^*}{dr^*}\right)}{(1+\epsilon)\nu u^* + \epsilon R + \epsilon\mu r^*}$$

which to leading order is

$$\frac{d^2u^*}{dr^{*2}} = \frac{\mu^2\lambda R u^*}{\nu u^* + \epsilon R}; \tag{3.26}$$

all the other terms can certainly be neglected to leading order. There are then a number of possibilities, according to the orders chosen for μ and ν:

(a) $\mu^2 \sim \nu \sim \epsilon$. This is discussed in detail below.

(b) $\mu^2 \sim \nu \gg \epsilon$. Then $d^2u^*/dr^{*2} = \lambda R$ to leading order; the parabolic layer solution cannot match the zero solution to the right of the layer.

(c) $\mu^2 \sim \epsilon \gg \nu$. Here to leading order $d^2u^*/dr^{*2} = \lambda u^*$, $\Rightarrow u^* \propto \exp(-\sqrt{\lambda}r^*)$ since $u^*(\infty) = 0$. This exponential solution cannot be matched to the left of the layer.

(d) $\mu^2 \gg \nu$ and $\mu^2 \gg \epsilon$. In this case all terms in any asymptotic expansion for u^* are zero.

(e) $\mu^2 \ll \nu$ or $\mu^2 \ll \epsilon$. Here $d^2u^*/dr^{*2} = 0$ to leading order; the linear solution cannot match the zero solution to the right of the layer.

Thus the only rescaling that can give an appropriate layer solution is (a), namely $u^* = u/\epsilon$, $r^* = (r-R)/\sqrt{\epsilon}$. Multiplying (3.26) by du^*/dr^* and integrating gives

$$\frac{1}{2}\left(\frac{du^*}{dr^*}\right)^2 = \lambda R^2\left[\frac{u^*}{R} - \log\left(1+\frac{u^*}{R}\right)\right] + \text{constant}.$$

Imposing $u^* = 0$ at $r^* = \infty$ shows that the leading order term in the layer solution is then

$$u_0^* = R\cdot H^{-1}\left(C - r^*\sqrt{2\lambda}\right) \quad \text{where } H(\xi) = \int_1^\xi \{\theta - \log(1+\theta)\}^{-1/2}\,d\theta\,,$$

and where C is a constant of integration.

In what follows, we will require asymptotic expansions of $H(\xi)$ and $H^{-1}(\xi)$ as $\xi \to \infty$, and we now derive these expansions. Writing the integrand in the definition of $H(\xi)$ as a power series in $\psi = \xi^{-1}\log(1+\xi)$ shows that for sufficiently large ξ

$$\begin{aligned}
\frac{d}{d\xi}\left[H(\xi) - 2\sqrt{\xi}\right] &= \xi^{-1/2}\left[(1-\psi)^{-1/2} - 1\right] \\
&= \xi^{-1/2}\left[\frac{1}{2}\psi + \frac{1}{2}\frac{3}{2}\frac{1}{2!}\psi^2 + \frac{1}{2}\frac{3}{2}\frac{5}{2}\frac{1}{3!}\psi^3 \ldots\right] \\
&= \frac{\xi^{-3/2}}{2}\log(1+\xi)\left[1 + \frac{3}{2}\frac{1}{2!}\psi + \frac{3}{2}\frac{5}{2}\frac{1}{3!}\psi^2 + \ldots\right] \\
&< \xi^{-3/2}\log(1+\xi)\left[1 + \frac{3}{2}\psi + \frac{3}{2}\frac{5}{2}\frac{1}{2!}\psi^2 + \ldots\right] \\
&= \xi^{-3/2}\log(1+\xi)\,[1-\psi]^{-3/2}\,.
\end{aligned}$$

Now for sufficiently large ξ, $\log(1+\xi) < \xi^{1/4}$, so that

$$\frac{d}{d\xi}\left[H(\xi) - 2\sqrt{\xi}\right] < \xi^{-1/8}\left[\xi^{3/4} - 1\right]^{-3/2}\,.$$

But for sufficiently large ξ, $\xi^{3/4} - 1 > \xi^{(3/4)-(2\gamma/3)}$ for any small γ, so that

$$\frac{d}{d\xi}\left[H(\xi) - 2\sqrt{\xi}\right] < \xi^{-(5/4)+\gamma}\,.$$

We now fix $\gamma < 1/4$ and integrate this inequality between $\xi = \omega$ and $\xi = \Omega$, where ω is sufficiently large and $\Omega > \omega$. This gives

$$H(\Omega) - 2\sqrt{\Omega} < \frac{\Omega^{\gamma-(1/4)}}{\gamma - (1/4)} + D_\omega < D_\omega$$

where D_ω is a constant depending on ω. Thus for sufficiently large Ω, $\left[H(\Omega) - 2\sqrt{\Omega}\right]$ is bounded above by D_ω; further it increases monotonically for $\Omega > 0$. Thus $\left[H(\Omega) - 2\sqrt{\Omega}\right]$ tends to a finite limit as $\Omega \to \infty$. The value of this limit, K say, is simply

$$K = -2 + \int_1^\infty \left[\{\theta - \log(1+\theta)\}^{-1/2} - \theta^{-1/2}\right] d\theta\,,$$

and numerical integration shows that $K \approx 0.899$. Term-wise integration of the above series expansion for $\frac{d}{d\xi}\left[H(\xi) - 2\sqrt{\xi}\right]$ suggests that $H(\xi) - 2\sqrt{\xi} - K$ has the form $-\xi^{-1/2}\log\xi - 2\xi^{-1/2} + O(\xi^{-3/2}\log^2\xi)$ as $\xi \to \infty$, and this is confirmed by numerical integration. We therefore have, in this limit,

$$H(\xi) = 2\xi^{1/2} + K - \xi^{-1/2}\log\xi - 2\xi^{-1/2} + O(\xi^{-3/2}\log^2\xi)\,. \qquad (3.27)$$

From this, it is clear that to leading order, $H^{-1}(x) = (x-K)^2/4$ as $x \to \infty$. Substituting $H^{-1}(x) = (x-K)^2/4 + y(x)$ into (3.27) and expanding for large x implies that

$$\begin{aligned} x &= 2\left\{\frac{1}{4}(x-K)^2+y\right\}^{1/2} + K - \left\{\frac{1}{4}(x-K)^2+y\right\}^{-1/2}\left[\log\left\{\frac{1}{4}(x-K)^2+y\right\}+2\right] \\ &\quad -\frac{1}{4}\left\{\frac{1}{4}(x-K)^2+y\right\}^{-3/2}\left[\log\left\{\frac{1}{4}(x-K)^2+y\right\}+2\right]^2 + O(x^{-3}\log^2 x) \\ &= (x-K)\left\{1+\frac{2y}{(x-K)^2}-\frac{y^2}{2(x-K)^4}+\frac{y^3}{8(x-K)^6}+\ldots\right\}+K \\ &\quad -\left(\frac{2}{x-K}\right)\left\{1-\frac{2y}{(x-K)^2}-\frac{y^2}{2(x-K)^4}+\ldots\right\}\left[2\log x+2(1-\log 2)\right. \\ &\quad \left.-\frac{2K}{x}+\frac{K^2}{x^2}+\ldots+\frac{4y}{(x-K)^2}+\frac{8y^2}{(x-K)^4}+\ldots\right]+O(x^{-3}\log^2 x) \\ &= x+\frac{2}{x-K}\left[y-2\log x-2(1-\log 2)+\frac{2K}{x}+O\left(\frac{\log^2 x+y^2+y\log x}{x^2}\right)\right]. \end{aligned}$$

Therefore as $x \to \infty$

$$H^{-1}(x) = \frac{(x-K)^2}{4} + 2\log x + 2(1-\log 2) - \frac{2K}{x} + o\left(\frac{1}{x}\right). \qquad (3.28)$$

3.5.2 Matching to leading order

Matching to the right of the layer is guaranteed by the boundary condition at $r^* = \infty$. For matching to the left of the layer we use an intermediate variable $r_\eta = (r-R)/\eta(\epsilon)$, with $\sqrt{\epsilon} \ll \eta(\epsilon) \ll 1$, and consider the behaviour of the left-hand and layer solutions as $\epsilon \to 0$ with r_η fixed. Then $r \to R$ and $r^* \to -\infty$. Now (3.28) implies that

$$u_0^* = \frac{\lambda R}{2}\left[r^* + \frac{K-C}{\sqrt{2\lambda}}\right]^2 + o(r^*) \quad \text{as } r^* \to -\infty. \qquad (3.29)$$

Matching to leading order therefore requires

$$\frac{1}{\delta(\epsilon)}\left\{\tilde{u}_0(R) + \eta r_\eta \tilde{u}_0'(R) + \frac{\eta^2 r_\eta^2}{2}\tilde{u}_0''(R) + O(\eta^3)\right\} =$$

$$\frac{\epsilon\lambda R}{2\delta(\epsilon)}\left[\frac{\eta r_\eta}{\sqrt{\epsilon}} + \frac{K-C}{\sqrt{2\lambda}}\right]^2 + o\left(\frac{\eta\sqrt{\epsilon}+\delta(\epsilon)}{\delta(\epsilon)}\right)$$

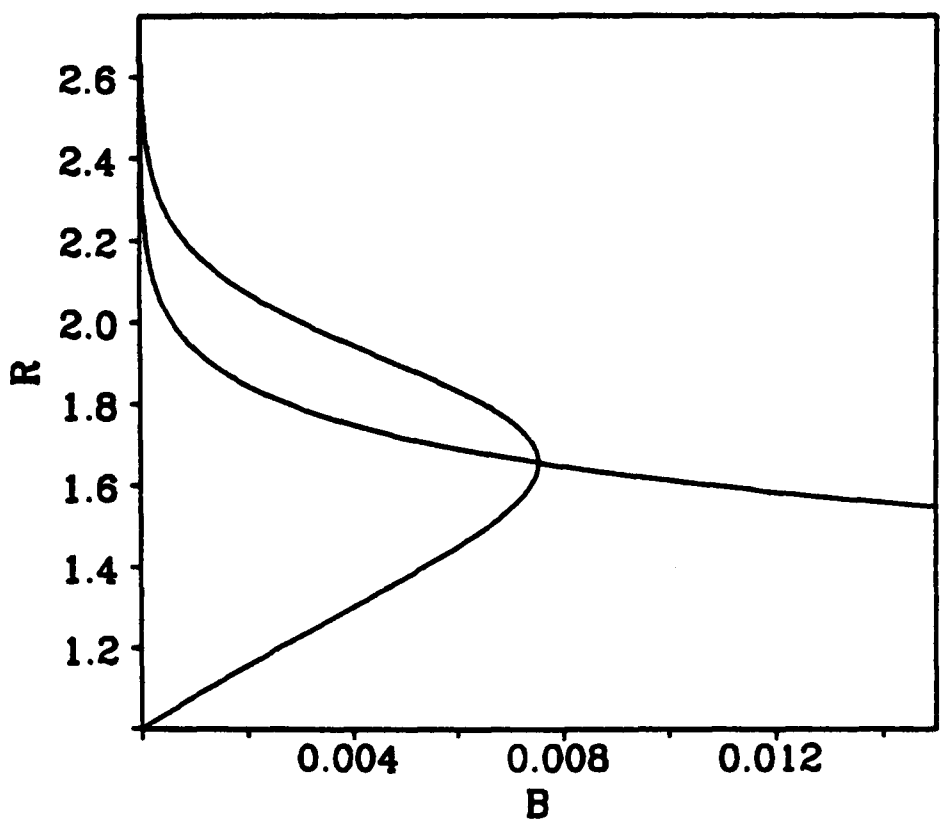

Figure 3.15: The curves given by equations (3.30) and (3.31) in the first quadrant of the B–R plane. These are plotted for $\lambda = 4$ and $T = 20$, but the qualitative forms are the same for all positive values of these parameters. In particular, the single intersection implies that equations (3.30) and (3.31) have unique real positive solutions for B and R.

as $\epsilon \to 0$, where $\delta(\epsilon)$ is an intermediate scaling for the dependent variable, with $\epsilon \ll \delta \ll 1$, and $\tilde{u}_0$ is the leading order solution (3.25) near $r = 1$, which has been expanded in a Taylor series about $r = R$; as previously, prime denotes d/dr. This matching requirement holds provided the following conditions are satisfied:

(i) $\tilde{u}_0(R) = \tilde{u}_0'(R) = 0$. By straightforward differentiation and simplification, this implies that

$$B\left\{\lambda(T+1) - 1 + \exp[\lambda(R^2-1)/2]\right\} = (R^2-1)/2 \qquad (3.30)$$

$$\lambda B \exp[\lambda(R^2-1)/2] = 1. \qquad (3.31)$$

The forms of (3.30) and (3.31) in the first quadrant of the B–R plane are shown in Figure 3.15. From these, it is clear that the transcendental equations have unique real positive solutions for B and R, which can easily be found numerically for given values of λ and T.

(ii) $\tilde{u}_0''(R) = \lambda R$, which we now prove:

$$\begin{aligned}
\tilde{u}_0''(R) &= \frac{1}{R^3} + \frac{2B}{R^3}\left\{\lambda(T+1) - 1 + \exp[\lambda(R^2-1)/2]\right\} \\
&\qquad - \frac{\lambda B}{R}\exp[\lambda(R^2-1)/2] + \lambda^2 BR\exp[\lambda(R^2-1)/2] \\
&= \frac{1}{R^3} + \frac{1}{R^3}(R^2-1) - \frac{1}{R} + \lambda R \\
&= \lambda R,
\end{aligned}$$

using (3.30) and (3.31).

(iii) $\eta^3 \ll \delta$.

(iv) $\sqrt{\epsilon}\,\eta = O(\delta)$. If we further specify $\sqrt{\epsilon}\,\eta \ll \delta$, then C is not determined by the leading order matching. However, the absence of a $\sqrt{\epsilon}$ term in the expansion near $r = 1$ (see below) requires that $C = K$.

Thus we have obtained matched asymptotic expansions to leading order for the solution of (3.22) subject to (3.23). We obtain a composite expansion in the usual way, as "outer solution + inner solution − common part" (see, for example, Murray, 1984; Kevorkian and Cole, 1985). This gives

$$u_{comp0}(r) = \begin{cases} \tilde{u}_0(r) + \epsilon u_0^*(r^*) - \frac{1}{2}\lambda R(r-R)^2 & r < R \\ \epsilon u_0^*(r^*) & r > R. \end{cases} \tag{3.32}$$

Figure 3.16 shows $\tilde{u}_0$, ϵu_0^*, u_{comp0} and the numerical solution of (3.22) subject to (3.23), plotted against r, for $\epsilon = 0.03$ and 0.003. The difference between u_{comp0} and $\tilde{u}_0$ decreases to zero as r decreases below 1. This figure demonstrates very clearly that the problem is singular as $\epsilon \to 0$: the numerical solutions of the full system are quite different in parts (a) and (b) of Figure 3.16, despite ϵ being very small in both cases. Moreover, the difference between these numerical solutions and $\tilde{u}_0$, the solution for $\epsilon = 0$ subject only to boundary condition (3.23a), is very considerable even for $\epsilon = 0.003$. In Figure 3.16, we use parameter values $\lambda = 4$ and $T = 20$ rather than the values $\lambda = 40$, $T = 0.5$ used in the solutions in Figure 3.12, which capture the overall features of the initial response to wounding. We do this for reasons of clarity: as λ increases and T decreases, R decreases towards 1, and at $\lambda = 40$ and $T = 0.5$, $R \approx 1.08$. The analysis is of course valid for all parameter values.

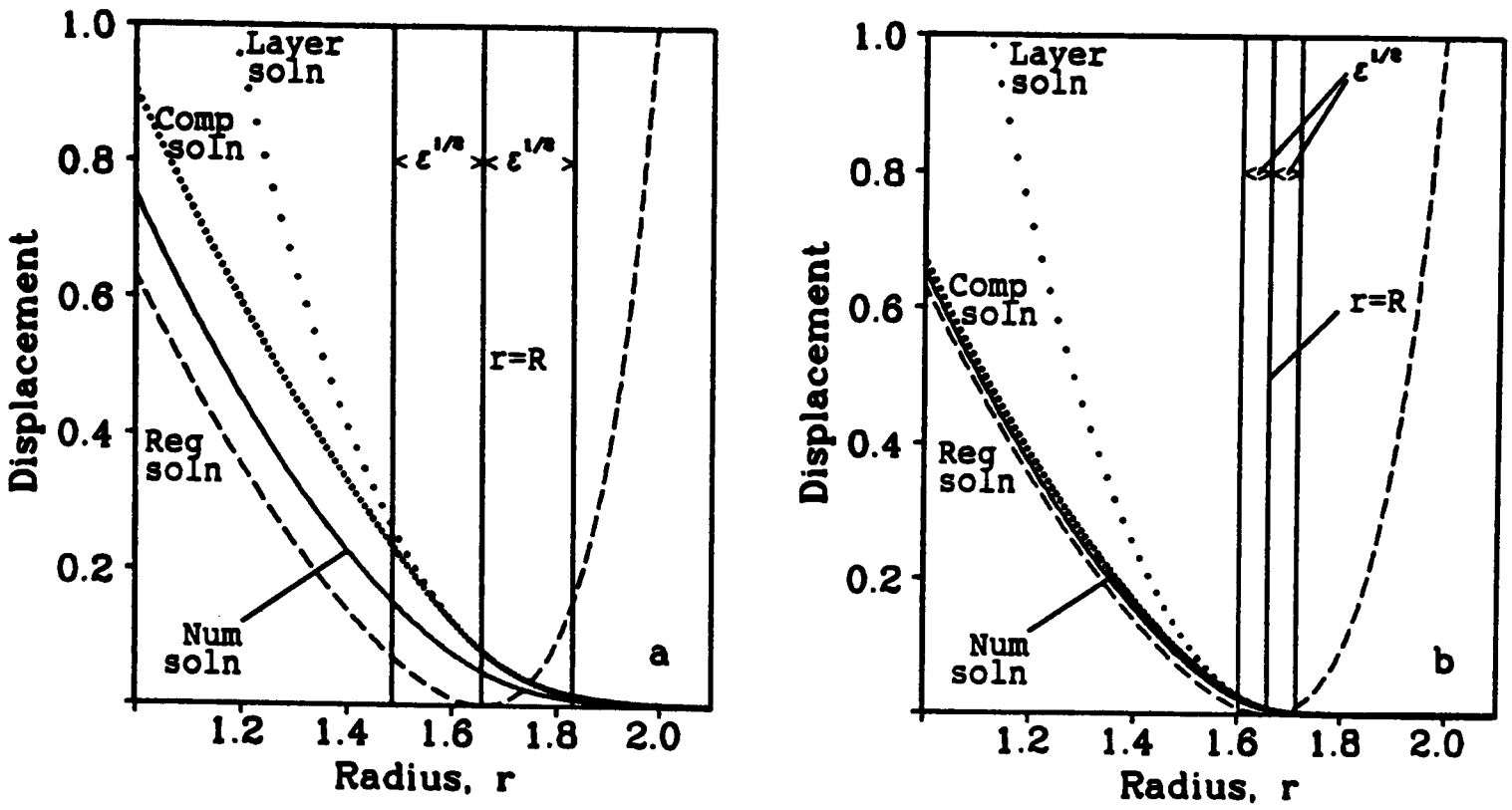

Figure 3.16: Plots of the regular solution, $\tilde{u}_0(r)$, the leading order layer solution, $\epsilon u_0^*(r^*)$, the leading order composite solution, $u_{comp0}(r)$, and the numerical solution of (3.22) subject to (3.23), against r, for (a) $\epsilon = 0.03$ and (b) $\epsilon = 0.003$, with $\lambda = 4$ and $T = 20$. The numerical solutions were obtained using Newton iteration and deferred correction, with $u_{comp0}(r)$ as the initial approximation. To indicate the layer regions, the lines $r = R$ and $r = R \pm \sqrt{\epsilon}$ are drawn. The error in the leading order composite solution appears to be $O(\sqrt{\epsilon})$, and this is confirmed by our investigation of the higher order terms.

3.5.3 Higher order corrections

The leading order composite solution differs significantly from the numerical solution of (3.22) subject to (3.23) even for values of the parameter ϵ as small as 0.03. We now consider higher order corrections to the leading order approximation obtained above. The full equation for u^* contains $\sqrt{\epsilon}$ terms, so that the first order correction to u_0^* is $O(\sqrt{\epsilon})$. Substituting $u^* = u_0^* + \sqrt{\epsilon}\, u_1^*$ in the full equation for u^* and equating coefficients of $\sqrt{\epsilon}$ gives

$$\frac{d^2u_1^*}{dr^{*2}} - \frac{\lambda R^2}{(u_0^* + R)^2} u_1^* = \frac{\lambda u_0^*}{u_0^* + R}\left[\frac{u_0^* r^*}{u_0^* + R} + R\frac{du_0^*}{dr^*}\right] - \frac{1}{R}\frac{du_0^*}{dr^*}.$$

Now $u_0^*(r^*)$ is monotonically decreasing, so we can use u_0^* as the independent variable; this is feasible since du_0^*/dr^* and $d^2u_0^*/dr^{*2}$ are known functions of u_0^*. We then have

$$2R^2\left\{\frac{u_0^*}{R} - \log\left(1 + \frac{u_0^*}{R}\right)\right\}\frac{d^2u_1^*}{du_0^{*2}} + \frac{Ru_0^*}{u_0^* + R}\frac{du_1^*}{du_0^*} - \frac{R^2}{(u_0^* + R)^2}u_1^* =$$

$$\frac{u_0^*}{u_0^* + R}\left[\frac{u_0^* r^*}{u_0^* + R} + R\frac{du_0^*}{dr^*}\right] - \frac{1}{\lambda R}\frac{du_0^*}{dr^*} \qquad (3.33)$$

where $\dfrac{du_0^*}{dr^*} = -\left\{2\lambda R^2\left[\dfrac{u_0^*}{R} - \log\left(1+\dfrac{u_0^*}{R}\right)\right]\right\}^{1/2}$ and $r^* = \dfrac{K - H(u_0^*/R)}{\sqrt{2\lambda}}$,

subject to $u_1^* = 0$ at $u_0^* = 0$. Here we use the identities

$$\frac{du_1^*}{dr^*} = \frac{du_0^*}{dr^*}\frac{du_1^*}{du_0^*} \qquad \text{and} \qquad \frac{d^2u_1^*}{dr^{*2}} = \frac{d^2u_0^*}{dr^{*2}}\frac{du_1^*}{du_0^*} + \left(\frac{du_0^*}{dr^*}\right)^2\frac{d^2u_1^*}{du_0^{*2}}\,.$$

The homogeneous equation corresponding to (3.33) can be integrated directly, giving linearly independent solutions

$$\begin{aligned} y_1(u_0^*) &= \left\{\frac{u_0^*}{R} - \log\left(1+\frac{u_0^*}{R}\right)\right\}^{1/2} \\ y_2(u_0^*) &= \left\{\frac{u_0^*}{R} - \log\left(1+\frac{u_0^*}{R}\right)\right\}^{1/2} I(u_0^*/R), \end{aligned}$$

where $I(\xi) = \int_1^\xi \{\theta - \log(1+\theta)\}^{-3/2} d\theta$. The inhomogeneous equation can thus be solved using the method of undetermined coefficients, that is, we look for a solution of the form

$$u_1^* = a_1(u_0^*)y_1(u_0^*) + a_2(u_0^*)y_2(u_0^*)$$

subject to the constraint

$$\frac{da_1}{du_0^*}y_1(u_0^*) + \frac{da_2}{du_0^*}y_2(u_0^*) = 0\,.$$

Substituting this into (3.33) gives linear equations for da_1/du_0^* and da_2/du_0^*. Solving these gives the general solution of (3.33) as

$$u_1^* = \frac{1}{2}\left\{\frac{u_0^*}{R} - \log\left(1+\frac{u_0^*}{R}\right)\right\}^{1/2}\left[I(u_0^*/R)\int_0^{u_0^*/R} F(\xi)\,d\xi - \int_1^{u_0^*/R} I(\xi)F(\xi)\,d\xi + P_1 + Q_1 I(u_0^*/R)\right], \qquad (3.34)$$

where $F(u_0^*/R)$ is the right-hand side of (3.33), and P_1 and Q_1 are constants of integration. F is integrable near zero, since straightforward series expansion shows that as $\xi \to 0$, $F(\xi) = \xi/\sqrt{\lambda} + O(\xi^2 \log \xi)$. Expanding the integral $I(\xi)$ for small ξ shows that as $u_0^* \to 0$ (so that $r^* \to \infty$), $u_1^* = -Q_1(3Ru_0^{*-1} + 5)/6 + o(1)$, and thus the boundary condition at $u_0^* = 0$ requires the constant of integration Q_1 to be zero.

For the purposes of matching, it is the behaviour of u_1^* as $u_0^* \to \infty$ (so that $r^* \to -\infty$) that is of interest. Expanding for large ξ gives

$$\begin{aligned} F(\xi) &= R^2\sqrt{\lambda/2}\left[-2\xi^{1/2} + \xi^{-1/2}\log\xi + \left(\frac{6}{\lambda R^2} + 2\right)\xi^{-1/2}\right] + O(\xi^{-3/2}\log^2\xi) \\ I(\xi)F(\xi) &= R^2\sqrt{\lambda/2}\left[-2I_\infty\xi^{1/2} + 4 + I_\infty\xi^{-1/2}\log\xi + I_\infty\left(\frac{6}{\lambda R^2} + 2\right)\xi^{-1/2}\right. \\ &\qquad \left. -4\left(\frac{3}{\lambda R^2} + \frac{2}{3}\right)\xi^{-1}\right] + O(\xi^{-3/2}\log^2\xi) \end{aligned}$$

where $I_\infty = \lim_{\xi\to\infty} I(\xi)$. Here we have used the expansion (3.27) of $H(\xi)$ for large ξ. Integrating term-wise and substituting into (3.34) suggests that as $u_0^* \to \infty$,

$$u_1^* = -\frac{\sqrt{2\lambda R}}{3}u_0^{*3/2} + \left[\frac{6}{\sqrt{2\lambda}} + \frac{R^2\sqrt{2\lambda}}{6}\right]\left(\frac{u_0^*}{R}\right)^{1/2}\log u_0^* + U_1^* u_0^{*1/2} + O(\log^2 u_0^*)\,. \quad (3.35)$$

Here the constant U_1^* is dependent on the outstanding constant of integration P_1:

$$U_1^* = \frac{P_1}{\sqrt{R}} - \frac{\log R}{\sqrt{R}}\left[\frac{R^2\sqrt{2\lambda}}{6} + \frac{6}{\sqrt{2\lambda}}\right] - \frac{1}{\sqrt{R}}\left[7R^2\sqrt{2\lambda} + \frac{12}{\sqrt{2\lambda}}\right].$$

These results are confirmed by numerical integration.

Consider now higher order corrections to $\tilde{u}_0$. Substituting $u = \tilde{u}_0 + \sqrt{\epsilon}\tilde{u}_1$ in (3.22) and (3.23), and equating coefficients of $\sqrt{\epsilon}$, gives

$$\tilde{u}_1'' + \frac{\tilde{u}_1'}{r} - \frac{\tilde{u}_1}{r^2} = \lambda r\left(\frac{\tilde{u}_1}{r} + \tilde{u}_1'\right) \quad (3.36)$$

subject to $\tilde{u}_1'(1) = -T\tilde{u}_1(1)/(T+1)$, where as previously, prime denotes d/dr. This can be solved in the same way as (3.25) was obtained, giving

$$\tilde{u}_1 = \frac{B_1}{r}\left\{\lambda T + \lambda - 1 + \exp[\lambda(r^2-1)/2]\right\}$$

where B_1 is a constant of integration. Now matching even to $O(\sqrt{\epsilon})$ clearly requires $\tilde{u}_1(R) = 0$, so that $B_1 = 0$ and thus $\tilde{u}_1 \equiv 0$.

We therefore look for a $O(\epsilon)$ correction to $\tilde{u}_0$. Substituting $u = \tilde{u}_0 + \epsilon\tilde{u}_2$ in (3.22) and (3.23), and equating coefficients of ϵ, gives

$$\tilde{u}_2'' + \left(\frac{1}{r} - \lambda r\right)\tilde{u}_2' - \left(\lambda + \frac{1}{r^2}\right)\tilde{u}_2 = -\frac{\lambda r}{\tilde{u}_0}(\tilde{u}_0 + r)\left(1 + \frac{\tilde{u}_0}{r} + \tilde{u}_0'\right) \quad (3.37)$$

subject to $\tilde{u}_2'(1) = -[T\tilde{u}_2(1) + \tilde{u}_0'(1)]/(T+1)$. This equation can again be solved using the method of undetermined coefficients: the homogeneous equation has linearly independent solutions $1/r$ and $e^{\lambda r^2/2}/r$. This gives

$$\tilde{u}_2(r) = \frac{B_2}{r}\left\{\lambda T + \lambda - 1 + \exp[\lambda(r^2-1)/2]\right\} - \frac{1+\lambda TB}{r} + \frac{\lambda B e^{-\lambda/2}}{2r}\int_1^{r^2} \frac{2B\exp[\lambda(u-1)/2] + D + u}{2B\exp[\lambda(u-1)/2] + D - u}\left(e^{\lambda u/2} - e^{\lambda r^2/2}\right) du \quad (3.38)$$

where $D = 1 + 2B(\lambda T + \lambda - 1)$ and B_2 is a constant of integration. For the purposes of matching, it is the behaviour of this solution as $r \to R^-$ that is of interest. This can be obtained directly by series expansion, but the algebra required is rather involved. Instead, we derive the behaviour of the solution in this limit directly from the differential equation (3.37). Expanding the coefficients as power series in $\zeta = r - R$ gives

$$\frac{d^2\tilde{u}_2}{d\zeta^2} + \left[\left(\frac{1}{R} - \lambda R\right) - \left(\lambda + \frac{1}{R^2}\right)\zeta + O(\zeta^2)\right]\frac{d\tilde{u}_2}{d\zeta} - \left[\left(\lambda + \frac{1}{R^2}\right) - \frac{2}{R^3}\zeta + O(\zeta^2)\right]\tilde{u}_2 = -\frac{2R}{\zeta^2} - \frac{4\lambda R^2 + 12}{3\zeta} + O(1)\,. \quad (3.39)$$

Let $\tilde{u}_{2,lead}$ be the solution of the equation given by taking only the leading order term of each coefficient in (3.39), so that

$$\frac{d^2\tilde{u}_{2,lead}}{d\zeta^2} + \left(\frac{1}{R} - \lambda R\right)\frac{d\tilde{u}_{2,lead}}{d\zeta} - \left(\lambda + \frac{1}{R^2}\right)\tilde{u}_{2,lead} = -\frac{2R}{\zeta^2}\,. \quad (3.40)$$

The corresponding homogeneous equation has linearly independent solutions $e^{\alpha^+\zeta}$ and $e^{\alpha^-\zeta}$, where $\alpha^\pm$ are the roots of the characteristic equation. Using the method of undetermined coefficients, we therefore look for a solution of the form

$$\tilde{u}_{2,lead} = a^+(\zeta)\exp[\alpha^+\zeta] + a^-(\zeta)\exp[\alpha^-\zeta]\,, \quad (3.41)$$

where the unknown functions $a^\pm(\zeta)$ are constrained to satisfy

$$\frac{da^+}{d\zeta}\exp[\alpha^+\zeta] + \frac{da^-}{d\zeta}\exp[\alpha^-\zeta] = 0\,. \quad (3.42)$$

Substituting (3.41) into (3.40) and using (3.42) gives

$$\frac{da^\pm}{d\zeta} = -\frac{2R}{(\alpha^+ + \alpha^-)}\frac{1}{\zeta^2}\exp[-\alpha^\pm\zeta]\,.$$

But

$$\int \frac{e^x\,dx}{x^2} = -\frac{e^x}{x} + \left[\log|x| + \frac{x}{1!} + \frac{x^2}{2\cdot 2!} + \frac{x^3}{3\cdot 3!} + \cdots\right]$$

(see, for example, Beyer, 1981). Using this expansion and (3.41), the general solution of (3.40) is

$$\tilde{u}_{2,lead} = 2R\log|\zeta| + 2(\lambda R^2 - 1)\zeta\log|\zeta| + O(\zeta^2\log|\zeta|) + A_2^+ e^{\alpha^+\zeta} + A_2^- e^{\alpha^-\zeta} \quad (3.43)$$

as $\zeta \to 0$, where $A_2^{\pm}$ are constants of integration.

Denoting the correction to this leading order solution by $\tilde{u}_{2,corr}(r)$ and substituting $\tilde{u}_2 = \tilde{u}_{2,lead} + \tilde{u}_{2,corr}$ into (3.39) implies that to leading order as $\zeta \to 0$, $\tilde{u}_{2,corr}$ satisfies

$$\frac{d^2\tilde{u}_{2,corr}}{d\zeta^2} + \left(\frac{1}{R} - \lambda R\right)\frac{d\tilde{u}_{2,corr}}{d\zeta} - \left(\lambda + \frac{1}{R^2}\right)\tilde{u}_{2,corr} = -\frac{4\lambda R^2 + 12}{3\zeta}.$$

This can again be solved using the method of undetermined coefficients, and the solution has the form

$$\tilde{u}_{2,corr} = -4(1 + \lambda R^2/3)\zeta\log|\zeta| + O(\zeta^2\log|\zeta|) + A_3^+ e^{\alpha^+\zeta} + A_3^- e^{\alpha^-\zeta} \quad (3.44)$$

as $\zeta \to 0$, where $A_3^{\pm}$ are constants of integration. Since we require $\tilde{u}_{2,lead} \gg \tilde{u}_{2,corr}$ as $\zeta \to 0$, $A_3^+ = A_3^- = 0$. Adding the two solutions (3.43) and (3.44) implies that as $r \to R^-$,

$$\tilde{u}_2 = 2R\log|\zeta| + \tilde{U}_2 + \left(\tfrac{2}{3}\lambda R^2 - 6\right)\zeta\log|\zeta| + \tilde{U}_{2,1}\zeta + O\left[\zeta^2\log|\zeta|\right] \quad (3.45)$$

where $\tilde{U}_2$ is an outstanding constant of integration, the value of which determines the constant B_2 in (3.38), and thus $\tilde{U}_{2,1}$. This expansion is confirmed by numerical integration.

3.5.4 Intermediate terms and conclusions

Comparison of the expansions (3.35), (3.45) and the leading order expansions in Section 3.5.2 indicates that a number of terms remain unmatched at the left of the layer, even to $O(\sqrt{\epsilon})$. We found that in order to complete the process of matching to higher order it was necessary to introduce logarithmic terms between the leading

and higher order terms found previously, in both the left-hand and layer solutions. Specifically, we introduce a term $\epsilon \log \epsilon \, \tilde{u}_l(r)$ in the left-hand solution and a term $\sqrt{\epsilon} \log \epsilon \, u_l^*(r^*)$ in the layer solution.

Substituting $u = \tilde{u}_0 + \epsilon \log \epsilon \, \tilde{u}_l$ in (3.22) and (3.23) and equating coefficients of $\epsilon \log \epsilon$ shows that $\tilde{u}_l$ satisfies the same equation (3.36) and boundary condition as $\tilde{u}_1$. Thus

$$\tilde{u}_l = \frac{B_l}{r} \left\{ \lambda T + \lambda - 1 + \exp[\lambda(r^2 - 1)/2] \right\} \tag{3.46}$$

where B_l is a constant of integration.

The equation satisfied by u_l^* is obtained in the same way; using u_0^* as the independent variable, as in Section 3.5.3, gives

$$2R \left\{ \frac{u_0^*}{R} - \log\left(1 + \frac{u_0^*}{R}\right) \right\} \frac{d^2 u_l^*}{du_0^{*2}} + \frac{u_0^*}{u_0^* + R} \frac{du_l^*}{du_0^*} - \frac{R \, u_l^*}{(u_0^* + R)^2} = 0 .$$

subject to $u_l^* = 0$ at $u_0^* = 0$. This equation can be solved by integrating once, multiplying by the integrating factor $\{u_0^*/R + \log(1 + u_0^*/R)\}^{-3/2}$ and integrating again, giving the general solution as

$$u_l^* = \left\{ \frac{u_0^*}{R} - \log\left(1 + \frac{u_0^*}{R}\right) \right\}^{1/2} \left[C_1 + C_2 \int_1^{u_0^*/R} \{\xi - \log(1 + \xi)\}^{-3/2} \, d\xi \right]$$

where C_1, C_2 are constants of integration. Straightforward series expansion shows that the behaviour of this solution as $u_0^* \to 0$ (so that $r^* \to \infty$) is

$$u_l^* = C_1 \left[\frac{u_0^*}{R\sqrt{2}} + O(u_0^{*2}) \right] - C_2 \left[\frac{R}{u_0^*} + \frac{5}{3} + o(1) \right] .$$

Thus the boundary condition at $u_0^* = 0$ requires $C_2 = 0$, so that as $u_0^* \to \infty$ (so that $r^* \to -\infty$),

$$u_l^* = \frac{C_1}{\sqrt{R}} u_0^{*1/2} + O(u_0^{*-1/2} \log u_0^*) . \tag{3.47}$$

We can now consider matching the amended left-hand and layer solutions: as in Section 3.5.2, matching to the right of the layer is trivially satisfied. Using (3.35), (3.45), (3.47) and the leading order expansions in Section 3.5.2, and expanding (3.46) in a Taylor series about $r = R$, the condition for matching to $O(\sqrt{\epsilon})$ is

$$\frac{1}{\sqrt{\epsilon}\delta(\epsilon)}\left\{\tilde{u}_0'''(R)\frac{\eta^3 r_\eta^3}{6}+O(\eta^4)+\tilde{U}_l\epsilon\log\epsilon+\frac{\tilde{U}_l(R^2+1)}{R(R^2-1)}\eta r_\eta\epsilon\log\epsilon+O(\eta^2\epsilon\log\epsilon)\right.$$

$$\left.+2R\epsilon\log|\eta r_\eta|+\tilde{U}_2\epsilon+\left(\tfrac{2}{3}\lambda R^2-6\right)\epsilon\eta r_\eta\log|\eta r_\eta|+\tilde{U}_{2,1}\epsilon\eta r_\eta+O(\epsilon\eta^2\log\eta)\right\}$$

$$=\frac{\sqrt{\epsilon}}{\delta(\epsilon)}\left\{2R\log\left|\frac{\eta r_\eta}{\sqrt{\epsilon}}\right|+R[2+\log(\lambda/2)]+O\left(\frac{\sqrt{\epsilon}}{\eta}\right)-C_l\sqrt{\lambda/2}\left(\frac{\eta r_\eta}{\sqrt{\epsilon}}\right)\sqrt{\epsilon}\log\epsilon\right.$$

$$+O\left(\frac{\epsilon\log\epsilon\log\eta}{\eta}\right)+\frac{\lambda^2R^2}{6}\left(\frac{\eta r_\eta}{\sqrt{\epsilon}}\right)^3\sqrt{\epsilon}+\left(\tfrac{2}{3}\lambda R^2-6\right)\eta r_\eta\log\left|\frac{\eta r_\eta}{\sqrt{\epsilon}}\right|$$

$$\left.+\sqrt{\epsilon}\,U_1^*\sqrt{\lambda R/2}\left(\frac{\eta r_\eta}{\sqrt{\epsilon}}\right)+O(\sqrt{\epsilon}\log^2\eta)\right\}+o(1) \qquad (3.48)$$

as $\epsilon\to 0$, where $\tilde{U}_l=B_l\left\{\lambda T+\lambda-1+\exp[\lambda(R^2-1)/2]\right\}/R$. Here we have obtained higher order terms in the behaviour of u_0^* as $r^*\to-\infty$, using (3.28). Simplifying the expression for $\tilde{u}_0'''(R)$, using (3.3) and (3.4), shows that $\tilde{u}_0'''(R)=\lambda^2R^2$. Thus the matching condition determines the outstanding constants of integration as follows:

$$\tilde{U}_l=-R \qquad \tilde{U}_2=R[2+\log(\lambda/2)]$$

$$U_1^*=\tilde{U}_{2,1}\sqrt{2/(\lambda R)} \qquad C_l=-\sqrt{2/\lambda}\,[\lambda R^2/3-3-(R^2+1)/(R^2-1)]\,.$$

We then have matching to $O(\sqrt{\epsilon})$ provided the following conditions are satisfied by $\delta(\epsilon)$ and $\eta(\epsilon)$ as $\epsilon\to 0$:

(a) $\eta^4=o(\sqrt{\epsilon}\delta)$ (b) $\eta^2\sqrt{\epsilon}\log\epsilon=o(\delta)$ (c) $\eta^2\sqrt{\epsilon}\log\eta=o(\delta)$

(d) $\epsilon=o(\eta\delta)$ (e) $\epsilon^{3/2}\log\epsilon\log\eta=o(\eta\delta)$ (f) $\epsilon\log^2\eta=o(\delta)$.

Trivially (d)⇒(f). Moreover, $\eta\gg\sqrt{\epsilon}$, so that $\log\eta=O(\log\epsilon)$; thus (b)⇒(c) and (d)⇒(e). Also, $\delta\gg\epsilon\gg\epsilon^{3/2}\log^2\epsilon$, and multiplying (a) by this result implies (b). Thus for matching to $O(\sqrt{\epsilon})$ it is necessary and sufficient that $\eta^4\ll\sqrt{\epsilon}\delta$ and $\epsilon\ll\delta\eta$. These conditions can be portrayed graphically if we consider only orders of magnitude that are powers of ϵ: intermediate orders involving logarithms need not concern us. Thus, we write $\delta=O_s(\epsilon^p)$, $\eta=O_s(\epsilon^q)$, where, as usual, the notation $f=O_s(g)$ means that $f=O(g)$ and $f\neq o(g)$. The two conditions are then $4q>p+1/2$ and $p+q<1$. We also require $q<1/2$; the conditions $\eta^3\ll\delta$ and $\sqrt{\epsilon}\eta=O(\delta)$ for leading order matching are implied by (a) and (d). The p–q domain such that

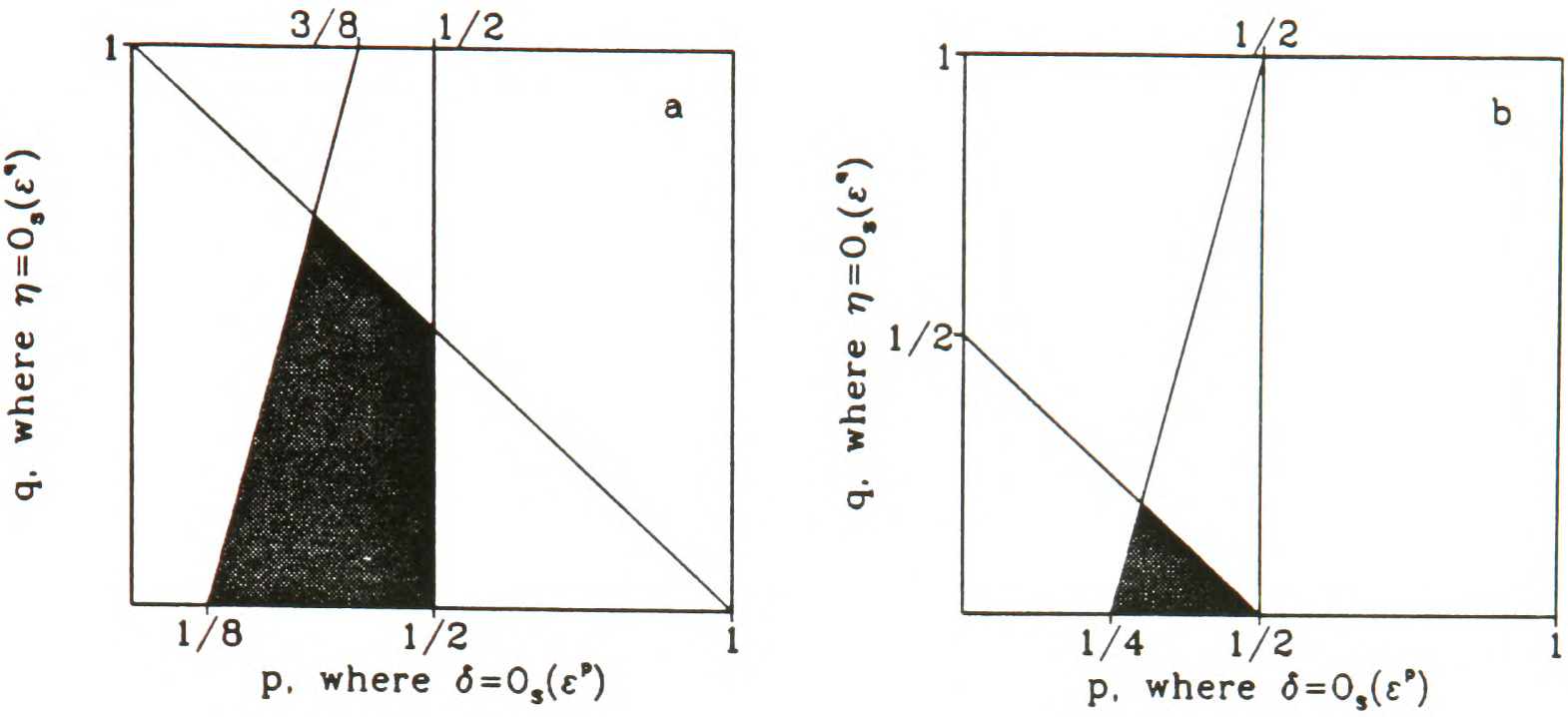

Figure 3.17: The domain of orders of magnitude of δ and η for the matching condition (3.48) to be satisfied. We are considering only orders of magnitude that are powers of ϵ, with $\delta = O_s(\epsilon^p)$, $\eta = O_s(\epsilon^q)$. The shaded region is the p–q domain such that the matching condition is satisfied, (a) for matching to $O(\sqrt{\epsilon})$, and (b) for matching to $O(\epsilon)$.

these conditions are satisfied is illustrated in Figure 3.17a. For matching to $O(\epsilon)$, the corresponding conditions are $4q > p + 1$ and $p + q < 1/2$, and the p–q domain in this case is illustrated in Figure 3.17b. The corresponding p–q domain exists, so that matching is possible, to any order that is $\gg \epsilon^{6/5}$.

We obtain a higher order composite expansion as in Section 3.5.2, giving

$$u_{comp1}(r) = \begin{cases} \tilde{u}_0(r) + \epsilon \log \epsilon \tilde{u}_l(r) + \epsilon \tilde{u}_2(r) + \epsilon u_0^*(r^*) + \epsilon^{3/2} \log \epsilon u_l^*(r^*) \\ +\epsilon^{3/2} u_1^*(r^*) - \frac{1}{2}\lambda R \zeta^2 - \frac{1}{6}\lambda^2 R^2 \zeta^3 + R\epsilon \log \epsilon \\ + \left(\frac{R^2+1}{R^2-1}\right) \zeta \epsilon \log \epsilon - 2R\epsilon \log |\zeta| - R[2 + \log(\lambda/2)]\epsilon \\ +\epsilon(6 - \frac{2}{3}\lambda R^2)\zeta \log |\zeta| - \epsilon \tilde{U}_{2,1} \zeta & r < R \\ \\ \epsilon u_0^*(r^*) + \epsilon^{3/2} \log \epsilon u_l^*(r^*) + \epsilon^{3/2} u_1^*(r^*) & r > R. \end{cases}$$

where $\zeta = r - R$. Figure 3.18 shows u_{comp1}, u_{comp0} and the numerical solution of (3.22) subject to (3.23), plotted against r, for $\epsilon = 0.03$. The higher order corrections dramatically improve the quality of the composite expansion as an approximation to the exact solution.

In addition to being an interesting problem in singular perturbation theory, the

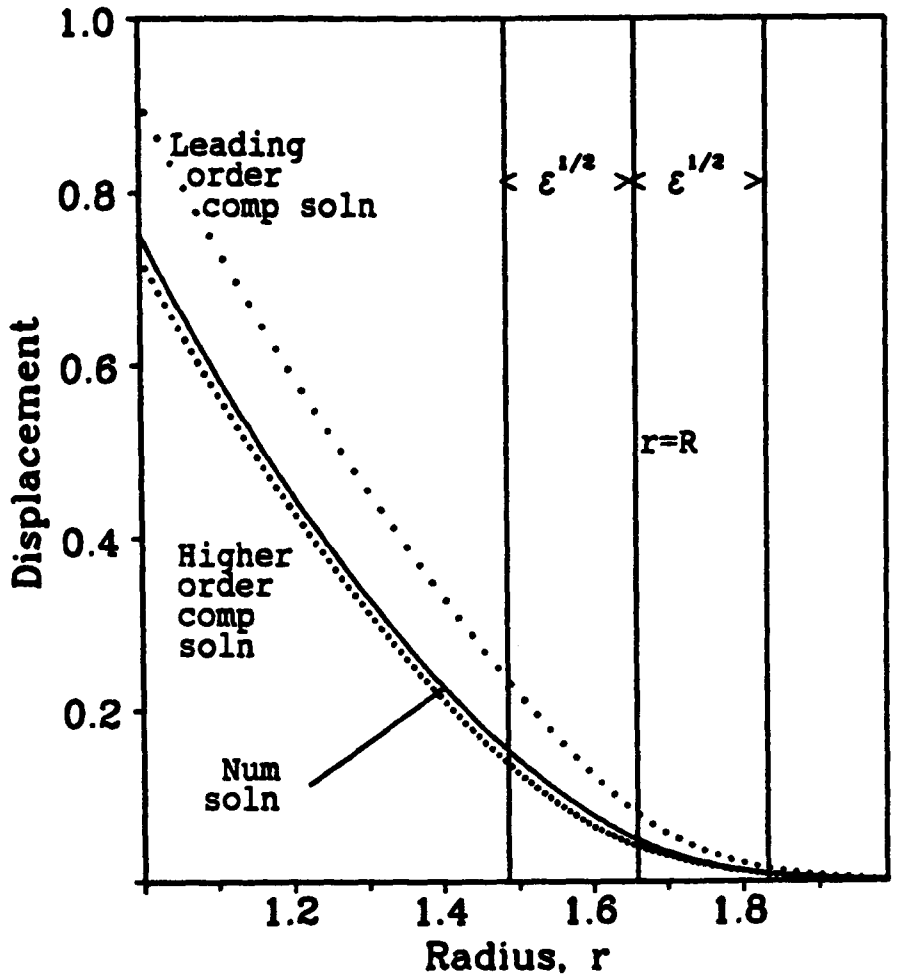

Figure 3.18: Plots of the leading order composite solution $u_{comp0}(r)$, the higher order composite solution $u_{comp1}(r)$ and the numerical solution of (3.22) subject to (3.23), against r, for $\epsilon = 0.03$, $\lambda = 4$, $T = 20$. The numerical solution was obtained using Newton iteration and deferred correction, with $u_{comp0}(r)$ as the initial approximation. To indicate the layer regions, the lines $r = R$ and $r = R \pm \sqrt{\epsilon}$ are drawn.

good analytic approximation to the solution given by this higher order composite expansion served two purposes. Firstly, it increased our understanding of the structure of this solution. In particular, the layer structure of the solution enabled us to understand various difficulties experienced in solving equation (3.22) numerically, as explained on page 96. Secondly, it provided a crucial first approximation in numerical solutions of the more biologically relevant improved model, as discussed in the next chapter.

Chapter 4

Extending the Model: the Formation of the Actin Cable

4.1 The Need for an Improved Model

In the previous chapter, we developed and analysed a basic model for the initial response of embryonic epidermis to wounding. The one-dimensional solutions compare well with experimental observations. However, numerical solutions of the model equations in a radially symmetric geometry indicate that changes are required in these equations. Specifically, as explained in Section 3.4.2, the approximation $\Delta \approx -\nabla \cdot \underline{u}$ must be improved. Here Δ is the fraction of the pre-wounding volume by which a small region of cytogel contracts in the initial response to wounding. Now when the sides of an infinitesimal rectangle are oriented along the principal axes of the local two-dimensional strain tensor $\underline{\underline{\varepsilon}}$, a deformation changes the rectangle into another rectangle. Therefore, the full expression for Δ is $1-(1+p_1)(1+p_2)$, where p_1 and p_2 are the principal values of the local two-dimensional strain tensor $\underline{\underline{\varepsilon}}$ (Segel, 1977a). In the previous chapter we used the approximation $\Delta \approx -(p_1+p_2) = -\nabla \cdot \underline{u}$, following linear elasticity theory. However, this ceases to be a valid approximation as one of the p_i's approaches -1, which occurs in the solutions presented in Section 3.4.2. We now consider the model equations with the full form for Δ, which in a radially symmetric two-dimensional geometry is $\Delta = -(u' + u/r + uu'/r)$; the one-dimensional model equations are unchanged, since then only one of the p_i's is non-zero. The linear form (3.1) for the stress tensor is still valid (Segel, 1977a), so that the radial and tangential principal components of stress are now

$$\Sigma_r = \frac{Eu' + \Gamma(u' + u/r) + 1/\left[1 + \beta(u' + u/r + uu'/r)\right]}{1 + u' + u/r + uu'/r} \tag{4.1a}$$

$$\Sigma_\theta = \frac{Eu/r + \Gamma(u' + u/r) + 1/\left[1 + \beta(u' + u/r + uu'/r)\right]}{1 + u' + u/r + uu'/r}; \tag{4.1b}$$

these replace $p(r)$ and $q(r)$ respectively in (3.12). Using (3.13), the amended dimensionless model equation is therefore

$$r\frac{d}{dr}\left[\frac{Eu' + \Gamma(u' + u/r) + 1/\left[1 + \beta(u' + u/r + uu'/r)\right]}{1 + u' + u/r + uu'/r}\right]$$

$$+ E\frac{u' - u/r}{1 + u' + u/r + uu'/r} = \frac{\lambda r u}{1 + u' + u/r + uu'/r}\,.$$

This simplifies to

$$u'' = \frac{1}{(E + \tau_2)(r + u) + \Gamma(r - u^2/r)} \cdot \left\{\lambda r u\left[1 + u' + \frac{u}{r} + \frac{uu'}{r}\right]\right.$$

$$\left. - \left(u' - \frac{u}{r}\right)\left[E\left(1 + \frac{u}{r} - u'^2 + \frac{uu'}{r}\right) + \Gamma(1 - u'^2) + \tau_2(1 + u')\right]\right\} \qquad (4.2)$$

where

$$\tau_2 = -\left[\frac{1}{1 + \beta(u' + u/r + uu'/r)} + \frac{\beta(1 + u' + u/r + uu'/r)}{\{1 + \beta(u' + u/r + uu'/r)\}^2}\right].$$

The boundary conditions are

$$Eu' + \Gamma(u' + u) + \frac{1}{1 + \beta(u' + u/r + uu'/r)} = 0 \quad \text{at} \quad r = 1 \qquad (4.3a)$$

$$u = 0 \quad \text{at} \quad r = \infty\,. \qquad (4.3b)$$

We solved this equation numerically both for $\beta = 0$ (constant traction per actin filament) and $\beta \neq 0$ (variable traction per actin filament). As in Section 3.4.2, we obtained numerical solutions using deferred correction and Newton iteration, with continuation in the parameter β. As in the one-dimensional equations investigated in Section 3.3 and also the two-dimensional solutions in Section 3.4.2, there appeared to be a critical value of β, dependent on the other parameters, above which solutions could not be obtained. Moreover, as β approached this critical upper limit, the band of aggregated actin became much sharper, so that the model solutions did reflect the phenomenon of the actin cable. However, we were unable to capture both this intense aggregation of filamentous actin at the wound edge and the more superficial aspects of the experimentally observed response to wounding, that is a retraction of the wound edges by 10–15%, with only the leading 4–5 cell layers contracted. A

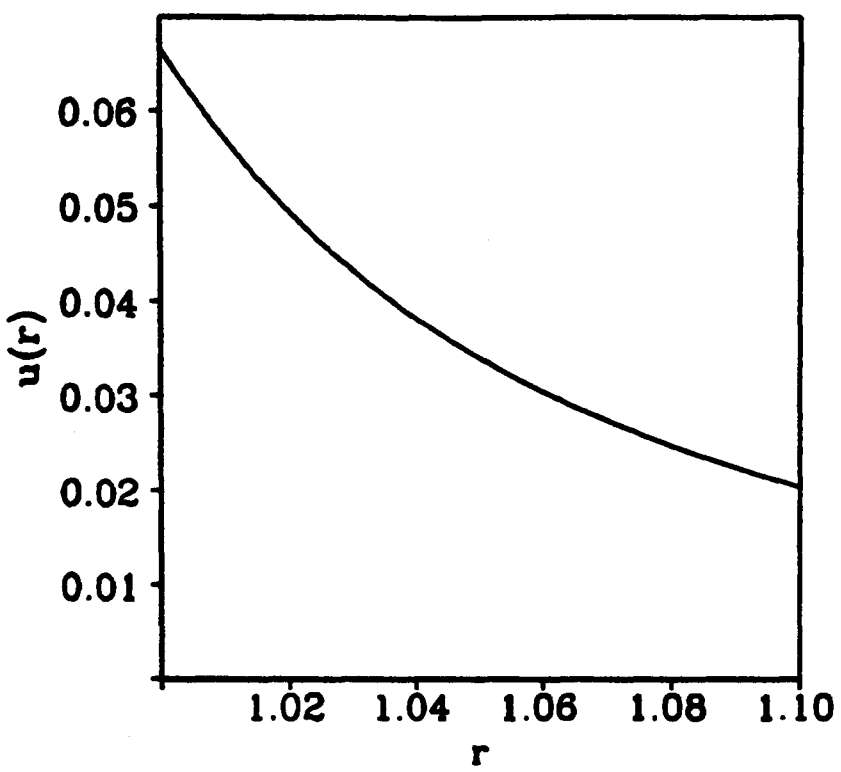

Figure 4.1: The numerical solution of (4.2) subject to (4.3) as β approaches its critical upper limit. The stopping criterion applied to the increase of β in the numerical solutions is discussed on page 140. The other parameter values are $\lambda = 3.0$, $E = 0.3$, $\Gamma = 0.8$.

typical limiting solution for $u(r)$ as β approaches its critical upper limit is illustrated in Figure 4.1.

Therefore, although the improvement in the representation of the local compaction Δ changes the precise form of the model solutions for a given set of parameter values, comparison of these solutions with experimental data still indicates that improvements are required in the model. A key aspect of the basic model (3.3) is that the representation of the filamentous actin density is scalar, so that any preferential alignment of the filaments is neglected. We now reconsider this aspect of the model.

4.2 Stress Alignment of Actin Filaments

There is considerable evidence in the biological literature that, as illustrated in Figure 4.2, when a mesh of actin fibres is subjected to a stress field, the fibres tend to align along the directions of maximum stress. The seminal paper on this topic is a study involving micromanipulation of fish epidermal cells by Kolega (1986). He found that in cytoplasm held under tension either by micromanipulation or by the

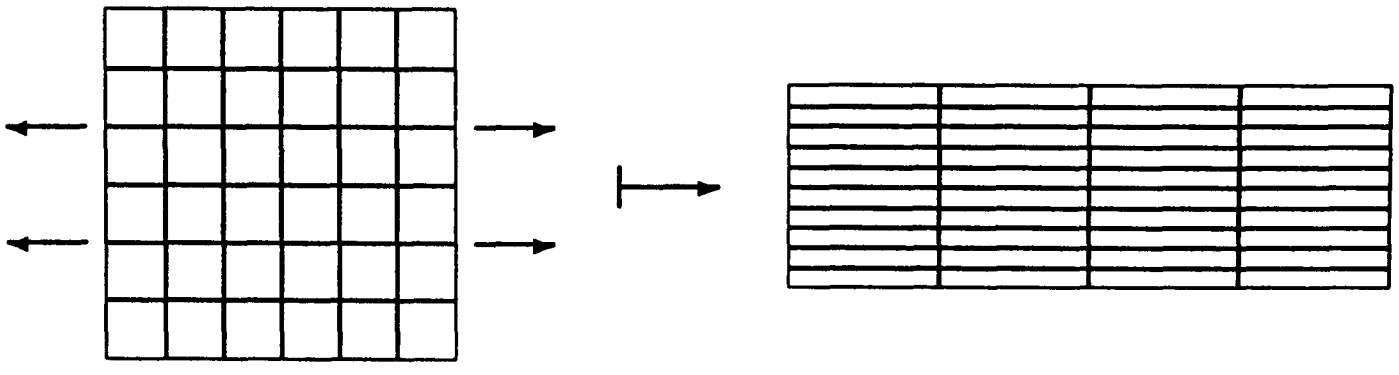

Figure 4.2: A diagrammatic representation of actin filament alignment in response to a non-isotropic stress field. The filaments tend to align along the directions of maximum stress. For clarity we show filaments oriented in two orthogonal directions only, but in the epidermis they are oriented in all directions.

locomotive activity of other cells, actin filaments were aligned parallel to the tension. Moreover, he found that when the tension was due to micromanipulation, actin filament alignment occurred within a few seconds, as a direct response to the applied tension.

In a previous but quite similar study, Chen (1981) applied micromanipulation to chick heart fibroblasts. His observations of the cytoskeleton suggest that the actin filament network is like a three-dimensional fish net under tension, oriented along directions of stress. A similar analogy is used by Kolega (1986). Chen (1981) found that upon detachment of a fibroblast tail from the substratum, with a consequent reduction of the stress in the cytoskeleton, the microfilament bundles lost their orientation and reassumed a random meshwork arrangement, over a time scale of about 15 seconds. This rearrangement was a simple reorientation, and not a disassembly and reassembly of actin filaments.

Valberg and Albertini (1985) exerted forces on pulmonary macrophages from the lungs of hamsters by causing the macrophages to ingest magnetic particles. They then applied external magnetic fields, which exerted forces on the magnetic particles present in the phagosome organelles, and thus on the cell as a whole. They observed changes in the organization of the actin filament network, resulting in prominent patches of positive staining for actin coinciding with the location of magnetic particles, aligned with the magnetic force field. Although not in the authors' conclusions, these observations suggest alignment of actin filaments along directions of stress.

Finally, there is a considerable body of literature on stress-induced alignment of "stress fibres", that is actin filament bundles, in endothelial cells under shear stress, which is an important feature of blood flow. The studies by Wechezak *et al.* (1985, 1989) are typical. In these, shear stress was applied to bovine carotid artery endothelial cells via the steady laminar flow of fluid through a cuboidal channel, one wall of which was a cell-lined coverslip. The experimental technique is described in detail by Viggers *et al.* (1986). In the 1985 study, stress was applied to confluent monolayers. Basal "stress fibres" developed, aligned with the flow direction, that is the direction of applied stress. This was in contrast to the prominent peripheral rings of actin filaments in control cells. The 1989 study concerned isolated cells. The "stress fibre" network reorganized to give a preponderance of actin at proximal (relative to the flow direction) cell margins. The authors claim that these observations support those of Kolega (1986). It should be noted that the time scale of the cytoskeletal reorganization in these studies was several hours, compared to that of a few seconds in the experiments of Chen (1981) and Kolega (1986). However, the micromanipulation and flow chamber techniques are very different, with the former unquestionably more relevant to the epithelial wound situation. Thus we treat the process of actin filament alignment in response to stress as instantaneous.

Based on the considerable biological evidence for stress alignment of actin filaments, we incorporate such alignment into our model. We are not aware of previous attempts to incorporate stress alignment of actin filaments into mechanochemical models of cytogel. This is due in part to the fact that many such models are formulated in a one-dimensional geometry, while filament alignment is an intrinsically higher-dimensional phenomenon. The reference to filament alignment in Oster and Odell (1984a) is typical: they simply state that in more than one dimension "more elastic parameters are required to account for fibre alignment".

We amend our model as follows. In a radially symmetric two-dimensional geometry, the stress tensor $\underline{\underline{\sigma}}$, defined in (3.1), has the form

$$\underline{\underline{\sigma}} = \begin{bmatrix} \Sigma_r & 0 \\ 0 & \Sigma_\theta \end{bmatrix}$$

where the principal values of stress, Σ_r and Σ_θ, are defined in (4.1). To incorporate filament alignment, we replace this with the form

$$\underline{\underline{\sigma}} = \begin{bmatrix} f(\rho)\Sigma_r & 0 \\ 0 & f(1/\rho)\Sigma_\theta \end{bmatrix} \tag{4.4}$$

where ρ is the ratio of the principal values of the amended stress tensor, that is $\rho = \sigma_{rr}/\sigma_{\theta\theta}$, and f is a function reflecting the effect of filament alignment on the mechanical properties of the actin filament network. We are assuming that the actin filament network exhibits preferential alignment in response to non-isotropic stress, to an extent which depends on the ratio of the principal values of stress. The result of this alignment is effective radial and tangential 'components' of actin filament density, given by $Gf(\rho)$ and $Gf(1/\rho)$ respectively, where G is the local 'scalar' actin filament density. The function f is subject to the following conditions:

(i) $f(0) = 0$: when the stress is unidirectional, all the filaments are aligned in its direction.

(ii) $f(1) = 1$: when the stress is isotropic, there is no preferential alignment of the filaments.

(iii) f is an increasing function.

In the absence of detailed experimental evidence for the functional form of f, we use a simple form satisfying these conditions, specifically

$$f(\rho) = \frac{(1+a)\rho}{\rho + a} \tag{4.5}$$

where a is a constant, $0 \leq a < 1$. The case $a = 0$ gives $f \equiv 1$, that is no preferential filament alignment. With this form for f, the implicit equation (4.4) can be solved for the principal values of stress, giving

$$\sigma_{rr} = \frac{1}{1-a}(\Sigma_r - a\Sigma_\theta) \tag{4.6a}$$

$$\sigma_{\theta\theta} = \frac{1}{1-a}(\Sigma_\theta - a\Sigma_r)\ . \tag{4.6b}$$

Equation (4.4) also has solutions in which one of the principal values of stress is identically zero, with the other non-zero. However, these solutions are unstable to

small perturbations in the stress field, such as could arise from movements of the underlying mesenchyme, and they are therefore not biologically relevant.

For simplicity, we have developed this improved model, which incorporates stress alignment of actin filaments, in a radially symmetric geometry only. In a more general two-dimensional geometry, the procedure is as follows. At each point in space, one must rotate the local coordinate axes so that they are aligned with the principal axes of the stress tensor $\underline{\underline{\sigma}}$, defined in (3.1). These principal axes are orthogonal since $\underline{\underline{\sigma}}$ is symmetric. In this new coordinate system $\underline{\underline{\sigma}}$ has the form

$$\underline{\underline{\sigma}} = \begin{bmatrix} \Sigma_1 & 0 \\ 0 & \Sigma_2 \end{bmatrix},$$

say. To incorporate filament alignment, we replace this by

$$\underline{\underline{\sigma}} = \begin{bmatrix} f(\sigma_{11}/\sigma_{22})\Sigma_1 & 0 \\ 0 & f(\sigma_{22}/\sigma_{11})\Sigma_2 \end{bmatrix},$$

where σ_{11}, σ_{22} are the diagonal entries in this amended stress tensor. Having solved these implicit equations for σ_{11} and σ_{22}, one must then rotate the local coordinate axes back to their original orientations. A key aspect of this procedure is that the 'original' and 'improved' stress tensor have the same principal axes, though the principal values are different. In the radially symmetric geometry considered above, this procedure is particularly simple since at each point the principal axes of $\underline{\underline{\sigma}}$ are just the $\underline{\hat{r}}$ and $\underline{\hat{\theta}}$ axes. Application of filament alignment in another simple geometry is considered in Section 4.3.1.

We consider the implications of $a \neq 0$ for the solutions of the governing equation (3.2) in a radially symmetric geometry in the next section. In the remainder of this section we make the form taken for f in (4.5) more plausible by applying heuristic arguments on the structure of the actin filament network at a more fundamental level. For clarity, we again develop this argument in the context of a radially symmetric geometry, though it is completely general.

4.2.1 A detailed model of filament alignment

We model the actin filament network in detail via the density function $F(\phi;\rho)$, defined by the condition that $F(\phi;\rho)\delta\phi$ is the continuum average of the proportion of the actin filaments inclined to the $\hat{\underline{r}}$ axis at angles in the range $(\phi, \phi+\delta\phi)$, when $\sigma_{rr}/\sigma_{\theta\theta} = \rho$. Thus F is also a function of space, but since all our calculations will be at a single point in space, we do not include $\underline{r}$ as an argument of F, for notational simplicity. We restrict ϕ to lie in $[0, \pi/2]$, since filaments inclined at positive and negative angles are equivalent for our purposes. Then resolving in the $\hat{\underline{r}}$ direction, we have

$$f(\rho) = f_0 \int_0^{\pi/2} F(\phi;\rho)\cos\phi\, d\phi \tag{4.7}$$

where f_0 is a constant. The condition $f(1) = 1$ implies that

$$f_0 = \left[\int_0^{\pi/2} F(\phi;1)\cos\phi\, d\phi\right]^{-1}.$$

Again, there is no detailed experimental evidence for the functional form of F, but there are a number of fairly restrictive conditions that it must satisfy:

(a) $F(\phi;\rho) \to \delta(\pi/2-\phi)$ as $\rho \to 0$ and $F(\phi;\rho) \to \delta(\phi)$ as $\rho \to \infty$, where δ denotes the Dirac delta function. That is, when $\sigma_{\theta\theta} = 0$, all filaments are oriented radially, and when $\sigma_{rr} = 0$, all filaments are oriented tangentially. This implies that the requirement $f(0) = 0$ is satisfied.

(b) $\int_0^{\pi/2} F(\phi;\rho)\, d\phi = 1$, since F is a density function. Thus the total number of fibres is unchanged by the process of stress alignment.

(c) $F(\phi;1)$ is a constant. That is, when the stress field is isotropic the filaments are oriented randomly. Condition (b) implies that the value of this constant is $2/\pi$, so that $f_0 = \pi/2$. The requirement $f(1) = 1$ is then satisfied.

(d) $F(\phi;\rho) = F(\pi/2-\phi;1/\rho)$, by symmetry.

Considering these conditions, we take

$$F(\phi;\rho) = F_0(\rho)\left[\frac{1}{\psi(\rho)}\exp\left\{-\frac{k(\pi/2-\phi)^2}{\psi(\rho)^2}\right\} + \psi(\rho)\exp\left\{-k\psi(\rho)^2\phi^2\right\}\right] \tag{4.8}$$

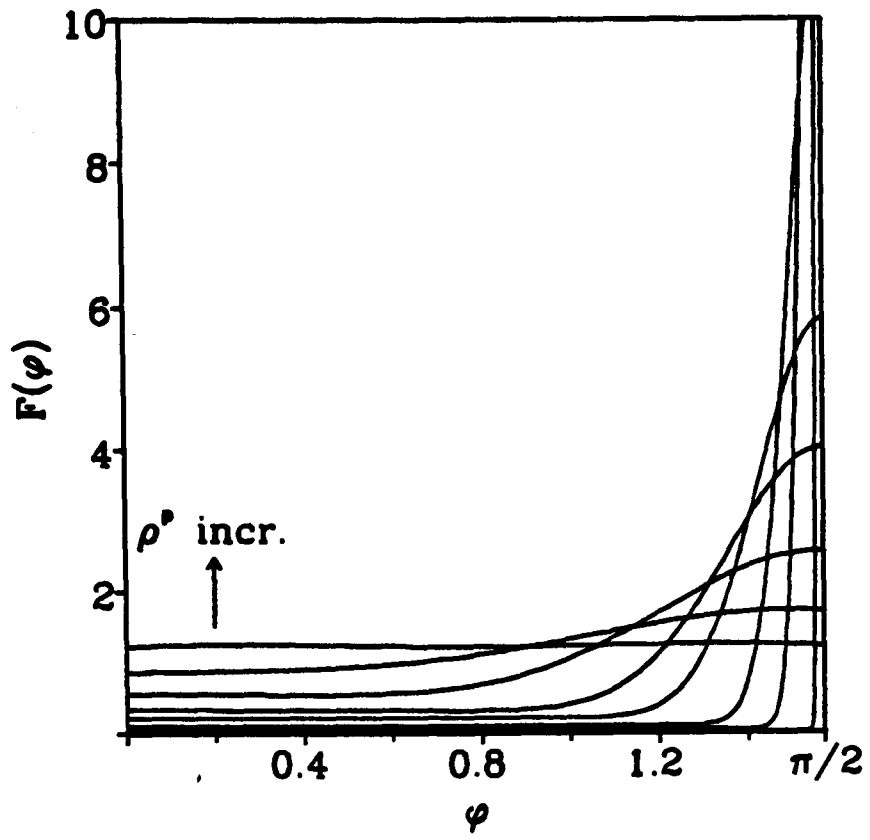

Figure 4.3: The form of $F(\phi;\rho)$, defined in (4.8), plotted as a function of ϕ, for $\rho^p = 0.01$, 0.05, 0.1, 0.2, 0.3, 0.5, 0.75, 1.0; $F(0;\rho)$ increases with ρ^p.

where k is a positive constant and $\psi(0) = 0$, $\psi(1) = 1$ and $\psi(\infty) = \infty$. $F_0(\rho)$ is chosen such that condition (b) is satisfied. The form (4.8) satisfies condition (a), since the Dirac delta function satisfies

$$\delta(x) = \lim_{\varepsilon \to 0} \frac{1}{\varepsilon\sqrt{\pi}} \exp\left(-x^2/\varepsilon^2\right)$$

(see, for example, Courant and Hilbert, 1962). Further, if we take $\psi(\rho) = \rho^p$ for some $p > 0$ then condition (d) is satisfied.

It remains to consider condition (c), which is equivalent to the condition that

$$g(\phi) = \exp\left[-k\phi^2\right] + \exp\left[-k(\pi/2 - \phi)^2\right] \tag{4.9}$$

is constant on $0 \leq \phi \leq \pi/2$. While this does not hold exactly for any non-zero value of k, it is approximately true for values of k close to 1. We choose k to minimize the variation of $g(\phi)$ on $[0, \pi/2]$, and we show below that this gives $k \approx 0.988$. The variation of $g(\phi)$ on $[0, \pi/2]$ is then less than 3%.

$F(\phi;\rho)$ is plotted in Figure 4.3 as a function of ϕ for a range of values of ρ^p in $[0, 1]$; the parameter p remains undetermined. The form for $f(\rho)$ implied by this function F is shown in Figure 4.4, in which we plot both $f(\rho)$ and $f(1/\rho)$ against ρ^p for $0 \leq \rho \leq 1$.

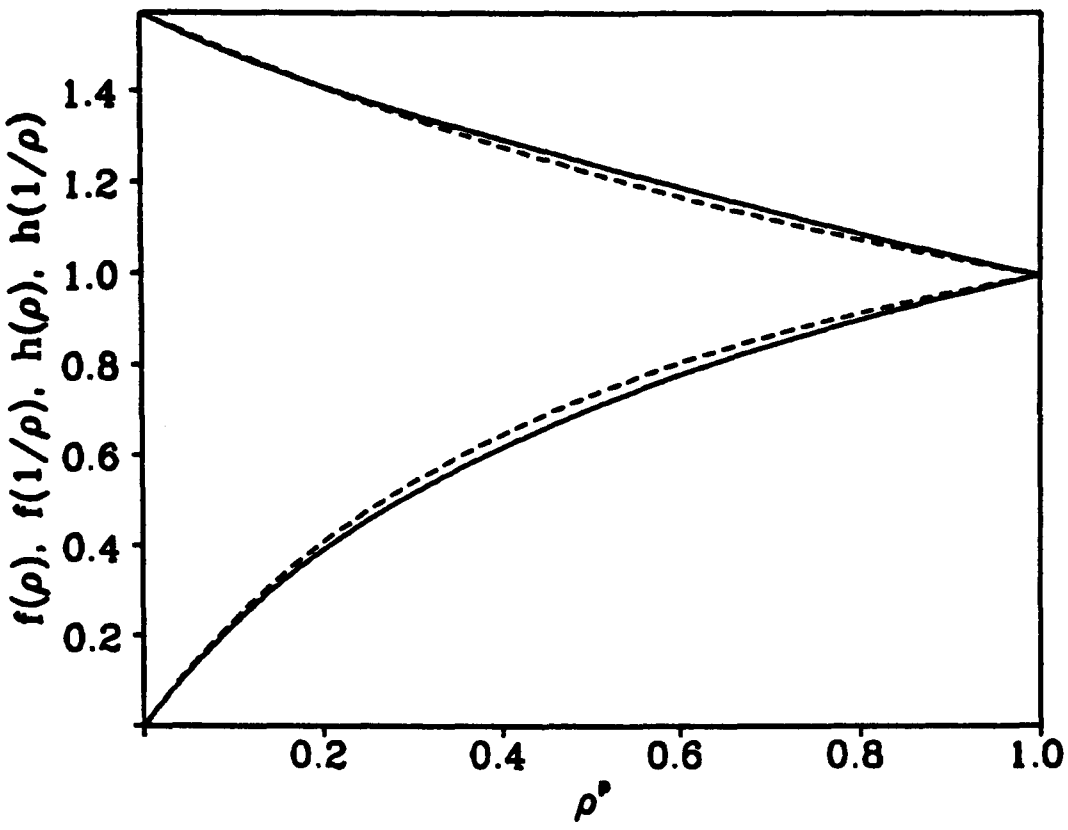

Figure 4.4: The functions $f(\rho)$ (full curve) and $h(\rho)$ (dashed curve) plotted against ρ^p. Here $h(\rho) = (1+a)\rho^p/(\rho^p + a)$, and the form of $f(\rho)$ is that defined in terms of $F(\phi;\rho)$ in (4.7), with $F(\phi;\rho)$ defined in (4.8). Rather than plotting on $[0,\infty)$, we plot both $f(\rho)$ and $f(1/\rho)$, and $h(\rho)$ and $h(1/\rho)$, on $[0,1]$. The close approximation of $h(\rho)$ to $f(\rho)$ justifies the form given for $f(\rho)$ in (4.5), and predicts the value of the constant a as $(\pi/2-1)$.

These functions were calculated by evaluating the integral in (4.7) numerically for a range of values of ρ^p. In Figure 4.4 we also plot $h(\rho) = (1+a)\rho^p/(\rho^p+a)$ and $h(1/\rho)$ against ρ^p, with a chosen such that $h(\infty) = f(\infty)$. Specifically, (4.7) and properties (a) and (c) of $F(\phi;\rho)$ together imply that

$$f(\infty) = \int_0^{\pi/2} \frac{\pi}{2}\delta(\phi)\cos\phi\, d\phi\,,$$

so that $a = \pi/2 - 1$. This value of a is independent of p. Thus

$$h(\rho) = (\pi/2)\rho^p/(\rho^p + \pi/2 - 1)\,. \tag{4.10}$$

It is clear from Figure 4.4 that to a good approximation, the form (4.8) for $F(\phi;\rho)$ implies that

$$f(\rho) = \frac{(\pi/2)\rho^p}{\rho^p + \pi/2 - 1}\,. \tag{4.11}$$

If we choose $p = 1$ for algebraic simplicity, this is the form given in (4.5), with $a = \pi/2 - 1$. Until relevant experimental data is available, it is inappropriate to take more complicated functional forms.

4.2.2 The value of k

We now determine the value of k, not near zero, that minimizes the variation of $g(\phi)$, defined in equation (4.9), on $0 \leq \phi \leq \pi/2$. (Trivially, $g(\phi) \equiv 2$ when $k = 0$, but this case is not biologically relevant). The form of $g(\phi)$ for a selection of values of k is shown in Figure 4.5. Differentiating (4.9) with respect to ϕ gives

$$\frac{dg}{d\phi} = 2ke^{-k\phi^2}(\pi/2 - \phi)\left[\exp\{k\pi(\phi - \pi/4)\} - \frac{\phi}{\pi/2 - \phi}\right].$$

Therefore

$$\frac{dg}{d\phi} = 0 \quad \Longleftrightarrow \quad \exp\{k\pi(\phi - \pi/4)\} = \frac{\phi}{\pi/2 - \phi}. \tag{4.12}$$

It is sufficient to consider this equation on $[0, \pi/4]$, by the symmetry of $g(\phi)$ about $\phi = \pi/4$. The two sides of (4.12) are plotted in Figure 4.6 for a range of values of k. From this, it is clear that in addition to the root at $\phi = \pi/4$, equation (4.12) has a second root in $(0, \pi/4)$ if $k > k_{crit1}$, where k_{crit1} satisfies

$$\frac{d}{d\phi}\left[\exp\{k\pi(\phi - \pi/4)\} - \frac{\phi}{\pi/2 - \phi}\right]\Bigg|_{\phi=\pi/4} = 0.$$

This uniquely determines k_{crit1} as $8/\pi^2$, ≈ 0.81.

We now write

$$g_{max}(k) = \max_{0\leq\phi\leq\pi/2} g(\phi) \quad \text{and} \quad g_{min}(k) = \min_{0\leq\phi\leq\pi/2} g(\phi).$$

By symmetry these are also the maximum and minimum values respectively on $[0, \pi/4]$. Then for $k < k_{crit1}$,

$$\begin{aligned} g_{max}(k) &= g(\pi/4) = 2e^{-k\pi^2/16} \\ \text{and} \quad g_{min}(k) &= g(0) \quad = 1 + e^{-k\pi^2/4}. \end{aligned}$$

For $k > k_{crit1}$, $g_{max}(k) = g(\phi_{max})$, where ϕ_{max} is the unique solution of

$$\exp\{k\pi(\phi - \pi/4)\} = \frac{\phi}{\pi/2 - \phi}$$

in the open interval $(0, \pi/4)$. This cannot be found analytically, but can easily be calculated numerically for a given value of k. Also, for $k > k_{crit1}$, $g_{min}(k) =$

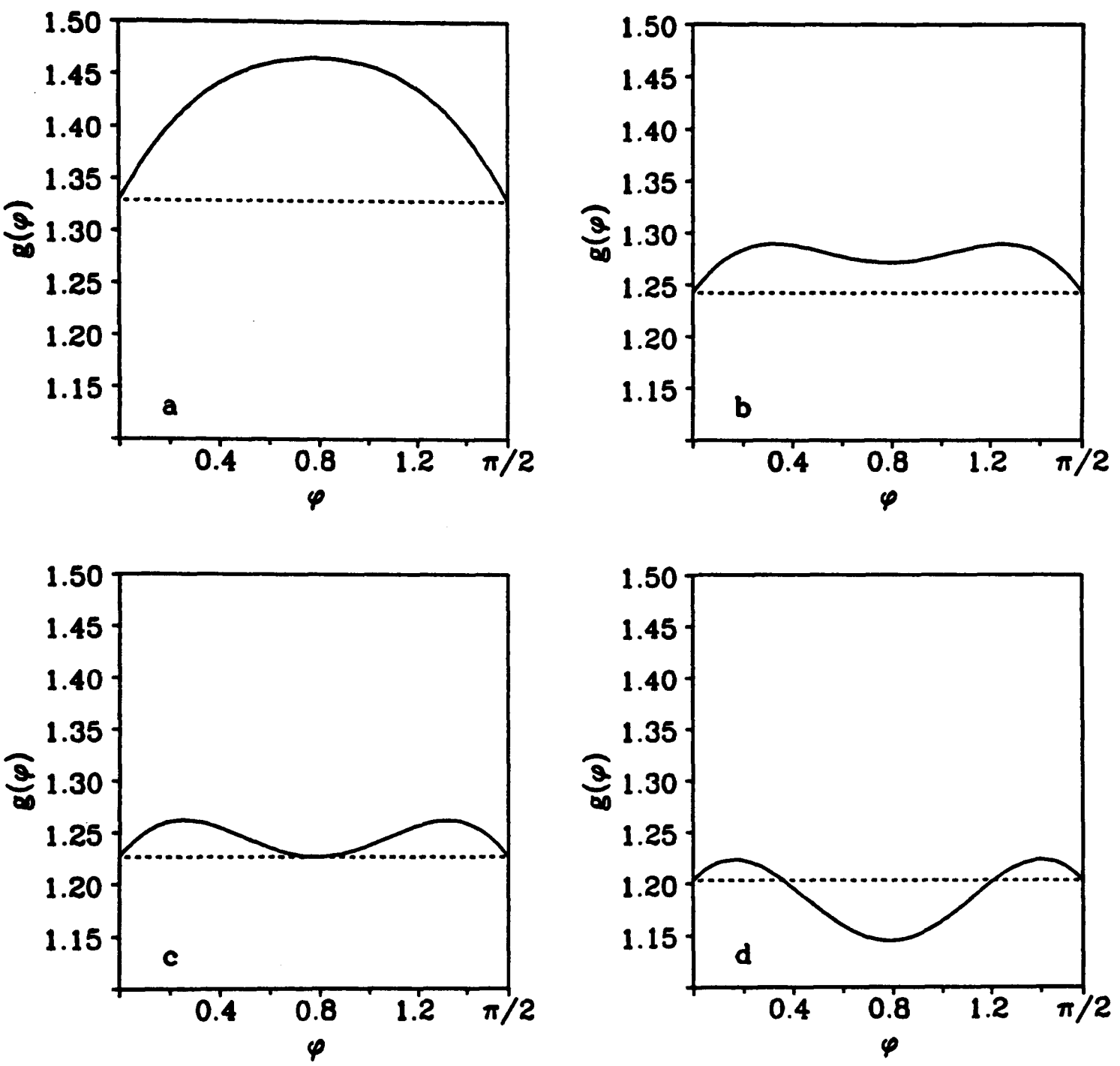

Figure 4.5: The form of the function $g(\phi)$, defined in (4.9), as the parameter k varies. (a) $k = 0.7$; (b) $k = 0.93$; (c) $k = k_{crit2} \approx 0.988$ (see page 130); (d) $k = 1.1$. The dashed line indicates the equal values of $g(0)$ and $g(\pi/2)$.

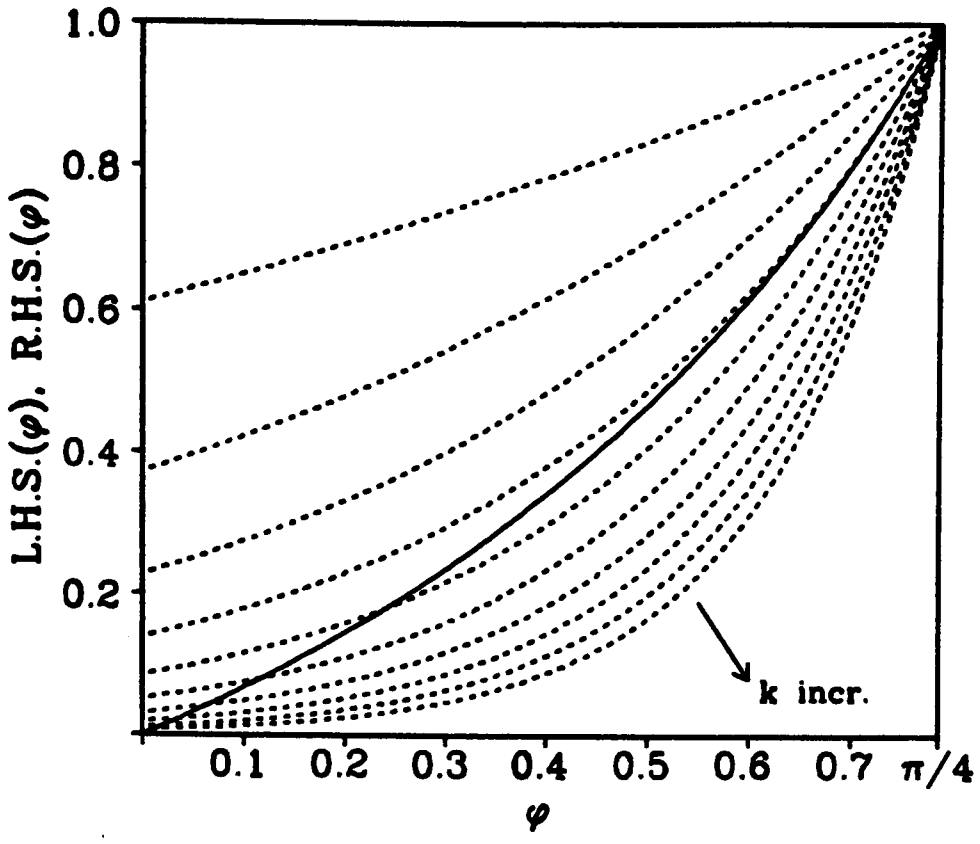

Figure 4.6: The right-hand (full curve) and left-hand (dashed curves) sides of equation (4.12) for k =0.2, 0.4, 0.6,...,2.0; the value of the left-hand side decreases, for any given ϕ, as k increases. The number of solutions of the equation on $[0, \pi/4]$ increases from one to two as k increases through a critical value, k_{crit1}.

$\min\{g(0), g(\pi/4)\}$. It is clear from Figure 4.5 that there is a critical value k_{crit2} such that

$$\text{for } k_{crit1} < k < k_{crit2}\,, \quad g(0) < g(\pi/4), \qquad \text{so that } g_{min}(k) = 1 + e^{-k\pi^2/4}$$
$$\text{and for } k > k_{crit2}\,, \quad g(0) > g(\pi/4), \qquad \text{so that } g_{min}(k) = 2e^{-k\pi^2/16}\,.$$

Here k_{crit2} satisfies $g(0) = g(\pi/4)$, that is

$$1 + e^{-k\pi^2/4} = 2e^{-k\pi^2/16}\,.$$

Thus $k_{crit2} = -(16/\pi^2)\log x$, where x is a solution of $x^4 - 2x + 1 = 0$. Now

$$x^4 - 2x + 1 = (x-1)(x^3 + x^2 + x - 1)\,.$$

The root $x = 1$ corresponds to the trivial case of $g(\phi) \equiv 2$ when $k = 0$. The cubic equation has the form

$$4\gamma^3 + 3\gamma = \frac{17}{2\sqrt{2}} \quad \text{where } \gamma = \frac{3}{2\sqrt{2}}\left(x + \frac{1}{3}\right)\,.$$

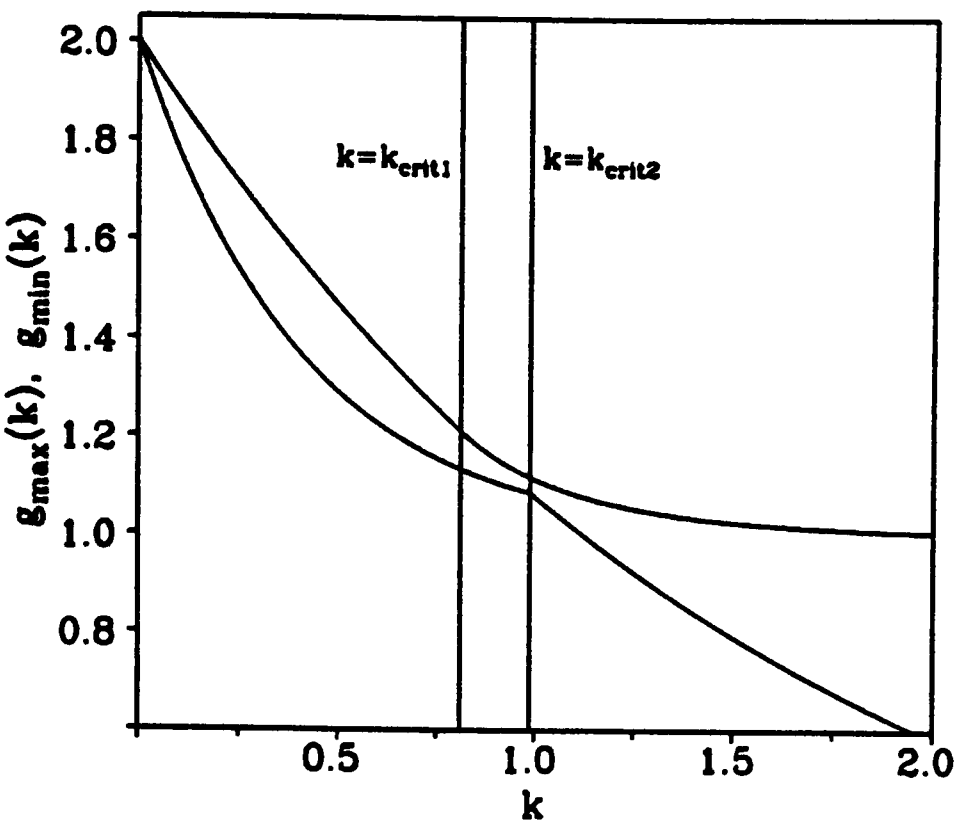

Figure 4.7: The maximum and minimum values of $g(\phi)$ on $[0, \pi/2]$, $g_{max}(k)$ and $g_{min}(k)$, plotted as functions of the parameter k. The vertical lines $k = k_{crit1}$ and $k = k_{crit2}$ are also drawn.

We now substitute $\gamma = \sinh \xi$, which gives a 1–1 correspondence between γ and ξ. Using the identity

$$\sinh 3\xi = 4 \sinh^3 \xi + 3 \sinh \xi$$

this gives

$$\xi = \frac{1}{3} \sinh^{-1} \left(\frac{17}{2\sqrt{2}} \right) ,$$

so that the cubic equation has a unique solution, and

$$k_{crit2} = -\frac{16}{\pi^2} \log \left\{ \frac{2\sqrt{2}}{3} \sinh \left[\frac{1}{3} \sinh^{-1} \left(\frac{17}{2\sqrt{2}} \right) \right] - \frac{1}{3} \right\} \approx 0.987886 .$$

In Figure 4.7 we plot $g_{max}(k)$ and $g_{min}(k)$ as functions of k. These suggest that the variation of $g(\phi)$ is minimized when $k = k_{crit2}$, and this is confirmed by numerical minimization using quadratic interpolation. Specifically, numerical calculations show that both $[g_{max}(k) - g_{min}(k)]$ and $[g_{max}(k) - g_{min}(k)]/[g_{max}(k) + g_{min}(k)]$ are minimized at $k = k_{crit2}$, for k not near zero. (Trivially, $g_{max}(k) = g_{min}(k)$ when $k = 0$, since then $g(\phi) \equiv 2$). Thus the variation of $g(\phi)$ on $0 \leq \phi \leq \pi/2$ is minimized in both an absolute and relative sense when $k = k_{crit2}$.

4.3 Solutions of the Improved Model

4.3.1 One-dimensional solutions

To incorporate the concept of filament alignment into the one-dimensional model equations, we consider a two-dimensional epithelial sheet in cartesian coordinates, with no variation in the y-direction. The dimensionless stress tensor $\underline{\underline{\sigma}}$, without inclusion of stress alignment of actin filaments, is then given by

$$\underline{\underline{\sigma}} = \begin{bmatrix} G\left\{(E+\Gamma)u_x + \frac{1}{1+\beta u_x}\right\} & 0 \\ 0 & G\left\{\Gamma u_x + \frac{1}{1+\beta u_x}\right\} \end{bmatrix}$$

where $G = 1/(1+u_x)$ is the scalar actin filament density. The procedure for incorporating actin alignment in a general two-dimensional geometry was explained on page 123; in this case it is particularly simple since at all points the principal axes of $\underline{\underline{\sigma}}$ are aligned with the coordinate axes. Thus the diagonal components of the 'improved' stress tensor satisfy

$$\begin{aligned} \sigma_{xx} &= f(\sigma_{xx}/\sigma_{yy}) \cdot G\left[(E+\Gamma)u_x + \frac{1}{1+\beta u_x}\right] \\ \sigma_{yy} &= f(\sigma_{yy}/\sigma_{xx}) \cdot G\left[\Gamma u_x + \frac{1}{1+\beta u_x}\right]. \end{aligned}$$

Using the functional form for f in (4.5), this implies

$$\begin{aligned} \sigma_{xx} &= G\left[\Gamma u_x + \frac{1}{1+\beta u_x} + \frac{E u_x}{1-a}\right] \\ \sigma_{yy} &= G\left[\Gamma u_x + \frac{1}{1+\beta u_x} - \frac{a E u_x}{1-a}\right]. \end{aligned}$$

Substituting these into the governing equation $\nabla \cdot \underline{\underline{\sigma}} = \lambda G \underline{u}$ gives

$$\frac{d}{dx}\left[\frac{1}{1+u_x}\left\{\left(\frac{E}{1-a}+\Gamma\right)u_x + \frac{1}{1+\beta u_x}\right\}\right] - \frac{\lambda}{1+u_x}u = 0.$$

The boundary condition at the wound edge ($x = 0$, say) is $\sigma_{xx} = 0$, that is

$$\left(\frac{E}{1-a}+\Gamma\right)u_x + \frac{1}{1+\beta u_x} = 0 \qquad \text{at} \quad x = 0;$$

the boundary condition at $x = \infty$ remains $u = 0$. This system, which is in fact independent of the form of σ_{yy}, differs from (3.5) subject to (3.6) only in E being replaced by $E/(1-a)$. Therefore, the analytical and numerical investigation in Section 3.3 remains valid if we reinterpret $\hat{E}$ as $E/(1-a)+\Gamma$.

4.3.2 Two-dimensional radially symmetric solutions

The relations (4.1) and (4.6) together imply that in a radially symmetric geometry, the non-zero components of the dimensionless stress tensor incorporating stress alignment of actin filaments are

$$\sigma_{rr} = \frac{E(u' - au/r)/(1-a) + \Gamma(u' + u/r) + 1/[1 + \beta(u' + u/r + uu'/r)]}{1 + u' + u/r + uu'/r} \quad (4.13a)$$

$$\sigma_{\theta\theta} = \frac{E(u/r - au')/(1-a) + \Gamma(u' + u/r) + 1/[1 + \beta(u' + u/r + uu'/r)]}{1 + u' + u/r + uu'/r} . \quad (4.13b)$$

Substituting these into the governing equation $\nabla \cdot \underline{\underline{\sigma}} = \lambda G \underline{u}$ and using the expression for the divergence of a tensor in plane polar coordinates given in (3.13) gives

$$r\frac{d}{dr}\left[\frac{\frac{E}{1-a}(u' - au/r) + \Gamma(u' + u/r) + 1/[1 + \beta(u' + u/r + uu'/r)]}{1 + u' + u/r + uu'/r}\right]$$

$$+ E\left(\frac{1+a}{1-a}\right)\left(\frac{u' - u/r}{1 + u' + u/r + uu'/r}\right) = \frac{\lambda r u}{1 + u' + u/r + uu'/r} . \quad (4.14)$$

Note that the substratum adhesion term is proportional to the scalar actin filament density, and is unaffected by stress alignment of the actin filaments. Expanding (4.14) gives

$$r\left(1 + u' + \frac{u}{r} + \frac{uu'}{r}\right)\left[\bar{E}\left(u'' - \frac{au'}{r} + \frac{au}{r^2}\right) - \Gamma\left(\frac{uu''}{r} + \frac{u'^2}{r} - \frac{uu'}{r^2}\right)\right]$$

$$-r\left(u'' + \frac{u'}{r} - \frac{u}{r^2} + \frac{uu''}{r} + \frac{u'^2}{r} - \frac{uu'}{r^2}\right)\left[\bar{E}\left(u' - \frac{au}{r}\right) - \Gamma\left(1 + \frac{uu'}{r}\right)\right.$$

$$\left. + \frac{1 + \beta + 2\beta(u' + u/r + uu'/r)}{[1 + \beta(u' + u/r + uu'/r)]^2}\right] + \bar{E}(1+a)\left(u' - \frac{u}{r}\right) \cdot$$

$$\left(1 + u' + \frac{u}{r} + \frac{uu'}{r}\right) = \lambda r u \left(1 + u' + \frac{u}{r} + \frac{uu'}{r}\right) ,$$

where $\bar{E} = E/(1-a)$. Writing

$$\Psi = \frac{a\bar{E}u}{r} - \frac{1 + \beta + 2\beta(u' + u/r + uu'/r)}{[1 + \beta(u' + u/r + uu'/r)]^2} ,$$

this simplifies to

$$u'' = \frac{1}{(\bar{E} + \Psi)(r + u) + \Gamma(r - u^2/r)} \cdot \left\{\lambda r u \left[1 + u' + \frac{u}{r} + \frac{uu'}{r}\right]\right.$$

$$\left. - \left(u' - \frac{u}{r}\right)\left[\bar{E}\left(1 + \frac{u}{r} - u'^2 + \frac{uu'}{r}\right) + \Gamma(1 - u'^2) + \Psi(1 + u')\right]\right\} . \quad (4.15)$$

The boundary conditions are $\sigma_{rr} = 0$ at $r = 1$, the wound edge, and $u = 0$ at $r = \infty$. Using (4.13a) and simplifying, the boundary conditions become

$$\bar{E}(u' - au) + \Gamma(u' + u) + \frac{1}{1 + \beta(u' + u/r + uu'/r)} = 0 \quad \text{at} \quad r = 1 \qquad (4.16a)$$

$$u = 0 \quad \text{at} \quad r = \infty. \qquad (4.16b)$$

We solved (4.15) subject to (4.16) numerically, using continuation in β. That is, we gradually increased β, using the solution for the previous β as the initial approximation at each stage. The solution for $\beta = 0$ was obtained using the solution for $\beta = a = 0$ as the initial approximation; numerical determination of this latter solution was discussed in Section 4.1. As in both the one-dimensional solutions investigated in Sections 3.3 and 4.3.1, and the two-dimensional solutions without filament alignment, presented in Section 4.1, there appeared to be a critical upper limit on the value of β, above which solutions could not be obtained. Moreover, as β approached this critical upper limit, β_{crit} say, the band of aggregated actin at the wound edge became sharper, so that the model solutions did reflect the phenomenon of the actin cable. However, in contrast to solutions in the absence of filament alignment, we were able to capture both this phenomenon and the more superficial aspects of the response to wounding observed experimentally, that is a retraction of the wound edges by 10-15%, with only the leading 4–5 cell layers significantly contracted. Such a solution is illustrated in Figure 4.8. In previous illustrations of model solutions, we have plotted the scalar actin filament density $G(r)$. However, for this improved model, more relevant functions are the effective dimensionless densities of filamentous actin aligned radially and tangentially. These are $G_r(r) = f(\sigma_{rr}/\sigma_{\theta\theta}) \cdot G(r)$ and $G_\theta(r) = f(\sigma_{\theta\theta}/\sigma_{rr}) \cdot G(r)$ respectively. Using (4.13), these are

$$G_r = G(r)\frac{\Gamma(u' + u/r) + 1/[1 + \beta(u' + u/r + uu'/r)] + \bar{E}(u' - au/r)}{\Gamma(u' + u/r) + 1/[1 + \beta(u' + u/r + uu'/r)] + (1 - a)\bar{E}u'} \qquad (4.17a)$$

$$G_\theta = G(r)\frac{\Gamma(u' + u/r) + 1/[1 + \beta(u' + u/r + uu'/r)] + \bar{E}(u/r - au')}{\Gamma(u' + u/r) + 1/[1 + \beta(u' + u/r + uu'/r)] + (1 - a)\bar{E}u/r} \qquad (4.17b)$$

where $G(r) = 1/(1 + u' + u/r + uu'/r)$. The parameter values λ, E, Γ and a used in Figure 4.8 are consistent with the biologically relevant one-dimensional solutions discussed in Section 3.3, since we are interpreting $\hat{E} = \bar{E} + \Gamma$. However, the value of

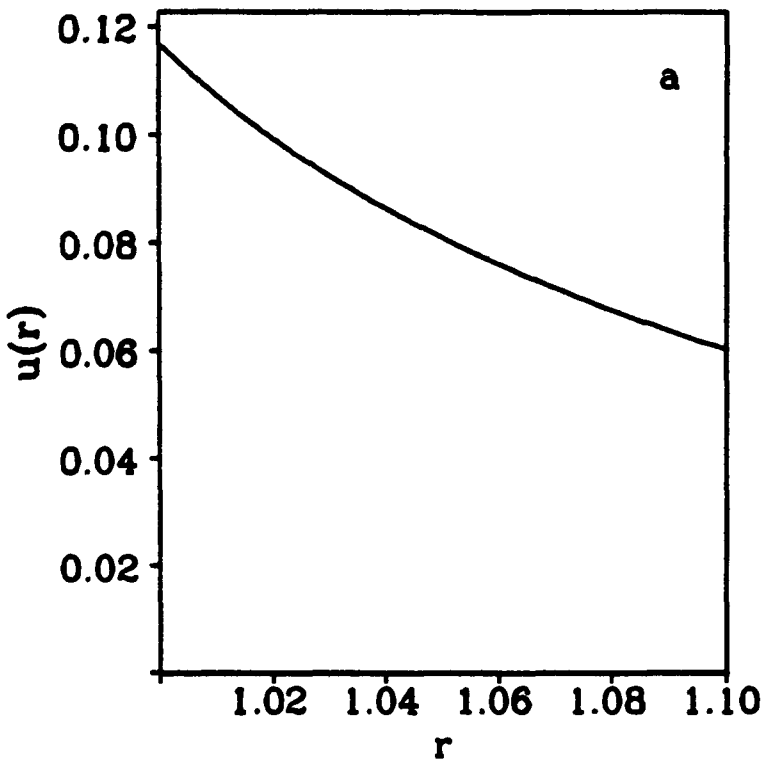

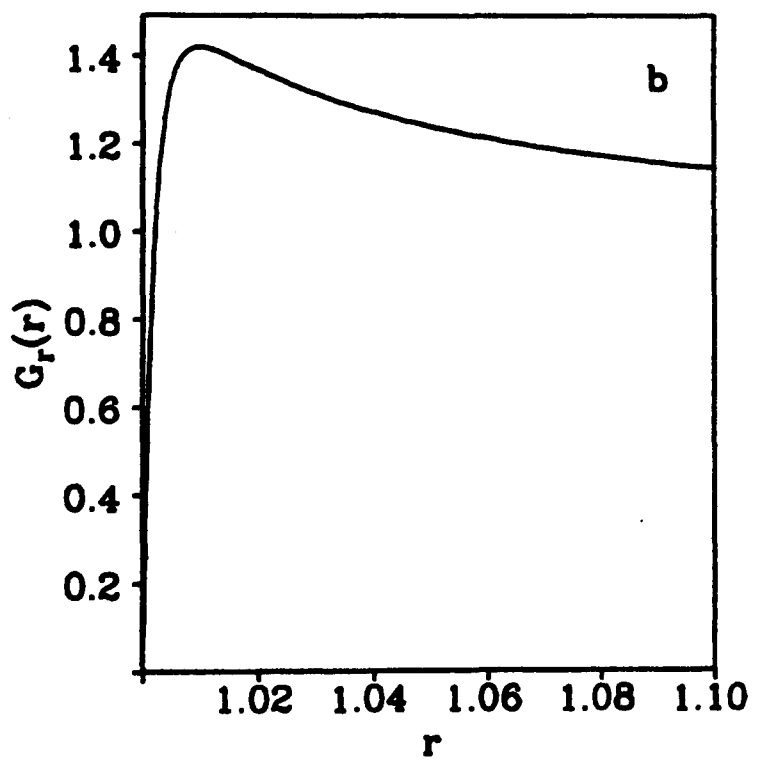

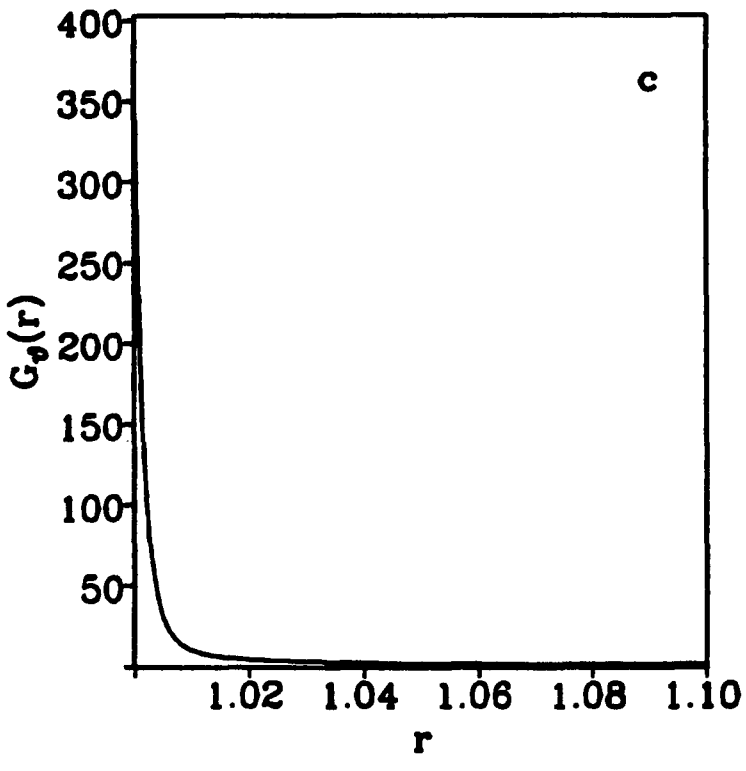

Figure 4.8: (a) The numerical solution of (4.15) subject to (4.16). (b,c) The corresponding effective radially and tangentially aligned dimensionless actin filament densities G_r and G_θ, defined in (4.17). The parameter values are $\lambda = 3.0$, $E = 0.3$, $\Gamma = 0.8$, $\beta = 0.31$, $a = \pi/2 - 1$; this value of the filament alignment parameter a is that predicted by the heuristic model of the actin filament network (see Section 4.2). This solution captures the key aspects of the experimentally observed response of the epidermis to wounding.

β is significantly smaller than in the one-dimensional geometry, as explained in the next section.

4.4 The Critical Upper Limit on β

Numerical solutions of the model suggest that for given values of λ, E, Γ and a, the value of the critical upper limit β_{crit} on the value of the parameter β is different in the one-dimensional and two-dimensional radially symmetric geometries. While we have been unable to derive an exact analytical expression for β_{crit} in the latter case, we have obtained an analytic approximation that is valid for large λ. As explained in Section 4.5, biologically relevant solutions certainly require $\lambda > 1$.

Recall that the nondimensionalization we have used implies that the dimensionless parameter $\lambda = \Lambda R^2$, where R is the dimensional wound radius, and the dimensional quantity Λ is the ratio of the dimensional parameters λ^{dim} and τ_0. But in the limit $R \to \infty$, the radially symmetric geometry approaches the one-dimensional geometry, in which the critical upper limit on β is $[1 - 1/(\bar{E} + \Gamma)]$ (see Section 3.3). Thus as $\lambda \to \infty$, $\beta_{crit} = 1 - 1/(\bar{E} + \Gamma) + o(1)$. Here λ denotes the dimensionless parameter.

The one-dimensional equations were analysed fully in Section 3.3, and we showed there that as $\beta \to 1 - 1/(\bar{E} + \Gamma)$, $u_x\,|_{w.e.} \to -1$. Here '$|_{w.e.}$' denotes 'at the wound edge'. Recalling (3.7), that $\frac{1}{2}\lambda u^2 = P(u_x)$ in one dimension, the displacement at the wound edge in this limiting case is given by

$$\begin{aligned} u\,|_{w.e.} &= \sqrt{2P(-1)/\lambda} \\ &= \left[\frac{2}{\lambda} \cdot \frac{2-\beta}{\beta(1-\beta)} \left\{ -\log(1-\beta) - \frac{2\beta}{2-\beta} \right\}\right]^{1/2} \Bigg|_{\beta = 1 - 1/(\bar{E}+\Gamma)} \\ &= \left[\frac{2}{\lambda} \left\{ \frac{(\bar{E}+\Gamma)(\bar{E}+\Gamma+1)}{(\bar{E}+\Gamma-1)} \log(\bar{E}+\Gamma) - 2(\bar{E}+\Gamma) \right\}\right]^{1/2}. \end{aligned}$$

Now in one dimension, $\lambda = \Lambda L^2$, where L is the length scale used in the nondimensionalization. Thus the dimensional value of the displacement at the wound edge in

the one-dimensional geometry is

$$u(0).L = \left[\frac{2}{\Lambda}\left\{\frac{(\bar{E}+\Gamma)(\bar{E}+\Gamma+1)}{(\bar{E}+\Gamma-1)}\log(\bar{E}+\Gamma) - 2(\bar{E}+\Gamma)\right\}\right]^{1/2}. \qquad (4.18)$$

Returning to the two-dimensional radially symmetric geometry, the singularity as $\beta \to \beta_{crit}$ arises in this case because $du/dr(1) \to -1$. Therefore the boundary condition (4.16a) implies that in this critical case

$$u(1) = \frac{1}{\Gamma - a\bar{E}}\left(\bar{E} + \Gamma - \frac{1}{1-\beta_{crit}}\right).$$

Now in the limit as the wound radius $R \to \infty$, the dimensional displacement at the wound edge in the two-dimensional radially symmetric geometry must tend to the dimensional displacement at the wound edge in the one-dimensional geometry. (Of course, the dimensionless displacement tends to zero). That is, as $R \to \infty$,

$$\frac{R}{\Gamma - a\bar{E}}\left(\bar{E} + \Gamma - \frac{1}{1-\beta_{crit}}\right) =$$

$$\left[\frac{2}{\Lambda}\left\{\frac{(\bar{E}+\Gamma)(\bar{E}+\Gamma+1)}{(\bar{E}+\Gamma-1)}\log(\bar{E}+\Gamma) - 2(\bar{E}+\Gamma)\right\}\right]^{1/2} + o(1)$$

$$\Longrightarrow \frac{1}{\Gamma - a\bar{E}}\left(\bar{E} + \Gamma - \frac{1}{1-\beta_{crit}}\right) =$$

$$\left[\frac{2}{\lambda}\left\{\frac{(\bar{E}+\Gamma)(\bar{E}+\Gamma+1)}{(\bar{E}+\Gamma-1)}\log(\bar{E}+\Gamma) - 2(\bar{E}+\Gamma)\right\}\right]^{1/2} + o\left(\lambda^{-1/2}\right)$$

as $\lambda \to \infty$. Simplifying this gives

$$\beta_{crit} = 1 - \left\{\bar{E} + \Gamma - (\Gamma - a\bar{E})\Omega\right\}^{-1} + o(\lambda^{-1/2}) \qquad (4.19)$$

as $\lambda \to \infty$, where

$$\Omega = \left[\frac{2}{\lambda}\cdot\left\{\frac{(\bar{E}+\Gamma)(\bar{E}+\Gamma+1)}{(\bar{E}+\Gamma-1)}\log(\bar{E}+\Gamma) - 2(\bar{E}+\Gamma)\right\}\right]^{1/2}.$$

This approximation is illustrated in Figure 4.9, where for given values of E, Γ and a we have estimated β_{crit} numerically for a number of values of λ. These numerical estimates are obtained by successively increasing β in the continuation numerical method, with smaller and smaller increments, until $u'(1) < -0.999995$.

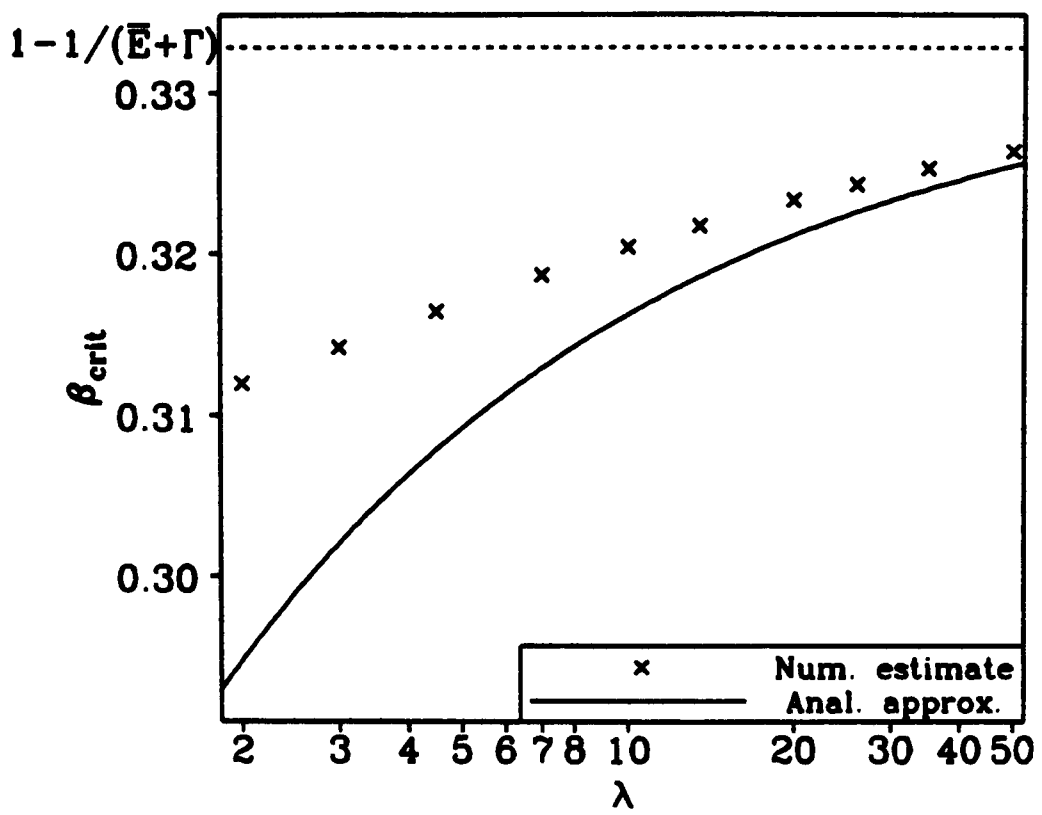

Figure 4.9: The analytical approximation (4.19) of β_{crit} compared to numerical estimates for a range of values of λ. The other parameter values are $E = 0.3$, $\Gamma = 0.8$, $a = \pi/2 - 1$. For clarity, λ is plotted on a logarithmic scale.

An important issue raised by the model is the biological interpretation of the result that solutions only reflect the phenomenon of the actin cable when β is very close to β_{crit}. Such an interpretation emerged when we examined the biological literature on the relative rates of intracellular rearrangement of myosin and filamentous actin. Myosin is a generic term for a class of proteins that bind to filamentous actin. While the role of myosin in muscle contraction has been understood for some time (see, for example, Alberts *et al.*, 1989, Chapter 11), many questions concerning nonmuscle myosins remain unanswered; for a detailed review, see Korn and Hammer (1990). However, there is little doubt that the exertion of traction forces by actin filaments does depend on interaction with myosin (Citi and Kendrick-Jones, 1987; Langanger *et al.*, 1986).

In experiments described above on actin filament reorganization, Chen (1981) and Kolega (1986) found that this process occurred on the time scale of a few seconds. In contrast, Nachmias *et al.* (1989) investigated the intracellular movement of myosin in *Dictyostelium discoideum* amoebae following a micromolar stimulus of cyclic AMP, and found that myosin translocation to the cell cortex was considerably slower, with

a maximal response after about 2 minutes. McKenna *et al.* (1989) observed the movement of "bead-like" myosin-containing structures in 3T3 fibroblasts following microinjection with fluorescently labelled myosin. They observed a movement towards the centre of the cell with a speed of 0.18 ($\pm$ 0.09) μm/min, which would again correspond to a time scale of a few minutes for post-wounding myosin reorganization. Finally, DeBiasio *et al.* (1988) studied the actin and myosin content of cellular protrusions in migrating Swiss 3T3 fibroblasts by microinjecting fluorescent derivatives. They found that while actin was present in these protrusions initially, in fact at somewhat elevated levels, myosin only became detectable after 1–2 minutes.

Thus it seems that the reorganization of actin filaments in response to wounding might be considerably quicker than the corresponding movement of intracellular myosin. Recalling that the parameter β reflects the extent of myosin cross-bridging between actin filaments, we can think of β as a parameter whose value increases gradually with time. With this interpretation, we can regard the variation in the model solutions with increasing β as the time evolution of epidermal displacements in the first few minutes after wounding. The corresponding sequence of scalar actin filament densities $G(r;\beta)$ is illustrated in Figure 4.10. In this figure, $G(r;\beta)$ is plotted against $u + r$, the post-wounding radial position of the material point initially at radius r. This shows that as myosin rearrangement proceeds, not only does the actin aggregation at the wound edge increase, but also the wound edges begin to move inwards. The parameter β is of course prevented from reaching β_{crit} by physical constraints on the packing of actin filaments, which are not included in our model. We should, however, stress that this interpretation of the variation of β is at best heuristic; full theoretical investigation of the role of myosin in the formation of the actin cable would require new detailed modelling of actomyosin interaction in non-muscle cells.

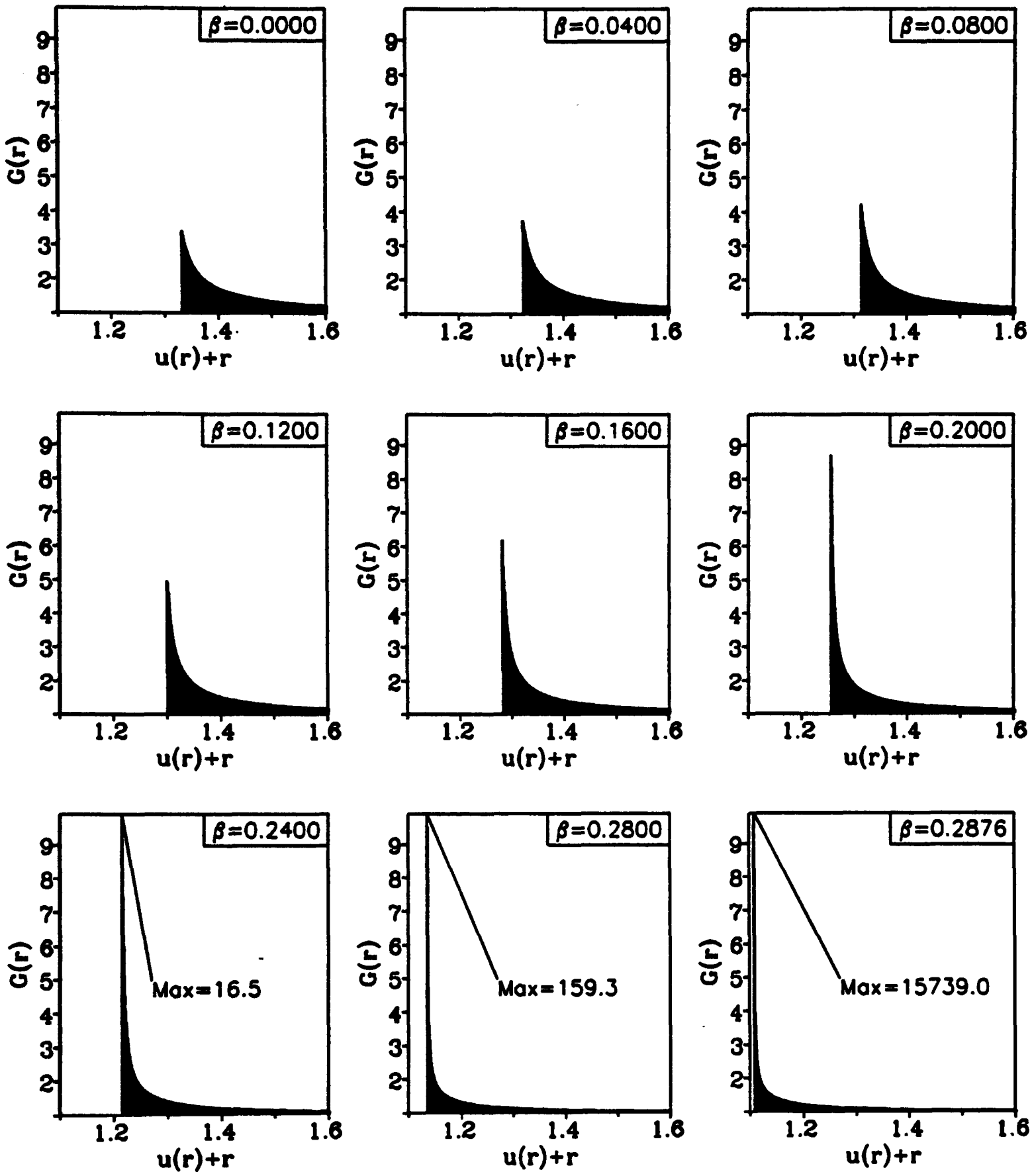

Figure 4.10: The scalar actin filament density $G(r)$ plotted against $u(r) + r$, for a range of values of the parameter β. The other parameter values are $\lambda = 1.5$, $E = 0.29$, $\Gamma = 0.77$, $a = \pi/2 - 1$. For these values, we estimate numerically that $\beta_{crit} \approx 0.28784$. When $G(1.0)$ is greater than the upper limit of the vertical axis, its value is indicated. Since we are interpreting β as a parameter whose value increases gradually with time, we can regard this figure as a time sequence of actin filament densities during the first few minutes after wounding.

4.5 Appropriate Parameter Values

We have shown that in the limit as $\beta \to \beta_{crit}$, the solutions of the improved model (4.15) subject to (4.16) can reflect the experimentally observed response of embryonic epidermis to wounding. One aspect of this response involves conditions on the post-wounding displacements. In this section, we investigate the effects of variations in the parameters λ, E , Γ and a on the limiting value of these displacements $u(r)$ as $\beta \to \beta_{crit}$. In the absence of a full analytic solution, these limiting displacements can only be estimated numerically. Our method of numerical solution involves gradual increase in the parameter β, with successively smaller increments, using the solution for the previous value of β at each stage (see page 133). Therefore, numerical estimation of the limiting displacements requires a stopping criterion: when this criterion is satisfied, we can end our incrementation of β and take the current $u(r)$ as a good approximation to the limiting displacements. Such a criterion cannot involve the value of either β_{crit} or $\lim_{\beta \to \beta_{crit}} u(1)$, since we do not have analytical expressions for these. However, as $\beta \to \beta_{crit}$, $u'(1) \to -1$, and we use this as the basis for our stopping criterion. Table 4.1 shows numerically calculated values of $u(1)$ and the corresponding values of $u'(1)$ as β is increased, for a typical set of values of λ, E, Γ and a; the computer processing time required to achieve the last value shown was about 26 hours on a 6 MIPS machine. These values suggest that $u(1)$ is within 1% of its limiting value when $u'(1) = -0.99995$. Based on this, we take the condition $u'(1) < -0.99995$ as our stopping criterion for the numerical increase of β.

Having established this stopping criterion, we can investigate the effect of parameter variations. Figures 4.11 and 4.12 show the effect on $u(r)$ and $u'(r)$ respectively of $\pm 10\%$ changes in the values of each of the parameters λ, E, Γ and a, for a given set of reference parameter values. To use graphs such as these effectively, we must establish exact criteria under which the model solutions will be said to agree with experimental observations. Since the experimental data is only semi-quantitative, such criteria are necessarily somewhat arbitrary. However, they do make a precise investigation of parameter variation possible, leading ultimately to the determination of a full parameter domain. The qualitative form of this domain will not depend on

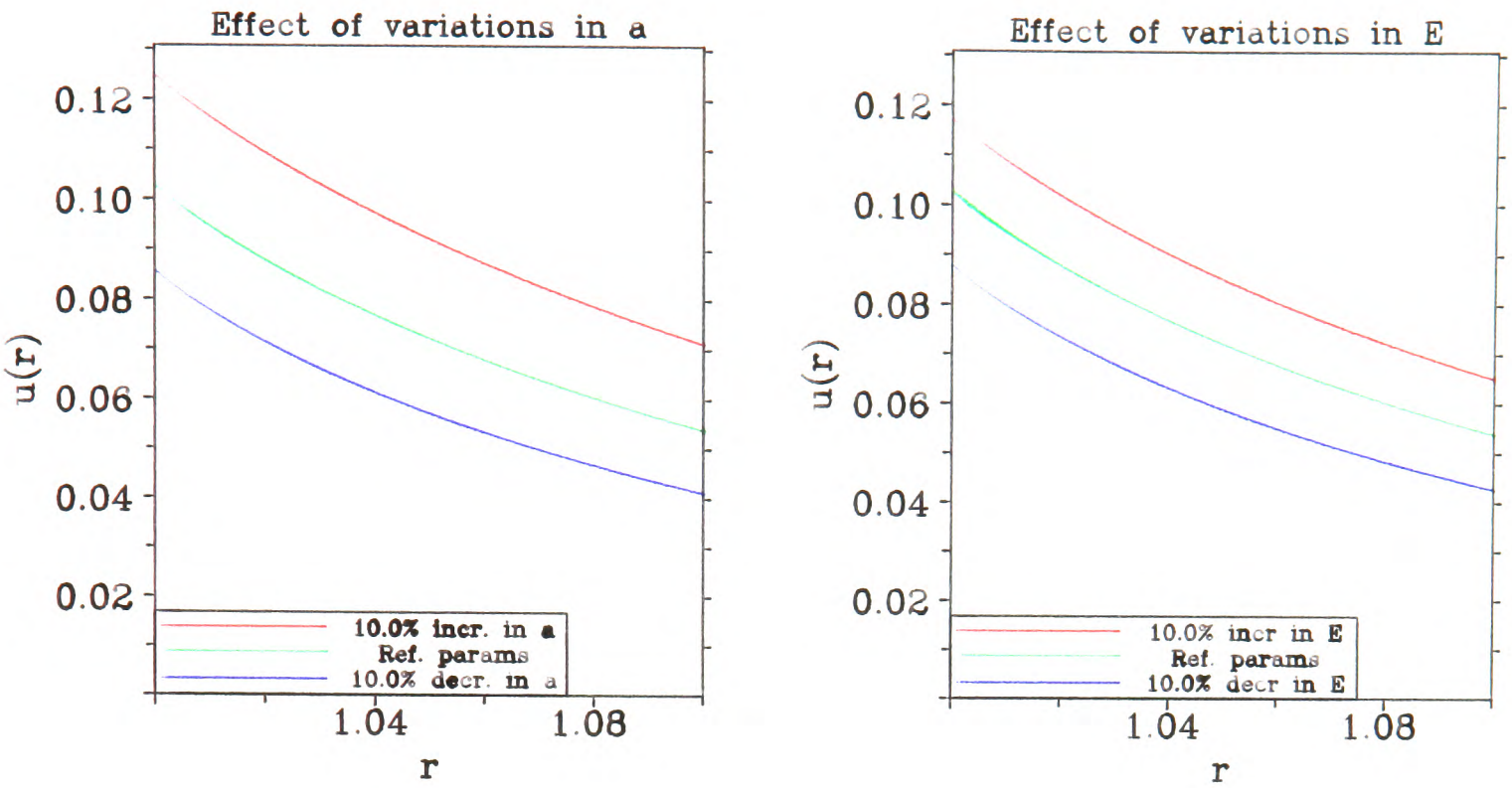

Figure 4.11: The effect of parameter variation on the limiting solution $\lim_{\beta \to \beta_{crit}} u(r)$ of the improved model (4.15) subject to (4.16). The solutions in green are for the parameter values $\lambda = 3.0$, $E = 0.3$, $\Gamma = 0.8$, $a = \pi/2 - 1$. Those in red correspond to a 10% increase in one parameter, and those in blue correspond to a 10% decrease in that parameter. The r interval shown corresponds to the leading 5 cell layers. In contrast to Figure 3.6, these solutions are not highly sensitive to changes in any of the parameter values, because we are plotting the solution in the limit as $\beta \to \beta_{crit}$ in this case, rather than fixing the value of β.

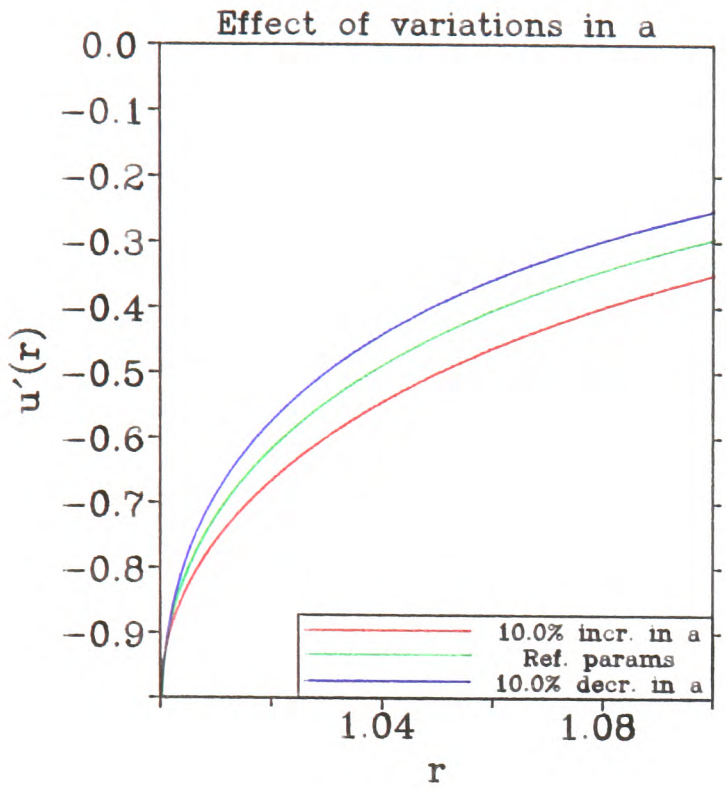

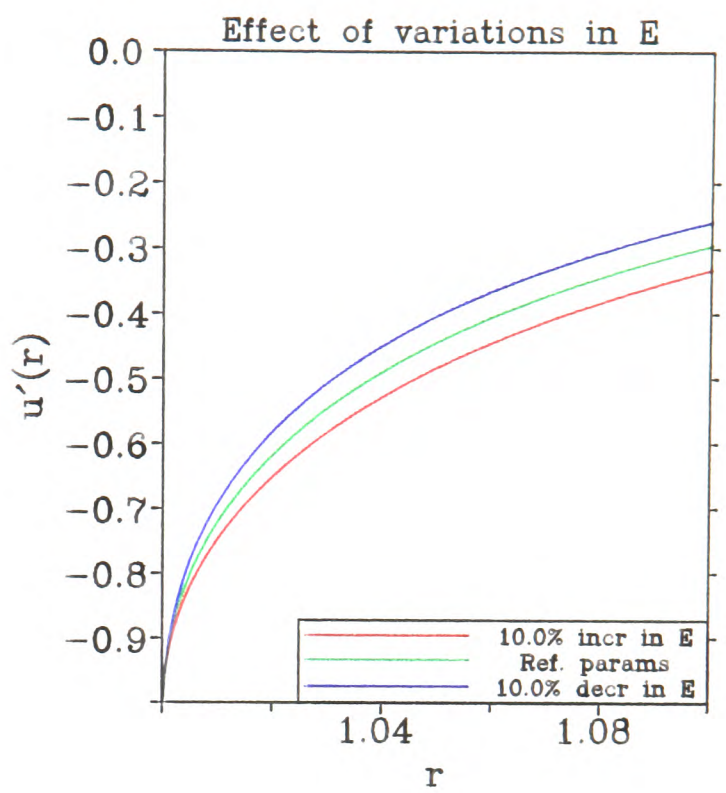

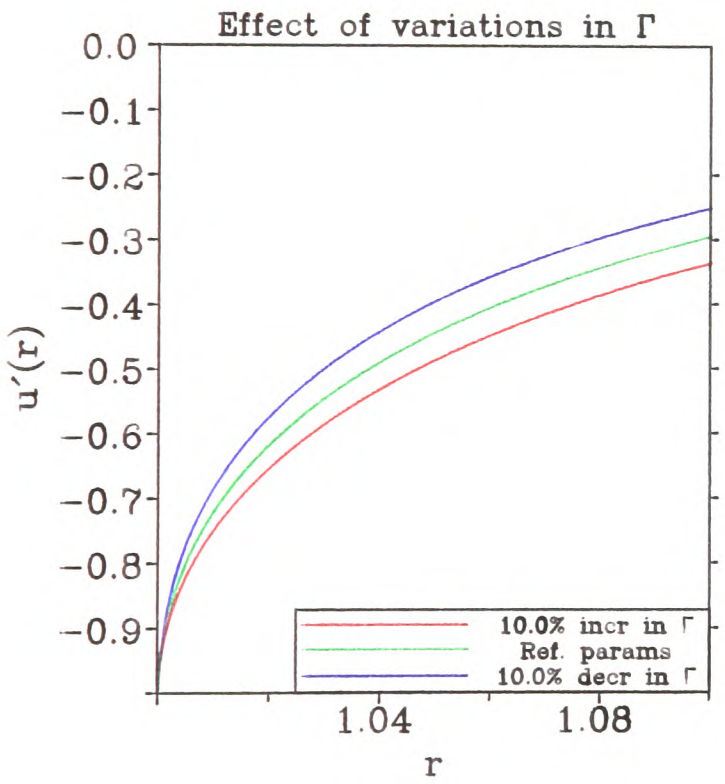

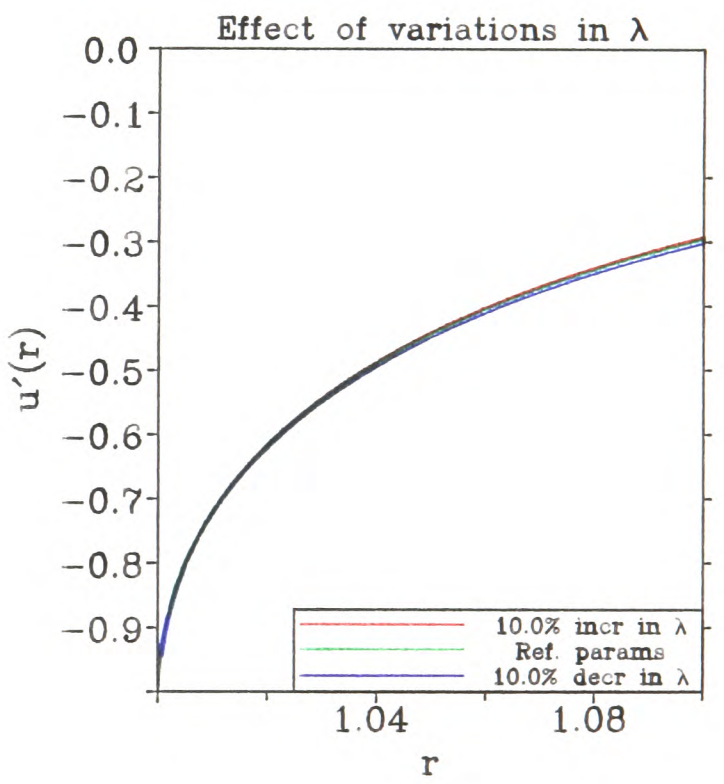

Figure 4.12: The effect of parameter variation on the first derivative $\lim_{\beta \to \beta_{crit}} u'(r)$ of the limiting solution of the improved model (4.15) subject to (4.16). The solutions in green are for the parameter values $\lambda = 3.0$, $E = 0.3$, $\Gamma = 0.8$, $a = \pi/2 - 1$. Those in red correspond to a 10% increase in one parameter, and those in blue correspond to a 10% decrease in that parameter. The r interval shown corresponds to the leading 5 cell layers. In contrast to Figure 3.7, these solutions are not highly sensitive to changes in any of the parameter values, because we are plotting the solution in the limit as $\beta \to \beta_{crit}$ in this case, rather than fixing the value of β.

$u(1)$	$u'(1)$	$u(1)$ (contd.)	$u'(1)$ (contd.)
0.27150514	-0.7397632141	0.10132417	-0.9999999627
0.26442440	-0.7710649009	0.10132355	-0.9999999724
0.21274625	-0.9026135748	0.10132325	-0.9999999768
0.17732859	-0.9524641872	0.10132294	-0.9999999812
0.12988162	-0.9907010891	0.10132258	-0.9999999860
0.12025231	-0.9950627865	0.10132244	-0.9999999878
0.10758155	-0.9990186839	0.10132231	-0.9999999894
0.10517315	-0.9995040370	0.10132225	-0.9999999901
0.10251351	-0.9999007044	0.10132209	-0.9999999919
0.10203441	-0.9999503350	0.10132201	-0.9999999928
0.10153526	-0.9999900167	0.10132195	-0.9999999935
0.10144749	-0.9999950304	0.10132190	-0.9999999940
0.10133821	-0.9999996413	0.10132184	-0.9999999946
0.10132591	-0.9999999323	0.10132181	-0.9999999949
0.10132476	-0.9999999528	0.10132179	-0.9999999951

Table 4.1: Numerically calculated values of $u(1)$ and the corresponding values of $u'(1)$ as β is increased from zero towards β_{crit}, for $\lambda = 3.0$, $E = 0.3$, $\Gamma = 0.8$, $a = \pi/2 - 1$. These values suggest that for this set of parameter values, $u(1)$ is 1% greater than its limiting value when $u'(1) \approx -0.99992$.

the quantitative detail of the criteria used to calculate it.

The criteria must reflect the two aspects of the experimental data which we require the limiting displacements to satisfy, namely a retraction of the wound edges by 10–15% of the wound radius, with only the leading 4–5 cell layers significantly contracted. The first of these conditions simply corresponds to $0.1 < u(1) < 0.15$. The second is a condition on $u'(r)$ at values of r corresponding to the fifth or sixth cell layer from the wound edge, and we take the condition to be $u'(1.1) > -0.3$; this ensures that the contraction of the sixth and subsequent cell layers is less than 30%.

In principle, we are now able to determine the precise region of the full four-dimensional parameter space in which the limiting displacements satisfy these two conditions. However, finding the full parameter domain was computationally infeasible. Instead, we have investigated a particularly interesting two-dimensional cross-section of this four-dimensional domain, namely that given by fixing the ratio $\Gamma/\bar{E}$ as 8/3, which is the ratio in the solutions illustrated in Figure 4.8, and by taking

$a = \pi/2 - 1$. This value of a is that predicted by the detailed heuristic model of the actin filament network developed in Section 4.2. This cross-section is of particular interest because of its relevance to the one-dimensional system, in which the ratio $\Gamma/\bar{E}$ is irrelevant, and only the sum $(\bar{E} + \Gamma)$ is important. The form of the cross-section is shown in Figure 4.13. In this figure, we have taken ten equally spaced values of λ and ten equally spaced values of $(\bar{E} + \Gamma)$, and for each of the 100 parameter sets we have determined whether or not the limiting displacements satisfy the above conditions. The figure also shows contours of the value of β reached when the stopping criterion was satisfied; this is a numerical estimate of the critical upper limit β_{crit}.

4.6 Conclusions

The recent discovery by Martin and Lewis (1991a,b) of an actin cable at the wound edge in embryonic epidermal wounds raises a number of interesting and important biological questions, prominent amongst which is the issue of how the cable forms over such a short time scale. In this chapter we have addressed the possibility that the cable forms by compaction and reorientation of the actin filament network, without either depolymerization of actin in one part of the cell and corresponding repolymerization in another part, or intracellular movement of intact actin filaments, or *de novo* synthesis of filamentous actin. Although there is experimental evidence that this is the mechanism of cytoskeletal reorganization in some *in vitro* situations (Chen, 1981; Albrecht-Buehler, 1987), this is very much a hypothesis.

Our modelling has investigated the new equilibrium state of the actin filament network after wounding, under this hypothesis. We have shown that this mechanism can explain the actin cable observed experimentally, and that if this is the mechanism of formation, it depends crucially on the properties of actin filament alignment in response to stress and of actin filament synergy in cell traction forces. The latter property involves interaction between intracellular actin and myosin, and we have been able to interpret the singular limit near which the model captures the phenomenon of the actin cable in terms of the relative rates of post-wounding rearrangement of

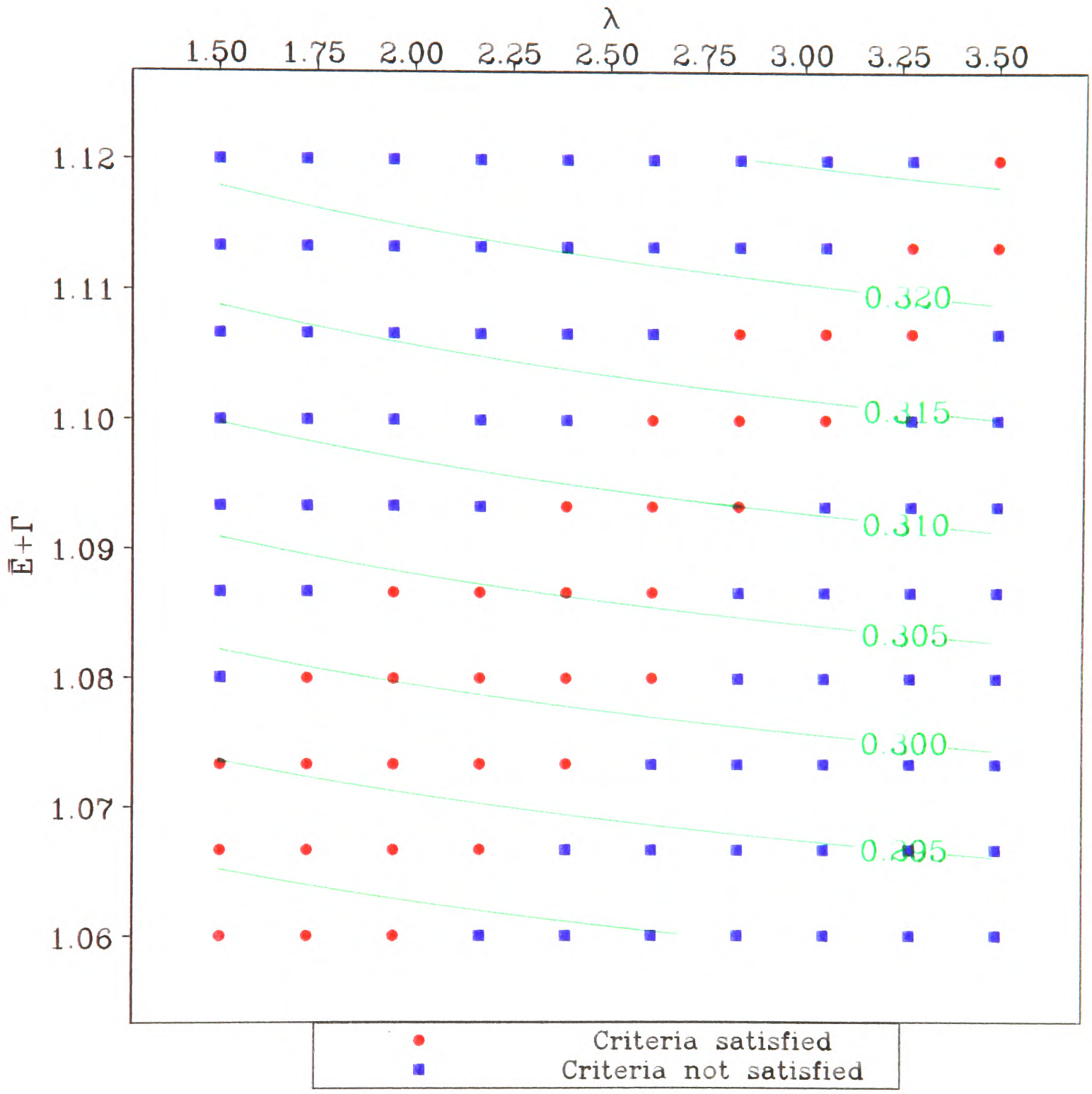

Figure 4.13: A two-dimensional cross-section of the full four-dimensional parameter space, given by fixing $a = \pi/2 - 1$ and $\Gamma/\bar{E} = 8/3$. For each of the 100 parameter sets, the conditions $0.1 < u(1) < 0.15$ and $u'(1.1) > -0.3$ were tested on the numerical estimates of the limiting displacements. The points are marked with red circles or blue squares, corresponding to these conditions being satisfied or not satisfied, respectively. Contours of the corresponding numerical estimates of β_{crit} are shown in green.

actin and myosin.

To clarify the agreement between the model solutions and experimental data, we have used these solutions to simulate an optical section through the basal layer of the epidermis, after staining with fluorescently tagged phalloidin. We described on page 72 how Martin and Lewis (1991a,b) used this staining technique to visualize the actin cable experimentally; a typical experimental result is shown in Figure 3.2. To simulate this experimental photograph from our model solutions, we treated the filamentous actin distribution predicted by the model, appropriately normalized, as a probability distribution for phalloidin staining. Thus we marked in white, against a black background, the post-wounding positions $[u(r)+r]\underline{\hat{r}}$ of a large number of points, with radial coordinate chosen at random from this distribution, and angular coordinate chosen at random from a uniform distribution. We found that about 9 million points were required to give a 'staining level' equivalent to that used experimentally. Such a simulation is shown in Figure 4.14; it compares well with the corresponding experimental result (Figure 3.2).

We end this chapter by suggesting three possible experimental approaches to testing the basic conclusion of our modelling, that the formation of an actin cable in response to wounding in embryonic epidermis is consistent with the assumption that the amount of filamentous actin in a given region of cytogel remains constant as that region is deformed. The first involves detailed quantitative experiments to determine whether the parameter values for which the model predicts the formation of the actin cable are appropriate for the cell types in which the cable has been observed. The relevant quantitative data currently available is reviewed on page 79.

The second experimental approach is to investigate the wounding response in the presence of cytochalasin. This is the generic name for a group of fungal metabolites which act as actin filament capping proteins; cytochalasins B and D are the most commonly used. Their function has been reviewed by Cooper (1987). Briefly, they bind to the barbed ends of actin filaments, in a ratio of about one molecule per filament, and inhibit both association and dissociation of actin filament subunits at that end. (The structure of actin filaments, including their inherent polarity, is

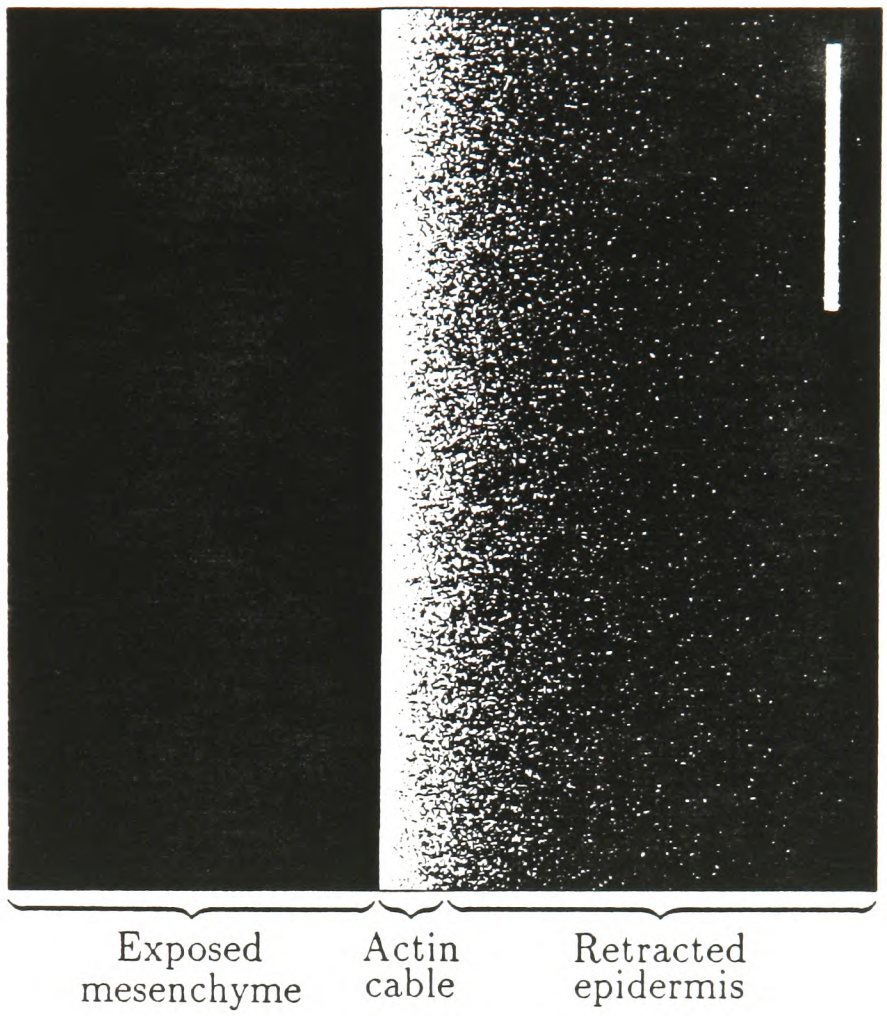

Figure 4.14: A simulation of an optical section through the basal layer of the epidermis after staining with fluorescently labelled phalloidin, as predicted by the model solutions. We treat the filamentous actin distribution predicted by the model, appropriately normalized, as a probability distribution for phalloidin staining. The figure shows the post-wounding positions of 9 million points, with radial coordinate chosen at random from this distribution, and angular coordinate chosen at random from a uniform distribution. The parameter values are $\lambda = 1.5$, $E = 0.29$, $\Gamma = 0.77$, $a = \pi/2 - 1$, $\beta = 0.2876$. For these values of λ, E, Γ and a, $\beta_{crit} \approx 0.2878$. (Scale bar = 10μm).

discussed in the book by Alberts *et al.*, 1989, Chapter 11, and in more detail in the recent review by Pollard, 1990). For example, Bonder and Mooseker (1986) found a reduction of about 90% in both the association and dissociation rates of subunits at the barbed ends of acrosomal actin filament bundles in *Limulus* sperm, at the (relatively high) concentration of 2μM of cytochalasin B.

In an *in vivo* study on HEp-2 cells, Morris and Tannenbaum (1980) successfully used cytochalasin to stabilize the filamentous actin concentration, and we suggest that it might be possible to use cytochalasins in a similar way in the embryonic wounding system. If this were possible, our hypothesis would predict that many

aspects of the initial response to wounding, including the formation of the actin cable, would be unaffected. However, some studies have found cytochalasins to have highly disruptive effects on the actin filament network. For example, Schliwa (1982) found that cytochalasin D caused extensive disruption to the cytoskeleton of African Green Monkey kidney cells, over a time scale of a few minutes, and Forscher and Smith (1988) found that cytochalasin B caused almost complete loss of filamentous actin in growth cones from *Aplysia* neurons, again within a few minutes. Further, Pollard (1990) urges caution when interpreting experiments involving cytochalasins because of difficulties arising from the low-affinity binding of cytochalasins to actin monomers. Thus, a necessary precursor to any investigation of the response to wounding in the presence of cytochalasins is a preliminary study to determine the precise effects of the various cytochalasins on the embryonic epidermal cells concerned, in a control situation.

The final possible experimental approach to testing our hypothesis involves the technique of photobleaching, which has been used by Wang (1985, 1987) to study the actin filament network. The technique is to first microinject cells with fluorescently labelled actin, a procedure which is now well established (Pollard, 1990). The fluorescent actin is rapidly incorporated into the filament network, which in most systems then functions normally. Wang's approach is to then photobleach a spot of the fluorescent filament network, a few μm across, and to follow the subsequent progress of the bleached region. In the 1985 study, Wang used this technique to investigate the movement of actin subunits within lamellipodia of gerbil fibroma cells, and in the 1987 study he used it to investigate the reorganization of actin filaments during division of 3T3 cells. We suggest that it might be possible to amend this technique to study in detail the dynamics of the actin filament network after wounding. Again, preliminary investigations in control situations would be necessary to determine whether or not this is a viable experimental approach. In particular, it requires that the rate of movement of actin subunits within filaments is not too large in the cell type concerned.

In conclusion, our modelling predicts that the formation of the actin cable ob-

served by Martin and Lewis (1991a,b) is consistent with the hypothesis that the amount of filamentous actin in a given region of cytogel remains constant as that region is deformed. Moreover, we have suggested three approaches to testing this model prediction experimentally.

Chapter 5

Chemical Control of Cell Movement and the Boyden Chamber Assay

5.1 Biological Background and Previous Models

In the Introduction, we discussed the important role played in dermal wound healing by chemical regulation of cell motion, via both chemotaxis and chemokinesis. In this chapter we develop a new model for chemically controlled cell movement. We focus on endothelial cells, which move into the wound space in response to chemical stimuli during the process of angiogenesis, resulting in a dense capillary network in the granulation tissue of healing dermal wounds. However, the model is also applicable to other aspects of wound healing, in particular the influx of white blood cells during the early "inflammation" phase of healing, and the invasion of the wound space by fibroblasts during the formation of granulation tissue.

To clarify a serious confusion of terminology, Keller *et al.* (1977) proposed definitions of the terms chemotaxis and chemokinesis which established their current meanings. They defined chemokinesis as "a reaction by which the speed or frequency of locomotion and/or the frequency and magnitude of turning of cells or organisms moving at random is determined by substances in the environment", while chemotaxis is "a reaction by which the direction of locomotion of cells or organisms is determined by substances in their environment". Although there is still debate in the biological literature on some finer points of the interpretation of these definitions (Wilkinson, 1988a,b; Bignold, 1988a), the terms are now in widespread use.

The available experimental evidence, reviewed by Devreotes and Zigmond (1988), suggests that chemotaxis and chemokinesis occur in eukaryotic cells via the binding

of regulatory chemicals to receptors on the cell surface; the number and location of bound receptors modulates pseudopod extension and thus cell motion. The systems that have been studied in most detail are the response of polymorphonuclear leukocytes to N-formylated peptides and of *Dictyostelium discoideum* amoebae to cyclic AMP. The mechanisms in the two cases are remarkably similar. The receptor-chemical complex is rapidly internalized in intracellular vesicles, and once inside the cell it dissociates, yielding free intracellular chemical and receptors. Experiments and modelling by Zigmond *et al.* (1982) suggest that in at least the leukocyte-peptide system, the intracellular chemical is partitioned into two pools, with a proportion of the chemical degraded and released, and the remainder kept in a long term 'storage pool'. The internalized receptors appear to be recycled back to the cell surface (Sullivan and Zigmond, 1980; Van Haarstert, 1987), and moreover in the presence of extracellular regulatory chemical, additional receptors (up to 30-fold) can be released to the cell surface from an intracellular pool (Janssens and Van Driel, 1984; Zimmerli *et al.*, 1986; Fletcher and Gallin, 1980).

A number of mathematical models have been proposed for chemically modulated cell movement. The oldest and most widely used is the continuum model of Keller and Segel (1971a,b). They take the cell flux $\underline{J}_n$ to be directly dependent on the local extracellular chemical concentration, via the expression

$$\underline{J}_n = \underbrace{-D_n(c)\nabla n}_{\text{Chemokinesis}} + \underbrace{\chi_n(c) n \nabla c}_{\substack{\text{Chemotaxis and} \\ \text{chemokinesis}}} , \tag{5.1}$$

where n and c are the local cell density and chemical concentration respectively, and the transport coefficients $D_n(c)$ and $\chi_n(c)$ are strictly positive for all c. Since variations in c affect both the magnitude and direction of the second term, this term represents a combination of chemotaxis and chemokinesis effects, under the definitions of Keller *et al.* (1977). This model was originally applied by Keller and Segel (1971a,b) to bacterial movement, but has more recently been used with considerable success in a wide range of cellular and whole organism applications. The Keller-Segel approach takes no account of the role of receptor kinetics in the cellular response to chemotactic and chemokinetic factors: indeed, these kinetics were very

poorly understood when the model was formulated. More recently, Segel (1976) incorporated receptor kinetics into the model when applied to bacterial movement. His model consists of 9 coupled partial differential equations, and a simplification reducing the system to 6 equations is considered in a second paper (Segel, 1977b). Subsequent experimental work on receptor modification in bacteria is reflected in the models of Goldbeter and Koshland (1984) and Segel *et al.* (1986). However, this work has little relevance to wound healing, since the receptor-based mechanisms responsible for chemotaxis are quite different in bacteria and eukaryotic cells. In particular, the latter respond to spatial gradients in the chemoattractant, while bacteria can only modify the length of time they spend moving in a particular direction, in response to a temporal gradient of chemical concentration.

At the single cell level, Tranquillo and coworkers have developed a detailed stochastic model for the motion of a single leukocyte in the presence of chemoattractants (Tranquillo and Lauffenburger, 1987; Tranquillo *et al.*, 1988; Tranquillo, 1990). This model applies exclusively to a single cell, but in an attempt to combine single cell and cell population models, Rivero *et al.* (1989) proposed a continuum model in which the transport coefficients are related to the parameters of a simple stochastic model for the movement of an individual cell. Their expressions for these parameters in terms of the number of bound receptors per cell and the extracellular concentration of chemoattractant assume that the receptor-chemical binding is at equilibrium. Yet another approach is used by Fisher and Lauffenburger (1987) and Charnick and Lauffenburger (1990), who take cell-cell encounters to be determined by a random walk that is biased due to chemotaxis.

5.2 Shortcomings of the Keller-Segel Approach, Highlighted by the Boyden Chamber Assay

The Boyden chamber assay is a relatively simple *in vitro* system which enables chemotactic and chemokinetic effects to be quantitatively tested. The assay was developed by Boyden (1962), and its subsequent use is reviewed by Bignold (1988b). It consists

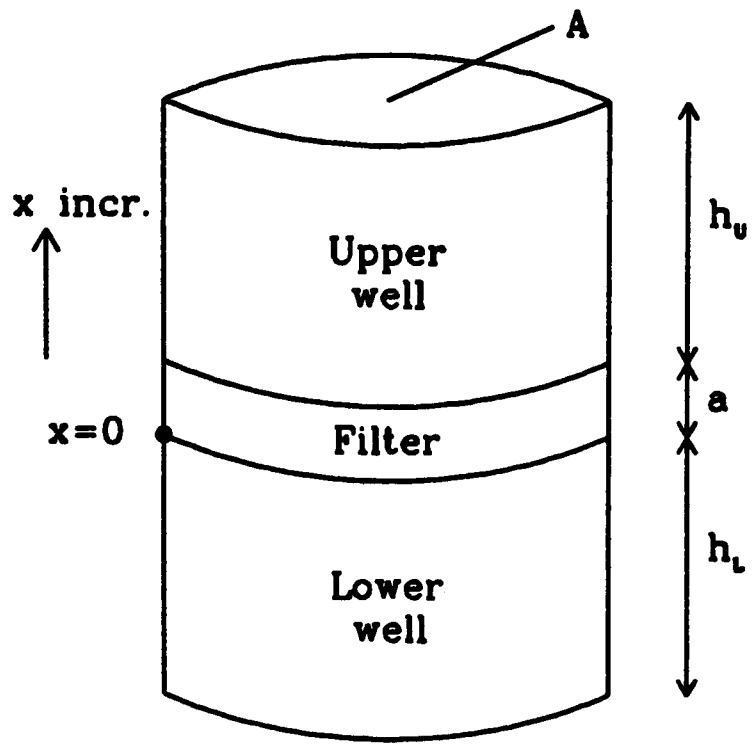

Figure 5.1: A diagrammatic representation of the Boyden chamber assay.

of two wells separated by a thin filter whose porosity enables cells to crawl actively through, but prevents passive falling of cells under gravity between the upper and lower wells (Figure 5.1). The lower well is filled with a solution of the chemical under test, and the filter is placed on top of this. The pores of the filter rapidly fill with the chemical solution, due to capillary action. The upper well is then filled with a suspension of the cells under test; the cells rapidly settle onto the top of the filter. The system is left for a given length of time (a few hours), during which the cells crawl through the filter in response to the concentration gradient in the regulatory chemical. Having passed through the filter, the cells rapidly spread across the lower surface of the filter; they are prevented from dropping into the lower well by coating the filter with an adhesive substance such as fibronectin. At the end of the given time period, the number of cells on the lower surface of the filter is counted. To distinguish between chemotaxis and chemokinesis, it is usual to repeat the experiment with the cells in the upper well suspended in a solution of the chemical under test. A chemical gradient will then only arise due to cellular degradation of active chemical.

In this section we apply a model based on that of Keller and Segel (1971a,b) to chemically controlled cell movement in the Boyden chamber assay. Previously, Lauffenburger and Zigmond (1981) and Lauffenburger *et al.* (1988) have solved the

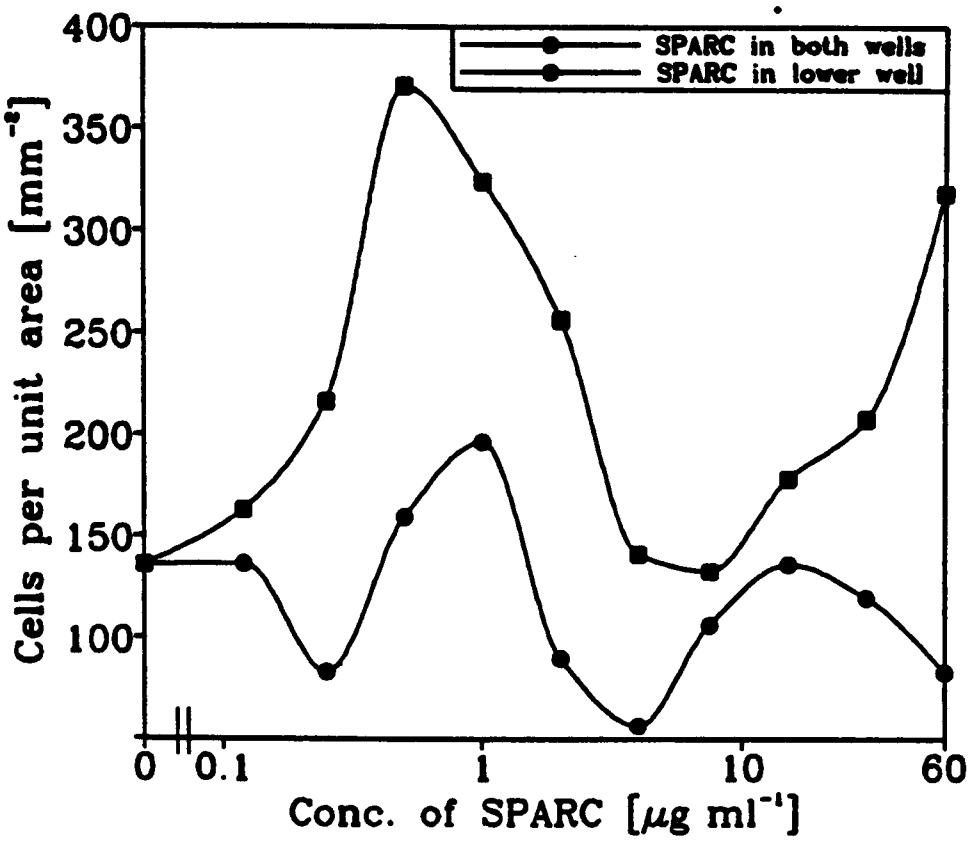

Figure 5.2: A typical set of results from the Boyden chamber experiments of Sage *et al.* (in preparation). The number of cells on the lower surface of the filter after 5 hours of wounding is plotted against the concentration of SPARC, for the cases of SPARC present initially only in the lower well (squares) and in both wells (circles). For clarity, these concentrations are plotted on a logarithmic scale. The dimensions of the chamber were, in the notation of Figure 5.1, $h_L = 3.25$mm, $h_U = 5.5$mm, $a = 10\mu$m and $A = 7$mm^2. The filters were polycarbonate, coated with fibronectin, with 200 pores per mm^2, each 8μm in diameter. The cells were bovine aortic endothelial cells, suspended in DMEM with 0.25% ovalbumin. The SPARC was also diluted in DMEM with 0.25% ovalbumin. The chambers were incubated for 5 hours at 37 °C in a mixture of 5% carbon dioxide and 95% air. At the end of this time the filters were removed, fixed, and stained with Diff-Quik, and the cells on the lower surface of the filter were counted.

diffusion equation to predict the chemical concentration as a function of time in the filter and wells of the Boyden chamber, and Buettner *et al.* (1989a,b) have applied the Keller-Segel approach to leukocyte movement in the Boyden chamber assay. We will compare the model predictions with the experimental data of Sage *et al.* (in preparation) to estimate the transport coefficients in the model. Sage *et al.* study the motile response of bovine aortic endothelial cells to concentration gradients of SPARC ("secreted protein acidic and rich in cysteine"). SPARC is a recently identified biochemical regulator, which may play an important role in wound healing (Mason *et al.*, 1986; Engel *et al.*, 1987; Sage *et al.*, 1989). A typical set of results from the Boyden chamber experiments of Sage *et al.* is illustrated in Figure 5.2. The precise

number of cells passing through the filter during the 5 hours of the experiment varies by a factor 2 or 3 for given concentrations of chemical in the wells, due to slight differences in the cells used. However, the basic trend, when SPARC is present both in the upper and lower wells and in the lower well only, is of a bell-shaped dose-response curve, and this shape of curve has been found in Boyden chamber studies for a range of chemicals and cell types, in a variety of Boyden chambers (see Bignold, 1988b, for references).

Following Keller and Segel (1971a,b), we use the representation (5.1) for chemically controlled cell flux, and our model consists of two partial differential equations:

$$\frac{\partial n}{\partial t} = \frac{\partial}{\partial x}\left[D_n(c)\frac{\partial n}{\partial x}\right] - \frac{\partial}{\partial x}\left[\chi_n(c)n\frac{\partial c}{\partial x}\right] \tag{5.2a}$$

$$\frac{\partial c}{\partial t} = D_c\frac{\partial^2 c}{\partial x^2} \tag{5.2b}$$

where $n(x,t)$ and $c(x,t)$ are the local cell density and chemical concentration respectively, x is distance measured vertically, and t is time. The dependence of the transport coefficients D_n and χ_n on c will be estimated using the data of Sage *et al.* We take $x = 0$ as the lower surface of the filter, and neglect any horizontal variations. This is a reasonable approximation, since the cross-sectional diameter of the chamber is very much larger than the thickness of the filter. The chemical diffuses throughout the upper and lower wells and the filter, so that c is defined on $-h_L < x < h_U + a$ (notation as in Figure 5.1), with zero flux boundary conditions at the endpoints. We assume that the diffusion of SPARC is unaffected by the presence of the filter, since the effective radius of a molecule of SPARC in aqueous solution is about $2 \times 10^{-3}\mu$m (see page 159), while the pores of the filter have a diameter of 8μm.

The cells are restricted to the filter region of the chamber, so that n is defined only on $0 \leq x \leq a$. Since a large number of cells are added to the upper well (about 7000 per mm^2 cross-sectional area), they form a confluent sheet when they settle onto the upper surface of the filter. In the 5 hours of the experiment, only a small fraction of these cells move through the filter (Figure 5.2), and thus to a good approximation we can take $n = 1/V_{cell}$ at $x = a$ and $n = 0$ at $x = 0$, for all $t \geq 0$. Here V_{cell} is the volume

of one cell, which is about $1000\mu m^3$ for bovine aortic endothelial cells (Helene Sage, personal communication, 1990). The approximation $n = 0$ at $x = 0$ is further justified by the fact that cells will spread rapidly across the lower surface of the filter once they have passed through it: the pores represent only about 1% of the total cross-sectional area of the filter. The appropriate initial conditions are $n = 0$ on $0 \leq x < a$ with $n = 1/V_{cell}$ at $x = a$, and $c = c_L$ on $-h_L < x < a$, $c = c_U$ on $a \leq x < h_U$; here c_U and c_L are the initial concentrations of chemical in the upper and lower wells, respectively. In the model (5.2), there is no contribution from cell division. The average cell cycle time for bovine aortic endothelial cells is about 28 hours, and careful investigation by Sage *et al.* has shown that there is no mitosis in the Boyden chamber during their experiments. We also neglect any degradation of chemical by the cells; Lauffenburger *et al.* (1988) have suggested including a degradation term dependent on n and c in (5.2b) when applied to the Boyden chamber assay, but we postpone inclusion of such a term to Section 5.3, where we develop a new model based on the receptor mechanisms responsible for this degradation.

We nondimensionalize (5.2) by defining the following dimensionless quantities, denoted by *:

$$x^* = x/a \qquad t^* = t/T \qquad n^* = nV_{cell} \qquad c^* = c/c_L \qquad c_U^* = c_U/c_L$$

$$D_n^*(c^*) = D_n(c_L \cdot c^*)T/a^2 \qquad D_c^* = D_c T/a^2 \qquad \chi_n^*(c^*) = \chi_n(c_L \cdot c^*)Tc_L/a^2 ,$$

where we take the time scale T as 1 hour. For the chamber used by Sage *et al.*, the dimensionless values of h_U and h_L, the heights of the upper and lower wells, are 325 and 550 respectively. Therefore we approximate both h_U and h_L by infinity. With these rescalings, the model equations are then, dropping the asterisks for notational simplicity,

$$\frac{\partial n}{\partial t} = \frac{\partial}{\partial x}\left[D_n(c)\frac{\partial n}{\partial x}\right] - \frac{\partial}{\partial x}\left[\chi_n(c)n\frac{\partial c}{\partial x}\right], \quad 0 < x < 1 \tag{5.3a}$$

$$\frac{\partial c}{\partial t} = D_c\frac{\partial^2 c}{\partial x^2}, \quad -\infty < x < \infty . \tag{5.3b}$$

These are subject to boundary conditions $n = 1$ at $x = 1$, $n = 0$ at $x = 0$ and

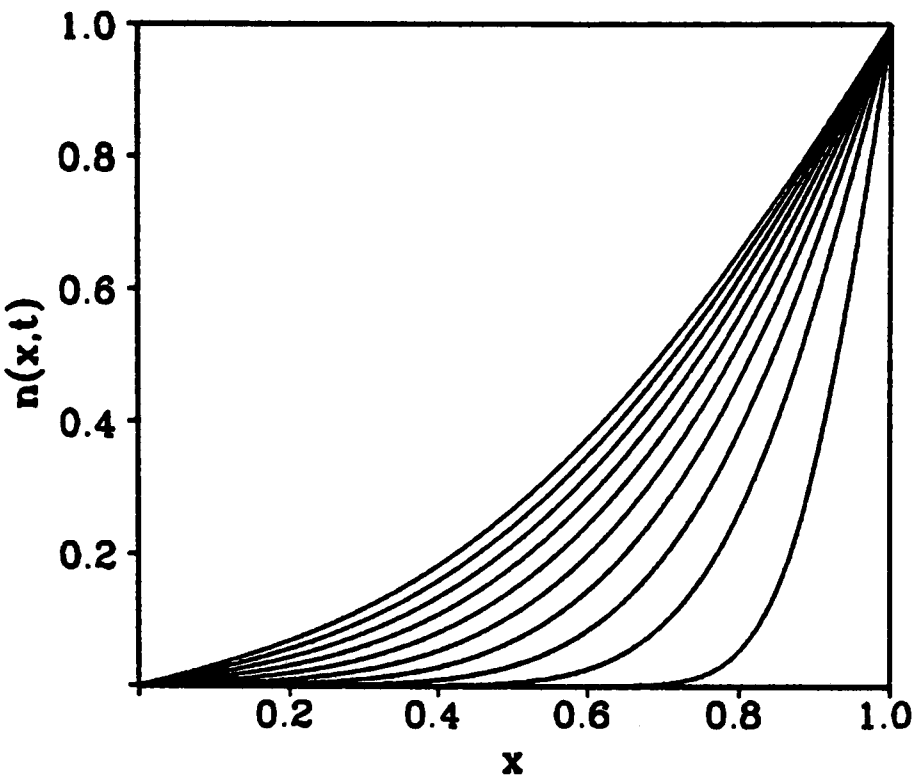

Figure 5.3: The solution for $n(x,t)$ of equation (5.3a) when $c_U = 1$, so that $c \equiv 1$ for all x and t. We plot n against x at time intervals of 30 minutes for a dimensional cell diffusion coefficient of $6 \times 10^{-12}\text{cm}^2\text{s}^{-1}$, which is a biologically reasonable value. The solution gradually approaches the steady state $n = x$.

$\partial c/\partial x = 0$ at $x = \pm\infty$, and to initial conditions

$$n(x,0) = \begin{cases} 0, & 0 \le x < 1 \\ 1, & x = 1 \end{cases} \qquad c(x,0) = \begin{cases} 1, & x < 1 \\ c_U, & x \ge 1\,. \end{cases}$$

There are two cases to consider: $c_U = 1$, so that chemical is initially present in both wells, and $c_U = 0$, so that chemical is initially present only in the lower well. In the former case, $c \equiv 1$ for all x and t, so that we have simply to solve the diffusion equation for n. The form of the solutions is illustrated in Figure 5.3, in which we plot n as a function of x at time intervals of 30 minutes for a dimensional cell diffusion coefficient of $6 \times 10^{-12}\text{cm}^2\text{s}^{-1}$. The solution for n gradually approaches the steady state $n = x$. We can solve the equation for the difference $n(x,t) - x$, which has homogeneous boundary conditions, by straightforward summation of separable solutions. This gives the series solution

$$n(x,t) = x + \sum_{m=1}^{\infty} \frac{2}{m\pi}(-1)^m \exp\left[-D_n m^2 \pi^2 t\right] \sin\left[m\pi x\right]\,.$$

At times $t \gg 1/(\pi^2 D_n)$, this solution approaches the steady state $n = x$ with an approximate dimensionless half-life of $\log 2/(D_n \pi^2)$; for a biologically reasonable value

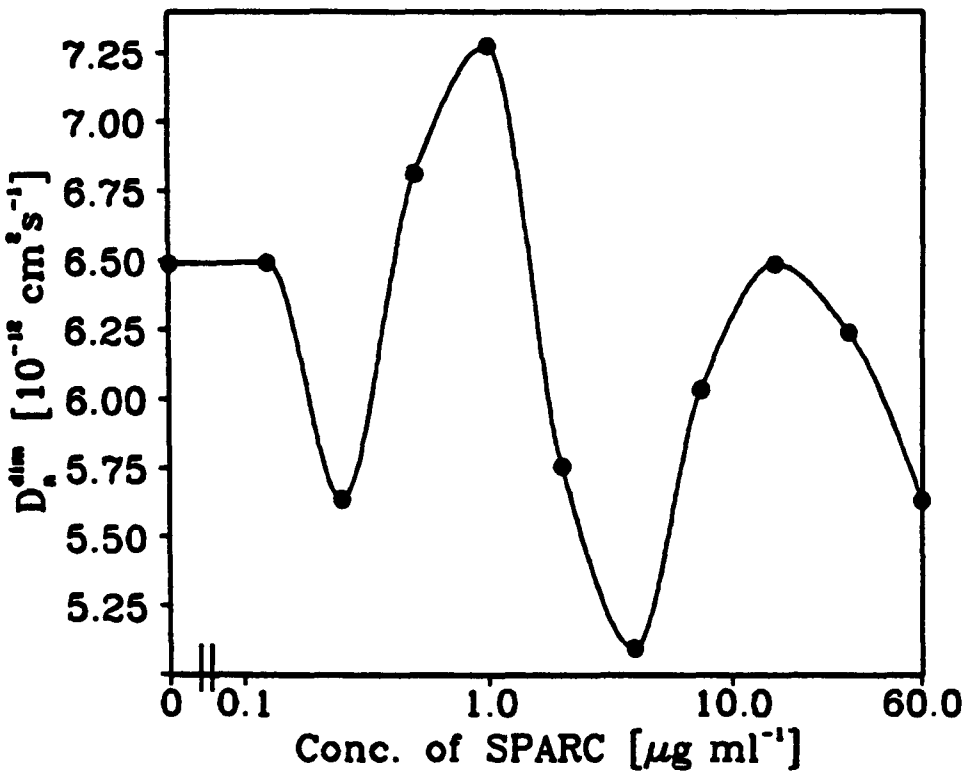

Figure 5.4: The variation in the dimensional diffusion coefficient of bovine aortic endothelial cells with the concentration of SPARC, as predicted by the model (5.3) and the data of Sage *et al.*, which is illustrated in Figure 5.2. This variation represents a chemokinetic effect of SPARC on the cells. For clarity, we plot the concentrations on a logarithmic scale.

of the cell diffusion coefficient such as $6 \times 10^{-12}\text{cm}^2\text{s}^{-1}$, this corresponds to a dimensional half-life of about 3 hours at the end of the experiment.

The results of Sage *et al.* illustrated in Figure 5.2 enable us to estimate the value of D_n for a range of values of the chemical concentration c, for the SPARC–bovine aortic endothelial cell system. To do this, we must calculate the number of cells that pass through the filter during the five hours of the experiment, as predicted by the model (5.3). The dimensionless flux of cells through the lower surface of the filter is $D_n \partial n/\partial x|_{x=0}$, so that the total number of cells passing onto the lower surface of the filter per unit dimensional area is just

$$N_{cell} = \frac{aD_n}{V_{cell}} \int_0^5 \left. \frac{\partial n}{\partial x} \right|_{x=0} dt \,. \tag{5.4}$$

The variation in the dimensional diffusion coefficient with chemical concentration, as implied by this expression, the model solutions and the data of Sage *et al.*, is illustrated in Figure 5.4.

We consider now the case $c_U = 0$. Equation (5.3b) can then be solved analytically using the method of Fourier transforms. Denoting by $\hat{c}(\omega, t)$ the Fourier transform

of $c(x,t)$ with respect to x, we have

$$\frac{\partial \hat{c}}{\partial t} = -D_c \omega^2 \hat{c} \quad \Longrightarrow \quad \hat{c} = \hat{c}(\omega,0) e^{-D_c \omega^2 t} = e^{-D_c \omega^2 t} \int_{-\infty}^{1} e^{-i\omega\xi} d\xi \,,$$

since $c(x,0) = 1$ for $x < 1$ and $c(x,0) = 0$ for $x > 1$. Thus

$$\begin{aligned}
c(x,t) &= \frac{1}{2\pi} \int_{\omega=-\infty}^{+\infty} e^{-D_c \omega^2 t} e^{+i\omega x} \int_{\xi=-\infty}^{1} e^{-i\omega\xi} \, d\xi \, d\omega \\
&= \frac{1}{2\pi} \int_{\xi=-\infty}^{1} \exp\left[-\left\{ \frac{(\xi - x)^2}{4 D_c t} \right\} \right] \int_{\omega=-\infty}^{\infty} \exp\left[-\left\{ \omega \sqrt{D_c t} + \frac{i(\xi - x)}{2\sqrt{D_c t}} \right\}^2 \right] d\omega \, d\xi \\
&= \frac{1}{2\pi} \int_{-\infty}^{1} \exp\left[-\left\{ \frac{(\xi - x)^2}{4 D_c t} \right\} \right] \cdot \left(\frac{\pi}{D_c t} \right)^{1/2} d\xi \\
&= \frac{1}{\sqrt{\pi}} \int_{-\infty}^{(1-x)/\sqrt{4 D_c t}} \exp(-\zeta^2) \, d\zeta \\
&= \frac{1}{2} + \frac{1}{2} \operatorname{erf}\left[\frac{1 - x}{\sqrt{4 D_c t}} \right] .
\end{aligned} \tag{5.5}$$

The value of the value parameter D_c can be estimated theoretically. A straightforward calculation using kinetic theory and Stokes' law for viscous drag implies that for a substance such as SPARC that is composed of approximately spherical molecules which have few interactions with water molecules, the diffusion coefficient in aqueous solution is given by $kT/(6\pi\eta r)$ (Barrow, 1981; Berg and Von Hippel, 1985). Here k is the Boltzmann constant, T is the absolute temperature, η is the viscosity of water at temperature T, and r is the effective radius of a molecule of SPARC in aqueous solution. We can relate r to the specific volume v of SPARC, that is the volume of SPARC per unit mass when in aqueous solution:

$$\frac{4\pi r^3}{3} = v \cdot \begin{pmatrix} \text{mass of one} \\ \text{molecule} \\ \text{of SPARC} \end{pmatrix} = v \cdot \frac{M}{N_A}$$

where M is the molecular weight of SPARC (43,000), and N_A is the Avagadro constant. Thus we have a theoretical estimate for the diffusion coefficient of SPARC in aqueous solution,

$$D_{theor} = \frac{kT}{6\pi\eta} \cdot \left[\frac{4\pi N_A}{3Mv} \right]^{1/3} .$$

The specific volume v has not, to our knowledge, been measured for SPARC. However, for a wide range of other high molecular weight proteins, the specific volume lies between 0.71 and 0.75ml g^{-1} at 20 °C (Barrow, 1981). The experiments of Sage *et al.*

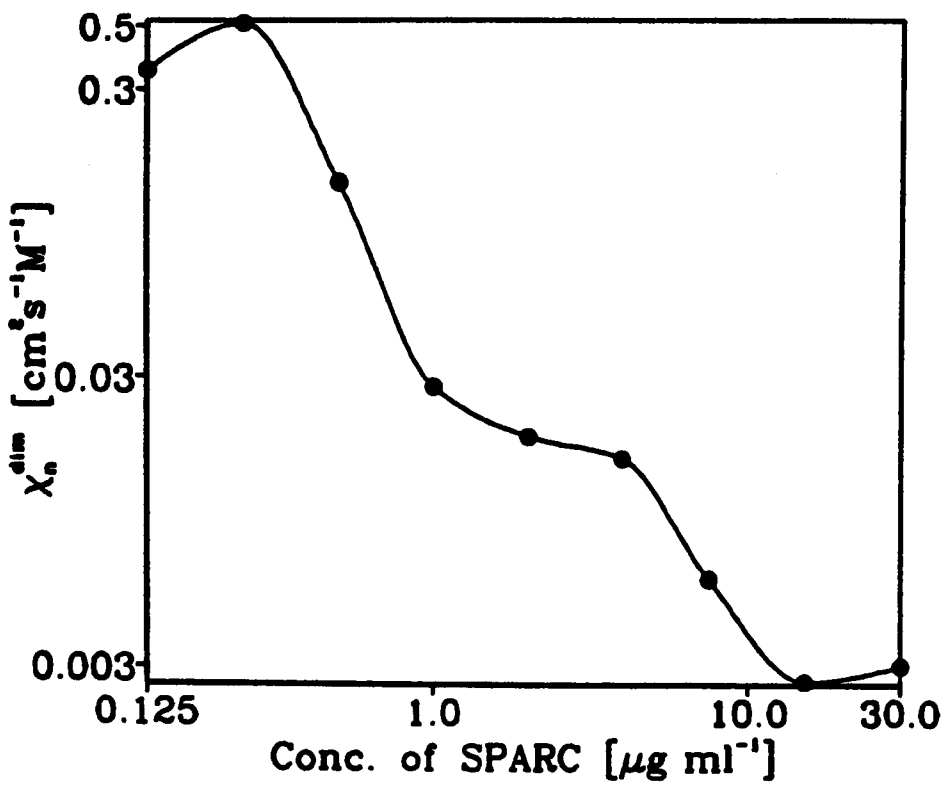

Figure 5.5: The variation in the dimensional chemotaxis coefficient of bovine aortic endothelial cells with the concentration of SPARC, as predicted by the model (5.3), the integral (5.4) and the data of Sage *et al.*, which is illustrated in Figure 5.2. For clarity, we use logarithmic scales on both axes.

were carried out at 37°C, however, and specific volume increases with temperature. We estimate this increase from the tabulated variation in the densities of water and ethyl alcohol with temperature. For these two liquids, the reciprocal of the density increases by 0.49% and 1.87% respectively when the temperature increases from 20°C to 37°C (Weast, 1989). Therefore, we assume that for SPARC at 37°C, the specific volume v lies between 0.72 and 0.77 $\mathrm{ml\,g^{-1}}$. This implies that to two significant figures, $D_{theor} = 1.4 \times 10^{-6}\mathrm{cm^2 s^{-1}}$. This corresponds to the dimensionless value $D_c = 5000$.

With this estimate for D_c and the solution (5.5) of equation (5.3b), we can use the data of Sage *et al.*, which is illustrated in Figure 5.2, and the numerical solutions of (5.3a), to estimate the value of the chemotaxis parameter χ_n for a range of concentrations of SPARC. These estimated values are illustrated in Figure 5.5. In the numerical solutions of (5.3a) used to determine this figure, we approximated $D_n \equiv D_n|_{c=1/2}$ and $\chi_n \equiv \chi_n|_{c=1/2}$ within the filter. Strictly, the value of c (and thus D_n and χ_n) varies within the filter, with $c|_{x=1} = 1/2$ and $c|_{x=0} = \frac{1}{2}[1+\mathrm{erf}(1/\sqrt{4D_c t})]$. However, these expressions imply that at times greater than 5 minutes after the start

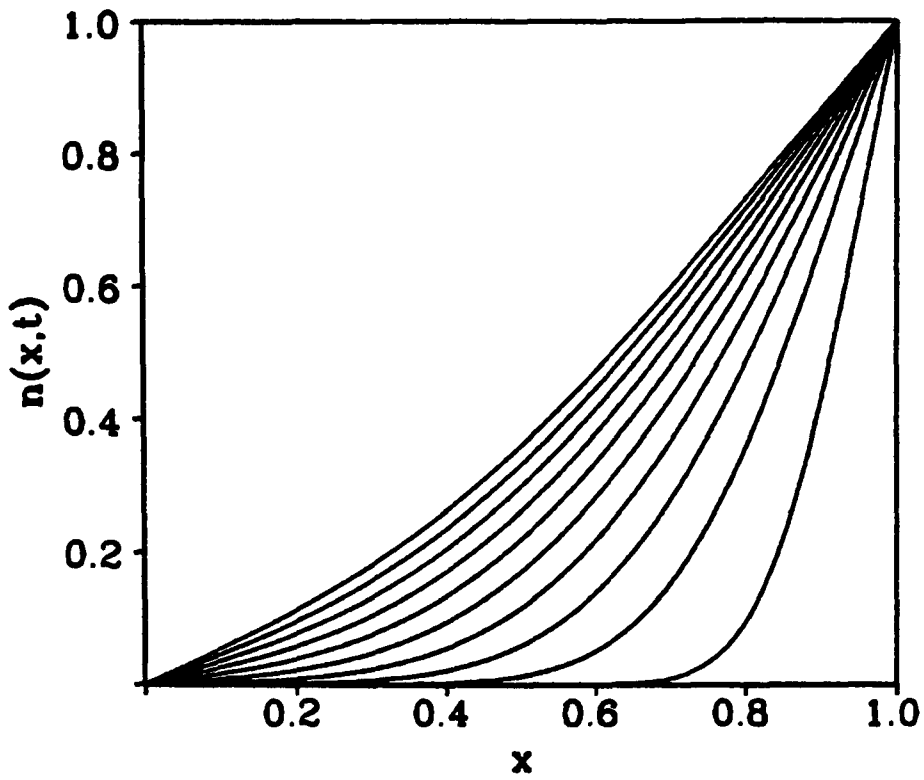

Figure 5.6: The solution for $n(x,t)$ of equations (5.3) when $c_U = 0$. We plot $n(x,t)$ against x at time intervals of 30 minutes for a dimensional cellular diffusion coefficient of $6 \times 10^{-12} \text{cm}^2\text{s}^{-1}$, with $\chi_n = 20$. The dimensional value corresponding to this typical dimensionless value depends on c_L (Figure 5.5). We take the diffusion coefficient of SPARC as $1.4 \times 10^{-6} \text{cm}^2\text{s}^{-1}$, which is the theoretical estimate derived in the text. The solution approaches the steady state $n = x$ more rapidly than in the case $c_U = 1$.

of the experiment, the value of c varies by less than 1% across the filter. Thus, since D_n and χ_n do not vary too rapidly with c (see Figures 5.4 and 5.5 respectively), the approximations of constant D_n and χ_n are reasonable. A typical numerical solution of (5.3a) when $c_U = 0$ is illustrated in Figure 5.6: the solution approaches the steady state $n = x$ more rapidly than in the case $c_U = 1$.

Shortcomings of the model

Using the data of Sage *et al.* on the movement of bovine aortic endothelial cells in response to concentration gradients of SPARC, we have been able to make quantitative estimates of the values of the diffusion and chemotaxis coefficients in the simple model (5.2) at different chemical concentrations, for this cell-chemical system. We could now apply this model to the process of *in vivo* angiogenesis, using this predicted variation in the transport coefficients. However, we feel that to specify a parameter variation such as that illustrated in Figure 5.4 or 5.5 runs counter to the basic philosophy underlying deterministic modelling of biological systems. The aim

of a mathematical model is to predict the complex behaviour of a biological system from simple rules reflecting the underlying biology. Thus, rather than specifying the parameter variations we have discussed, in the remainder of this chapter we develop a model which will predict such variations by addressing the receptor kinetics controlling cell-chemical interactions.

5.3 An Improved Model

The interaction between the receptors for a movement regulating chemical on the surface of a eukaryotic cell and the molecules of that chemical can be reasonably represented by the following simple scheme:

$$\underset{\text{chemical}}{\text{Extracellular}} + \underset{\text{the cell surface}}{\text{Receptors on}} \underset{k_d}{\overset{k_a}{\rightleftharpoons}} \underset{\text{chemical complex}}{\text{Bound receptor-}} \xrightarrow{k_i} \underset{\text{chemical complex}}{\text{Internalized receptor-}}$$

(Sullivan and Zigmond, 1980; Omann *et al.*, 1987; Zigmond *et al.*, 1982). Here k_a, k_d and k_i are respectively the rate constants for the processes of association, dissociation and internalization of the receptor-chemical complex on the cell surface. In the absence of spatial variations, the law of mass action then implies

$$\frac{\partial c}{\partial t} = k_d u - k_a c R \tag{5.6a}$$

$$\frac{\partial u}{\partial t} = k_a c R - k_d u - k_i u \tag{5.6b}$$

(see, for example, Segel, 1984). Here $c(\underline{r},t)$, $R(\underline{r},t)$ and $u(\underline{r},t)$ are the concentrations of extracellular chemical, free receptors and bound receptors per unit volume at position $\underline{r}$ and time t; the dynamics of $R(\underline{r},t)$ are discussed below. Following Zigmond (1981), we assume that the chemotactic effect of the chemical is due to differences in the number of bound receptors on opposite sides of a cell, while chemokinesis occurs as a response to the total number of bound receptors. We therefore take the local cell flux to be given by

$$\underline{J}_n = -\underbrace{D_0 \nabla n}_{\substack{\text{Random migration} \\ \text{in the absence} \\ \text{of chemical}}} - \underbrace{D_1 \rho \nabla n}_{\text{Chemokinesis}} + \underbrace{\chi n \nabla \rho}_{\substack{\text{Chemotaxis} \\ \text{and chemokinesis}}} \tag{5.7}$$

where $n(\underline{r},t)$ is the local cell density and $\rho(\underline{r},t)$ is the number of moles of bound receptor per cell. The third term in (5.7) is dependent both on the magnitude and direction of $\nabla\rho$, and thus represents a combination of chemotaxis and chemokinesis, under the definitions of Keller *et al.* (1977), discussed on page 150. Movement of receptors in space occurs only via passive convection with the cells, so that the flux of bound receptors at any point is given by $\rho\underline{J}_n$.

Substituting these expressions for spatial flux into (5.6) gives

$$\frac{\partial n}{\partial t} = -\nabla\cdot\underline{J}_n \tag{5.8a}$$

$$\frac{\partial c}{\partial t} = D_c\nabla^2 c + k_d u - k_a c R \tag{5.8b}$$

$$\frac{\partial u}{\partial t} = -\nabla\cdot(\rho\underline{J}_n) + k_a c R - k_d u - k_i u\,, \tag{5.8c}$$

where as in the previous section, D_c is the diffusion coefficient of the extracellular chemical. The dynamics of R, the number of free receptors per unit volume, depends on the processes of intracellular recycling of receptors and release of receptors from an intracellular pool, as discussed in Section 5.1. Though only partially understood, these processes are known to be extremely complex, and have been modelled in detail by a number of previous authors. Zigmond *et al.* (1982) investigated the kinetics of intracellular processing of peptide receptors on leukocytes. Despite a number of simplifications, their model consists of seven coupled nonlinear differential equations. Their model addresses only the kinetics of receptor processing, and makes no reference to the effects on cell movement. There is also an extensive literature on the mathematical modelling of intercellular communication by cyclic AMP waves in *Dictyostelium discoideum* (Martiel and Goldbeter, 1982; Tyson and Murray, 1989; Monk and Othmer, 1990). Again, these are complex models which take no account of cell movement. Moreover, the quantitative data available on the rates at which receptor recycling and release occur are extremely limited.

Therefore, rather than adding a large number of additional equations and unknown parameters to (5.8) in an attempt to take R as a dependent variable of the model, we assume that the total number of receptors (bound or free) on the cell surface is an increasing function of the number of bound receptors. That is, we assume

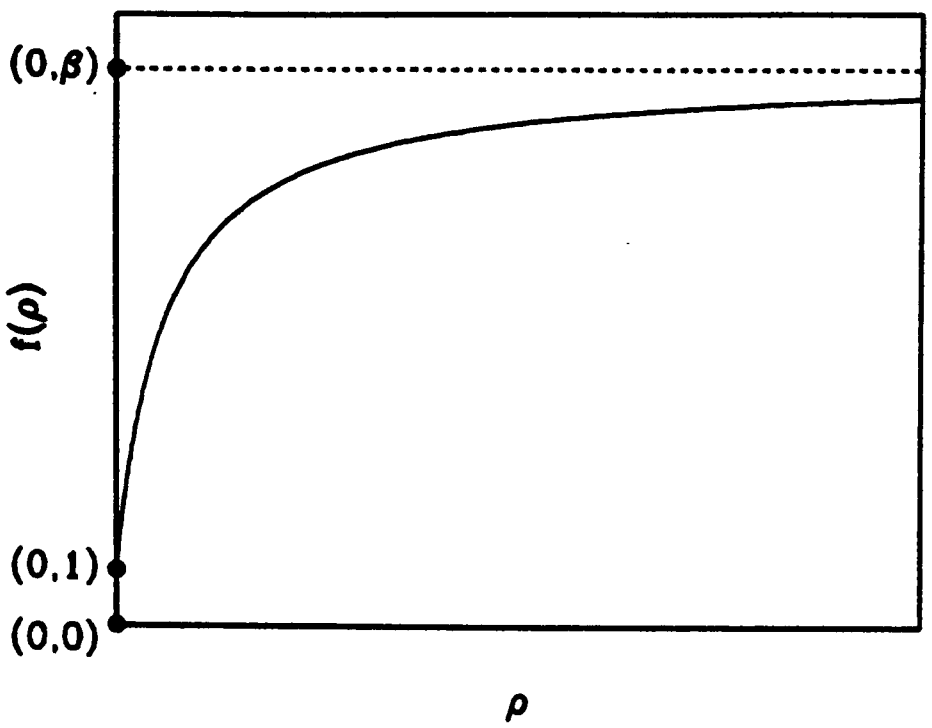

Figure 5.7: The qualitative form required for the function $f(\rho)$, which represents the increase in the total number of receptors (bound or free) per cell due to chemical binding at the cell surface. Receptors are released from an intracellular pool, and also internalized receptors are recycled back to the cell surface.

that $R + u = n\Gamma f(\rho)$, where the constant Γ is the total number of moles of (free) receptors on a cell in the absence of any chemical, and $f(0) = 1$. The increasing function $f(\rho)$ must saturate as $\rho \to \infty$, since there is a finite supply of receptors in the intracellular pool. Thus we require f to have the qualitative form shown in Figure 5.7, and we take a simple functional form corresponding to this, namely $f(\rho) = (\alpha + \beta\rho)/(\alpha + \rho)$, where α and β are positive constants. Substituting this into (5.8) gives

$$\frac{\partial n}{\partial t} = -\nabla \cdot \underline{J}_n \tag{5.9a}$$

$$\frac{\partial c}{\partial t} = D_c \nabla^2 c + k_d u + k_a c u - \Gamma k_a c n \frac{\alpha + \beta\rho}{\alpha + \rho} \tag{5.9b}$$

$$\frac{\partial u}{\partial t} = -\nabla \cdot (\rho \underline{J}_n) + \Gamma k_a c n \frac{\alpha + \beta\rho}{\alpha + \rho} - k_a c u - k_d u - k_i u\,. \tag{5.9c}$$

This is a system of three coupled partial differential equations for four dependent variables, namely cell density $n(\underline{r}, t)$, extracellular chemical concentration $c(\underline{r}, t)$, bound receptor concentration per unit volume $u(\underline{r}, t)$, and number of moles of bound receptor per cell $\rho(\underline{r}, t)$. However, we have the additional relation that when $n \neq 0$,

$\rho = u/n$; when $n = 0$, ρ is undefined. Therefore, when $n \neq 0$,

$$\begin{aligned}\frac{\partial \rho}{\partial t} &= \frac{1}{n}\frac{\partial u}{\partial t} - \frac{u}{n^2}\frac{\partial n}{\partial t} \\ &= -\frac{\underline{J}_n \cdot \nabla \rho}{n} + \Gamma k_a c \frac{\alpha + \beta\rho}{\alpha + \rho} - k_a c \rho - (k_d + k_i)\rho\end{aligned}$$

using (5.9a) and (5.9c). Taking n, c and ρ as the dependent variables, this implies the model equations

$$\frac{\partial n}{\partial t} = -\nabla \cdot \underline{J}_n \tag{5.10a}$$

$$\frac{\partial c}{\partial t} = D_c \nabla^2 c + k_d n \rho + k_a c n \rho - \Gamma k_a c n \frac{\alpha + \beta\rho}{\alpha + \rho} \tag{5.10b}$$

$$\frac{\partial \rho}{\partial t} = -\frac{\underline{J}_n \cdot \nabla \rho}{n} + \Gamma k_a c \frac{\alpha + \beta\rho}{\alpha + \rho} - k_a c \rho - (k_d + k_i)\rho \quad \text{when } n \neq 0, \tag{5.10c}$$

where $\underline{J}_n$ is given in (5.7). The model can also be expressed with n, c and u as dependent variables. However, the resulting conservation equation for u contains a backwards diffusion term, which results in prohibitively large computational expense of numerical solution when the model is applied to the Boyden chamber assay in this form. If $n(\underline{r}, t) = 0$, then $\rho(\underline{r}, t)$ and its derivatives are undefined; the condition $n \geq 0$ then implies that $\nabla n = \underline{0}$. If in addition $\nabla^2 n = 0$, then the value of ρ is immaterial; otherwise, $n \neq 0$ (so that ρ is defined) at points arbitrarily close to $\underline{r}$, and we define $\rho(\underline{r}, t)$ by continuity.

5.3.1 Application to the Boyden chamber assay

We now consider applying this model to the Boyden chamber experiments of Sage *et al.* (in preparation). As in the case of the Keller-Segel model discussed in the previous section, the variable c is defined in both the wells and the filter, that is $-h_{\text{L}} \leq x \leq h_{\text{U}} + a$, in the notation of Figure 5.1, while n is defined only within the filter, $0 \leq x \leq a$. For ρ, the strict inequality $n(x,t) > 0$ holds on $0 < x \leq a$ for all $t > 0$, so that ρ is defined on $0 < x \leq a$ for all $t > 0$. To prove this, suppose that on the contrary a sharp front of cell density exists within the filter, so that at times $t > 0$, $n = 0$ on $0 \leq x \leq \xi(t)$ and $n > 0$ on $\xi(t) < x \leq a$, with $\xi(t)$ a decreasing

function of time, not identically zero. Then $n[\xi(t),t] = 0$ for all t, so that

$$\begin{aligned} 0 &= \frac{d}{dt} n[\xi(t),t] \\ &= \frac{d\xi}{dt}\frac{\partial n}{\partial x}[\xi(t),t] + \frac{\partial n}{\partial t}[\xi(t),t] \\ &= \left\{ \frac{d\xi}{dt} + (D_1 - \chi)\frac{\partial \rho}{\partial x}[\xi(t),t] \right\} \frac{\partial n}{\partial x}[\xi(t),t] + \left\{ D_0 + D_1 \rho[\xi(t),t] \right\} \frac{\partial^2 n}{\partial x^2}[\xi(t),t] \,, \end{aligned} \tag{5.11}$$

using (5.10a); recall that $\rho[\xi(t),t]$ is defined as $\lim_{x \to \xi(t)+} \rho(x,t)$, and we interpret $\partial\rho/\partial x[\xi(t),t]$ as a right-hand derivative. The requirement that $n(x,t) \geq 0$ for all x and t implies that when $\xi(t) > 0$, $\partial n/\partial x[\xi(t),t] = 0$, so that $\partial^2 n/\partial x^2[\xi(t),t] = 0$, from (5.11). Equation (5.10a) then implies that $\partial n/\partial t[\xi(t),t] = 0$, so that n remains zero at $x = \xi(t)$ for all t. Moreover, successive differentiation of (5.10a) with respect to x the implies that as many spatial derivatives of n with respect to x as exist at $x = \xi(t)$ are zero; in particular, if n is infinitely differentiable with respect to x, then n is identically zero on some neighbourhood of $\xi(t)$, which contradicts the original definition of ξ. This phenomenon of the non-existence of sharp fronts is familiar from the diffusion equation (see, for example, Haberman, 1987).

Therefore equations (5.10) apply on the whole of $0 < x < a$ for all $t > 0$. In the well regions, the concentration of SPARC c satisfies the diffusion equation, $\partial c/\partial t = D_c\, \partial^2 c/\partial x^2$; we require continuity of chemical flux, $\partial c/\partial x$, at the ends $x = 0$ and $x = a$ of the filter, with $\partial c/\partial x = 0$ at $x = -h_{\mathrm{L}},\ h_{\mathrm{U}} + a$. As in Section 5.2, we take the boundary conditions satisfied by the cell density to be $n = 0$ at $x = 0$, and $n = 1/V_{cell}$ at $x = a$, where V_{cell} is the volume of an endothelial cell. For ρ, our approximation that the cell density is constant on the top surface of the filter implies that the bound receptor density there changes only as a result of association, dissociation and internalization, so that $\rho(1,t)$ satisfies

$$\frac{d}{dt}\rho(1,t) = \Gamma k_a c(1,t)\frac{\alpha + \beta\rho(1,t)}{\alpha + \rho(1,t)} - k_a c(1,t)\rho(1,t) - [k_d + k_i]\rho(1,t)\,.$$

As a cell emerges onto the lower surface of the filter, it moves rapidly away from the pore, and becomes surrounded by molecules of SPARC. Since the pores represent only about 1% of the total cross-sectional area of the filter, there are then no neighbouring

cells whose free receptors would compete for the binding of these SPARC molecules. Therefore, differences in the number of bound receptors across the length of a cell disappear as the cell emerges from the filter, so that $\partial\rho/\partial x = 0$ at $x = 0$.

5.3.2 Parameter values

In Section 5.2, we established the dimensional parameter values $D_c = 1.4\times10^{-6}\text{cm}^2\text{s}^{-1}$ and $V_{cell} = 1000\mu\text{m}^3$. We will determine the values of the transport coefficients D_0, D_1 and χ by comparing the model predictions with the data of Sage *et al.*, but we must first obtain estimates for the parameters k_a, k_d, k_i, Γ, α and β, which reflect the number and kinetics of the chemical receptors on the cell surface. We are not aware of any relevant quantitative data for the receptors to SPARC on endothelial cells. However, Sklar *et al.* (1984) have made a detailed study of the dynamics of the interaction between an N-formyl peptide and its receptors on human neutrophils. They use fluoresceinated peptide, and investigate the receptor kinetics using a combination of fluorimetric and cytometric techniques; these two experimental procedures are described in detail by Sklar *et al.* (1981) and Finney and Sklar (1983) respectively. They find that the kinetics are highly temperature-dependent: for example, internalization is essentially blocked at 4 °C. However, at 37 °C, they find the rate constants to be $k_a = 10^9\text{M}^{-1}\text{min}^{-1}$, $k_i = 0.24\,\text{min}^{-1}$ and $k_d = 0.35\,\text{min}^{-1}$. For Γ, α and β, recall that Γ is the number of moles of (free) receptor on the cell surface in the absence of chemical, while $\beta\Gamma$ is the upper limit on the total number of moles of receptor (free or bound) on the cell surface, due to the finiteness of the intracellular pool of receptors. Again, data for receptors to SPARC on endothelial cells is not available, but unactivated neutrophils have about 3000 peptide receptors, and this can increase to as much as 100,000 when the cells are exposed to a variety of stimuli (Devreotes and Zigmond, 1988). Therefore, we take $\Gamma = 3000/6.02\times10^{23} = 4.98\times10^{-21}\text{mol}$ and $\beta = 100{,}000/3000 = 33\frac{1}{3}$.

The presence of 100,000 peptide receptors on a neutrophil corresponds to all the receptors in the intracellular pool being released to the surface. This state cannot

be obtained simply by exposure to high concentrations of extracellular peptide: it requires a variety of additional stimuli. Correspondingly, the upper limit on the number of receptors on the cell surface in the model is lower than $\beta\Gamma$, since we require $\Gamma f(\rho) \geq \rho$ (the number of bound receptors cannot be greater than the total number of receptors). The maximum number of moles of receptors that can be expressed simply in response to high levels of extracellular chemical is therefore ρ_{max}, where $\Gamma f(\rho_{max}) = \rho_{max}$. This gives a quadratic equation for ρ_{max}, with unique positive solution

$$\rho_{max} = \frac{1}{2}\left[(\Gamma\beta - \alpha) + \left\{(\Gamma\beta - \alpha)^2 + 4\Gamma\alpha\right\}^{1/2}\right] .$$

When saturated with extracellular peptide in the absence of other stimuli, neutrophils express about 50,000 peptide receptors (Sklar *et al.*, 1984), and we therefore take $\rho_{max} = 50{,}000/6.02 \times 10^{23} = 8.3 \times 10^{-20}$mol, which implies $\alpha = 8.8 \times 10^{-20}$mol.

5.3.3 Nondimensionalization

We nondimensionalize the model (5.10) by defining the following dimensionless quantities, denoted by *:

$$n^* = n \cdot V_{cell} \qquad c^* = c/c_L \qquad \rho^* = \rho/\Gamma \qquad x^* = x/a \qquad t^* = t/T$$

$$D_0^* = D_0 T/a^2 \qquad D_1^* = D_1 T\Gamma/a^2 \qquad D_c^* = D_c T/a^2 \qquad \chi^* = \chi T\Gamma/a^2$$

$$k_a^* = k_a T c_L \qquad k_d^* = k_d T \qquad k_i^* = k_i T \qquad \alpha^* = \alpha/\Gamma \qquad \Gamma^* = \Gamma/(c_L V_{cell})$$

$$h_L^* = h_L/a \qquad h_U^* = h_U/a \qquad c_U^* = c_U/c_L \qquad J_n^* = J_n T V_{cell}/a\,;$$

we take the time scale T as 1 hour. In the remainder of this chapter, we will drop the asterisks denoting dimensionless quantities for notational simplicity, and we will use the superscript $^{\text{dim}}$ to denote the dimensional parameter corresponding to a given dimensionless parameter. With these rescalings, the dimensionless equations representing cell movement in the Boyden chamber are as follows:

$$\text{On } 0 < x < 1: \quad \frac{\partial n}{\partial t} = -\frac{\partial J_n}{\partial x} \tag{5.12a}$$

$$\frac{\partial c}{\partial t} = D_c \frac{\partial^2 c}{\partial x^2} + k_d \Gamma n \rho - k_a \Gamma c n \left\{ \frac{\alpha + \beta\rho}{\alpha + \rho} - \rho \right\} \tag{5.12b}$$

$$\frac{\partial \rho}{\partial t} = -\frac{J_n}{n}\frac{\partial \rho}{\partial x} + k_a c \left\{ \frac{\alpha + \beta\rho}{\alpha + \rho} - \rho \right\} - (k_d + k_i)\rho \tag{5.12c}$$

$$\text{where } J_n = -(D_0 + D_1\rho)\frac{\partial n}{\partial x} + \chi n \frac{\partial \rho}{\partial x}$$

$$\text{On } -h_L < x < 0 \text{ and } 1 < x < h_U: \quad \frac{\partial c}{\partial t} = D_c \frac{\partial^2 c}{\partial x^2}. \tag{5.12d}$$

These equations are subject to the following end conditions:

$$\text{At } t = 0: \quad n = 0 \text{ on } 0 \le x < 1,\ n = 1 \text{ at } x = 1 \tag{5.13a}$$

$$\rho = 0 \text{ on } 0 \le x \le 1 \tag{5.13b}$$

$$c = 1 \text{ on } -h_L \le x < 1,\ c = c_U \text{ on } 1 \le x \le h_U \tag{5.13c}$$

$$\text{At } x = 0: \quad n = 0 \tag{5.13d}$$

$$\frac{\partial \rho}{\partial x} = 0 \tag{5.13e}$$

$$\frac{\partial c}{\partial x} \text{ continuous} \tag{5.13f}$$

$$\text{At } x = 1: \quad n = 1 \tag{5.13g}$$

$$\frac{d\rho}{dt} = k_a c \left\{ \frac{\alpha + \beta\rho}{\alpha + \rho} - \rho \right\} - (k_d + k_i)\rho \tag{5.13h}$$

$$\frac{\partial c}{\partial x} \text{ continuous} \tag{5.13i}$$

$$\text{At } x = -h_L, h_U: \quad \frac{\partial c}{\partial x} = 0. \tag{5.13j}$$

Before discussing the model solutions in detail, we investigate, in the next section, methods of numerical solution. We will then obtain quantitative estimates for the transport coefficients D_0, D_1 and χ, using the experimental results of Sage *et al.* that are illustrated in Figure 5.2. However, before presenting this work, we show the form of the model solutions in Figures 5.8 and 5.9. We plot n, c and ρ against x at a selection of equally spaced times, for the parameter values discussed in Section 5.3.2 and for the estimates of D_0, D_1 and χ obtained in Section 5.5, with initial concentrations

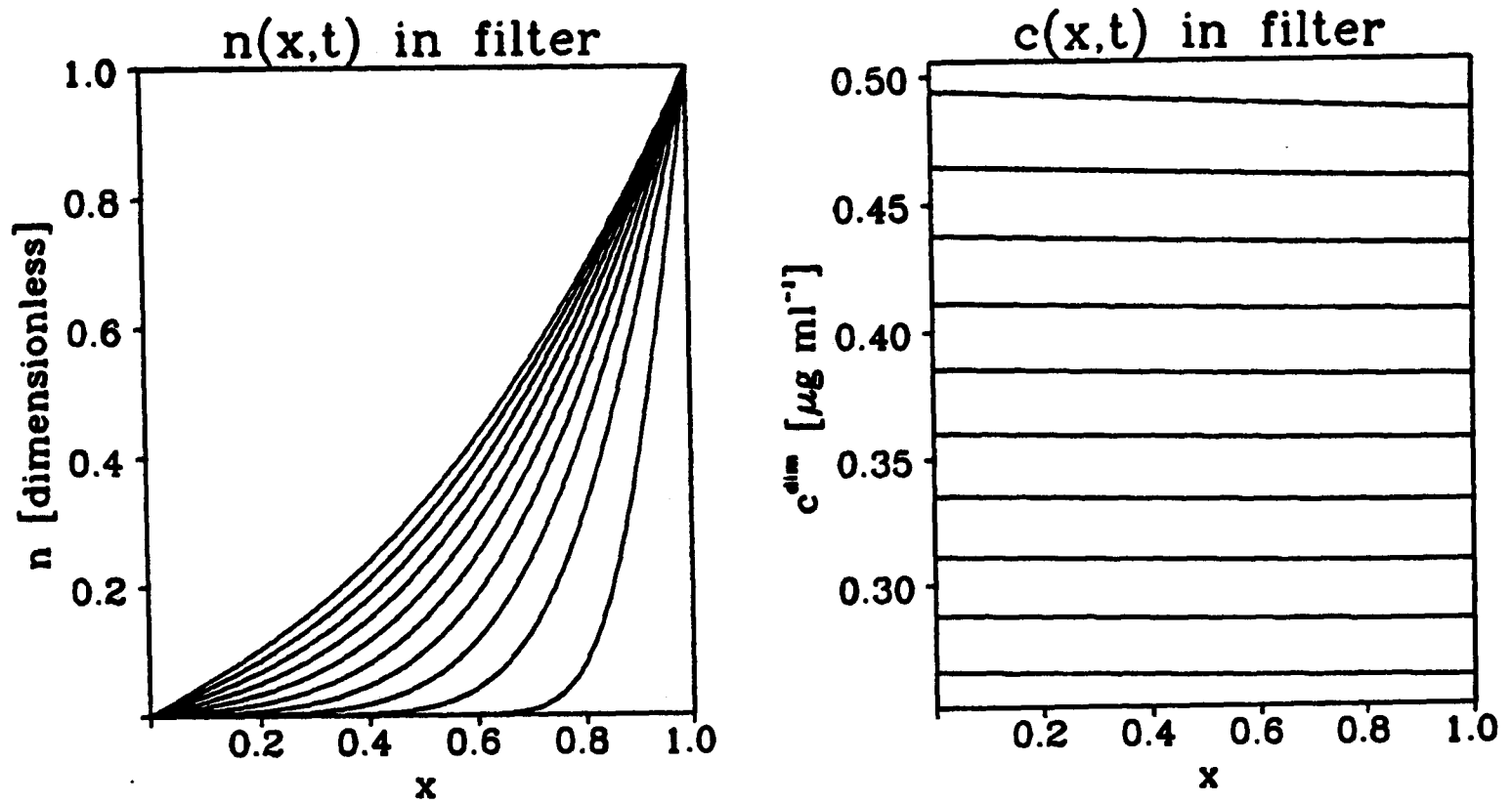

Figure 5.8: Numerical solutions for $n(x,t)$, $c(x,t)$ and $\rho(x,t)$ of (5.12) subject to (5.13), plotted against x at time intervals of 30 minutes. The parameter values are as discussed in Section 5.3.2, with $c_L = 1.0\mu g\,ml^{-1}$ and $c_U = 0$, and with D_0, D_1 and χ as estimated in Section 5.5. The method of numerical solution is as discussed in Section 5.4.

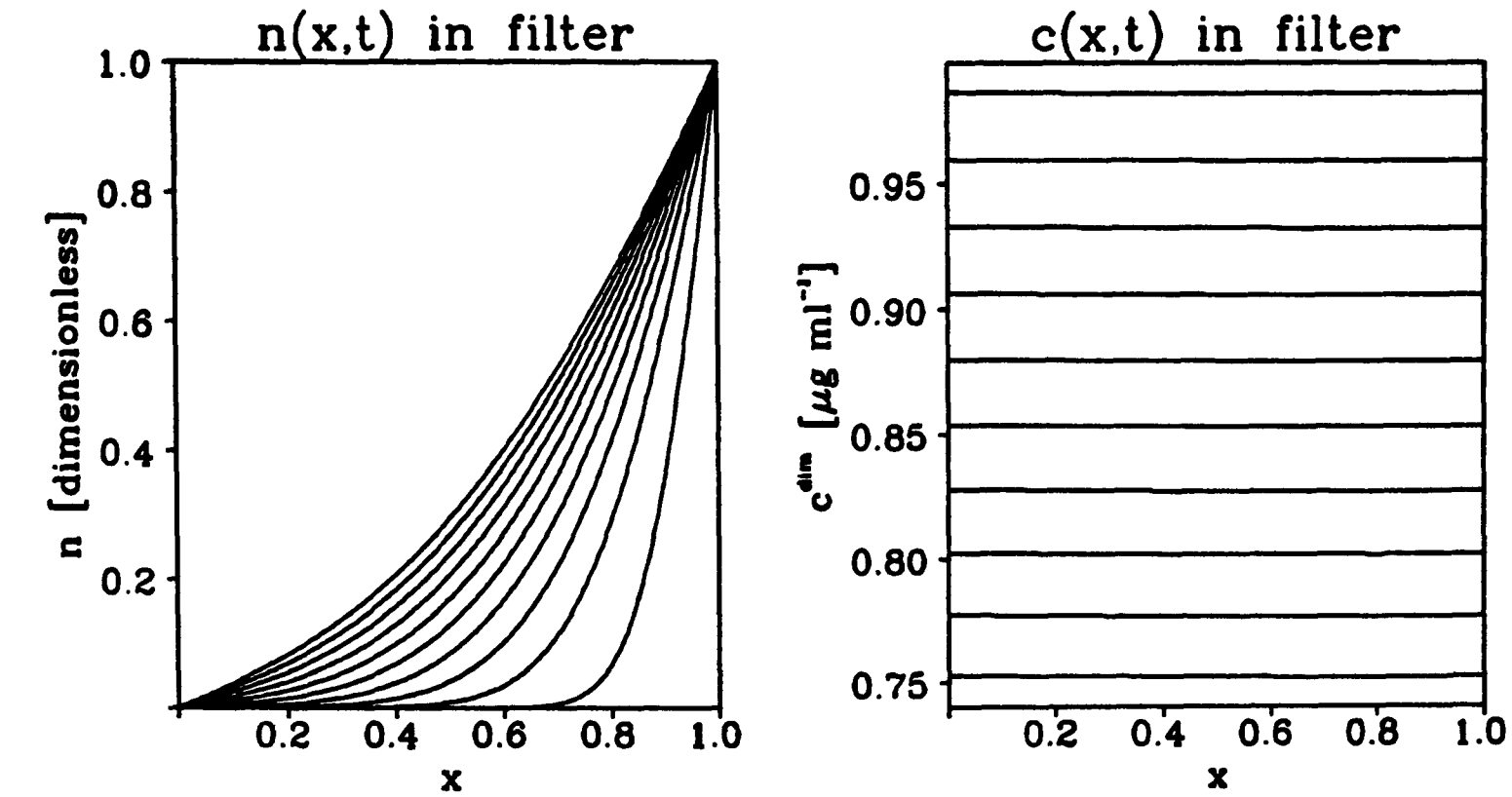

Figure 5.9: Numerical solutions for $n(x,t)$, $c(x,t)$ and $\rho(x,t)$ of (5.12) subject to (5.13), plotted against x at time intervals of 30 minutes. The parameter values are as discussed in Section 5.3.2, with $c_{\text{L}} = c_{\text{U}}^{\text{dim}} = 1.0\mu\text{g ml}^{-1}$, and with D_0, D_1 and χ as estimated in Section 5.5. The method of numerical solution is as discussed in Section 5.4.

of SPARC $c_L = 1.0\mu g\,ml^{-1}$, $c_U = 0$ and $c_L = c_U^{dim} = 1.0\mu g\,ml^{-1}$ respectively. In these figures, it is not immediately clear that conditions (5.13e,f and i) are satisfied, but this is confirmed by detailed numerical investigation. In both cases, a wave of cell density moves through the filter during the experiment. The concentration of extracellular SPARC decreases with time due to rapid binding and internalization of bound receptors at the cell surface, and after an initial rapid rise from zero, the number of these bound receptors per cell also decreases because dissociation and internalization of the receptor-chemical complex occur slightly more rapidly than its association. In both cases, the spatial gradients in both extracellular chemical concentration and bound receptors per cell are quite small.

5.4 Numerical Methods of Solution

Although (5.12) subject to (5.13) is essentially a system of three coupled reaction-diffusion equations, with given initial and boundary conditions, the equations are of a rather non-standard form, so that particular care must be applied when solving the system numerically. For a system of reaction-diffusion equations

$$\frac{\partial \underline{U}}{\partial t} = \underline{\underline{D}}_U \cdot \frac{\partial^2 \underline{U}}{\partial x^2} + \underline{F}(\underline{U}),$$

methods of numerical solution can be broadly divided into three types: explicit, semi-implicit and fully implicit. Denoting the solution at space node i and time step j by $\underline{U}_i^j$, the corresponding discretizations are:

$$\text{Explicit:} \quad \frac{\underline{U}_i^{j+1} - \underline{U}_i^j}{\delta t} = \underline{\underline{D}}_U \cdot \left(\frac{\underline{U}_{i+1}^j - 2\underline{U}_i^j + \underline{U}_{i-1}^j}{\delta x^2} \right) + \underline{F}(\underline{U}_i^j) \tag{5.14a}$$

$$\text{Semi-implicit:} \quad \frac{\underline{U}_i^{j+1} - \underline{U}_i^j}{\delta t} = \text{diag}(\underline{\underline{D}}_U) \cdot \left(\frac{\underline{U}_{i+1}^{j+1} - 2\underline{U}_i^{j+1} + \underline{U}_{i-1}^{j+1}}{\delta x^2} \right) + [\underline{\underline{D}}_U - \text{diag}(\underline{\underline{D}}_U)] \cdot \left(\frac{\underline{U}_{i+1}^j - 2\underline{U}_i^j + \underline{U}_{i-1}^j}{\delta x^2} \right) + \underline{F}(\underline{U}_i^j) \tag{5.14b}$$

$$\text{Fully implicit:} \quad \frac{\underline{U}_i^{j+1} - \underline{U}_i^j}{\delta t} = \underline{\underline{D}}_U \cdot \left(\frac{\underline{U}_{i+1}^{j+1} - 2\underline{U}_i^{j+1} + \underline{U}_{i-1}^{j+1}}{\delta x^2} \right) + \underline{F}(\underline{U}_i^{j+1}) \tag{5.14c}$$

where δx is the space node separation, δt is the time step, and $\text{diag}(\underline{\underline{M}})$ denotes the matrix of the diagonal entries of $\underline{\underline{M}}$, with all off-diagonal entries zero. These categories

refer to the spatial discretization of the equations; here we are, for simplicity, using an Eulerian discretization in time. In Chapter 1, we solved the reaction-diffusion systems (1.1), (1.2) and (1.6) numerically using the method of lines and Gear's method. This is an explicit method, but in contrast to (5.14a), the time discretization corresponds to solving the system of ordinary differential equations

$$\frac{\partial \underline{U}_i}{\partial t} = \underline{\underline{D}}_U \cdot \left(\frac{\underline{U}_{i+1} - 2\underline{U}_i + \underline{U}_{i-1}}{\delta x^2} \right) + \underline{F}(\underline{U}_i)$$

using Gear's method, which is a numerical scheme based on the Adams-Bashforth-Moulton method, and is very much more stable than the simpler Euler scheme (Lambert, 1973); here $\underline{U}_i(t)$ denotes the solution at space node i and time t.

We have used each of the three methods (5.14a,b,c) of numerical solution for (5.12) subject to (5.13). As expected intuitively, the time step δt required for convergence with a given space mesh is smaller for (5.14b) than for (5.14c), and smaller still for (5.14a); this is the well-known phenomenon that feedback stabilizes numerical methods of solution (see, for example, Haberman, 1987). However, numerical solution of the nonlinear algebraic equations (5.14c) for $\{\underline{U}_i^{j+1}, i = 1, \ldots, n_{space}\}$ in terms of $\{\underline{U}_i^j, i = 1, \ldots, n_{space}\}$ required a great deal more processing time than for the linear equations (5.14b), so that the semi-implicit scheme was the most efficient of the three methods; here n_{space} denotes the number of nodes in the space mesh. In the remainder of this section, we present a detailed investigation of the space node separation δx and the time step δt required for convergence of the semi-implicit method of solution. Throughout, we use the dimensionless transport coefficients $D_0 = 3.6 \times 10^{-3}$, $D_1 = 9.7 \times 10^{-4}$, $\chi = 3.6$; the trends we will discuss are the same for a wide range of values of these parameters.

Since the initial conditions for n and c are discontinuous, the solutions of (5.12) subject to (5.13) change rapidly at small times t. Correspondingly, the time step required to give convergence of the semi-implicit method during the early part of the experiment is very small, as illustrated in Table 5.1. In this table we list, for the cases $c_U = 0$ and $c_U^{dim} = c_L$, and for a range of values of c_L, a time step such that the method converges for that time step, but fails to converge when twice that time step is used.

$c_L[\mu g\,ml^{-1}]$	$c_U^{dim}[\mu g\,ml^{-1}]$	*A time step giving convergence*	*Time of onset of instability when twice that time step is used*
0.03	0.0	1.0×10^{-4}	8.0×10^{-4}
0.03	0.03	4.5×10^{-5}	3.6×10^{-4}
1.0	0.0	1.0×10^{-6}	2.9×10^{-3}
1.0	1.0	5.0×10^{-7}	1.3×10^{-3}
30.0	0.0	7.0×10^{-8}	7.0×10^{-7}
30.0	30.0	5.0×10^{-8}	3.0×10^{-7}
60.0	0.0	4.0×10^{-8}	3.2×10^{-7}
60.0	60.0	3.0×10^{-8}	1.8×10^{-7}

Table 5.1: The time step required for initial convergence of the semi-implicit method (5.14b) for numerical solution of (5.12) subject to (5.13). The parameter values are as discussed in Section 5.3.2, with $D_0 = 3.6 \times 10^{-3}$, $D_1 = 9.7 \times 10^{-4}$ and $\chi = 3.6$. For each value of c_U^{dim} and c_L, we give a time step such that the method converges when that time step is used, but fails to converge when twice that time step is used. We also give the time of the onset of numerical instability in the latter case, which we define as the first time at which one of n, c or ρ is negative. In each case, a full numerical blow up ensues.

We also give the dimensionless time at which the numerical method becomes unstable in the latter case. Here we define the onset of instability as the time at which one of the dependent variables n, c or ρ becomes negative; in each case, a full numerical blow up ensues. The time step required for convergence decreases markedly as c_L increases, causing the dimensionless parameters k_a and Γ to increase and decrease respectively. We initially suspected that this decrease was due to changes in the value of ρ: as discussed in Section 5.5, the value of ρ increases with c_L, so that the effective cellular diffusion coefficient $(D_0 + D_1\rho)$ increases, and the effective chemotaxis coefficient $\chi\partial\rho/\partial x$ also changes. These variations in the effective transport coefficients might be expected to affect stability, since such changes are known to control the stability of the explicit method (5.14a) of numerical solution (see page 49). However, careful investigation has shown that in this case the major factor controlling stability is the values of the dimensionless parameters Γ and k_a, which depend on c_L, rather than the values of the transport coefficients.

After rapid initial changes, the solution of (5.12) subject to (5.13) changes more

$c_L[\mu g\,ml^{-1}]$	$c_U^{dim}[\mu g\,ml^{-1}]$	*A value of s_1 giving convergence*	*Time of onset of instability when twice that value is used*
0.03	0.0	7.0×10^{-3}	9.0×10^{-2}
0.03	0.03	3.5×10^{-3}	2.3×10^{-2}
1.0	0.0	8.7×10^{-4}	2.7×10^{-3}
1.0	1.0	8.7×10^{-4}	2.5×10^{-3}
30.0	0.0	3.1×10^{-4}	0.32
30.0	30.0	1.6×10^{-4}	0.31
60.0	0.0	1.0×10^{-4}	0.497
60.0	60.0	5.0×10^{-5}	0.6135

Table 5.2: The value of the time step parameter s_1 required for convergence up to times $t \gg s_0/s_1$ of the semi-implicit method (5.14b) for numerical solution of (5.12) subject to (5.13), when the time step is given by (5.15). The parameter values and the value of s_0 are as in Table 5.1. For each value of c_U^{dim} and c_L, we give a value of s_1 such that the method converges when that value is used, but fails to converge when twice that value is used. We also give the time of the onset of numerical instability in the latter case, which we define as the first time at which one of n, c or ρ is negative. In each case, a full numerical blow up ensues.

slowly with time. We exploited this in our numerical solutions by using a time step which increased with time, namely

$$\delta t = s_0 + s_1 t\,. \tag{5.15}$$

The values of s_0 required for initial convergence as c_L and c_U vary are simply the time steps listed in Table 5.1. In Table 5.2 we list, again for the two cases $c_U = 0$ and $c_U^{dim} = c_L$, and for a range of values of c_L, a value of s_1 giving convergence (when s_0 is sufficiently small), but such that convergence fails when twice that value is used.

This method of increasing the time step as t increased was very successful in reducing the computational expense of solution. However, the time step cannot be increased indefinitely, so that with a time step of the form (5.15), the numerical scheme (5.14b) becomes unstable for sufficiently large t. We therefore used a time step of the form

$$\delta t = \min\{s_0 + s_1 t, s_2\}\,. \tag{5.16}$$

The values of s_2 required for convergence in the various cases are listed in Table 5.3: for small values of c_L, introduction of an upper limit s_2 on the time step was not

$c_L[\mu g\,ml^{-1}]$	$c_U^{dim}[\mu g\,ml^{-1}]$	*The value of s_2 required for convergence up to t=5*
0.03	0.0	–
0.03	0.03	–
1.0	0.0	–
1.0	1.0	3.9×10^{-3}
30.0	0.0	1.9×10^{-4}
30.0	30.0	9.9×10^{-5}
60.0	0.0	9.9×10^{-5}
60.0	60.0	6.1×10^{-5}

Table 5.3: The value, to two significant figures, of the time step parameter s_2 required for convergence up to $t = 5$ of the semi-implicit method (5.14b) for numerical solution of (5.12) subject to (5.13), when the time step is given by (5.16), with the values of s_0 and s_1 as in Tables 5.1 and 5.2 respectively. The parameter values are as in Table 5.1. The first three entries in the table are left blank because a time step of the form (5.15), with s_0 and s_1 as in Tables 5.1 and 5.2 respectively, gives convergence up to $t = 5$ in these cases.

necessary for convergence up to $t = 5$, the end of the experiment. As in Tables 5.1 and 5.2, the numerical method becomes less stable as c_L increases.

To calculate the number of iterations n_{max} required to integrate the model equations up to a time t_{max} when the time step is given by (5.16), we must consider two cases. If $s_0 + s_1 t_{max} \leq s_2$, then throughout the solution, the time t_j at the end of the jth iteration satisfies

$$\begin{aligned} t_j &= t_{j-1} + s_0 + s_1 t_{j-1} \\ &= s_0 + (1 + s_1) t_{j-1} \\ &= s_0 + (1 + s_1) s_0 + (1 + s_1)^2 s_0 + \ldots + (1 + s_1)^{j-1} s_0 \\ &= \frac{s_0}{s_1} \left[(1 + s_1)^j - 1 \right] . \end{aligned}$$

Thus

$$n_{max} = \frac{\log\left(1 + s_1 t_{max}/s_0\right)}{\log(1 + s_1)} \qquad \text{when } t_{max} \leq \frac{s_2 - s_0}{s_1} . \tag{5.17}$$

If $s_0 + s_1 t_{max} \geq s_2$, then (5.17) implies that to integrate the equations up to $t = (s_2 - s_0)/s_1$ takes $\log(s_2/s_0)/\log(1 + s_1)$ iterations. For $t \geq (s_2 - s_0)/s_1$, the time

$c_L[\mu g\,ml^{-1}]$	$c_U^{dim}[\mu g\,ml^{-1}]$	*Number of iterations to integrate up to t=5*
0.03	0.0	840
0.03	0.03	1707
1.0	0.0	9634
1.0	1.0	10439
30.0	0.0	48600
30.0	30.0	91705
60.0	0.0	118653
60.0	60.0	214330

Table 5.4: The number of iterations required to integrate the model equations (5.12) subject to (5.13) up to $t = 5$, the dimensionless duration of the experiments of Sage *et al.* The listed values are calculated using (5.17) and (5.18), with the values of the time step parameters s_0, s_1 and s_2 as in Tables 5.1, 5.2 and 5.3. Each iteration takes an average of about 0.05 seconds of processing time on a 6 MIPS machine.

step has the constant value s_2, so that

$$n_{max} = \frac{1}{s_2}\left[t_{max} - \frac{s_2 - s_0}{s_1}\right] + \frac{\log(s_2/s_0)}{\log(1+s_1)} \qquad \text{when } t_{max} \geq \frac{s_2 - s_0}{s_1}. \tag{5.18}$$

In Table 5.4 we list the values of n_{max} corresponding to $t_{max} = 5$, the dimensionless duration of the experiments of Sage *et al.*, as implied by the values of s_0, s_1 and s_2 given in Tables 5.1, 5.2 and 5.3 respectively. The required number of iterations, and thus the computational expense of solution, increases markedly with c_L.

In our numerical simulations, we used a space mesh which was uniform in the filter region $0 < x < 1$, and which in the well regions increased in a geometric progression, moving away from the filter. In the simulations used to determine Tables 5.1, 5.2 and 5.3, we used $n_f = 60$ and $n_w = 500$, where n_f and n_w are the number of space nodes in the filter and well regions respectively. However, the values of the time step parameters s_0, s_1 and s_2 required for convergence are very insensitive to variations in n_f and n_w, and the values listed in Tables 5.1, 5.2 and 5.3 give convergence for values of n_f and n_w as large as 300 and 2000 respectively. This insensitivity is in marked contrast to the explicit method of numerical solution (5.14a), which we used in Sections 2.2 and 2.3; for the explicit method, convergence requires the time step to be less than a critical value, which is proportional to the square of the space node

n_f	N_{cell} for $c_U^{dim} = c_L$	N_{cell} for $c_U = 0$
60	23.30	130.1
120	23.22	127.4
240	23.20	125.2
480	23.18	123.3
960	23.17	122.2

Table 5.5: The effect of varying the space node separation on the value of N_{cell}, the model prediction of the number of cells per unit area passing through the lower surface of the filter during the experiment. For $c_L = 1.0\mu g\,ml^{-1}$, with both $c_U = 0$ and $c_U^{dim} = c_L$, we list the value of N_{cell}, calculated using (5.19), that is predicted by the semi-implicit method (5.14b) of numerical solution, for a range of values of n_f, the number of space nodes in the filter region. The parameter values are as in Table 5.1, with $n_w = 500$ in each case.

separation (see page 49).

Increasing the values of n_f and n_w above 60 and 500 respectively has a negligible effect on the numerical solutions for n, c and ρ. However, the model predictions of N_{cell}, the number of cells per unit area passing through the lower surface of the filter during the experiment, decreases slightly as n_f increases. The extent of this decrease depends on c_U and c_L, and is illustrated in Table 5.5 for a particularly sensitive case, namely $c_L = 1.0\mu g\,ml^{-1}$, $c_U = 0$, and for comparison, also for the case $c_L = c_U^{dim} = 1.0\mu g\,ml^{-1}$. As a compromise between computational expense and accuracy, we have used $n_f = 240$ and $n_w = 300$ in the simulations discussed in the remainder of the chapter. The results given in Table 5.5 suggest that as c_L varies, the model prediction of N_{cell} with $n_f = 240$ is at worst within a few percent of the true value.

5.5 Application of the Improved Model to the Boyden Chamber Assay

In the previous two sections, we have developed a model for chemically controlled cell movement based on chemical-receptor interactions on the cell surface, and we

have discussed in detail a semi-implicit method for numerical solution of the model equations when applied to the Boyden chamber assay. We now use the data of Sage *et al.*, illustrated in Figure 5.2, to obtain quantitative estimates for the transport coefficients D_0, D_1 and χ; we have obtained estimates for the other parameter values, based on biological data, in Section 5.3.2.

The dimensionless flux of cells through the lower surface of the filter is, for the improved model (5.12), $(D_0 + D_1\rho|_{x=0}) \cdot (\partial n/\partial x)|_{x=0}$. Thus the model prediction of the number of cells passing onto the lower surface of the filter per unit dimensional area during the 5 hours of the experiment is

$$N_{cell} = \frac{a}{V_{cell}} \int_0^5 (D_0 + D_1\rho|_{x=0}) \left.\frac{\partial n}{\partial x}\right|_{x=0} dt\,. \tag{5.19}$$

This expression, together with the numerical method of solution discussed in the previous section, enables us to predict the value of N_{cell} for given values of D_0, D_1, χ, c_U and c_L. However, fitting these predictions to all the experimental data illustrated in Figure 5.2 would be computationally infeasible (see Table 5.4). Rather, we use the estimate for D_0 obtained as $D_n(0)$ in Section 5.2: when there is no chemical present, (5.12) and the simple model (5.3) both reduce to a linear diffusion equation for n. We then estimate D_1 and χ using the results obtained experimentally by Sage *et al.* for the number of cells on the lower surface of the filter after 5 hours, when $c_L = 0.5\mu\text{g ml}^{-1}$, $c_U = 0$, and when $c_L = c_U^{dim} = 0.5\mu\text{g ml}^{-1}$; we select $0.5\mu\text{g ml}^{-1}$ as the concentration giving the greatest difference between the cases $c_U = 0$ and $c_U^{dim} = c_L$ in the experiments of Sage *et al.* This approach gives two coupled nonlinear algebraic equations to be solved for D_1 and χ.

The estimates for the dimensional parameter values obtained in this way are

$$\begin{aligned} D_0^{dim} &= 6.5 \times 10^{-12}\text{cm}^2\text{s}^{-1} \\ D_1^{dim} &= 9.9 \times 10^{9}\text{cm}^2\text{s}^{-1}\text{mol}^{-1} \\ \chi^{dim} &= 1.5 \times 10^{14}\text{cm}^2\text{s}^{-1}\text{mol}^{-1}\,. \end{aligned}$$

With these values, the variation in N_{cell} with c_L in the two cases $c_U = 0$ and $c_U^{dim} = c_L$, as predicted by the model, is shown in Figure 5.10. In both cases, the dose-response

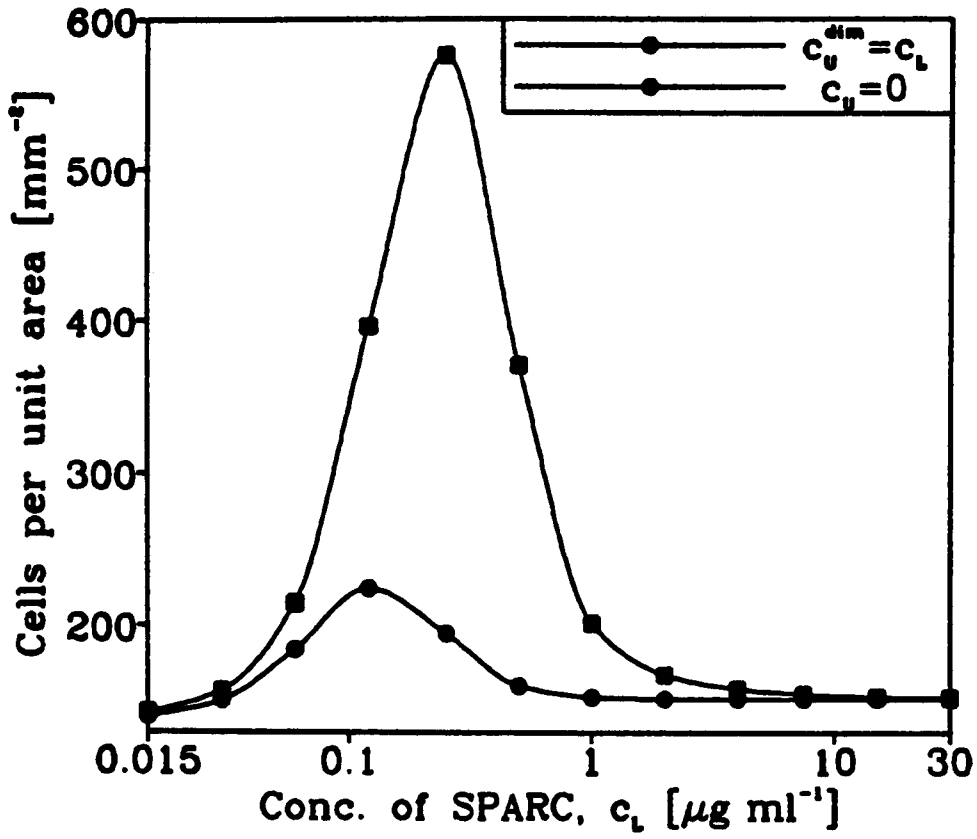

Figure 5.10: The variation with c_L of the model prediction of the number of cells per unit area on the lower surface of the filter after 5 hours. The parameter values are as discussed in Section 5.3.2, with the estimates for D_0, D_1 and χ that are described in the text. The method of numerical solution of (5.12) subject to (5.13) is discussed in Section 5.4, and the number of cells per unit area on the lower surface of the filter at the end of the experiment is calculated using (5.19). For clarity, we plot c_L on a logarithmic scale.

curves are bell-shaped, and this shape of curve has been found in Boyden chamber assays for a wide range of chemicals and cell types (see Bignold, 1988b, for references). For low chemical concentrations, the response is low due to the small number of bound receptors per cell, so that the chemokinetic response is low. In contrast, for high chemical concentrations, the cells are saturated with extracellular chemical, so that the spatial variation in the number of bound receptors per cell, and thus the chemotactic response, is low. In comparison to the case $c_U = 0$, when $c_U^{dim} = c_L$ the number of bound receptors per cell is larger due to the higher extracellular chemical concentration in the filter, but the consequent increase in chemokinetic response is smaller than the reduction in chemotactic response, which results from the lower spatial gradient in extracellular chemical concentration and thus in the number of bound receptors per cell. These trends are illustrated in Figures 5.11, 5.12, 5.13 and 5.14, in which we plot the solutions of (5.12) subject to (5.13) for $c_L = 0.03\mu g\,ml^{-1}$ and $c_L = 30\mu g ml^{-1}$, with $c_U = 0$ and $c_U^{dim} = c_L$ in both cases.

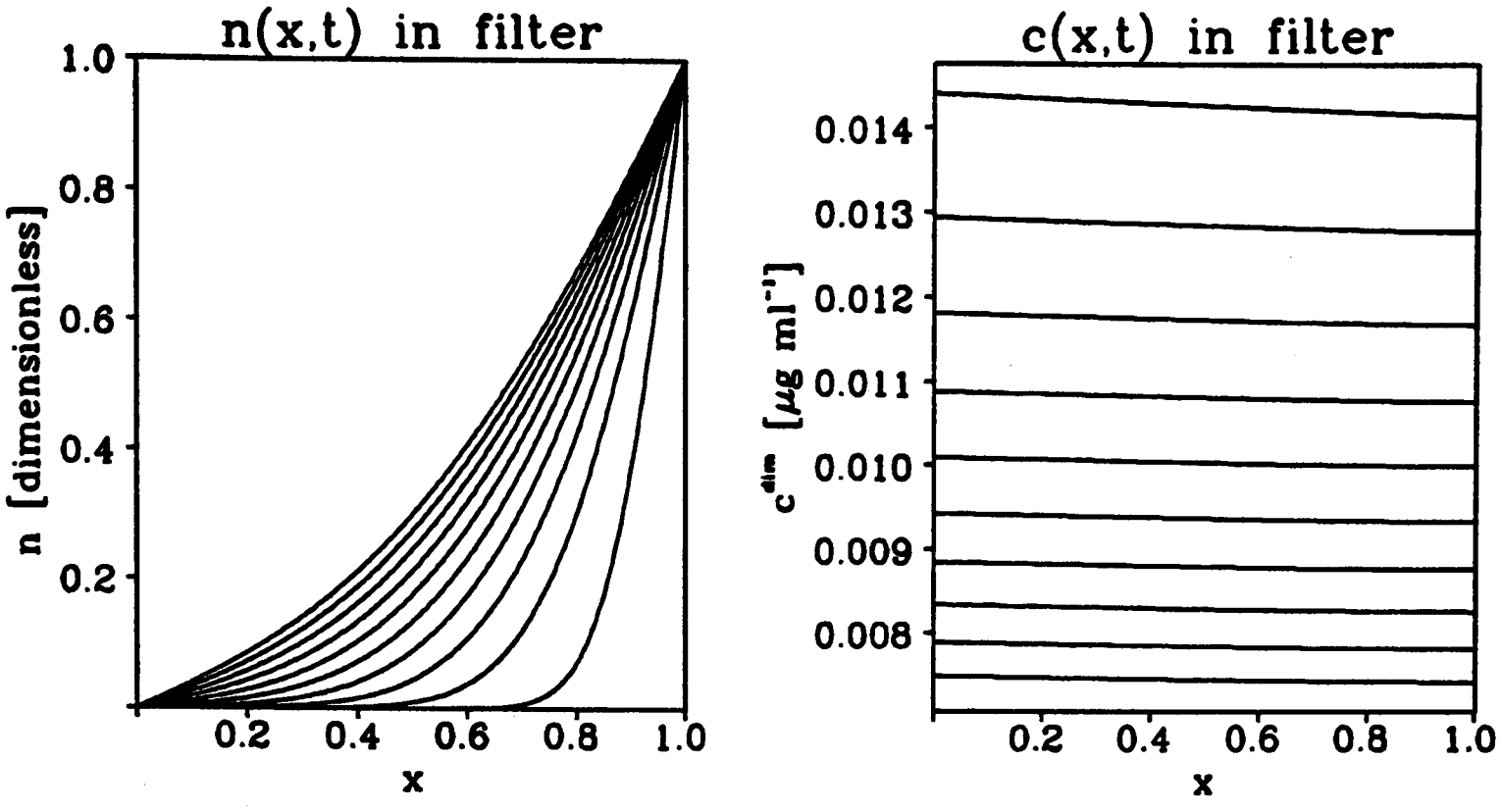

Figure 5.11: Numerical solutions for $n(x,t)$, $c(x,t)$ and $\rho(x,t)$ of (5.12) subject to (5.13), plotted against x at time intervals of 30 minutes. The parameter values are as in Figure 5.10, with $c_{\text{L}} = 0.03\mu\text{g ml}^{-1}$ and $c_{\text{U}} = 0$.

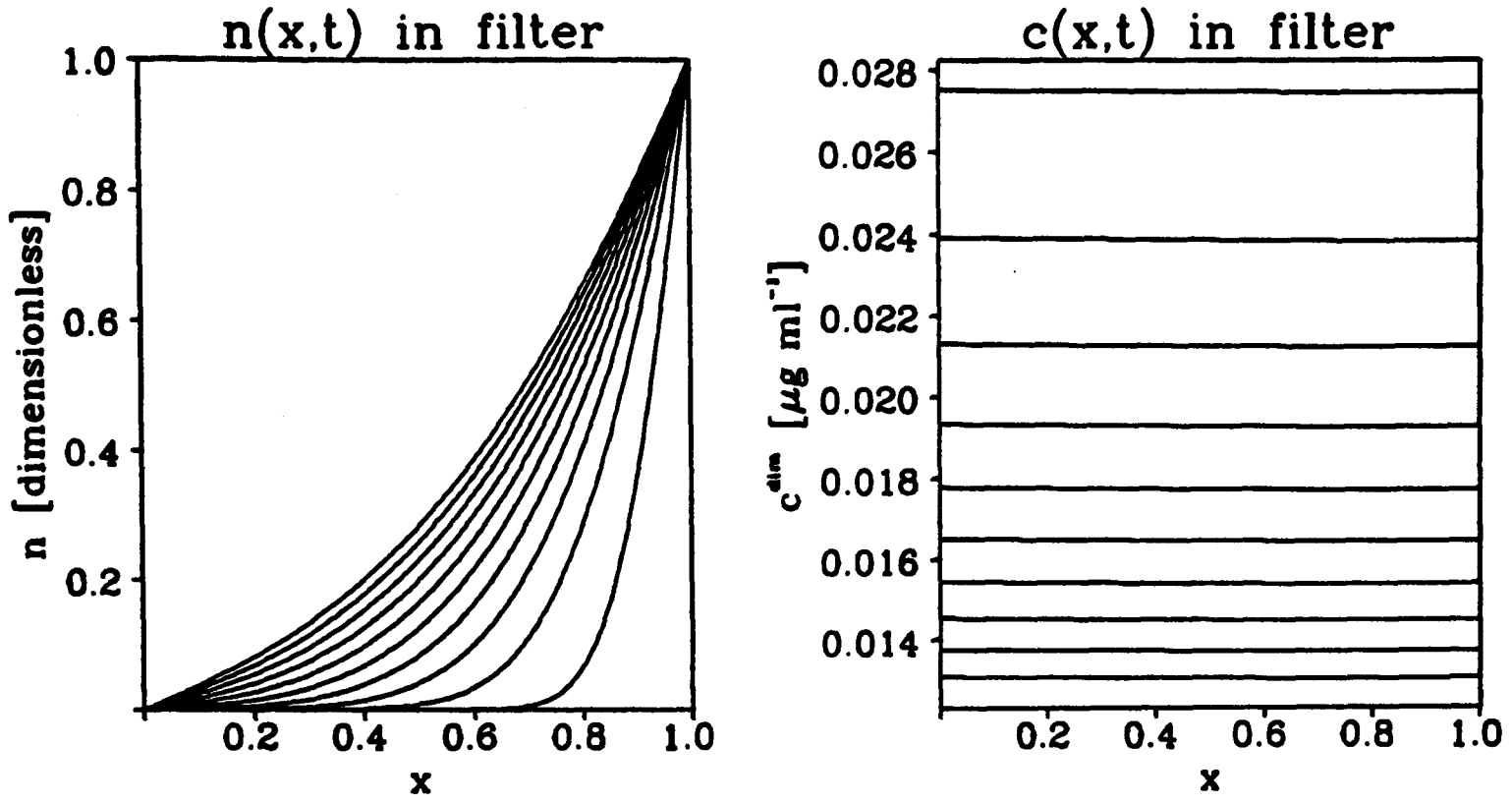

Figure 5.12: Numerical solutions for $n(x,t)$, $c(x,t)$ and $\rho(x,t)$ of (5.12) subject to (5.13), plotted against x at time intervals of 30 minutes. The parameter values are as in Figure 5.10, with $c_{\mathrm{L}} = c_{\mathrm{U}}^{\mathrm{dim}} = 0.03\mu\mathrm{g\,ml}^{-1}$.

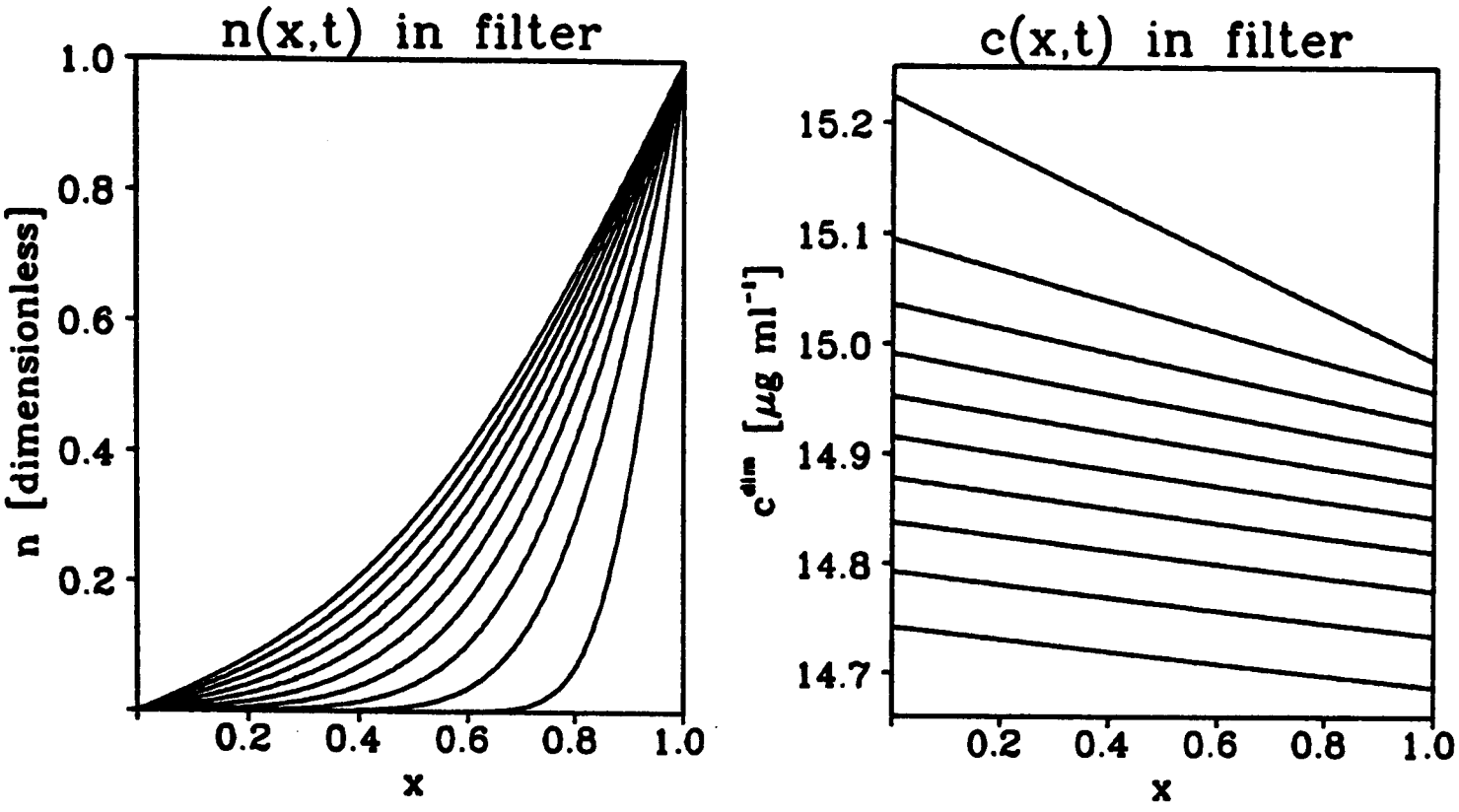

Figure 5.13: Numerical solutions for $n(x,t)$, $c(x,t)$ and $\rho(x,t)$ of (5.12) subject to (5.13), plotted against x at time intervals of 30 minutes. The parameter values are as in Figure 5.10, with $c_L = 30\mu g\,ml^{-1}$ and $c_U = 0$.

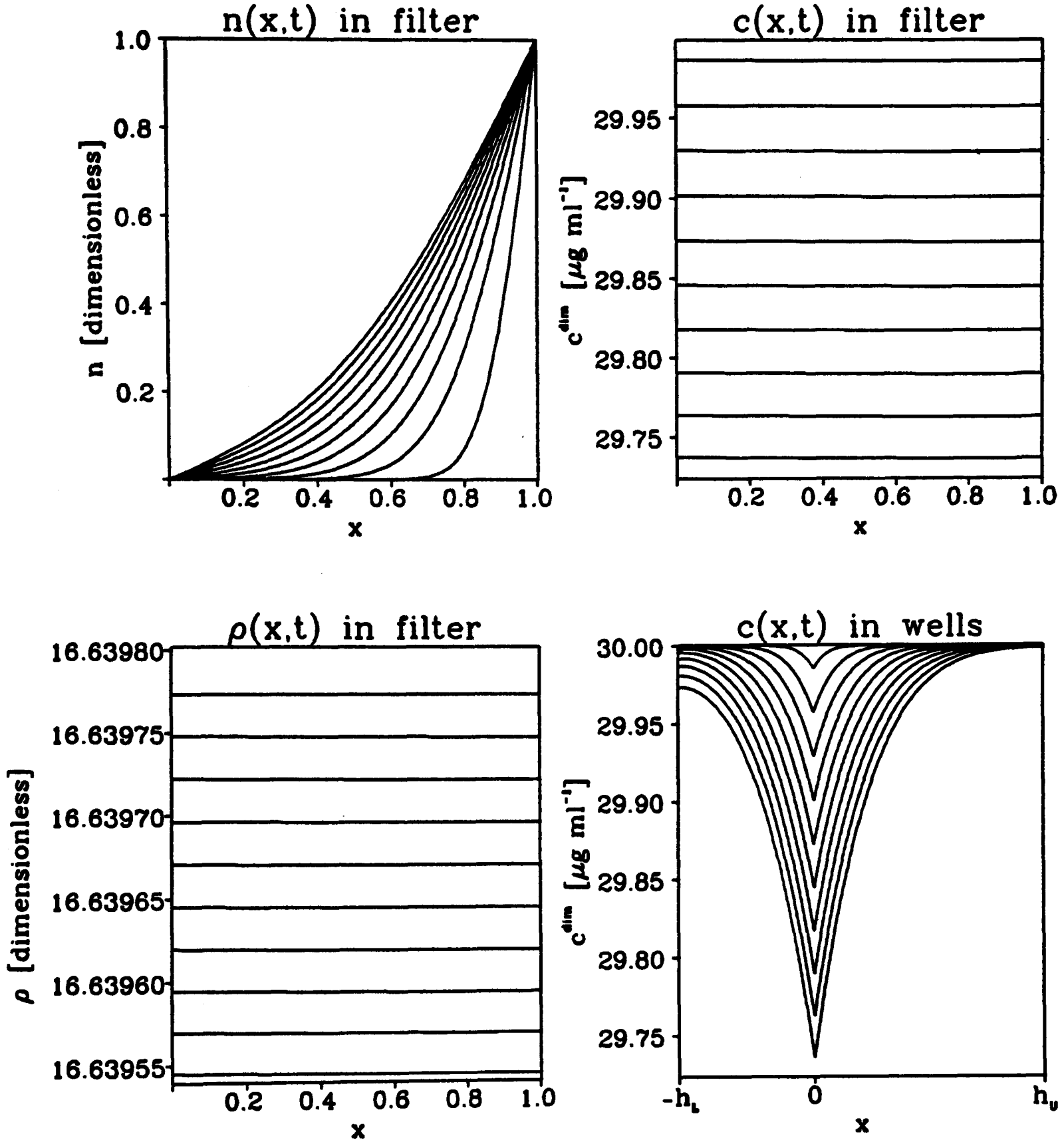

Figure 5.14: Numerical solutions for $n(x,t)$, $c(x,t)$ and $\rho(x,t)$ of (5.12) subject to (5.13), plotted against x at time intervals of 30 minutes. The parameter values are as in Figure 5.10, with $c_L = c_U^{dim} = 30\mu g\,ml^{-1}$.

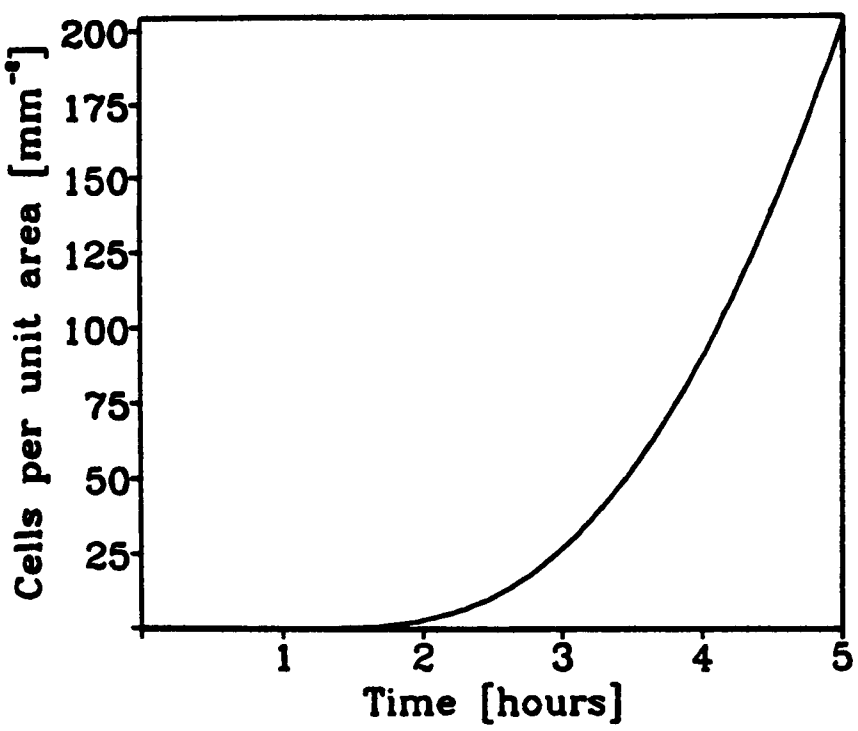

Figure 5.15: The model prediction of the increase with time of the number of cells per unit area on the lower surface of the filter. The parameter values are as in Figure 5.10, and the number of cells per unit area on the lower surface of the filter is calculated as $(a/V_{cell})\int_0^t (D_0 + D_1\rho|_{x=0}) \cdot (\partial n/\partial x)|_{x=0}\, dt'$, which corresponds to the expression (5.19) for the number at $t = 5$.

These should be compared with the solutions for the cases $c_L = 1.0\mu g\,ml^{-1}$, $c_U = 0$ and $c_L = c_U^{dim} = 1.0\mu g ml^{-1}$, which are illustrated in Figures 5.8 and 5.9 respectively. The number of cells on the lower surface of the filter increases gradually during the experiment. The model prediction of this increase is illustrated in Figure 5.15 for the case $c_L = 1.0\mu g\,ml^{-1}$, $c_U = 0$, and the shape of the curve is qualitatively similar for all the values of c_U and c_L we have considered. Quantitative data to which such curves could be compared is not currently available.

The experimental results of Sage *et al.* that are illustrated in Figure 5.2 are only preliminary results. Therefore, the differences between the model predictions illustrated in Figure 5.10 and the experimental results in Figure 5.2 can to some extent be attributed to experimental inaccuracies: additional sets of experiments are currently in progress. However, another major factor responsible for these differences is that the kinetic parameters and receptor numbers will not be exactly the same for the endothelial cell-SPARC system and the leukocyte-peptide system. Thus our estimates for k_a, k_d, k_i, Γ, α and β, based on data for the latter system, are only semi-quantitative when applied to the experiments of Sage *et al.* Experimental work to

determine quantitative data on the receptors to SPARC on endothelial cells is currently in progress (Helene Sage, personal communication, 1990).

5.6 Conclusions

In this chapter, we have developed a new model for chemically controlled cell movement. In contrast to the highly successful model of Keller and Segel (1971a,b), our model reflects the receptor based mechanisms that are responsible for chemotaxis and chemokinesis in eukaryotic cells. We are therefore able to predict the bell-shaped dose-response curves observed experimentally, without externally specifying the dependence of the transport coefficients on extracellular chemical concentration. Using the data of Sage *et al.* (in preparation) on the movement of bovine aortic endothelial cells in response to concentration gradients of SPARC in the Boyden chamber assay, we have quantitatively estimated the values of the transport coefficients in our model for this cell-chemical system; we were able to estimate the other model parameters from data in the biological literature.

The movement of endothelial cells in response to concentration gradients of regulatory chemicals such as SPARC is an important aspect of the process of angiogenesis, in which a dense capillary network enters the granulation tissue of a healing wound. Our model could therefore be used in a study of angiogenesis, and it is also relevant to other processes in which cell influx into the wound space is mediated by chemotactic and chemokinetic factors, in particular the influx of white blood cells during the early "inflammation" phase of healing, and the invasion of the wound space by fibroblasts during the formation of granulation tissue.

The complex mechanisms responsible for mammalian wound healing raise many biological questions that are amenable to theoretical investigation. In this thesis, we have developed and analysed models relevant to three aspects of the healing process: adult epidermal wound healing, embryonic epidermal wound healing, and chemically controlled cell movement. We have made a number of biologically testable predictions, and the work is relevant to both experimental and theoretical cell biologists.

References

Alberts, B., Bray, D., Lewis, J., Raff, M., Roberts, K., Watson, J. D.: The molecular biology of the cell. Garland Publ. Inc., New York (1989).

Albrecht-Buehler, G.: Role of cortical tension in fibroblast shape and movement. *Cell Motil.* **7**: 54-67 (1987).

Arcuri, P. A.: Reaction diffusion mechanisms for biological pattern formation. D.Phil. thesis, University of Oxford (1984).

Aronson, D. G., Cafferelli, L. A., Kamin, S.: How an initially stationary interface begins to move in porous medium flow. *SIAM J. Math. Anal.* **14**: 639-658 (1983).

Barnes, D.: Growth factors involved in the repair process: an overview. *Meth. Enzymol.* **163**: 707-715 (1988).

Barrow, G. M.: Physical chemistry for the life sciences. McGraw-Hill Inc., New York (1981).

Bereiter-Hahn, J.: Epidermal cell migration and wound repair. In: Bereiter-Hahn, J., Matoltsy, A. G., Richards, K. S. (eds.) Biology of the integument, vol. 2: vertebrates. Springer-Verlag, Berlin, pp. 443-471 (1986).

Berg, O. G., Von Hippel, P. H.: Diffusion-controlled macromolecular interactions. *Ann. Rev. Biophys. Biophys. Chem.* **14**: 131-160 (1985).

Beyer, W. H. (ed.): CRC standard mathematical tables, 26th Edition. CRC Press Inc., Boca Raton, Florida, USA (1981).

Bignold, L. P.: Chemotaxis and chemokinesis of neutrophils: a reply. *J. Immunol. Meth.* **110**: 145-148 (1988a).

Bignold, L. P.: Measurement of chemotaxis of polymorphonuclear leukocytes in vitro. *J. Immunol. Meth.* **108**: 1-18 (1988b).

Bonder, E. M., Mooseker, M. S.: Cytochalasin B slows but does not prevent monomer addition at the barbed end of the actin filament. *J. Cell Biol.* **102**: 282-288 (1986).

Boyden, S. V.: The chemotactic effect of mixtures of antibody and antigen on polymorphonuclear leukocytes. *J. Exp. Med.* **115**: 453-466 (1962).

Brugal, G., Pelmont, J.: Existence of two chalone-like substances in intestinal extract from the adult newt, inhibiting embryonic intestinal cell proliferation. *Cell Tissue Kinet.* **8**: 171-187 (1975).

Buettner, H. M., Lauffenburger, D. A., Zigmond, S. H.: Measurement of leukocyte motility and chemotaxis parameters with the Millipore filter assay. *J. Immunol. Meth.* **123**: 25-37 (1989a).

Buettner, H. M., Lauffenburger, D. A., Zigmond, S. H.: Cell transport in the Millipore filter assay. *Am. Inst. Chem. Eng. J.* **35**: 459-465 (1989b).

Canosa, J.: On a nonlinear diffusion equation describing population growth. *IBM J. Res. Dev.* **17**: 307-313 (1973).

Carson, M., Weber, A., Zigmond, S. H.: An actin-nucleating activity in polymorphonuclear leukocytes is modulated by chemotactic peptides. *J. Cell Biol.* **103**: 2707-2714 (1986).

Charnick, S. B., Lauffenburger, D. A.: Mathematical analysis of cell-target encounter rates in three dimensions. *Biophys. J.* **57**: 1009-1023 (1990).

Chen, W.: Mechanism of retraction of the trailing edge during fibroblast movement. *J. Cell Biol.* **90**: 187-200 (1981).

Citi, S., Kendrick-Jones, J.: Regulation of non-muscle myosin structure and function. *Bioessays* **7**: 155-159 (1987).

Clark, R. A. F.: Overview and general considerations of wound repair. In: Clark, R. A. F., Henson, P. M. (eds.) The molecular and cellular biology of wound repair. Plenum press, New York, pp. 3-34 (1988).

Clark, R. A. F.: Wound repair. *Curr. Op. Cell Biol.* **1**: 1000-1008 (1989).

Coffey, R. J., Derynck, R., Wilcox, J. N., Bringman, T. S., Goustin, A. S., Moses, H. L., Pittelkow, M. R.: Production and auto-activation of transforming growth factor–α in human keratinocytes. *Nature* **328**: 817-820 (1987).

Compton, C. C., Gill, J. M., Bradford, D. A., Regauer, S., Galico, C. G., O'Conner, N. E.: Skin regenerated from cultured epithelial autografts on full-thickness burn wounds from 6 days to 5 years after grafting. A light, electron microscope and immunohistochemical study. *Lab. Invest.* **60**: 600-612 (1989).

Cooper, J. A.: Effects of cytochalasin and phalloidin on actin. *J. Cell Biol.* **105**: 1473-1478 (1987).

Courant, R., Hilbert, D.: Methods of mathematical physics. Interscience, New York (1962).

Crosson, C. E., Klyce, S. D., Beuerman, R. W.: Epithelial wound closure in the rabbit cornea. *Invest. Ophthalmol. Vis. Sci.* **27**: 464-473 (1986).

Danjo, S., Friend, J., Throft, R. A.: Conjunctival epithelium in healing of corneal epithelial wounds. *Invest. Ophthalmol. Vis. Sci.* **28**: 1445-1449 (1987).

DeBiasio, R. L., Wang, L. L., Fisher, G. W., Taylor, D. L.: The dynamic distribution of fluorescent analogues of actin and myosin in protrusions at the leading edge of migrating Swiss 3T3 fibroblasts. *J. Cell Biol.* **107**: 2631-2645 (1988).

Dennerll, T. J., Joshi, H. C., Steel, V. L., Buxbaum, R. E., Heidemann, S. R.: Tension and compression in the cytoskeleton of PC-12 neurites II: quantitative measurements. *J. Cell Biol.* **107**: 665-674 (1988).

Devreotes, P. N., Zigmond, S. H.: Chemotaxis in eukaryotic cells: a focus on leukocytes and *Dictyostelium. Ann. Rev. Cell Biol.* **4**: 649-686 (1988).

Dvorak, H. F., Kaplan, A. P., Clark, R. A. F.: Potential functions of the clotting system in wound repair. In: Clark, R. A. F., Henson, P. M. (eds.) The molecular and cellular biology of wound repair. Plenum Press, New York, pp. 57-86 (1988).

Eisinger, M., Sadan, S., Soehnchen, R., Silver, I. A.: Wound healing by epidermal-derived factors: experimental and preliminary chemical studies. In: Barbul, A., Pines, E., Caldwell, M., Hunt, T. K. (eds.) Growth factors and other aspects of wound healing. Alan R. Liss Inc., New York, pp. 291-302 (1988a).

Eisinger, M., Sadan, S., Silver, I. A., Flick, R. B.: Growth regulation of skin cells by epidermal cell-derived factors: implications for wound healing. *Proc. Natl. Acad. Sci. USA* **85**: 1937-1941 (1988b).

Elgjo, K., Reichelt, K. L., Edminson, P., Moen, E.: Endogenous peptides in epidermal growth control. In: Baserga, R., Foa, P., Metcalf, D., Polli, E. E. (eds.) Biological regulation of cell proliferation. Raven Press, New York, pp. 259-265 (1986a).

Elgjo, K., Reichelt, K. L., Hennings, H., Michael, D., Yuspa, S. H.: Purified epidermal pentapeptide inhibits proliferation and enhances terminal differentiation in cultured mouse epidermal cells. *J. Invest. Dermatol.* **87**: 553-558 (1986b).

Elson, E. L.: Cellular mechanics as an indicator of cytoskeletal structure and function. *Ann. Rev. Biophys. Biophys. Chem.* **17**: 397-430 (1988).

Engel, J., Taylor, W., Paulsson, M., Sage, H., Hogan, B.: Calcium binding domains and calcium-induced conformational transition of SPARC/BM–40/Osteonectin, an extracellular glycoprotein expressed in mineralized and nonmineralized tissues. *Biochem.* **26**: 6958-6965 (1987).

Faulstich, E., Trischmann, H., Mayer, D.: Preparation of trimethylrhodaminyl-phalloidin and uptake of the toxin into short-term cultured hepatocytes by endocytosis. *Exp. Cell Res.* **144**: 73-82 (1983).

Ferry, J. D.: Viscoelastic properties of polymers. John Wiley and Sons, New York (1980).

Finney, D. A., Sklar, L. A.: Ligand/receptor internalization: a kinetic, flow cytometric analysis of the internalization of N-formyl peptides by human neutrophils. *Cytometry* **4**: 54-60 (1983).

Fisher, E. S., Lauffenburger, D. A.: Mathematical analysis of cell-target encounter rates in two dimensions. The effect of chemotaxis. *Biophys. J.* **51**: 705-716 (1987).

Fletcher, M. P., Gallin, J. I.: Degranulating stimuli increase the availability of receptors on human neutrophils for the chemoattractant f-Meu-Leu-Phe. *J. Immunol.* **124**: 1585-1588 (1980).

Folkman, J., Moscona, A.: Role of cell shape in growth control. *Nature* **273**: 345-349 (1978).

Forrest, L.: Current concepts in soft connective tissue wound healing. *Br. J. Surg.* **70**: 133-140 (1983).

Forscher, P., Smith, S. J.: Actions of cytochalasins on the organization of actin filaments and microtubules in a neuronal growth cone. *J. Cell Biol.* **107**: 1505-1516 (1988).

Frantz, J. M., Dupuy, B. M., Kaufman, H. E., Beuerman, R. W.: The effect of collagen shields on epithelial wound healing in rabbits. *Am. J. Ophthalmol.* **108**: 524-528 (1989).

Fremuth, F.: Chalones and specific growth factors in normal and tumor growth. *Acta Univ. Carol. Monogr.* **110** (1984).

Furie, B., Furie, B. C.: The molecular basis of blood coagulation. *Cell* **53**: 505-518 (1988).

el-Ghorab, M., Capone, A., Underwood, B. A., Hatchell, D., Friend, J., Throft, R. A.: Response of ocular surface epithelium to corneal wounding in retinol-deficient rabbits. *Invest. Ophthalmol. Vis. Sci.* **29**: 1671-1676 (1988).

Goldbeter, A., Koshland, D. E.: Simple molecular model for sensing and adaptation based on receptor modification with application to bacterial chemotaxis. *J. Mol. Biol.* **161**: 395-416 (1982).

Gordon, S.: The biology of the macrophage. *J. Cell Sci.* Suppl. **4**: 267-286 (1986).

Grotendorst, G. R., Grotendorst, C. A., Gilman, T.: Production of growth factors (PDGF and TGF-β) at the site of tissue repair. In: Barbul, A., Pines, E., Caldwell, M., Hunt, T. K. (eds.) Growth factors and other aspects of wound healing. Alan R. Liss Inc., New York, pp. 47-54 (1988).

Haberman, R.: Elementary applied partial differential equations. Prentice-Hall Inc., Englewood Cliffs, New Jersey, USA (1987).

Halaban, R., Langdon, R., Birchall, N., Cuono, C., Baird, A., Scott, G., Moellmann, G., McGuire, J.: Basic fibroblast growth factor from human keratinocytes is a natural mitogen for melanocytes. *J. Cell Biol.* **107**: 1611-1619 (1988).

Harris, A. K.: Traction, and its relations to contraction in tissue cell locomotion. In: Bellairs, R., Curtis, A., Dunn, G. (eds.) Cell behaviour. Cambridge Univ. Press, Cambridge, England, pp. 109-134 (1982).

Harris, A. K., Stopak, D., Wild, P.: Fibroblast traction as a mechanism for collagen morphogenesis. *Nature* **290**: 249-251 (1981).

Hennings, H., Elgjo, K., Iversen, O. H.: Delayed inhibition of epidermal DNA synthesis after injection of an aqueous skin extract (chalone). *Virchows Arch.* B **4**: 45-53 (1969).

Hergott, G. J., Sandig, M., Kalnins, V. I.: Cytoskeletal organisation of migrating retinal pigment epithelial cells during wound healing in organ culture. *Cell Motil.* **13**: 83-93 (1989).

Hildebrand, F. B.: Finite-difference equations and simulations. Prentice-Hall Inc., Englewood Cliffs, New Jersey, USA (1968).

Irvin, T. T.: The healing wound. In: Bucknall, T. E., Ellis, H. (eds.) Wound healing for surgeons. Bailliere Tindall, Eastbourne, England, pp. 3-28 (1984).

Iversen, O. H.: What's new in endogenous growth stimulators and inhibitors (chalones). *Path. Res. Pract.* **180**: 77-80 (1985).

Iversen, O. H.: The chalones. In: Baserga, R. (ed.) Tissue growth factors. Springer-Verlag, Berlin, pp. 491-550 (1981).

Janmey, P. A., Hvidt, S., Peetermans J., Lamb, J., Ferry, J. D., Stossel, T. P.: Viscoelasticity of F-actin and F-actin/gelsolin complexes. *Biochem.* **27**: 8218-8227 (1988).

Janssens, P. M. W., Van Driel, R.: *Dictyostelium discoideum* cell membranes contain masked chemotactic receptors for cyclic AMP. *FEBS Lett.* **176**: 245-249 (1984).

Jen, C. J., McIntire, L. V., Bryan, J.: The viscoelastic properties of actin solutions. *Arch. Biochem. Biophys.* **216**: 126-132 (1982).

Jensen, P. K., Bolund, L.: Low Ca^{2+} stripping of differentiating cell layers in human epidermal cultures: an *in vitro* model of epidermal regeneration. *Exp. Cell Res.* **175**: 63-73 (1988).

Kath, W. L.: Waiting and propagating fronts in nonlinear diffusion. *Physica* D **12**: 375-381 (1984).

Keller, E. F., Segel, L. A.: Model for chemotaxis. *J. Theor. Biol.* **30**: 225-234 (1971a).

Keller, E. F., Segel, L. A.: Travelling bands of chemotactic bacteria: a theoretical analysis. *J. Theor. Biol.* **30**: 235-248 (1971b).

Keller, H. U., Wilkinson, P. C., Abercrombie, M., Becker, E. L., Hirsch, J. G., Miller, M. E., Ramsey, W. S., Zigmond, S. H.: A proposal for the definition of terms related to locomotion of leucocytes and other cells. *Clin. exp. Immunol.* **27**: 377-380 (1977).

Kevorkian, J., Cole, J. D.: Perturbation methods in applied mathematics. Springer-Verlag, Berlin (1985).

Knerr, B. F.: The porous medium equation in one dimension. *Trans. Amer. Math. Soc.* **234**: 381-415 (1977).

Kolega, J.: Effects of mechanical tension on protrusive activity and microfilament and intermediate filament organization in an epidermal epithelium moving in culture. *J. Cell Biol.* **102**: 1400-1411 (1986).

Kolmogoroff, A., Petovsky, I., Piscounoff, N.: Etude de l'équation de la diffusion avec croissance de la quantité de matière et son application à un problème biologique. *Moscow Univ. Bull. Math.* **1**: 1-25 (1937).

Korn, E. D., Hammer, J. A.: Myosin I. *Curr. Op. Cell Biol.* **2**: 57-61 (1990).

Krawczyk, W. S.: A pattern of epidermal cell migration during wound healing. *J. Cell Biol.* **49**: 247-263 (1971).

Lacey, A. A., Ockendon, J. R., Tayler, A. B.: "Waiting-time" solutions of a nonlinear diffusion equation. *SIAM J. Appl. Math.* **42**: 1252-1264 (1982).

Lambert, J. D.: Computational methods in ordinary differential equations. John Wiley and Sons, New York (1973).

Langanger, G., Moeremans, M., Daniels, G., Sobieszek, A., De Brabander, M., De May, J.: The molecular organization of myosin in stress fibers of cultured cells. *J. Cell Biol.* **102**: 200-209 (1986).

Lauffenburger, D. A., Tranquillo, R. T., Zigmond, S. H.: Concentration gradients of chemotactic factors in chemotaxis assays. *Meth. Enzymol.* **162**: 85-101 (1988).

Lauffenburger, D. A., Zigmond, S. H.: Chemotactic factor concentration gradients in chemotaxis assay systems. *J. Immunol. Meth.* **40**: 45-60 (1981).

Leibovich, S. J., Wiseman, D. M.: Macrophages, wound repair and angiogenesis. In: Barbul, A., Pines, E., Caldwell, M., Hunt, T. K. (eds.) Growth factors and other aspects of wound healing. Alan R. Liss Inc., New York, pp. 131-145 (1988).

Lindquist, G.: Wound healing in case of retarded contraction. *Acta. Chir. Scandinav.* **94**, Suppl. 107: 53-61 (1946).

Madden, M. R., Nolan, E., Finkelstein, J. L., Yurt, R. W., Smeland, J., Goodwin, C. W., Hefton, J., Staiano-Coico, L.: Comparison of an occlusive and a semi-occlusive dressing and the effect of the wound exudate upon keratinocyte proliferation. *J. Trauma* **29**: 924-931 (1989).

Madri, J. A., Pratt, B. M.: Angiogenesis. In: Clark, R. A. F., Henson, P. M. (eds.) The molecular and cellular biology of wound repair. Plenum Press, New York, pp. 337-358 (1988).

Marks, F.: A tissue-specific factor inhibiting DNA synthesis in mouse epidermis. *Natl. Cancer Inst. Monogr.* **38**: 79-90 (1973).

Martiel, J. L., Goldbeter, A.: A model based on receptor desensitization for cyclic-AMP signaling in *Dictyostelium* cells. *Biophys. J.* **52**: 807-828 (1987).

Martin, P., Lewis, J.: The mechanics of embryonic skin wound healing–limb bud lesions in mouse and chick embryos. In: Adzick, N. S., Longaker, M. T. (eds.) Fetal wound healing: a paradigm of tissue repair. Elsevier, New York, in press (1991a).

Martin, P., Lewis, J.: Embryonic wound healing: actin cables and epidermal movement. Submitted (1991b).

Mason, I. J., Taylor, A., Williams, J. G., Sage, H., Hogan, B. L. M.: Evidence from molecular cloning that SPARC, a major product of mouse embryo parietal endoderm, is related to an endothelial cell 'culture shock' glycoprotein of M_r 43 000. *EMBO J.* **5**: 1465-1472 (1986).

Mattey, D. L., Garrod, D. R.: Organization of extracellular matrix by chick embryonic corneal epithelial cells in culture and the role of fibronectin in adhesion. *J. Cell Sci.* **67**: 171-188 (1984).

McDonald, J. A.: Fibronectin: a primitive matrix. In: Clark, R. A. F., Henson, P. M. (eds.) The molecular and cellular biology of wound repair. Plenum Press, New York, pp. 405-436 (1988).

Midwinter, K., McCluskey, J., Martin, P.: Healing of slash lesions to the embryonic chick limb bud. In preparation.

McKenna, N. M., Wang, Y. L., Konkel, M. E.: Formation and movement of myosin-containing structures in living fibroblasts. *J. Cell Biol.* **109**: 1163-1172 (1989).

Monk, P. B., Othmer, H. G.: Cyclic AMP oscillations in suspensions of *Dictyostelium discoideum*. *Phil. Trans. R. Soc.* B **323**: 185-224 (1989).

Morris, A., Tannenbaum, J.: Cytochalasin D does not produce net depolymerization of actin filaments in HEp-2 cells. *Nature* **287**: 637-639 (1980).

Murray, J. D.: Mathematical biology. Springer-Verlag, Berlin (1989).

Murray, J. D.: Asymptotic analysis. Springer-Verlag, Berlin (1984).

Murray, J. D., Maini, P. K., Tranquillo, R. T.: Mechanochemical models for generating biological pattern and form in development. *Phys. Rep.* **171**: 59-84 (1988).

Murray, J. D., Oster, G. F.: Generation of biological pattern and form. *IMA J. Math. Appl. Med. Biol.* **1**: 51-75 (1984).

Nachmias, V. T., Fukui, Y., Spudich, J. A.: Chemoattractant-elicited translocation of myosin in motile *Dictyostelium*. *Cell Motil.* **13**: 158-169 (1989).

Nusgens, B., Merrill, C., Lapiere, C., Bell, E.: Collagen biosynthesis by cells in a tissue equivalent matrix *in vitro*. *Coll. Rel. Res.* **4**: 351-363 (1984).

O'Keefe, E. J., Chiu, M. L., Payne, R. E.: Stimulation of growth of keratinocytes by basic fibroblast growth factor. *J. Invest. Dermatol.* **90**: 767-769 (1988).

Odell, G. M., Oster, G., Alberch, P., Burnside, B.: The mechanical basis of morphogenesis. *Devel. Biol.* **85**: 446-462 (1981).

Odland, G. F.: Structure of the skin. In: Goldsmith, L. A. (ed.) Biochemistry and physiology of the skin. Oxford Univ. Press, Oxford, England, pp. 3-63 (1983).

Okubo, A.: Diffusion and ecological problems: mathematical models. Springer-Verlag, Berlin (1980).

Oliveira-Pinto, F., Conolly, B. W.: Applicable mathematics of non-physical phenomena. John Wiley and Sons, New York (1982).

Omann, G. M., Allen, R. A., Bokosh, G. M., Painter, R. G., Traynor, A. E., Sklar, L. A.: Signal transduction and cytoskeletal activation in the neutrophil. *Physiol. Rev.* **67**: 285-322 (1987).

Ortonne, J. P., Loning, T., Schmitt, D., Thivolet, J.: Immunomorphological and ultrastructural aspects of keratinocyte migration in epidermal wound healing. *Virchows Arch.* A **392**: 217-230 (1981).

Oster, G. F.: On the crawling of cells. *J. Embryol. exp. Morphol.* **83** Suppl.: 329-364 (1984).

Oster, G. F., Murray, J. D., Harris, A. K.: Mechanical aspects of mesenchymal morphogenesis. *J. Embryol. exp. Morphol.* **78**: 83-125 (1983).

Oster, G. F., Murray, J. D., Odell, G. M.: The formation of microvilli. In: Edelman, G. M. (ed.) Molecular determinants of animal form. Alan R. Liss Inc., New York, pp. 365-384 (1985).

Oster, G. F., Odell, G. M.: Mechanics of cytogels I: oscillations in *Physarum*. *Cell Motil.* **4**: 469-503 (1984a).

Oster, G. F., Odell, G. M.: The mechanochemistry of cytogels. *Physica* D **12**: 333-350 (1984b).

Peacock, E. E.: Wound repair. W. B. Saunders and Co., Philadelphia, USA (1984).

Pollard, T. D.: Actin. *Curr. Op. Cell Biol.* **2**: 33-40 (1990).

Radice, G.: The spreading of epithelial cells during wound closure in *xenopus* larvae. *Dev. Biol.* **76**: 26-46 (1980).

Richter, K. H., Schnapke, R., Clauss, M., Furstenberger, G., Hinz, D., Marks, F.: Epidermal G1-chalone and transforming growth factor–β are two different endogenous inhibitors of epidermal cell proliferation. *J. Cell Physiol.* **142**: 496-504 (1990).

Rivero, M. A., Tranquillo, R. T., Buettner, H. M., Lauffenburger, D. A.: Transport models for chemotactic cell populations based on individual cell behaviour. *Chem. Eng. Sci.* **44**: 2881-2897 (1989).

Rudolph, R.: Contraction and the control of contraction. *World J. Surg.* **4**: 279-287 (1980).

Rytömaa, T., Kiviniemi, K.: Regression of generalised leukemia in rat induced by the granulocytic chalone. *Eur. J. Cancer* **6**: 401-410 (1970).

Rytömaa, T., Kiviniemi, K.: Chloroma regression induced by the granulocytic chalone. *Nature* **222**: 995-996 (1969).

Sage, H., Vernon, R. B., Funk, S. E., Everitt, E. A., Angello, J.: SPARC, a secreted protein associated with proliferation, inhibits cell spreading *in vitro* and exhibits Ca^{+2}-dependent binding to the extracellular matrix. *J. Cell Biol.* **109**: 341-356 (1989).

Sato, M., Leimbach, G., Schwarz, W. H., Pollard, T. D.: Mechanical properties of actin. *J. Biol. Chem.* **260**: 8585-8592 (1985).

Sato, M., Schwarz, W. H., Pollard, T. D.: Dependence of the mechanical properties of actin/α-actinin gels on deformation rate. *Nature* **325**: 828-830 (1987).

Schliwa, M.: Action of cytochalasin D on cytoskeletal networks. *J. Cell Biol.* **92**: 79-91 (1982).

Segel, L. A.: Modeling dynamic phenomena in molecular and cellular biology. Cambridge Univ. Press, Cambridge, England (1984).

Segel, L. A.: Mathematics applied to continuum mechanics. Macmillan Publ. Co., New York (1977a).

Segel, L. A.: A theoretical study of receptor mechanisms in bacterial chemotaxis. *SIAM J. Appl. Math.* **32**: 653-665 (1977b).

Segel, L. A.: Incorporation of receptor kinetics into a model for bacterial chemotaxis. *J. Theor. Biol.* **57**: 23-42 (1976).

Segel, L. A., Goldbeter, A., Devreotes, P. N., Knox, B. E.: A mechanism for exact sensory adaptation based on receptor modification. *J. Theor. Biol.* **120**: 151-179 (1986).

Skalli, O., Gabbiani, G.: The biology of the myofibroblast relationship to wound healing. In: Clark, R. A. F., Henson, P. M. (eds.) The molecular and cellular biology of wound repair. Plenum Press, New York, pp. 373-402 (1988).

Sklar, L. A., Finney, D. A., Oades, Z. G., Jesaitis, A. J., Painter, R. G., Cochrane, C. G.: The dynamics of ligand-receptor interactions. *J. Biol. Chem.* **259**: 5661-5669 (1984).

Sklar, L. A., Oades, Z. G., Jesaitis, A. J., Painter, R. G., Cochrane, C. G.: Fluoresceinated chemotactic peptide and high-affinity antifluorescein antibody as a probe of the temporal characteristics of neutrophil stimulation. *Proc. Natl. Acad. Sci. USA* **78**: 7540-7544 (1981).

Snowden, J. M.: Wound closure: an analysis of the relative contributions of contraction and epithelialization. *J. Surg. Res.* **37**: 453-463 (1984).

Sprugel, K. H., McPherson, J. M., Clowes, A. W., Ross, R.: Effects of growth factors *in vivo* I: cell ingrowth into porous subcutaneous chambers. *Am. J. Pathol.* **129**: 601-613 (1987).

Stenn, K. S., DePalma, L.: Re-epithelialization. In: Clark, R. A. F., Henson. P. M. (eds.) The molecular and cellular biology of wound repair. Plenum press, New York, pp. 321-335 (1988).

Stopak, D., Harris, A. K.: Connective tissue morphogenesis by fibroblast traction. I: Tissue culture observations. *Dev. Biol.* **90**: 383-398 (1982).

Sullivan, S. J., Zigmond, S. H.: Chemotactic peptide receptor modulation in polymorphonuclear leukocytes. *J. Cell Biol.* **85**: 703-711 (1980).

Tranquillo, R. T.: Theories and models of gradient perception. In: Armitage, J. P., Lackie, J. M. (eds.) Biology of the chemotactic response. Cambridge Univ. Press, Cambridge, England, pp. 35-75 (1990).

Tranquillo, R. T., Lauffenburger, D. A.: Stochastic model of leukocyte chemosensory movement. *J. Math. Biol.* **25**: 229-262 (1987).

Tranquillo, R. T., Lauffenburger, D. A., Zigmond, S. H.: A stochastic model for leukocyte random motility and chemotaxis based on receptor binding fluctuations. *J. Cell Biol.* **106**: 303-309 (1988).

Trinkaus, J. P.: Cells into organs. The forces that shape the embryo. Prentice-Hall Inc., Englewood Cliffs, New Jersey, USA (1984).

Tyson, J. J., Murray, J. D.: Cyclic AMP waves during aggregation of *Dictyostelium* amoebae. *Development* **106**: 421-426 (1989).

Valberg, P. A., Albertini, D. F.: Cytoplasmic motions, rheology, and structure probed by a novel magnetic particle method. *J. Cell Biol.* **101**: 130-140 (1985).

Van den Brenk, H. A. S.: Studies in restorative growth processes in mammalian wound healing. *Brit. J. Surg.* **43**: 525-550 (1956).

Van Haarstert, P. J. M.: Down-regulation of cell surface cyclic AMP receptors and desensitization of cyclic AMP-stimulated adenylate cyclase by cyclic AMP in *Dictyostelium discoideum.* Kinetics and concentration dependence. *J. Biol. Chem.* **262**: 7700-7704 (1987).

Viggers, R. F., Wechezak, A. R., Sauvage, L. R.: An apparatus to study the response of cultured endothelium to shear stress. *J. Biomech. Eng.* **108**: 332-337 (1986).

Wahl, S. M., Allen, J. B.: T lymphocyte-dependent mechanisms of fibrosis. In: Barbul, A., Pines, E., Caldwell, M., Hunt, T. K. (eds.) Growth factors and other aspects of wound healing. Alan R. Liss Inc., New York, pp. 147-160 (1988).

Wang, Y.: Mobility of filamentous actin in living cytoplasm. *J. Cell Biol.* **105**: 2811-2816 (1987).

Wang, Y.: Exchange of actin subunits at the leading edge of living fibroblasts: possible role of treadmilling. *J. Cell Biol.* **101**: 597-602 (1985).

Watt, F. M., Jordan, P. W., O'Neill, C. H.: Cell shape controls terminal differentiation of human epidermal keratinocytes. *Proc. Natl. Acad. Sci. USA* **85**: 5576-5580 (1988).

Weast, R. C. (ed.): CRC handbook of chemistry and physics. CRC Press Inc., Boca Raton, Florida, USA (1989).

Wechezak, A. R., Viggers, R. F., Sauvage, L. R.: Fibronectin and F-actin redistribution in cultured endothelial cells exposed to shear stress. *Lab. Invest.* **53**: 639-647 (1985).

Wechezak, A. R., Wight, T. N., Viggers, R. F., Sauvage, L. R.: Endothelial adherence under shear stress is dependent upon microfilament reorganisation. *J. Cell Physiol.* **139**: 136-146 (1989).

Wilkinson, P. C.: Chemotaxis and chemokinesis: confusion about definitions. *J. Immunol. Meth.* **110**: 143-144 (1988a).

Wilkinson, P. C.: Reply to the letter of L. P. Bignold. *J. Immunol. Meth.* **110**: 149 (1988b).

Winstanley, E. W.: The epithelial reaction of the healing of excised cutaneous wounds in the dog. *J. Comp. Pathol.* **85**: 61-75 (1975).

Winter, G. D.: Epidermal regeneration studied in the domestic pig. In: Maibach, H. I., Rovee, D. T. (eds.) Epidermal wound healing. Year Book Med. Publ. Inc., Chicago, USA, pp. 71-112 (1972).

Wright, N. A.: Cell proliferation kinetics of the epidermis. In: Goldsmith, L. A. (ed.) Biochemistry and physiology of the skin. Oxford Univ. Press, Oxford, England, pp. 203-229 (1983).

Wulf, E., Deboben, A., Bautz, F. A., Faulstich, H., Wieland, T.: Fluorescent phallotoxin, a tool for the visualization of cellular actin. *Proc. Natl. Acad. Sci. USA* **76**: 4498-4502 (1979).

Yamaguchi, T., Hirobe, T., Kinjo, Y., Manaka, K.: The effect of chalone on the cell cycle in the epidermis during wound healing. *Exp. Cell Res.* **89**: 247-254 (1974).

Zaner, K. S., Hartwig, J. H.: The effect of filament shortening on the mechanical properties of gel-filtered actin. *J. Biol. Chem.* **263**: 4532-4536 (1988).

Zieske, J. D., Higashij, S. C., Spurrmic, S. J., Gipson, I. K.: Biosynthetic response of the rabbit cornea to a keratectomy wound. *Invest. Ophthalmol. Vis. Sci.* **28**: 1668-1677 (1987).

Zigmond, S. H.: Consequences of chemotactic peptide receptor modulation for leukocyte orientation. *J. Cell. Biol.* **88**: 644-647 (1981).

Zigmond, S. H., Sullivan, S. J., Lauffenburger, D. A.: Kinetic analysis of chemotactic peptide receptor modulation. *J. Cell Biol.* **92**: 34-43 (1982).

Zimmerli, W., Seligmann, B., Gallin, J. I.: Exudation primes human and guinea pig neutrophils for subsequent responsiveness to chemotactic peptide N-formylmethionyl-leucylphenylalanine and increases complement component C3bi receptor expression. *J. Clin. Invest.* **77**: 925-933 (1986).